Structural inheritance of the Salta Rift basin and its control on exhumation patterns of the Eastern Cordillera between 23 and 24°S

Willemijn Sarah Maria Theresia van Kooten

Kumulative Dissertation

zur Erlangung des akademischen Grades

DOCTOR RERUM NATURALIUM

(Dr. rer. nat.)

in der Wissenschaftsdiziplin Geologie

eingereicht am

Institut für Geowissenschaften

Mathematisch-Naturwissenschaftliche Fakultät

Universität Potsdam

Datum der Disputation: 03.11.2023

Axams, Dezember 2023

Advisors

apl. Prof. Edward R. Sobel, PhD | University of Potsdam, Germany

Dr. Cecilia E. del Papa | CONICET-Universidad Nacional de Córdoba, Argentina

Reviewers

apl. Prof. Edward R. Sobel, PhD | University of Potsdam, Germany

Prof. David M. Pearson, PhD | Idaho State University, United States of America

Assoc. Prof. Matthias Bernet, PhD | Université Grenoble Alpes, France

Published online on the
Publication Server of the University of Potsdam:
https://doi.org/10.25932/publishup-61798
https://nbn-resolving.org/urn:nbn:de:kobv:517-opus4-617983

Voor mama

"Hurry up Big Panda, we're going to be late!"

Big Panda sat down. "I like to think I'm creating anticipation."

– James Norbury, Big Panda & Tiny Dragon

Eidesstattliche Erklärung

Hiermit erkläre ich, Willemijn Sarah Maria Theresia van Kooten, dass die vorliegende kumulative Dissertation mit dem Titel „Structural inheritance of the Salta Rift basin and its control on exhumation patterns of the Eastern Cordillera between 23 and 24°S“ selbständig von mir, nur mit den angegebenen Quellen und Hilfsmitteln und in eigenen Worten angefertigt wurde. Ich erkläre weiterhin, dass ich alle wörtlichen und sinngemäßen Übernahmen aus Quellen und anderen Werken als solche gekennzeichnet sowie vollständig aufgeführt habe. Zudem bestätige ich, dass die vorliegende Arbeit bisher nicht in dieser oder in anderer Form in einem anderen Prüfungsverfahren vorgelegt wurde und an keiner anderen Hochschule eingereicht wurde.

Axams, den

Willemijn S. M. T. van Kooten

Acknowledgements

For someone raised in what is arguably the flattest country on Earth, mountains are simply magical. When my supervisor, Ed Sobel, offered me the opportunity to work on a PhD project within the StRATEGy international research training group, the prospect of working in one of the largest mountain ranges on Earth was exciting. But beyond breathtaking geology and intriguing scientific questions, the project has offered a sense of community that has accompanied me throughout the years. Within this community, Ed has been an amazing supervisor and mentor on multiple levels, both the academic and personal. He has supported me throughout the entire scientific process – be it in the lab, in the field or while preparing manuscripts. Whenever personal challenges interfered or “life happened”, his door was always open. Ed, thank you for all the guidance that you provided during this journey.

My second supervisor in Argentina, Cecilia del Papa, has also offered invaluable support and input. She especially played an important role in the field and by engaging in discussions on Andean geology. I want to thank her for her unwavering patience and support.

Within the Potsdam geosciences community there have been numerous people who helped me by offering sound advice, opinions and the opportunity to discuss ideas. Especially Manfred Strecker has provided valuable insights and has taken on the mentor role for the Junior Teaching Professionals Program. Christine Fisher has helped in preparing thin sections. Martina Heidemann, Tanja Klaka-Tauscher, Cornelia Becker, Gabriela Da Poian, Verónica Torres Acosta and many more offered administrative and organizational support, which has been essential for completing the project. My fellow PhD colleagues have been the biggest collective source of inspiration, peer support and friendship. Together we have overcome challenges, talked science and generally enjoyed life in Potsdam. I am grateful for the tight community that we built together between Golm, Telegrafenberg and Argentina.

A team of amazing people in Argentina has helped me organize and conduct three successful field seasons. Armando Liques and members of the Hornocal community, Elias Frites, Sebastian Lamas and their families have allowed access to their lands and have accompanied us with mules. Juan Speroni, Pablo Maciel, Tamara Toledo and Florencia Wayar Córdoba have accompanied me on various trips and have invested a great amount of time in planning and organization. Alejandro Nieva has helped in sample preparation. I want to thank them all.

Within a family of scientists there is always someone who can offer rock-solid advice or a shoulder to lean on. I would like to thank my parents and my sisters Jojanneke, Elishevah and especially Mariëlle for their wisdom and unconditional support in the past years. Lukas Schifferle has been my rock and a source of inspiration for many years now — thank you.

This project was funded through the Deutsche Forschungsgemeinschaft, grant STR 373/34-1 and the Brandenburg Ministry of Sciences as part of the International Research Training Group StRATEGy.

Abstract

The deformation style of mountain belts is greatly influenced by the upper plate architecture created during preceding deformation phases. The Mesozoic Salta Rift extensional phase has created a dominant structural and lithological framework that controls Cenozoic deformation and exhumation patterns in the Central Andes. Studying the nature of these pre-existing anisotropies is a key to understanding the spatiotemporal distribution of exhumation and its controlling factors. The Eastern Cordillera in particular, has a structural grain that is in part controlled by Salta Rift structures and their orientation relative to Andean shortening. As a result, there are areas in which Andean deformation prevails and areas where the influence of the Salta Rift is the main control on deformation patterns.

Between 23 and 24°S, lithological and structural heterogeneities imposed by the Lomas de Olmedo sub-basin (Salta Rift basin) affect the development of the Eastern Cordillera fold-and-thrust belt. The inverted northern margin of the sub-basin now forms the southern boundary of the intermontane Cianzo basin. The former western margin of the sub-basin is located at the confluence of the Subandean Zone, the Santa Barbara System and the Eastern Cordillera. Here, the Salta Rift basin architecture is responsible for the distribution of these morphotectonic provinces. In this study we use a multi-method approach consisting of low-temperature (U-Th-Sm)/He and apatite fission track thermochronology, detrital geochronology, structural and sedimentological analyses to investigate the Mesozoic structural inheritance of the Lomas de Olmedo sub-basin and Cenozoic exhumation patterns.

Characterization of the extension-related Tacurú Group as an intermediate succession between Paleozoic basement and the syn-rift infill of the Lomas de Olmedo sub-basin reveals a Jurassic maximum depositional age. Zircon (U-Th-Sm)/He cooling ages record a pre-Cretaceous onset of exhumation for the rift shoulders in the northern part of the sub-basin, whereas the western shoulder shows a more recent onset (140–115 Ma). Variations in the sedimentary thickness of syn- and post-rift strata document the evolution of accommodation space in the sub-basin. While the thickness of syn-rift strata increases rapidly toward the northern basin margin, the post-rift strata thickness decreases toward the margin and forms a condensed section on the rift shoulder.

Inversion of Salta Rift structures commenced between the late Oligocene and Miocene (24–15 Ma) in the ranges surrounding the Cianzo basin. The eastern and western limbs of the Cianzo syncline, located in the hanging wall of the basin-bounding Hornocal fault, show diachronous exhumation. At the same time, western fault blocks of Tilcara Range, south of the Cianzo basin, began exhuming in the late Oligocene to early Miocene (26–16 Ma). Eastward propagation to the frontal thrust and to the Paleozoic strata east of the Tilcara Range occurred in the middle Miocene (22–10 Ma) and the late Miocene–early Pliocene (10–4 Ma), respectively.

Zusammenfassung

Der Deformationsstil von Gebirgsgürteln wird stark von der Architektur der oberen Platte beeinflusst, die während vorheriger Verformungsphasen entstanden ist. Die mesozoische Salta Rift Extensionsphase hat einen strukturellen und lithologischen Rahmen geschaffen, der die känozoischen Heraushebungsmuster in den Zentralanden kontrolliert. Die Charakterisierung dieser Anisotropien ist daher entscheidend, um die räumlich-zeitliche Verteilung der Heraushebung und ihrer kontrollierenden Faktoren zu verstehen. Insbesondere die Östliche Kordillere weist einen strukturellen Rahmen auf, der teilweise von Salta Rift-Strukturen und ihrer Orientierung in Bezug auf die Verkürzung im Zuge der Gebirgsbildung der Anden kontrolliert wird. Dadurch wurden Gebiete geschaffen, in denen die jüngere Anden-Deformation überwiegt, und Gebiete, in denen der Einfluss des Salta Rifts die Deformationsmuster prägt.

Zwischen 23 und 24°S beeinflussen lithologische und strukturelle Heterogenitäten des Lomas de Olmedo Beckens (Teil des Salta Rift Beckens) die Entwicklung des Faltengürtels der Östlichen Kordillere. Der invertierte nördliche Rand des Beckens bildet dabei die südliche Grenze des Cianzo Beckens, welches während der andinen Orogenese angelegt wurde. Der ehemalige westliche Rand des Lomas de Olmedo Beckens befindet sich am Übergang der Subandinen Zone, des Santa Barbara Systems und der Östlichen Kordillere. Hier ist die Architektur des Salta Rift-Beckens für die räumliche Verteilung dieser morphotektonischen Provinzen verantwortlich. In dieser Studie verwenden wir einen multi-methodischen Ansatz, bestehend aus Niedertemperatur (U-Th-Sm)/He und Apatit Spaltspur Thermochronologie, detritische Geochronologie sowie strukturelle und sedimentologische Analyse, um das mesozoische strukturelle Erbe des Lomas de Olmedo Beckens und die känozoischen Heraushebungsmuster zu untersuchen.

Die mit Extension verbundene Tacurú-Gruppe bildet eine Einheit, die dem paläozoischen Grundgebirge und der syn-rift Auffüllung des Lomas de Olmedo Beckens zwischengeschaltet ist. Sie hat ein Jurassisches maximales Ablagerungsalter. Zirkon (U-Th-Sm)/He Abkühlungsalter zeigen einen präkretazischen Beginn der Heraushebung für die Riftschulter im nördlichen Teil des Beckens, während die westliche Schulter einen jüngeren Beginn aufweist (140–115 Ma). Variationen in der stratigraphischen Mächtigkeit von Syn- und Postrift-Gesteinen dokumentieren die Entwicklung des Akommodationsraums. Während die Mächtigkeit der Synrift-Gesteine zum nördlichen Beckenrand hin zunimmt, schwindet die Mächtigkeit der Postrift-Gesteine in Richtung des Beckenrandes und bildet dort eine kondensierte Abfolge. Die Inversion der Salta Rift Strukturen begann im Cianzo Becken zwischen dem späten Oligozän und Miozän (24–15 Ma) mit einer diachronen Heraushebung des östlichen und westlichen Schenkels der Cianzo Synklinale, welche sich im Hangenden der Hornocal Störung befindet. Gleichzeitig begann im Tilcara Gebirge, südlich des Cianzo Beckens, im späten Oligozän bis frühen Miozän (26–16 Ma) die Heraushebung westlicher Störungsblöcke. Die ostwärtige Ausbreitung zur frontalen Überschiebung erfolgte im mittleren Miozän (22–10 Ma) und zum San Lucas Block im späten Miozän bis frühen Pliozän (10–4 Ma).

Allgemeinverständliche Zusammenfassung

Die Anden bilden die längste kontinentale Gebirgskette der Welt und erstrecken sich über eine Länge von rund 7000 km. Mit der Subduktion der Nazca-Platte unter die Südamerikanische Platte begann vor ca. 100 Millionen Jahren die Gebirgsbildung in den Zentralanden. Die tektonische Entwicklung dieses Gebirges wird jedoch maßgeblich von der Struktur der oberen Südamerikanischen Platte beeinflusst, welche von verschiedenen vorhergehenden Verformungsphasen geprägt ist. In den Zentralanden ist insbesondere eine Extensionsphase im Mesozoikum, die das weitreichende Salta Riftbecken formte, sowohl für strukturelle als auch lithologische Anisotropien verantwortlich, welche in späterer Folge die känozoische Gebirgsbildung beeinflussen.

Der Fokus vorliegender Studie konzentriert sich auf die argentinische Östliche Kordillere zwischen 23 und 24°S. Dort befindet sich das Cianzo Becken, welches allseits durch reaktivierte und neu gebildete Störungen begrenzt ist. Die südöstliche Grenze dieses Beckens wird von der Hornocal Aufschiebung gebildet, welche die ehemalige Nordgrenze eines mesozoischen Riftbeckens bildete. Diese und weitere präexistierende Störungen üben eine starke Kontrolle auf die tektonische Entwicklung der Östlichen Kordillere als Falten- und Überschiebungsgürtel aus. In dieser Arbeit untersuche ich diese Strukturen der oberen Kruste, sowie ihre Auswirkung auf die räumlich-zeitliche Verteilung von Heraushebung in der argentinischen Östlichen Kordillere. Dabei wende ich einen multi-methodischen Ansatz an, welcher strukturelle und sedimentologische Analyse, sowie Datierung von sedimentären Abkühlungsaltern umfasst.

Die Heraushebung des ehemaligen Nordrandes des Riftbeckens fand ab dem Jura statt, während die westliche Schulter des Beckens ab der frühen Kreide herausgehoben wurde. Dies bestätigen Abkühlungsalter von Zirkonen und die Ablagerung von klastischen Sedimenten der Tacurú Gruppe, welche in Verbindung mit Störungsaktivität stehen. Die darauffolgende Ablagerung von Synriftsedimenten zeigt, wie sich das Becken mit dem Fortschreiten der Extension vertiefte. In einer späten Phase der Extension, als die Störungsaktivität schon nachgelassen hat, belegen karbonatische Sedimente wie das Becken von seinem Zentrum aus zum Rand hin aufgefüllt wurde. Die Reaktivierung von den mesozoischen Strukturen im Cianzo Becken begann zwischen dem späten Oligozän und dem Miozän (24–15 Ma). Dabei formte sich unter anderem die Cianzo Synklinale südlich der Hornocal Aufschiebung. Gleichzeitig fand im Tilcara Gebirgszug, südlich des Cianzo Beckens, vom späten Oligozän bis frühen Miozän (26–16 Ma) die Hebung entlang von Nord-Süd verlaufenden steilstehenden Störungen statt. Die Deformation und Heraushebung schritt im mittleren Miozän (22–10 Ma) nach Osten hin fort. So wurden am östlichen Rand des Untersuchungsgebietes paläozoische Gesteine von späten Miozän bis frühes Pliozän (10–4 Ma) herausgehoben.

List of Abbreviations

ζ	Zeta, zeta correction factor
σ	Sigma, standard deviation
σ_1, σ_3	Maximum and minimum principal stress
AHe	Apatite (U-Th-Sm)/He thermochronology
AFT	Apatite fission track thermochronology
APAZ	Apatite partial annealing zone
APRZ	Apatite partial retention zone
BSE	Backscatter electron
CDF	Cumulative distribution function
CL	Cathodoluminescence
DEM	Digital elevation model
DI	Diiodomethane
Dpar	Etch pit diameter
ESR	Equivalent sphere radius
eU	Effective Uranium
Fm	Formation
F_T	Alpha-ejection correction factor
ICP-MS	Inductively coupled plasma - mass spectrometry
KDE	Kernel density estimate
LL	Log likelihood
LW	Leeward
Ma	Million years before present
MDA	Maximum depositional age
MLA	Maximum likelihood age
$P(\chi^2)$	Chi-square probability
SD	Standard deviation

SE	Standard error
SPT	Sodium polytungstate
TB	Tectonic block
T_c	Closure temperature
TDA	True depositional age
TINT	Track-in-track
WM	Weighted mean
WW	Windward
YC1σ	Youngest 1σ grain cluster
YC2σ	Youngest 2σ grain cluster
YSG	Youngest single grain
ZHe	Zircon (U-Th-Sm)/He thermochronology
ZPRZ	Zircon partial retention zone

Table of Contents

Chapter 1. Introduction

Earth's lithosphere is constantly moving, causing the opening of ocean basins, subduction of tectonic plates and the formation of mountain ranges in what is called the "Wilson Cycle" (Wilson, 1966; Wilson et al., 2019). These processes drive deformation in the lithosphere, creating a structural grain that may affect the timing and localization of deformation during later phases (e.g., Butler et al., 2006; Erdős et al., 2014; Jammes and Huismans, 2012; Salazar-Mora et al., 2018). At plate margins, existing architectural elements are able to control the tectonic structure of mountain belts and spatial changes therein (Marshak, 2004). On a regional scale, structural inheritance in upper crustal levels is often expressed and recognized as basin inversion and/or fault reactivation (Lowell, 1995). Understanding structural inheritance is therefore fundamental to the geological study of mountain belts (Butler et al., 2006). In the presence of pre-existing crustal heterogeneities that control deformation, the geological analysis of mountainous regions can be a daunting task. Using a multi-method approach, various types of data can be combined in order to decipher the geological history of an orogen (e.g., Nakapelyukh et al., 2018; Spiegel et al., 2004; Zapata et al., 2019b).

The Andes are the longest continental mountain range on Earth with a total length of ~7000 km and elevations up to 6961 m (Figure 1.1a). They are located along the western margin on the South American plate and are described as the archetype of a non-collisional subduction orogeny (e.g., Giambiagi et al., 2022; Haschke et al., 2006). At the ocean-continent plate boundary, the oceanic Nazca slab is subducted eastward underneath the continental South American plate (e.g., Barazangi and Isacks, 1976; Cahill and Isacks, 1992). The Andes show a pronounced segmentation and along-strike stratigraphic, morphological and structural variations (e.g., Jordan et al., 1983; Kley, 1999; Pearson et al., 2013). The Central Andes in particular are divided into morphotectonic provinces (Kley et al., 1999; Strecker et al., 2007) (Figure 1.1a). These include, from west to east, the Principal Cordillera, Western Cordillera, Altiplano-Puna Plateau, Eastern Cordillera, Inter- and Subandean Zone (Bolivia), and Santa Barbara System (NW Argentina). Each of the morphotectonic provinces shows a different structural style and morphological expression. While the geometry of the Nazca plate has been proposed as a controlling factor for the along-strike tectonic segmentation of the Andes (Jordan et al., 1983), other studies suggest that structural, rheological and stratigraphic inheritance play a major role (Gautheron et al., 2013; Kley and Monaldi, 2002; McGroder et al., 2015). In a recent study, Horton et al. (2022) propose that the angle of subduction is not the main controlling factor, but rather the inherited properties of the South American plate are crucial for strain localization in the Andes.

The present-day South American plate structure resulted from several phases of terrane accretion and the breakup of supercontinents during the Proterozoic and Paleozoic. During the Proterozoic formation of Rodinia, Laurentia and the Arequipa-Antofalla terrane were amalgamated to the Amazonian Craton (Casquet et al., 2010; Ramos, 2008). In the Paleozoic, terranes were accreted to the western margin of Gondwana (Lucassen et al., 1999; Ramos, 2018; Rapela et al., 1998). The various tectonic events in the history of the South American plate are reflected in a heterogeneous present-day geological framework (Figure 1.1b). As such, the basement of the Andes has been shaped by many tectonic phases, both extensional and compressional (Oncken et al., 2006; Ramos, 2008), each forming a distinct structural grain and reactivating existing structures from previous phases (e.g., Carrera et al., 2006; Giambiagi et al., 2008; Grier et al., 1991; Kortyna et al., 2019; Pearson et al., 2012).

The crustal anisotropies and resulting segmentation of the upper plate were a controlling factor in the development and geometry of a major Mesozoic rift system (Hernández et al., 2005), driven by the opening of the Atlantic Ocean and related extension within the South American plate (Moulin et al., 2010). This Mesozoic system is characterized by a series of discontinuous rift basins (Marquillas et al., 2005; Viramonte et al., 1999). In the southern Central Andes, extension was accommodated within the Salta Rift basin, which consisted of several sub-basins that radiated from the central Salta-Jujuy high (Salfity and Marquillas, 1994) (Figure 1.1c). Syn- and post-rift sediments of the Salta Group show a thickness up to 5000 m (Marquillas et al., 2005). The structural and sedimentological development of and within the Salta Rift sub-basins thus created major structural and stratigraphic anisotropies (Kley and Monaldi, 2002). At present, the western sub-basins have been fully incorporated into the Andean wedge, whereas the eastern sub-basins have only been partially inverted during Andean orogeny.

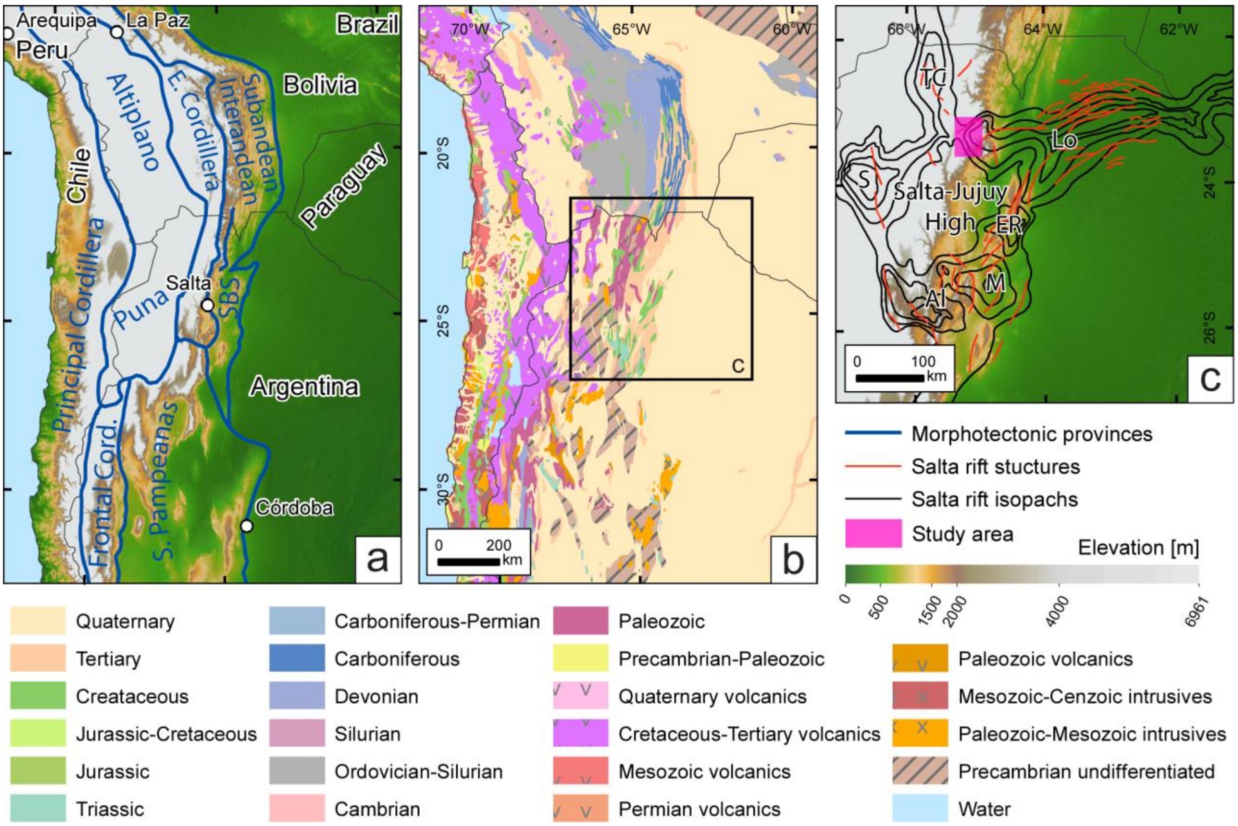

Figure 1.1 Overview maps of the Central Andes showing (a) the distribution of elevation and the outlines of morphotectonic provinces (modified after Anderson et al., 2017), (b) a geologic map (modified after Schenk et al., 1999), and (c) the location of the Salta Rift sub-basins, major extensional structures (after Starck, 2011) and ispoachs of the syn-rift succession (after Salfity and Marquillas, 1994). A rectangle marks the study area between 23 and 24°S. SBS: Santa Barbara System, TC: Tres Cruces, Lo: Lomas de Olmedo, S: Sey, ER: El Rey, M: Metán, Al: Alemanía.

The Cenozoic evolution of the Andes is characterized by the transition from post-rift thermal subsidence to retro-arc shortening (e.g., Horton, 2018a, 2018b). In the Central Andes, the amount and timing of deformation shows large variations with latitude (see review in Stalder et al., 2020). Differences in the compressional regime over time and space depend on e.g., variations in plate coupling and relative conversion rates between the South American and Nazca plate (Chen et al., 2019; Horton, 2018b; Sobolev and Babeyko, 2005), creating along-strike variations in the width of the orogenic belt. The largest documented amount of shortening is found in northern latitudes (18–28°S) and coincides with the greatest width and regional elevation in the Central Andes (e.g., Anderson et al., 2017; Horton, 2018b; Kley and Monaldi, 1998; McQuarrie, 2002; Oncken et al., 2006). The amount of shortening then decreases southward. Protracted Cenozoic shortening led to the formation of substantial topography in the Central Andes, which affects atmospheric circulation and produces precipitation gradients across and along the mountain belt (e.g., Bookhagen and Strecker, 2012; Rech et al., 2006; Rech et al., 2010). The humid side of an orogen is prone to enhanced erosion, which in turn may impact exhumation rates and the development of the Andean foreland basin (e.g., Kleinert and Strecker, 2001; Pingel et al., 2014; Schoenbohm et al., 2015; Sobel and Strecker, 2003).

The timing of exhumation and deformation in the Central Andes has been extensively studied (see review in Stalder et al., 2020). The following is a condensed summary outlining broad deformation phases. Initiation of mountain building occurred around the Late Cretaceous to early Paleocene (Horton, 2018a; Horton and DeCelles, 1997; McQuarrie et al., 2005) and may date as far back as ~90 Ma (Amilibia et al., 2008; Arriagada et al., 2006). North of 23°S, shortening propagated to the Eastern Cordillera at ~40 Ma (McQuarrie et al., 2005; McQuarrie and DeCelles, 2001); maximum shortening rates there occurred between the Oligocene and early Miocene (Elger et al., 2005; Müller et al., 2002). From 25 to 10 Ma, deformation was mostly accommodated in the Interandean Zone (Anderson et al., 2017; Elger et al., 2005; Horton, 2005), ceased by 12–10 Ma and then moved eastward to the Subandean Zone (e.g., Anderson et al., 2017; Echavarría et al., 2003; Elger et al., 2005; Kley, 1996, 1999; Uba et al., 2006).

South of 24°S, the interior of the Puna Plateau shows continuous tectonic activity since the late Eocene-Oligocene to the Pliocene (Coutand et al., 2001; Kraemer et al., 1999) and deformation of the Eastern Cordillera started in the middle Eocene (e.g., Hongn et al., 2007; Montero-López et al., 2018). Deformation moved to the Sierras Pampeanas in the late Miocene with a culmination after 6 Ma (Carrapa and DeCelles, 2008; Strecker et al., 1989; Zapata et al., 2019b). Dissection of the unrestricted foreland basin, caused by uplift of the Eastern Cordillera and Sierras Pampeanas, occurred by the middle–late Miocene (Carrera and Muñoz, 2008; Coutand et al., 2006; Deeken et al., 2006; Hain et al., 2011). Deformation of the Central Andean foreland continued during Pliocene and Pleistocene times (e.g., Carrera and Muñoz, 2008; Coutand et al., 2006; Strecker et al., 1989). Thus, the Andean thrust front shows a general eastward propagation (e.g., Barnes et al., 2008; Carrera and Muñoz, 2008; Ege et al., 2007; Henríquez et al., 2019; Henríquez et al., 2020; Horton and DeCelles, 1997; Kley, 1996; Rak et al., 2017) and a corresponding migration of the Andean foreland basin (Carrapa and DeCelles, 2008; DeCelles et al., 2011; DeCelles and Horton, 2003).

The region between 23 and 24°S is a transitional area within the Central Andes, where major changes in the spatial and temporal distribution, the geometry and kinematics of shortening occur (Allmendinger and Gubbels, 1996). Three general structural styles characterize deformation in the Central Andes and are associated with different types of foreland basins (e.g., Allmendinger et al., 1983; Horton and Folguera, 2022; Kley et al., 1999). 1) Thin-skinned deformation is associated with a continuous foreland basin. The development of the orogenic wedge leads to crustal thickening, flexural loading and the creation of accommodation space (e.g., DeCelles and Giles, 1996; Horton and DeCelles, 1997). This type of deformation is known from the Subandean fold-and-thrust belt and the Chaco-Paraná foreland basin (e.g., Allmendinger et al., 1983; Baby et al., 1992; Dunn et al., 1995; Kley, 1996). 2) For thick-skinned deformation, shortening is accommodated by basement-core uplifts leading to the formation of a broken foreland basin type (e.g., Jordan and Allmendinger, 1986; Strecker et al., 2011). Here, the inherited structural framework of the upper plate controls the pattern of Andean uplift (e.g., Hilley et al., 2005; Iaffa et al., 2011; Kley and Monaldi, 2002; Monaldi et al., 2008). This type is mainly found in the Sierras Pampeanas, south of 24°S (Fielding and Jordan, 1988; Zapata et al., 2019b). 3) A combination of thick- and thin-skinned deformation is found in e.g., the Eastern Cordillera (e.g., McQuarrie and DeCelles, 2001; Müller et al., 2002), Interandean Zone (e.g., Anderson et al., 2017; Kley, 1996), Altiplano-Puna Plateau (e.g., Carrapa and DeCelles, 2008; Coutand et al., 2001), and the Santa Barbara System (Kley and Monaldi, 2002). This type involves a combination of ramp-flat-ramp thrusts and structures that are steeper and root in the deeper basement (Stalder et al., 2020).

Whereas exhumation has steadily propagated eastward within the thin-skinned Subandean Zone, uplift is disparate within the thick-skinned Sierras Pampeanas (Zapata et al., 2019b). The Eastern Cordillera and Santa Barbara System are located in a structural transition zone between these two end members (Kley et al., 1999). The influence of the Mesozoic Salta Rift basin between 22 and 26°S is incontestable (Kley et al., 2005; Kley and Monaldi, 2002; Monaldi et al., 2008). Therefore, the study area at 23–24°S is strategically positioned at the northern margin of the Lomas de Olmedo sub-basin (Figure 1.1c), a northeastern sub-basin of the Salta Rift basin. The eastern part of the sub-basin has not been deformed during the Andean orogeny and is at present covered by foreland basin sediments. Toward the west, the amount of Andean shortening increases and the former sub-basin has increasingly been incorporated into the Eastern Cordillera. Reactivation and inversion of basin-bounding faults led to an increase in structural elevation; in the Eastern Cordillera, the Salta Group can now be found at > 4000 m elevation (Amengual and Zanettini, 1973; Kley et al., 2005). Extensional structures and Salta Group strata can thus be found alongside syn-orogenic sediments and Andean contractional structures. This makes the Eastern Cordillera between 23 and 24°S an excellent natural laboratory to study the development and propagation of a fold-and-thrust belt in a highly anisotropic upper crust.

In this publication-based dissertation the depositional and exhumation history of the Lomas de Olmedo sub-basin is addressed, from the Mesozoic rift shoulder exhumation and deposition of the Salta Group to the inversion and reactivation of the northern basin margin and its incorporation into the Eastern Cordillera. The Andean orogeny has partly erased the evidence of former deformation phases. Therefore, a multi-method approach is applied with a combination of structural and sedimentological analyses, detrital zircon U-Pb geochronology and low-temperature thermochronology. I use this approach to answer the following research questions:

I) When did the onset of extension and rift shoulder exhumation occur in the Lomas de Olmedo sub-basin?

II) What are the effects of Andean shortening on fault reactivation, deformation and exhumation in the southern Central Andes at 23–24°S?

In Chapter 2, I present detrital zircon U-Pb geochronology data from pre-Salta Group and syn-rift sediments. I combine these with provenance data from point counting, sedimentological field data and low-temperature zircon (U-Th-Sm)/He (ZHe) thermochronology data from the rift shoulder to determine the age and depositional nature of the Tacurú Group at the base of the Salta Group. I demonstrate that part of these strata are fault-related and provide evidence of Jurassic extension in NW Argentina. This chapter is published in the Journal of South American Earth Sciences by W. S. M. T. van Kooten, C. E. Del Papa, D. Starck, E. R. Sobel, P. Cavalleri, M. Agüera, V. van Schijndel and J. Glodny. For this chapter, I was responsible for the conceptualization and design of the study, sample and field data collection, sample preparation, provenance and low-temperature thermochronology analysis, data interpretation and writing of the original draft.

In Chapter 3, I present low-temperature apatite (U-Th-Sm)/He (AHe), ZHe and apatite fission track (AFT) dates from the Tilcara Range in the Eastern Cordillera to reconstruct its thermal history during the Andean orogeny. The data set and thermal models are put in a structural context. Thus, I provide new constraints for the onset of exhumation and the potential timing of deformation in this part of the Eastern Cordillera. This chapter is published in Tectonics by W. S. M. T. van Kooten, E. R. Sobel, C. E. del Papa, P. Payrola and J. Glodny. For this chapter, I was responsible for the conceptualization and design of the study, sample and field data collection, sample preparation, low-temperature thermochronology analysis, thermal modeling and data analysis, and writing of the original draft.

In Chapter 4, I present low-temperature AHe, AFT and ZHe data, combined with structural and sedimentological field data to constrain Mesozoic extension and Cenozoic inversion at the northern margin of the Lomas de Olmedo sub-basin. I show that the onset of rift shoulder inversion occurred during the Oligocene–middle Miocene, and that out-of-sequence thrusting and overall eastward propagation occurred in the middle Miocene–Pliocene. This chapter is under review in Tectonics, authored by W. S. M. T. van Kooten, M. Vallati, E. R. Sobel, C. E. del Papa, P. Payrola, D. Starck, A. Bande, M. F. Wayar Córdoba, A. T. Lapiana and J. Glodny. For this chapter, I was responsible for the conceptualization and design of the study, sample and field data collection, sample preparation, low-temperature thermochronology analysis, thermal modeling and data analysis, and writing of the original draft.

In Chapter 5, the constraints on the Mesozoic development of the Lomas de Olmedo sub-basin and the Andean reactivation of its NW border are summarized, compared to existing data from literature and discussed in the context of the current knowledge of the Andean geological evolution. The comprehensive data set of low-temperature thermochronology cooling ages and thermal models, combined with key sedimentological and structural data in this study offers new constraints on two major phases in the history of the Andes: Mesozoic extension (Salta Rift phase) and subsequent Andean contraction, which reactivated and inverted anisotropies of the Salta Rift phase. The reactivation of extensional structures related to the Lomas de Olmedo sub-basin during the Andean orogeny exemplifies the process of basin inversion and complex reactivation of upper plate heterogeneities during mountain building, which is ubiquitous in Earth's orogenic belts.

Chapter 2. Evidence of Jurassic extension in NW Argentina: Characterization of fault-related strata at the Salta Group base using sandstone provenance and zircon U–Pb geochronology

This chapter was published in the Journal of South American Earth Sciences (Vol. 120, 104048, 10.1016/j.jsames.2022.104048), by W. S. M. T. van Kooten, C. E. Del Papa, D. Starck, E. R. Sobel, P. Cavalleri, M. Agüera, V. van Schijndel, and J. Glodny. Copyright Elsevier (2022).

Abstract

The present-day structure of the Eastern Cordillera in NW Argentina is governed by structural and lithological heterogeneities inherited from preceding deformational phases, which influence the localization of newly-formed faults and the inversion of pre-existing structures. The Salta Rift basin formed during a Late Jurassic–Cretaceous extensional phase and created a dominant structural and stratigraphic imprint in NW Argentina that is particularly evident within the Eastern Cordillera, where uplift and exhumation have exposed the Salta Group syn-rift succession. Although in general, the Salta Group rests upon Paleozoic rocks, locally the Tacurú Group forms an intermediate succession, consisting of interfingering eolian sandstones and proximal fault-related conglomerates with a Jurassic maximum depositional age. This succession might be the key to unraveling the Mesozoic history of NW Argentina, prior to the deposition of the Salta Group. The conglomerates represent the earliest deposits related to extension in the western Lomas de Olmedo sub-basin, which is also documented in predominantly Jurassic ZHe cooling ages of the rift shoulders. The detrital zircon U-Pb age signature and sandstone provenance of the Tacurú Group conglomerates differs strongly from the Salta Group syn-rift strata, which show a more regional signal. These variations and the angularity of the unconformity may be connected to a rotation of the extension direction in the western Lomas de Olmedo sub-basin.

2.1 Introduction

The Central Andes in NW Argentina are part of the longest continental mountain range on Earth and are the type locality of a non-collisional subduction orogeny. They are divided into morphotectonic provinces, which exhibit characteristic structural and morphological variations. The Eastern Cordillera, in particular, shows a strong dependency of structural style on pre-existing heterogeneities (Carrera et al., 2006; Grier et al., 1991; Kley et al., 2005). Although Paleozoic structures also affect the pattern of Cenozoic reactivation and exhumation within the Eastern Cordillera (Hongn et al., 2010a), one of the most important causes of structural and lithological heterogeneities in this part of the Central Andes is the Cretaceous Salta Rift extensional phase that affected NW Argentina, Paraguay, Chile and Bolivia (Grier et al., 1991; Kley et al., 1999) (Figure 2.1a). Vast amounts of syn- and post-rift strata of the Salta Group accumulated in the various sub-basins of the Salta Rift basin, reaching a total thickness of up to

5 kilometers in the northern Tres Cruces and Lomas de Olmedo sub-basins (Boll et al., 1989; Marquillas et al., 2005) (Figure 2.1a).

During the Andean orogeny, Cenozoic inversion of normal faults bounding the Cretaceous Lomas de Olmedo sub-basin has caused inherent changes in structural elevation and the exhumation of Neoproterozoic–Paleozoic pre-rift basement and the overlying Salta Group syn-rift succession. As a result, these strata are now exposed in inverted and former half-grabens at various locations in the Central Andes, and can be studied in detail (Carrera et al., 2006; Kley et al., 2005; Kley and Monaldi, 2002; Kortyna et al., 2019) (Figure 2.1b). Although most of these studies focus on the overall age and depositional environment of the Salta Group (Boll et al., 1989; Marquillas et al., 2005; Moreno, 1970; Reyes and Salfity, 1973; Salfity and Marquillas, 1994; Starck, 2011), they fail to address the sedimentary provenance of the syn-rift strata at the very base of the Salta Rift, and the age and nature of the basal Salta Group unconformity.

In this study, we focus on the former westernmost margin of the Lomas de Olmedo sub-basin, where an intermediate succession of eolian sandstones and proximal conglomerates separates the Paleozoic sedimentary basement from the Salta Group syn-rift succession. These intermediate strata have been interpreted variously as Cretaceous syn-rift sediments of the Salta Group (Henríquez et al., 2023; Kley et al., 2005; Seggiaro et al., 2010; Siks and Horton, 2011), Jurassic pre-rift sediments (Starck, 2008), or a part of both (McBride, 2008), but have not been analyzed systematically. By characterizing clastic sediments above and below the Salta Group unconformity using detrital zircon U-Pb geochronology and sandstone point-counting, we aim to unravel the nature of this intermediate succession and the basal Salta Group unconformity. We compare our data set with previously published detrital zircon U-Pb and provenance data of Precambrian–Carboniferous source rocks and stratigraphically related Mesozoic rocks (Aparicio González et al., 2020; McBride, 2008) to determine whether proximal conglomerates below the Salta Group unconformity are related to early extension in the western Lomas de Olmedo sub-basin. Our results provide new insights into the Mesozoic tectonic evolution of NW Argentina, which forms the basis for the present-day structure of the Central Andes.

2.2 Geological setting

In order to identify and interpret detrital zircon U-Pb age signatures of recycled Mesozoic and Cenozoic strata within the Cianzo syncline, we present a review of the pre-Andean tectonic history of the Central Andes and the Neoproterozoic–Paleozoic lithostratigraphic units that form possible source lithologies for Mesozoic–Cenozoic strata (see also Figure 2.2).

Figure 2.1 (a) Overview map of Salta Rift structures in the Central Andes of NW Argentina. Syn-rift strata isopachs from Salfity and Marquillas (1994) and the locations of Cretaceous normal faults from Starck (2011) are shown. TC: Tres Cruces sub-basin; Lo: Lomas de Olmedo sub-basin. Blue square indicates location of b. (b) Geologic map of the Jujuy-Humahuaca region, modified from Coira et al. (2008). Sampling locations are marked on both (a) and (b) and the location of Figure 2.3a is shown in (b). (c) Schematic map of Central South America showing terranes, cratons and orogenic belts mentioned in this study. AA: Arequipa-Antofalla block; Fam: Famatinian arc. Polygon boundaries and names redrawn and modified from Franceschinis et al. (2020b).

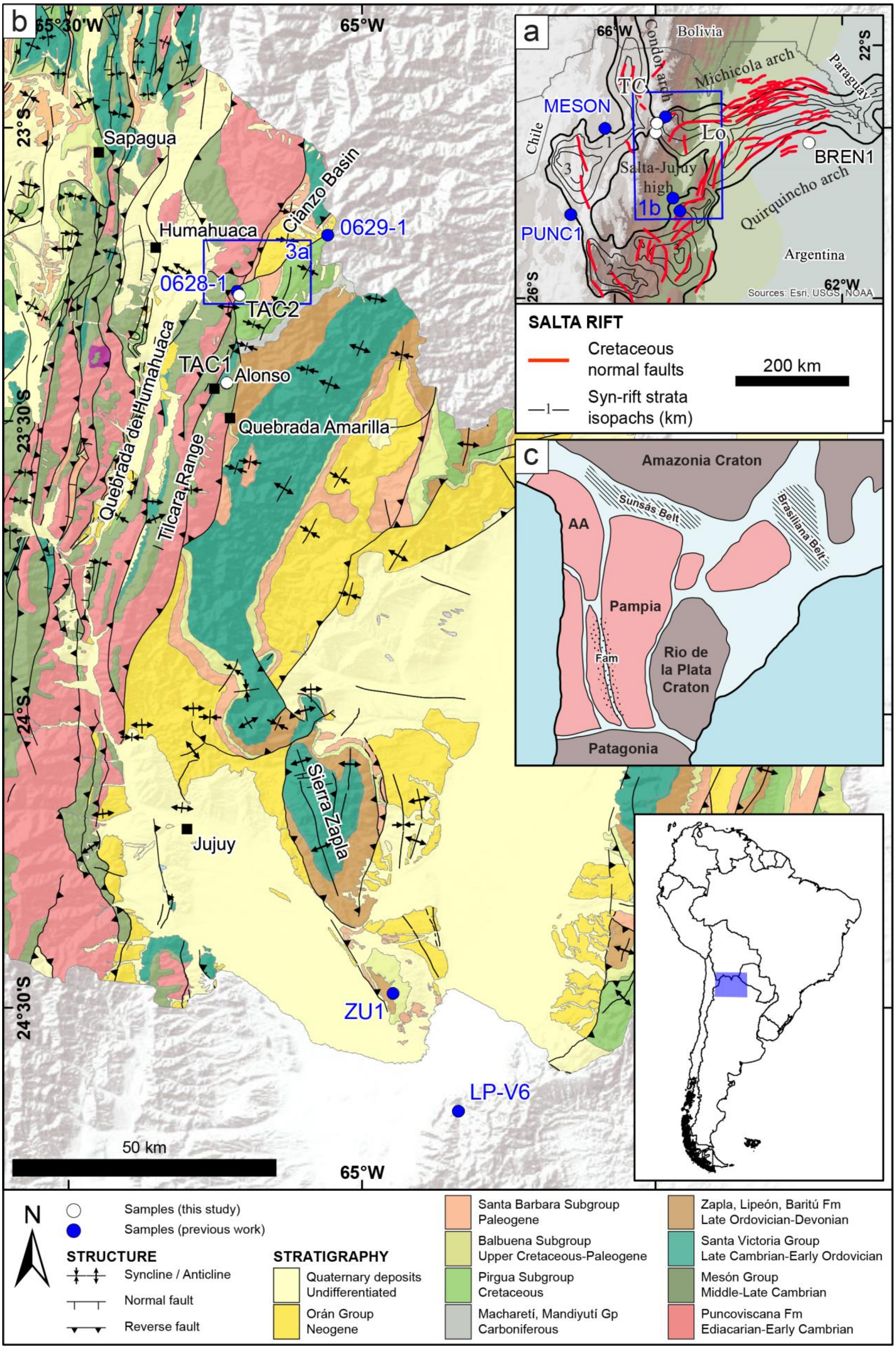

b
65°30'W
65°W
23°S
23°30'S
24°S
24°30'S
Sapagua
Humahuaca
Cianzo Basin
0629-1
3a
0628-1
TAC2
TAC1
Alonso
Quebrada Amarilla
Quebrada de Humahuaca
Tilcara Range
Sierra Zapla
Jujuy
ZU1
LP-V6
50 km
a
66°W
Bolivia
Condor arch
Michicola arch
Paraguay
22°S
TC
MESON
Chile
Lo
BREN1
Salta-Jujuy high
1b
PUNC1
Quirquincho arch
Argentina
26°S
62°W
Sources: Esri, USGS, NOAA
SALTA RIFT
Cretaceous normal faults
Syn-rift strata isopachs (km)
200 km
c
Amazonia Craton
Sunsás Belt
Brasiliana Belt
AA
Pampia
Fam
Rio de la Plata Craton
Patagonia
N
Samples (this study)
Samples (previous work)
STRUCTURE
Syncline / Anticline
Normal fault
Reverse fault
STRATIGRAPHY
Quaternary deposits Undifferentiated
Orán Group Neogene
Santa Barbara Subgroup Paleogene
Balbuena Subgroup Upper Cretaceous-Paleogene
Pirgua Subgroup Cretaceous
Macharetí, Mandiyutí Gp Carboniferous
Zapla, Lipeón, Baritú Fm Late Ordovician-Devonian
Santa Victoria Group Late Cambrian-Early Ordovician
Mesón Group Middle-Late Cambrian
Puncoviscana Fm Ediacarian-Early Cambrian

2.2.1 Neoproterozoic and Paleozoic

One of the earliest tectonic phases reflected in the geochronological record of Neoproterozoic and Paleozoic rocks of NW Argentina is the Sunsás-Grenville orogeny (1200–900 Ma; e.g., Casquet et al., 2010) (Figure 2.1c: Sunsás Belt), which was a result of the amalgamation of Laurentia and the Arequipa-Antofalla terrane to the Amazonian Craton), leading to the formation of the Rodinia supercontinent (Ramos, 2008) and the emplacement of multiple plutonic and metamorphic complexes. As a result, zircon U-Pb ages clustering between 1200 and 900 Ma are common in Neoproterozoic and Paleozoic strata (Adams et al., 2008; Adams et al., 2011; Einhorn et al., 2015; McBride, 2008), which form the sedimentary basement of the Central Andes. During the Precambrian–Cambrian, the Pampean-Brasiliano orogeny (760–525 Ma; e.g., Escayola et al., 2011; Lucassen et al., 1999) marks a tectonic reorganization and the breakup of Rodinia. During the initial stages, the formation of the Puncoviscana basin occurred (Ramos, 2008), in which the Puncoviscana Formation (Fm) was deposited. This unit consists of a dominantly clastic succession of weakly metamorphosed alternating green sandstones, siltstones and claystones with occasionally intercalated volcanics (Figure 2.2), which are attributed to a deep slope depositional setting with submarine fans (Aceñolaza, 2003). At present, outcrops of the Puncoviscana Fm form narrow, N–S striking belts within the Puna and Eastern Cordillera. The depositional age of the Puncoviscana Fm has been constrained to the Ediacarian–Early Cambrian, using e.g., (detrital) zircon U-Pb dating (Adams et al., 2011; Aparicio González et al., 2014; DeCelles et al., 2011; Einhorn et al., 2015; Escayola et al., 2011; McBride, 2008; Pearson et al., 2012) and paleontological data (Buatois and Mángano, 2003). Furthermore, Rb-Sr and U-Pb analyses of the Puncoviscana Fm cluster around 540–520 Ma (Rapela et al., 1998). The Pampean stage (570–525 Ma) marks the closure of the Puncoviscana basin and formation of the Puncoviscana belt (Omarini et al., 1999; Ramos, 1988, 2008). Collision of the Arequipa-Antofalla block and the Cordoba or Pampia terrane (Escayola et al., 2011 and Ramos et al., 2010, respectively) (Figure 2.1c) led to low-grade, sub- to lower-greenschist facies metamorphosis of the Puncoviscana Fm, which continued up to the Early Cambrian. K-Ar ages for the Puncoviscana Fm in NW Argentina indicate metamorphism at 568–565 Ma and 540–535 Ma (Adams et al., 1990). Based on the emplacement of Pampean intrusions into deformed Puncoviscana Fm strata, metamorphism ceased around 530–520 Ma (Do Campo and Nieto, 2003; Escayola et al., 2011; Pearson et al., 2012; Ramos, 2008).

The regional Tilcaric unconformity (Figure 2.2) marks the end of the Pampean cycle around 510–500 Ma (Adams et al., 2011) and forms the top of the Puncoviscana Fm. The Middle–Late Cambrian Mesón Group, consisting of conglomerates, coarse- to fine-grained sandstones and shales (Figure 2.2), was deposited on top of the Tilcaric unconformity in a shallow marine basin (Aceñolaza, 2003; Moya, 1998; Sanchéz and Salfity, 1999). The lower boundary of the Mesón Group is assumed to be indicated by the Tastil batholith (Mángano and Buatois, 2004), which is associated with magmatism of the Tilcaric phase at approximately 526 ± 2 Ma (Hongn et al., 2001a; Hongn et al., 2001b), although the exact stratigraphic setting of the Tastil batholith in relation to the Tilcaric unconformity has been debated (Hongn et al., 2010b; Omarini et al., 1999; Ramos, 2008). Detrital zircon U-Pb analyses of the Mesón Group give maximum depositional ages between 524.8 ± 4.1 and 502 ± 4 Ma (Adams et al., 2011; Aparicio González et al., 2014; Augustsson et al., 2011; Franceschinis et al., 2020a).

After a period of magmatic quiescence (Otamendi et al., 2020), the Famatinian orogeny (515–440 Ma; e.g., Casquet et al., 2010; Escayola et al., 2011; Lucassen et al., 1999; Ramos, 2018) led to the amalgamation of terranes to the western margin of Gondwana (Figure 2.1c). As a result, magmatic rocks were emplaced during middle (480–460 Ma) and late (453–444 Ma) Ordovician events (Bahlburg et al., 2016), forming the Famatinian arc (Figure 2.1c), which bounded the Ordovician clastic platform to the west, whereas the Pampean orogeny was situated to the east of this platform (Otamendi et al., 2020). The upper Cambrian–lower Ordovician Santa Victoria Group, overlying the Mesón Group, was deposited on this marine platform and is comprised of a characteristic alternation between shales, sandstones and occasional volcaniclastics (Figure 2.2), representing phases of transgression and regression (Moya, 1988). The age of the lower Santa Victoria Group has been determined to be late Cambrian to Tremadocian, based on regional and stratigraphic correlations, as well as the biostratigraphic framework based on trilobites, conodonts and graptolites zonation (Buatois et al., 2006; Nielsen, 1997; Waisfeld and Vaccari, 2003; Zeballo and Tortello, 2005). Within detrital zircon U-Pb data from the Santa Victoria Group, ages range from 500 to 410 Ma with a more prominent cluster between 485 to 460 Ma (Rapela et al., 2007). The proposed main sources of sediment for this unit were located in the Famatinian arc west of the Ordovician clastic platform, with minor sources in the Pampia/Cordoba Terrane or Rio de la Plata Craton (Ramos, 2008, 2018) (Figure 2.1c), located to the east or southeast of the Ordovician clastic platform. Contemporaneously to the deposition of the Santa Victoria Group, the Las Breñas Fm was deposited farther east in a regional, NE–SW striking basin (Chebli et al., 1999). The proposed depositional age of the Las Breñas Fm (sample BREN1) is Cambrian–Ordovician, based on a lithological correlation with other units outcropping in the Subandean Zone and Eastern Cordillera, and overlying strata with an uppermost Ordovician age (Rubinstein, 2005).

A phase of intracratonic basin development from the late Ordovician to the Devonian facilitated the deposition of a thick Ordovician–Devonian sedimentary succession (Starck, 1995). These strata (Ciclo Cordillerano; Figure 2.2) overlie the Santa Victoria Group. Similar to the Santa Victoria Group, the Ciclo Cordillerano succession shows cyclic alternations of shales and sandstones, which are separated from the Santa Victoria Group by a marked unconformity that is especially visible in the eastern limb of the Cianzo syncline, where it has an angular character (Figure 2.2c) (Amengual and Zanettini, 1973). The lowermost part of the Ciclo Cordillerano (Zapla Fm) contains trilobite fragments that indicate a late Ordovician age (Hirnantian; Monaldi and Boso, 1987). These strata are overlied by beds with graptolites and trilobites, constraining their age to the earliest Devonian (Baldis et al., 1976; Rickards et al., 2002; Waisfeld and Sánchez, 1993). Palynomorphs and biostratigraphic analyses from Devonian strata show that the depositional ages of these rocks span almost the entire Devonian (Aráoz et al., 2016; Noetinger et al., 2016).

The Late Devonian–Early Carboniferous Chanic orogeny terminated the deposition of Silurian–Devonian strata (Starck, 1995) and eroded large parts of the succession in the Tilcara Range (Figure 2.1b, 2.2). The Silurian–Devonian succession is overlain with a low-angle unconformity by predominantly Carboniferous strata deposited in an intracontinental basin, which are subdivided into the Macharetí and Mandiyutí Supersequences (Figure 2.2). These are separated by unconformities and show a general thinning toward the SW, related to the original boundaries of the basin in which they were deposited (Starck, 1995). The Macharetí and Mandiyutí Groups both consist of braided fluvial and deltaic/subaqueous sedimentation with diamictites, pointing toward a glacigenic and postglacial origin (Starck and Del Papa, 2006). A Pennsylvanian depositional age has been determined from their palynologic content (Aráoz et al., 2016; Di Pasquo, 2013; Di Pasquo et al., 2014; Di Pasquo et al., 2019; Di Pasquo and Azcuy, 1999; Di Pasquo and Vergel, 2008). Detrital zircon U-Pb analyses of the Mandiyuti Group show youngest age clusters between 400 and 240 Ma (Einhorn et al., 2015; McBride, 2008). Siks and Horton (2011) ascribe these age components to late Paleozoic magmatism in the Precordillera basement in Chile (e.g., Breitkreuz and van Schmus, 1996; Lucassen et al., 1999; Ramos, 2008; Rocha-Campos et al., 2011).

2.2.2 Jurassic

Within the Cianzo syncline, Precambrian–Carboniferous lithologies (Section 2.2.1) are overlain by cross-bedded, eolian sandstones. Starck (1995) assigned these deposits to the Tacurú Group, based on regional correlations with outcrops of eolian sandstones of the Tapecua and Ichoa Formations in Bolivia that reach southward until approximately 22.5°S. The latter has been assigned an upper Jurassic age (Sempere, 1995; Tomezzoli, 1996), based on Semionotiformes fish found in the underlying unit, indicating a Late Triassic–Early Jurassic age (Sempere et al., 2002) and stratigraphic relations to the underlying Entre Rios basalt, dated at 181.5 ± 0.9 Ma ($^{40}Ar/^{39}Ar$, Kusaik, 2008). The eolian sandstones of the Tacurú Group crop out between the Carboniferous and the Salta Group succession in the eastern limb of the Cianzo syncline. In the western limb of the syncline, the eolianites unconformably overlie the upper Cambrian–lower Ordovician Santa Victoria Group with an angle of ~37–40° (Starck, 2008) (Figure 2.2, 2.3a). The Tacurú Group in the Cianzo syncline was assigned a Jurassic age (Starck, 1995; 2008) on the basis of an angular unconformity between this unit and the overlying Cretaceous Pirgua Subgroup (Figure 2.3b–c). Apart from the results from one eolian sandstone detrital zircon U-Pb sample from McBride (2008), showing a youngest single grain with an age of 167 ± 3 Ma, the depositional age of the Tacurú Group in the Cianzo syncline has not been confirmed by absolute dating methods. The eolian sandstones of the Tacurú Group locally interfinger with and are overlain by coarse, poorly-sorted conglomerates ("agglomerates" in local literature) that were deposited as proximal alluvial fan facies (Starck, 2008) (Figure 2.2b, 2.3a–c). These strata are informally referred to as "Ocumazo conglomerate" in this study and are further described in the results (Section 2.4.1).

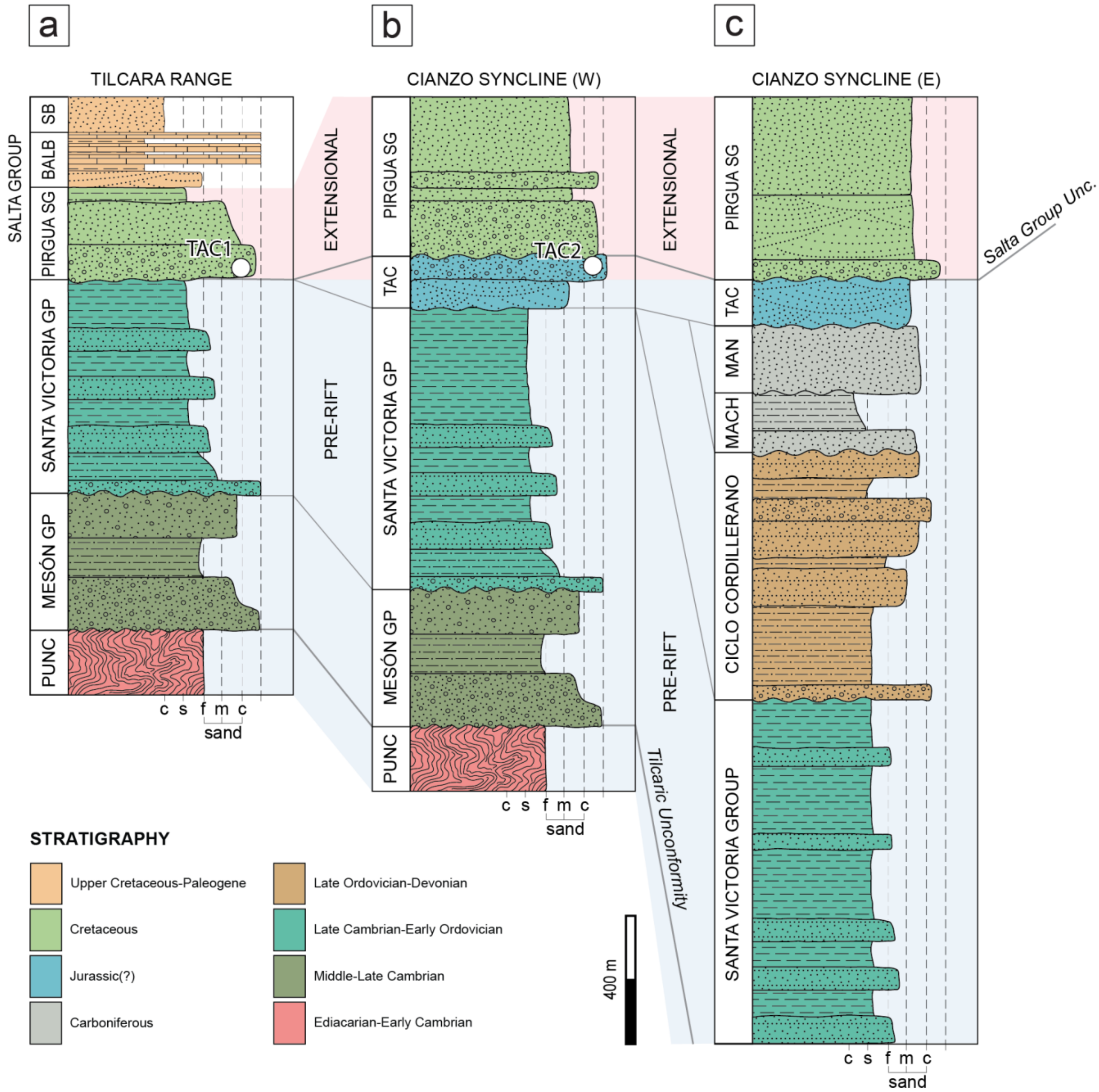

Figure 2.2 Stratigraphic synthesis of (a) the Tilcara Range, and the western (b) and eastern (c) limbs of the Cianzo syncline. Compilated and simplified from Moya (1988), Boll et al. (1989), Starck (1995), Sanchéz and Salfity (1999) and Marquillas et al. (2005). PUNC: Puncoviscana Formation, MACH: Macharetí Group, MAN: Mandiyutí Group, TAC: Tacurú Group. The stratigraphic positions of TAC1 and TAC2 are indicated.

2.2.3 Cretaceous and Paleogene

Mesozoic extension related to the Salta Rift ended the long-lasting phase of convergence and intracratonic basin development in NW Argentina (e.g., Marquillas et al., 2005; Starck, 1995). The Salta Rift basin in NW Argentina consisted of multiple sub-basins that radiated from the central Salta-Jujuy high (Figure 2.1a). The Tres Cruces and Lomas de Olmedo sub-basins formed the northernmost depocenters of the Salta Rift basin, separated by the Condor arch (Salfity and Marquillas, 1994) (Figure 2.1a). The infill of the Salta Rift basin, the Salta Group, is separated from the underlying Precambrian–Jurassic(?) rocks by an unconformity that locally shows a strong angular character. For example, within the Cianzo syncline, the unconformity between the Jurassic(?) Tacurú Group and the Salta Group shows an angle of 41–42° (Figure 2.2b–c, 2.3a–b). Farther south, in the Tilcara Range, the Salta Group overlies the uppermost Santa Victoria Group with local angular unconformities of 19° (Alonso) and 30° (Quebrada Amarilla) (Van Kooten et al., 2022b).

The Salta Group is subdivided into the clastic syn-rift Pirgua Subgroup (Reyes and Salfity, 1973), overlain by the carbonate-dominated Balbuena Subgroup and fluvial-clastic-dominated Santa Barbara Subgroup post-rift sediments (Moreno, 1970). Within the Cianzo syncline, the Pirgua Sugroup is comprised of a basal clast-supported conglomerate consisting of subangular to rounded gravel- to cobble-sized clasts. The clast lithologies are further described in the results (Section 2.4.1). The conglomerate is overlain by thick packages of massive red sandstones and siltstones (Boll et al., 1989; McBride, 2008). The age of the Pirgua Subgroup is known from the interbedded Alto de las Salinas volcanic event, dated at 128–112 Ma (K-Ar, whole rock: Bossi and Wampler, 1969), the Isonza basalt, dated at 96 ± 5 to 99 ± 5 Ma (K-Ar, whole rock: Valencio et al., 1976) and the Las Conchas basalt, dated at 78 ± 5 Ma and 76.4 ± 3.5 Ma (Reyes et al., 1976; Valencio et al., 1976) in the southern and central parts of the Salta Rift basin. Within the Lomas de Olmedo sub-basin, the Palmar Largo volcanic complex lies between the upper syn-rift and base of the post-rift succession and was assigned an age of 70 ± 5 Ma (K-Ar: Gómez Omil et al., 1989).

During the Andean orogeny, former extensional structures related to the Salta Rift were reactivated and inverted, increasing the structural elevation and exposing Mesozoic strata at the surface in the Eastern Cordillera. In this study, we highlight two examples of Salta Rift half-grabens where the basal Salta Group unconformity is now exposed. 1) The SW–NE striking Hornocal fault, which currently bounds the Cianzo basin (Figure 2.3a), is a prime example of an inverted rift basin-bounding normal fault. Whereas its footwall is marked by a condensed section of the Salta Group, the hanging wall shows syn- and post-rift strata with a thickness > 1600 m incorporated in the Cianzo syncline (Boll et al., 1989; Kley et al., 2005; McBride, 2008). 2) WNW–ESE striking faults within the Tilcara Range (Figure 2.1b) show evidence of pre-Cenozoic normal movement with spatially abrupt changes in the thickness of syn-rift strata (Kley et al., 2005; Van Kooten et al., 2022b). The basal angular Salta Group unconformity (Figure 2.2) crops out in both locations. In the Tilcara Range, the Salta Group was deposited on top of the Paleozoic sedimentary basement. In contrast, in the Cianzo syncline an underlying thick succession of eolian sandstones and conglomerates forms an intermediate stratigraphic section, bound by angular unconformities with the underlying Paleozoic strata and the overlying basal conglomerate of the Salta Group syn-rift strata (Figure 2.3a).

Figure 2.3 (a) Geologic map of the Hornocal area. Inset shows outcrop photo of Ocumazo conglomerate. For signatures of Paleozoic units (pC: Puncoviscana Fm, Me: Mesón Group, SV: Santa Victoria Group), see legend in Figure 2.1. Angular unconformity between the Tacurú Group and the Cretaceous Pirgua Subgroup as seen (b) on aerial images (© 2011 Microsoft Corporation and its data suppliers), and (c) in the field. Continuous white line shows the trace of the unconformity. Dashed white lines show traces of bedding. (d) Eolian sandstones showing cross-stratification in basal levels of the Tacurú Group. (e) Coarse-grained Ocumazo conglomerate (Tacurú Group), deposited in a proximal alluvial fan setting.

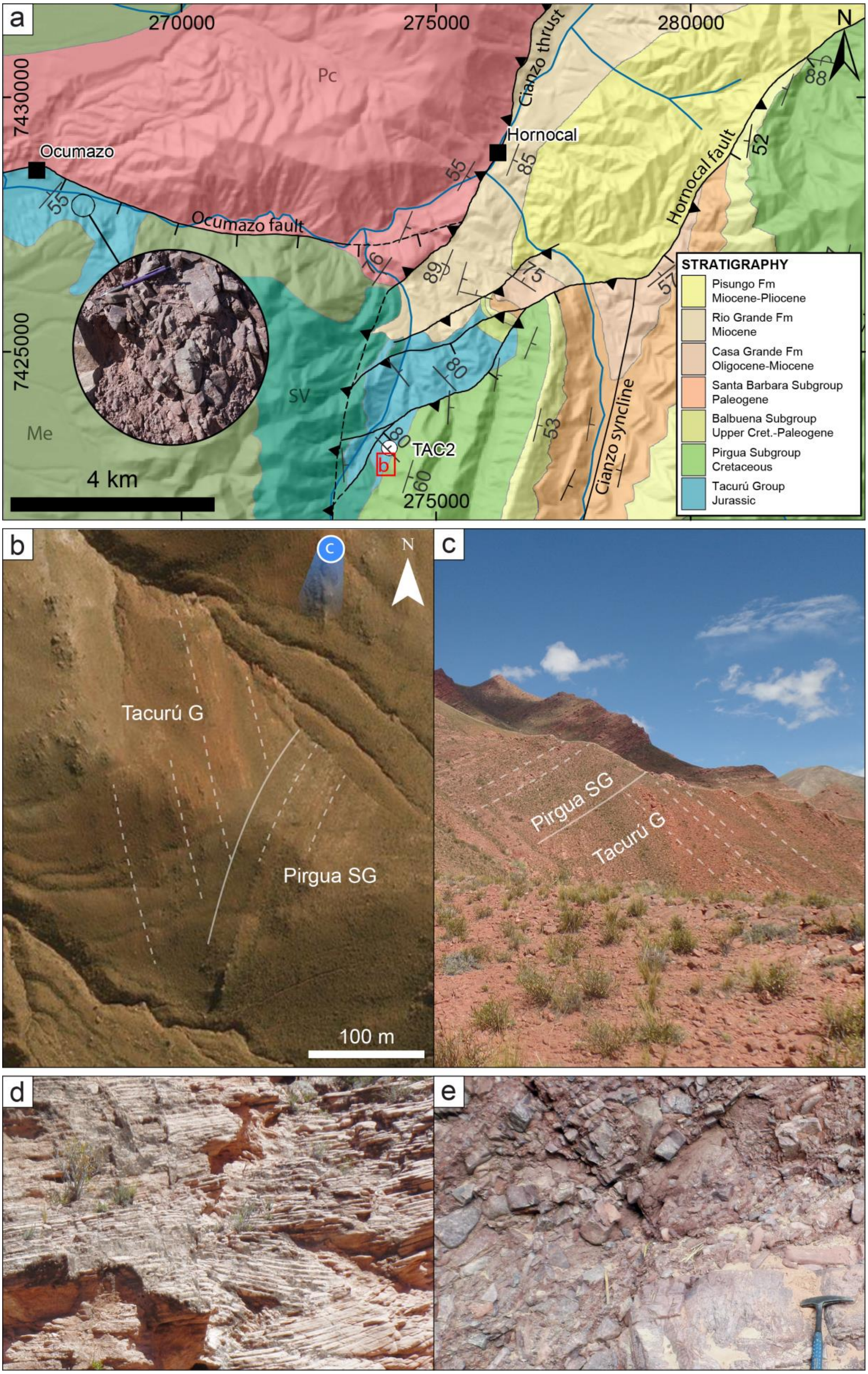
a
270000
275000
280000
7430000
7425000
Pc
Ocumazo
Hornocal
Cianzo thrust
Ocumazo fault
Hornocal fault
Cianzo syncline
SV
Me
TAC2
4 km
N
STRATIGRAPHY
Pisungo Fm
Miocene-Pliocene
Rio Grande Fm
Miocene
Casa Grande Fm
Oligocene-Miocene
Santa Barbara Subgroup
Paleogene
Balbuena Subgroup
Upper Cret.-Paleogene
Pirgua Subgroup
Cretaceous
Tacurú Group
Jurassic
b
Tacurú G
Pirgua SG
100 m
c
Pirgua SG
Tacurú G
d
e

2.3 Methods

2.3.1 Sample collection and preparation

We analyzed three sandstone samples collected near the basal Salta Group unconformity using detrital zircon U-Pb geochronology. Two samples (TAC1, TAC2) were taken from locations within the Eastern Cordillera, in the Cianzo syncline and the Tilcara Range. Sample TAC1 belongs to the earliest syn-rift Pirgua Subgroup, deposited unconformably on top of the upper Cambrian–lower Ordovician Santa Victoria Group (Van Kooten et al., 2022b). We chose this sample to characterize the basal Pirgua Subgroup more distal to the basin-bounding Hornocal fault. Sample TAC2 was collected from laminated, fine-grained sandstones that occur within the Ocumazo conglomerate, approximately 50 m below a clear angular unconformity with the Pirgua Subgroup (Figure 2.3a–b). This sample forms an intermediate sample between the eolian Tacurú Group (sample SM20070628-1) and basal Pirgua Subgroup (sample HOR1-297) samples from McBride (2008). Because different groups define the exact position of the unconformity between the Tacurú Group and the Pirgua Subgroup differently, the 297 m level of McBride (2008) (sample location of HOR1-297) is located at the base of the Pirgua Subgroup as defined by Starck (2008). Thus, sample HOR1-297 provides a good comparison to sample TAC1, from the distal basal Pirgua Subgroup in the Tilcara Range (Van Kooten et al., 2022b) and sample TAC2 (this study), sampled just below the Salta Group unconformity proximal to the basin-bounding Hornocal fault. The third sample (BREN1) was taken from the Los Blancos well (Agüera et al., 2019), located in the current Andean foreland basin at 23.6°S, 62.6°W. Sample BREN1 consists of drill cuttings at 2670 m depth from Cambrian–Ordovician strata (Las Breñas Fm), forming the uppermost southern rift shoulder of the Lomas de Olmedo sub-basin. This sample was chosen to characterize the rift shoulder strata of the Lomas de Olmedo sub-basin. Sample locations are marked in Figure 2.1 and coordinates are given in Table 2.1.

Preliminary mineral separations (including crushing, sieving, magnetic separation with a strong hand magnet) were conducted at the Universidad Nacional de Salta in Argentina. The samples were then further processed at the University of Potsdam, using a Frantz® magnetic separator, removal of clay and carbonate with 10 % acetic acid and 3 % H_2O_2, and density separation of the zircon fraction using Sodium Polytungstate (SPT) and Diiodomethane (DI).

2.3.2 Provenance

We conducted point-counting of standard, unstained petrographic thin sections to determine the modal framework composition of two samples (TAC1, TAC2) using the Gazzi-Dickinson method (e.g., Ingersoll et al., 1984). For each thin section, 450 grains were counted, following the amount of grains counted in McBride (2008). Grain classifications were based on descriptions of counted grain types from Siks and Horton (2011: their Table 3).

2.3.3 Detrital zircon U-Pb geochronology

For detrital zircon U-Pb analysis, the zircon fraction was hand-picked with a binocular polarizing microscope, taking care not to discriminate between grain geometries, to eliminate potential age bias. However, we aimed to exclude grains with visible cracks and large inclusions. Grains were

embedded in a 2.5 cm diameter epoxy mount and polished. The samples were analyzed on the JEOL JXA-8200 Superprobe at the University of Potsdam using backscatter electron (BSE) and cathodoluminescence (CL) imaging for a preliminary assessment of age domains and to choose measurement spots, so as to avoid cracks and metamict zones. Although some studies have avoided domains with high U concentration (i.e., dark CL response) to reduce the risk of measuring domains with Pb loss (Gehrels, 2014), we decided to not follow this strategy to avoid bias. To further eliminate biasing age populations, we only excluded grains with inclusions and/or fractures that could not be avoided during analysis. Representative BSE and CL images for all three samples are shown in Figure 2.4. U-Pb measurements were conducted using a laser ablation - sectorfield - inductively coupled plasma - mass spectrometry (LA-SF-ICP-MS) single-collector Thermo Finnigan Element2 mass spectrometer coupled to an NWR193 ArF Excimer laser ablation system. All ages represent single-spot zircon analyses with a spot diameter of 30 µm. The laser ablation system uses a He atmosphere and the carrier was mixed outside the ablation cell with sample N_2 and Ar gas, using a signal-smoothing device. The primary standard GJ-1 (Jackson et al., 2004) was analyzed every 10 sample spots to correct for laser-induced fractionation and calibration drift. Furthermore, the 91500 (Wiedenbeck et al., 1995), Plešovice (Sláma et al., 2008) and BB16 (Lana et al., 2017) reference materials were analyzed regularly for quality-control. All sample and standard measurement results are in agreement with published ID-TIMS ages. Full analytical details and results are reported in Appendix A.

Figure 2.4 BSE (top) and CL (bottom) images of representative zircons of samples (a) BREN1, (b) TAC1, and (c) TAC2. Red circles show measuring sites for LA-SF-ICP-MS analysis and ages are indicated.

The VizualAge data reduction scheme (Petrus and Kamber, 2012) for IOLITE (v4.5.5.4) (Paton et al., 2010; Paton et al., 2011) was used for data reduction. We corrected blank counts and instrumental bias using an automatic spline function, and downhole element fractionation using an exponential downhole correction fit to the time-resolved data for each analysis. Common Pb was monitored, but not corrected. Weighted mean, concordia and upper intercept ages (95 % confidence level) calculations, as well as concordia diagram plotting were conducted using Isoplot/Ex 4.15 (Ludwig, 2012).

Stacked distribution and probability density plots of all samples were created in the MATLAB script AgeCalcML v1.42 (Sundell, 2022). We allowed for a maximum discordance of 10 %. Intersample comparison of locally adaptive kernel density estimates using cumulative distribution functions and cross-correlation was conducted in the MATLAB script Dzstats v2.30 (Saylor and Sundell, 2016). We used a cross-correlation R^2 cut-off value > 0.4, above which we cannot reject the hypothesis that samples are taken from the same population. For likeness, we used a cut-off value < 0.45, below which we cannot reject the hypothesis that samples are taken from different populations (see Saylor and Sundell, 2016: their Figure 12).

Maximum depositional age

The law of detrital zircon (Gehrels, 2014; Herriott et al., 2019) states that "a sedimentary unit can be no older than the youngest detrital zircon grain(s)" (Gehrels, 2014, p. 134). As such, it has become common practice to tie the maximum depositional age (MDA) of a sample to the youngest single detrital zircon grain (YSG). However, various factors, most notably lead loss (Sharman and Malkowski, 2020) and sample contamination, can contribute to an MDA that is younger than the true depositional age (TDA). Other options for calculating an MDA include using the youngest 1σ grain cluster (YC1σ; Dickinson and Gehrels, 2009), the youngest 2σ grain cluster (YC2σ; Dickinson and Gehrels, 2009), or the maximum likelihood algorithm of Galbraith and Laslett (1993) as implemented by Vermeesch (2021). The latter provides a purely statistical approach to define the maximum likelihood age (MLA; Vermeesch, 2021). The methods presented by Dickinson and Gehrels (2009) become increasingly conservative from YSG to YC1σ to YC2σ and as such, the probability of calculating an MDA younger than the TDA of the sample decreases (Coutts et al., 2019; Dickinson and Gehrels, 2009). While more conservative methods (e.g., YC1σ, YC2σ) provide good results for large data sets (n > 300) with a high percentage of near-depositional-age grains, for small (n < 120) data sets and low percentages of near-depositional-age grains, YSG is more successful, even though it is highly susceptible to external sources of error (Coutts et al., 2019). Furthermore, the MDA calculated from the MLA will be identical to the YSG if there is a significant age difference between the two youngest grains in a sample (Vermeesch, 2021). Following the approach of e.g., Sickmann et al. (2018), we compare the YSG (as single-grain age ± 2σ error), YC1σ, YC2σ (both as weighted mean of population ± standard deviation) and MLA MDA for all samples.

2.3.4 Zircon (U-Th-Sm)/He thermochronology

Low-temperature zircon (U-Th-Sm)/He zircon (ZHe) thermochronology is based on the decay of U, Th and Sm parent isotopes, producing α-particles that are ejected from the zircon crystal.

Within the zircon partial retention zone (ZPRZ), He atoms (α particles) are “neither quantitatively retained nor lost by diffusion” on geological timescales (Wolf et al., 1998, p. 105). This temperature interval is located approximately between 170 and 190 °C. The closure temperature (T_c) of the ZHe system is dependent on crystal size, cooling rate and radiation damage; an average T_c for the ZHe system is 183 °C (Reiners et al., 2004). Zircon aliquots were hand-picked using a binocular polarizing microscope, taking care to eliminate grains with fractures, a grain size < 60 μm and/or broken terminations. We recorded the width, length of prism and total length of all grains. Zircon aliquots were packed into Nb tubes and loaded into the Australian Scientific Instruments (ASI) Alphachron He extraction and analysis system at the University of Potsdam. Analysis of U, Th and Sm abundances by isotope dilution was conducted at the GFZ Potsdam. Additional analytical data are provided in Galetto et al. (2021). ZHe ages are reported with a weighted error, which weights the relative contribution of each parent isotope to the total He production.

2.4 Results

2.4.1 Provenance

Provenance analysis was conducted for samples TAC1 and TAC2 using field data and point-counting. Sample TAC2 was collected from a laminated, deep red, fine-grained sandstone that forms minor intercalations in the Ocumazo conglomerate. This deep red to purple, poorly-sorted conglomerate with cobble to boulder sized (≤ 1 meter) angular clasts locally interfingers with and overlies the eolian sandstones of the Tacurú Group in the western limb of the Cianzo syncline. The clasts show a weak imbrication. Clast lithologies vary, depending on the location of the sample with respect to the normal fault. In the hanging wall of the Hornocal fault, the conglomerate clasts are lithic fragments that are mostly sourced from the Mesón Group quartzites, Puncoviscana Fm shales and sandstones, and Santa Victoria Group sandstones. In contrast, in the hanging wall of the Ocumazo fault, the clasts are predominantly sourced from the Puncoviscana Fm, which is found in the footwall of the Ocumazo fault (Figure 2.3a). Furthermore, the conglomerate shows strong lateral thickness variations between areas that are proximal and distal to the faults. The basal Salta Group unconformity forms the top of the Ocumazo conglomerate. The overlying basal Pirgua Subgroup is comprised of a clast-supported conglomerate consisting of subangular to rounded gravel- to cobble-sized clasts. The clasts consist of predominantly laminated, dark red and massive, coarse-grained, pinkish sandstones that might have been sourced from the Mesón Group. Volcanic clasts, quartzites, white sandstones, quartz pebbles and granite clasts form minor components. Sample TAC1 was collected from the basal Pirgua Subgroup in the Tilcara Range, south of the Cianzo syncline. Here, the basal Pirgua Subgroup locally consists of a basal breccia or conglomerate, overlain by parallel and cross-bedded coarse sandstones.

Sample TAC1 of the Pirgua Subgroup consists of moderately-sorted, fine- to medium-grained sandstones with subrounded to rounded grains (Figure 2.5a). The sample is well-laminated with coarser horizons that show more rounded grains. The average composition of the sample is $Q_{87}F_{05}L_{08}$ (sub-litharenite according to Folk, 1980) and there are large amounts of quartz cement.

Sample TAC2 of the Ocumazo conglomerate (Tacurú Group) consists of poorly sorted, very fine- to fine-grained sandstones with subangular grains (Figure 2.5a). Quartz grains comprise 83 % of the modal composition, feldspar 4 % and lithic fragments 13 % ($Q_{83}F_{04}L_{13}$, sub-litharenite according to Folk, 1980). The sample shows large amounts of iron oxide cement (as determined from optical properties under a polarized light microscope), sericitized feldspars, as well as highly weathered, mostly sedimentary (Ls) lithic fragments. TAC2 is more finely laminated than TAC1, although the latter shows a higher variation in grain size between individual layers. Both the Pirgua Subgroup (TAC1) and Ocumazo conglomerate (TAC2) sample contain high amounts (> 80 %) of quartz (predominantly Qm), low amounts of lithic fragments (< 15 %) and very low amounts of feldspar (≤ 5 %). The high quartz content, very high quartz to feldspar ratio and the high amount of sedimentary (and metamorphic) lithic fragments give the samples a recycled orogeny signature in ternary diagrams (Dickinson et al., 1983) (Figure 2.5b–d).

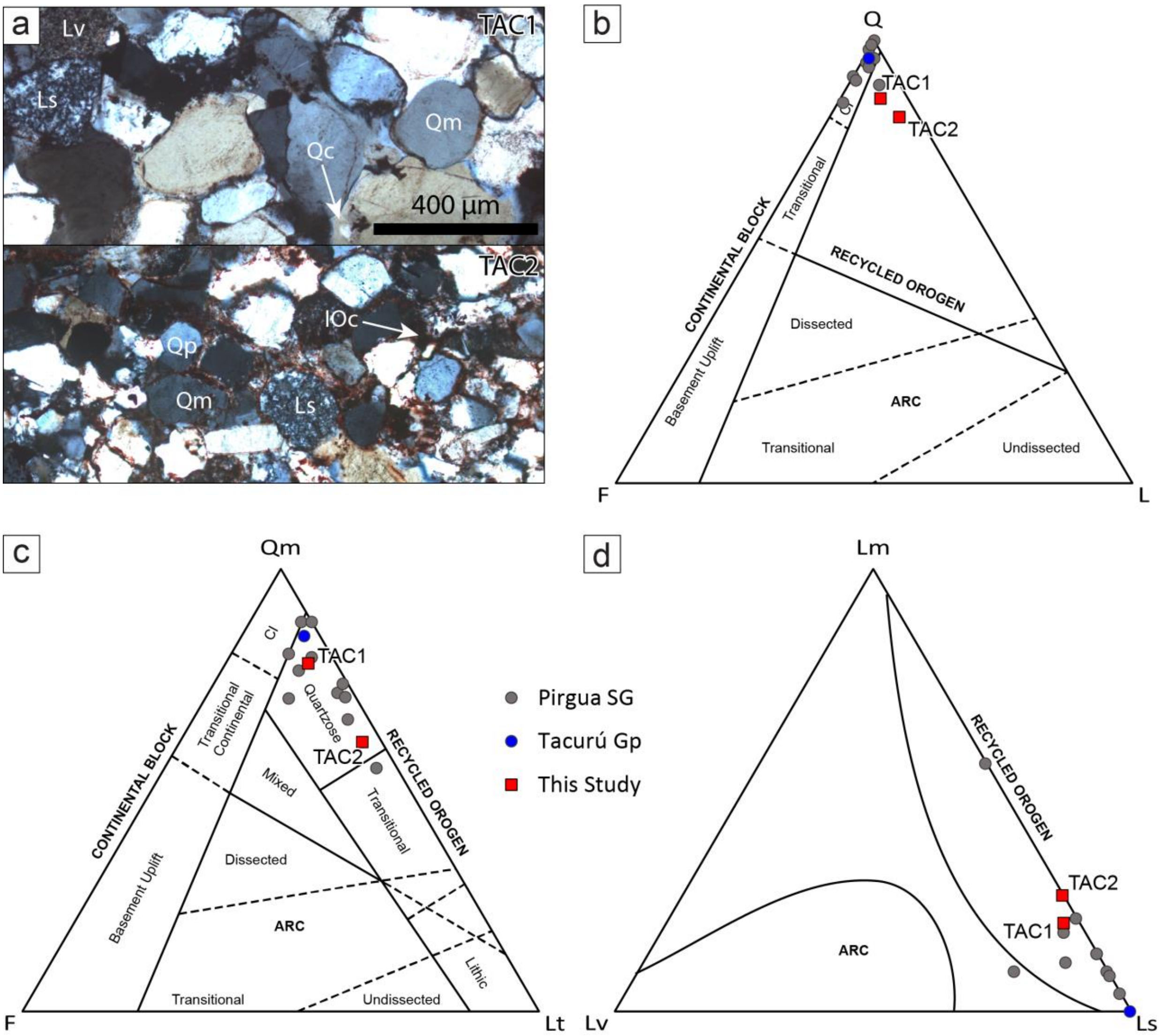

Figure 2.5 (a) Thin section microscopic images of sample TAC1 (top) and TAC2 (bottom). Quartz (Qc) and iron oxide (IOc) cement are indicated with arrows. Monocrystalline quartz (Qm), polycrystalline quartz (Qp), sedimentary lithic fragments (Ls) and volcanic lithic fragments (Lv) are marked. (b–d) Sandstone point-count data in ternary diagrams following Dickinson et al. (1983). Squares represent samples from this study, dots mark samples from McBride (2008). (b) Q-F-L (Dickinson et al., 1983), (c)

Qm-F-Lt (monocrystalline quartz-feldspar-total lithic fragments; Dickinson et al., 1983), (d) Lm-Ls-Lv (metamorphic-sedimentary-volcanic lithic fragments; field names and boundaries from Dickinson and Suczek, 1979).

Compared to samples from the Tacurú Group (SM20070628-1; McBride, 2008) and the Pirgua Subgroup (HOR1 and HOR2 samples; McBride, 2008), TAC2 shows a higher amount of lithics (Figure 2.5b–c). In the Qm-F-Lt diagram (Figure 2.5c), the samples overlap with the Pirgua samples (McBride, 2008) within the quartzose recycled orogen field. The Lm-Ls-Lv diagram (Figure 2.5d) shows that the amount of metamorphic lithic fragments for TAC1 and TAC2 is slightly higher compared to the samples of McBride (2008). In general, sample TAC1 shows a higher overlap with the Pirgua Subgroup samples than TAC2, even though the difference is small in Q-F-L and Lm-Ls-Lv diagrams (Figure 2.5b and d).

Table 2.1 Point-count data from this study and McBride (2008). For descriptions of counted grain types, see Siks and Horton (2011: their Table 3).

Sample	Lithology	Qm	F	Lt	Q	F	L	Lm	Lv	Ls	Source
TAC2	Tacurú Gp	0.61	0.04	0.35	0.83	0.04	0.13	0.26	0.00	0.74	This Study
TAC1	Pirgua SG	0.79	0.05	0.16	0.87	0.05	0.08	0.20	0.03	0.77	This Study
HOR2-894	Pirgua SG	0.70	0.13	0.16	0.86	0.13	0.01	0.09	0.18	0.73	McBride (2008)
HOR2-541	Pirgua SG	0.88	0.02	0.10	0.98	0.02	0.00	0.56	0.00	0.44	McBride (2008)
HOR2-337	Pirgua SG	0.72	0.03	0.25	0.97	0.03	0.01	0.04	0.00	0.96	McBride (2008)
HOR2-120	Pirgua SG	0.71	0.02	0.27	0.96	0.02	0.02	0.21	0.00	0.79	McBride (2008)
HOR1-1231	Pirgua SG	0.80	0.04	0.16	0.96	0.04	0.01	0.11	0.07	0.82	McBride (2008)
HOR1-1116	Pirgua SG	0.88	0.00	0.12	0.99	0.00	0.00	0.13	0.00	0.87	McBride (2008)
HOR1-937	Pirgua SG	0.77	0.08	0.15	0.91	0.08	0.00	0.13	0.00	0.87	McBride (2008)
HOR1-644	Pirgua SG	0.66	0.04	0.30	0.94	0.04	0.02	0.09	0.00	0.91	McBride (2008)
HOR1-594	Pirgua SG	0.74	0.01	0.25	0.99	0.01	0.00	0.08	0.00	0.92	McBride (2008)
HOR1-462	Pirgua SG	0.80	0.08	0.11	0.91	0.08	0.01	0.13	0.00	0.87	McBride (2008)
HOR1-185	Pirgua SG	0.55	0.04	0.41	0.90	0.04	0.06	0.18	0.04	0.79	McBride (2008)
0628-1	Tacurú Gp	0.84	0.03	0.12	0.96	0.03	0.01	0.00	0.00	1.00	McBride (2008)

2.4.2 Detrital zircon U-Pb geochronology

Maximum depositional age

We report 341 detrital zircon U-Pb ages from three sandstone samples (Table 2.2, Figure 2.6). The MDA of sample BREN1 (Las Breñas Fm) is late Cambrian, as shown by the YSG (498 ± 3 Ma), MLA (498 ± 5 Ma) and the YC1σ and YC2σ clusters (519 ± 1 and 523 ± 3, respectively), which all correlate well with each other. Whereas the YSG of the Las Breñas Fm (BREN1) is significantly older than that of the Santa Victoria Group (LP-V6; Aparicio González et al., 2020) and the Mesón Group (MESON; McBride, 2008), YC1σ and especially YC2σ ages are markedly similar to all the stratigraphically older samples, including the Puncoviscana Fm (PUNC1; McBride, 2008).

Sample TAC2 (Ocumazo conglomerate, Tacurú Group) has a YSG age of 155 ± 2 Ma, which corresponds to a younging-upward trend from the lower, eolian Tacurú Group (SM20070628-1; McBride, 2008) to the Pirgua Subgroup (HOR1-297; McBride, 2008) (Table 2.2) and overlaps with the MLA age (156 ± 2), due to the lack of further Jurassic ages. YC1σ and YC2σ provide

Ordovician ages of 451 ± 4 and 457 ± 5, respectively. Although these ages also young upwards within the Tacurú Group-Pirgua Subgroup succession, they show a marked difference to the proposed depositional age of the Tacurú Group. Therefore, the Ocumazo conglomerate has an upper Jurassic MDA (YSG, MLA).

Table 2.2 U-Pb data for samples TAC1, TAC2 and BREN1 (this study) and samples from McBride (2008) and Aparicio González et al. (2020). Coordinates are given in UTM Zone 20K. MDA ages (in Ma) were obtained by four methods: using YSG (single-grain age ± 2σ error), YC1σ, YC2σ (both as weighted mean of the population (WM_p) ± standard deviation (SD)) and MLA. Full U-Pb sample and standard data can be found in Appendix A.

Sample	UTM E	UTM N	Stratigraphic unit	N[a]	YSG	± 2σ	YC1σ	SD	YC2σ	SD	MLA	Error
PUNC1[1]	729741	7266620	Puncoviscana Fm	75	513	6	514	1	524	5		
MESON[1]	796197	7414806	Mesón Group	90	488	5	491	3	508	8		
LP-V6[2]	302683	7291793	Santa Victoria Gp	96	345	3	495	4	524	5		
BREN1	541532	7389079	Las Breñas Fm	85	498	3	519	1	523	3	498	5
ZU1[2]	314278	7269765	Zapla Formation	96	454	4	520	2	522	3		
SM20070629-1[1]	289330	7434706	Mandiyutí Group	85	310	8	314	3	314	3		
SM20070628-1[1]	273714	7423899	Tacurú Group	91	167	3	480	6	488	8		
TAC2	274077	7423106	Tacurú Group	101	155	2	451	4	457	5	156	2
TAC1	272118	7406576	Pirgua Subgroup	155	271	3	404	1	471	3	271	3
HOR1-297[1]	---	---	Pirgua Subgroup	79	150	1	262	1	262	1		

[1]Samples from McBride (2008)

[2]Samples from Aparicio González et al. (2020)

[a]Number of analyzed zircons with a discordance < 10 % (for samples in this study)

The YSG and MLA ages of sample TAC1 (Pirgua Subgroup in the Tilcara Range) are upper Permian (271 ± 3 Ma) and are older than for the samples in the Cianzo syncline (TAC2: this study; SM20070628-1 and HOR1-297: McBride, 2008). Similar to sample TAC2, YC1σ and YC2σ clusters (404 ± 0.6 and 471 ± 3 Ma, respectively) are significantly older than both the YSG and MLA age. Whereas YC1σ and YC2σ ages are much older than for HOR1-297 (Pirgua Subgroup; McBride, 2008), the YC2σ cluster has a similar age as for the Tacurú Group samples in the Cianzo syncline (TAC2: this study; SM20070628-1: McBride, 2008).

Provenance

Sample BREN1 (Las Breñas Fm) shows Pampean-Brasiliano (760–525 Ma; e.g., Escayola et al., 2011; Lucassen et al., 1999) age signatures, with clusters between 550–510 Ma (28 of 85 grains) and 680–580 Ma (32 grains) (Figure 2.6a). Part of the youngest cluster might be attributed to the Famatinian phase. The cluster between 1050–970 Ma (8 grains) is ascribed to the Sunsás phase (1200–900 Ma; e.g., Casquet et al., 2010). The distribution of clusters in the detrital age signal of the Las Breñas Fm (BREN1) is similar to that of the Mesón Group, showing high amounts of detrital zircons derived from the Pampean-Brasiliano phase rocks and low-probability clusters derived from the Sunsás orogeny rocks. However, the age peak of Brasiliano-derived zircons is markedly higher compared to the Precambrian–Ordovician samples from McBride (2008) and Aparicio González et al. (2020). Furthermore, the age signal between 780 and 810 Ma (3 grains) within the Santa Victoria Group and Zapla Fm (LP-V6, ZU1; Aparicio González et al., 2020), and the Las Breñas Fm (BREN1, this study), albeit minor, is lacking in the stratigraphically lower Mesón Group and Puncoviscana Fm samples (orange bar in Figure 2.6a).

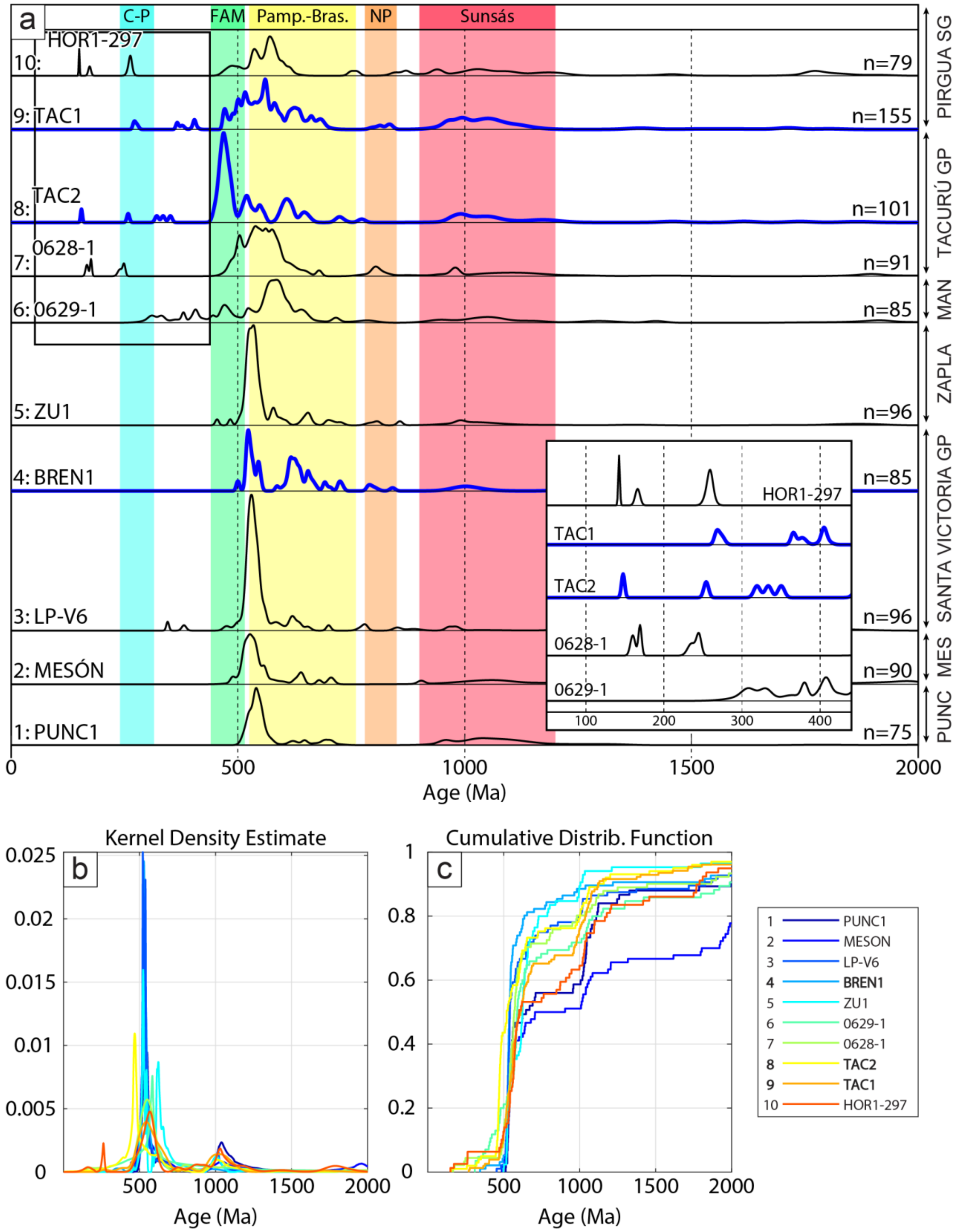

Figure 2.6 (a) Detrital zircon U-Pb age distributions for samples from McBride (2008) (1, 2, 6, 7, 10), Aparicio González et al. (2020) (3, 5) and this study (4, 8, 9; blue lines). The relative age probability is plotted as black and blue (this study) lines. Color shaded bars show characteristic age populations from section 2.2 (age intervals from Einhorn et al., 2015, based on references given in text). The inset shows the probability density distribution between 50 and 440 Ma in more detail. PUNC: Puncoviscana Fm, MES: Mesón Group, MAN: Mandiyutí Group. (b) Locally adaptive Kernel density estimate (KDE), and (c) cumulative distribution function (CDF) for all samples.

Within the detrital age distribution of sample TAC2 (Ocumazo conglomerate, Tacurú Group), the Famatinian (515–440 Ma; e.g., Casquet et al., 2010; Escayola et al., 2011; Lucassen et al., 1999) age signature between 490 and 430 Ma (39 of 101 grains) is clearly dominant (Figure 2.6a). Famatinian clusters in age distributions of Carboniferous–Cretaceous samples are very small in comparison. Further peaks are located in the interval of 550–510 Ma and 660–580 Ma (Pampean-Brasiliano age signature; 14 and 15 grains, respectively), and 1070–960 Ma (Sunsás age signature, 13 grains). Ages younger than 400 Ma are rare, similar to the other Tacurú Group and Pirgua Subgroup samples. Unlike the upper Cambrian–lower Ordovician samples, the Ocumazo conglomerate does not show ages in the interval between 850 and 780 Ma.

Sample TAC1 (Pirgua Subgroup in the Tilcara Range) predominantly contains detrital zircon ages in the Famatinian and Pampean-Brasiliano intervals between 700–460 Ma (95 of 155 grains; Figure 2.6a). A second peak is located in the interval between 1160–940 Ma (37 grains), showing Sunsás age signatures. The minor cluster between 850–780 Ma (4 grains) was also seen in the eolian Tacurú Group sample (SM20070628-1; McBride, 2008) and Paleozoic samples (e.g., BREN1). Similar to sample TAC2, young (< 400 Ma) grains are scarce.

Cross-correlation and likeness

Sample BREN1 (Las Breñas Fm) generally shows low R^2 (cross-correlation) and likeness values, especially when compared with stratigraphically younger samples. An acceptable likeness value is only reached for the Zapla Fm (ZU1; Aparicio González et al., 2020) (Table 2.3). R^2 values show a reasonable cross-correlation for the Mesón Group, Santa Victoria Group and Zapla Fm samples (MESON, LP-V6 and ZU1; Table 2.3).

The age signature of sample TAC2 (Ocumazo conglomerate, Tacurú Group) deviates strongly from all other samples, reaching no acceptable values for R^2 (cross-correlation) and likeness. R^2 values for stratigraphically older samples are highest for the Mesón Group and the Mandiyutí Group (MESON, SM20070629-1; McBride, 2008) (Table 2.3). Slightly higher cross-correlation values are reached for the underlying eolian Tacurú Group and the overlying Pirgua Subgroup (SM20070628-1, HOR1-297; McBride, 2008). Likeness values follow a similar pattern, with the highest likeness for the Mandiyutí Group (SM20070629-1; McBride, 2008) and the Pirgua Subgroup (TAC1).

Sample TAC1 (Pirgua Subgroup in the Tilcara Range) reaches high R^2 (cross-correlation) and likeness values for the Tacurú Group and the basal Pirgua Subgroup in the Cianzo syncline (SM20070628-1, HOR1-297; McBride, 2008) (Table 2.3). In stratigraphically older samples, R^2 (cross-correlation) and likeness values are the highest for the Puncoviscana Fm, Mesón Group and the Mandiyuti Group (PUNC1, MESON, SM20070629-1; McBride, 2008). Based solely on cut-off values, we cannot exclude any Precambrian–Carboniferous lithologies as sources, but the Santa Victoria Group and Zapla Fm (LP-V6, ZU1; Aparicio González et al., 2020) show the lowest values for both likeness and cross-correlation.

Table 2.3 Comparison of cross-correlation (R^2) and likeness values for all samples. R^2 and likeness values are 1 for identical age spectra. R^2 decreases with decreasing cross-correlation and the likeness value decreases with increasing area mismatch between samples. We consider $R^2 > 0.5$ and likeness values > 0.6 (green shading) to show reasonable correlation between samples.

Cross Correlation Coefficient

	PUNC1	MESON	LP-V6	ZU1	BREN1	0629-1	0628-1	TAC2	TAC1	HOR1
PUNC1		0.77	0.79	0.73	0.40	0.19	0.60	0.05	0.57	0.52
MESON	0.77		0.82	0.79	0.56	0.29	0.75	0.12	0.69	0.53
LP-V6	0.79	0.82		0.86	0.54	0.15	0.51	0.05	0.41	0.34
ZU1	0.73	0.79	0.86		0.52	0.13	0.47	0.06	0.41	0.31
BREN1	0.40	0.56	0.54	0.52		0.15	0.35	0.06	0.44	0.19
0629-1	0.19	0.29	0.15	0.13	0.15		0.65	0.15	0.61	0.65
0628-1	0.60	0.75	0.51	0.47	0.35	0.65		0.19	0.87	0.83
TAC2	0.05	0.12	0.05	0.06	0.06	0.15	0.19		0.25	0.12
TAC1	0.57	0.69	0.41	0.41	0.44	0.61	0.87	0.25		0.77
HOR1	0.52	0.53	0.34	0.31	0.19	0.65	0.83	0.12	0.77	

Likeness value

	PUNC1	MESON	LP-V6	ZU1	BREN1	0629-1	0628-1	TAC2	TAC1	HOR1
PUNC1		0.70	0.64	0.68	0.51	0.47	0.59	0.45	0.64	0.61
MESON	0.70		0.63	0.72	0.58	0.61	0.73	0.53	0.71	0.66
LP-V6	0.64	0.63		0.79	0.55	0.44	0.57	0.37	0.51	0.47
ZU1	0.68	0.72	0.79		0.63	0.47	0.59	0.45	0.58	0.52
BREN1	0.51	0.58	0.55	0.63		0.44	0.50	0.37	0.55	0.41
0629-1	0.47	0.61	0.44	0.47	0.44		0.68	0.59	0.69	0.67
0628-1	0.59	0.73	0.57	0.59	0.50	0.68		0.53	0.74	0.73
TAC2	0.45	0.53	0.37	0.45	0.37	0.59	0.53		0.59	0.50
TAC1	0.64	0.71	0.51	0.58	0.55	0.69	0.74	0.59		0.72
HOR1	0.61	0.66	0.47	0.52	0.41	0.67	0.73	0.50	0.72	

2.4.3 Zircon (U-Th-Sm)/He thermochronology

ZHe analysis of single-grain aliquots for sample BREN1 (Las Breñas Fm) yields Late Triassic to Early Cretaceous cooling ages. There are no age-eU, age-F_T and/or age-ESR trends that might explain overdispersion, although the youngest grain (BREN1_z1) shows high eU compared to the other aliquots, which could affect its closure temperature (Guenthner et al., 2013) and thus might explain why the cooling age is younger. Analytical data and ZHe cooling ages for sample BREN1 are provided in Table 2.4.

Table 2.4 ZHe results of sample BREN1 of the Las Breñas Fm.

#	Age (Ma)	± 2σ (Ma)	U (ppm)	Th (ppm)	^{147}Sm (ppm)	eU (ppm)	Th/^{238}U	He (nmol/g)	F_T	ESR (μm)[a]	# T[b]
z1	115.9	1.0	588.5	110.1	0.4	614.4	0.2	306.4	0.79	58.6	2
z2	196.8	2.0	184.3	94.9	0.3	206.6	0.5	171.0	0.77	52.8	2
z3	147.6	1.2	276.4	153.1	0.3	312.4	0.6	194.0	0.77	53.8	2
z4	225.6	3.6	308.9	65.8	0.6	324.4	0.2	296.8	0.74	46.1	2
z5	143.0	3.6	211.1	96.7	0.4	233.8	0.5	132.2	0.72	44.1	2

[a]Equivalent spherical radius
[b]Number of crystal terminations

2.5 Discussion

In the following section, we discuss the detrital zircon U-Pb, ZHe and point counting analyses of the Las Breñas Fm (BREN1), Ocumazo conglomerate (TAC2) and basal Pirgua Subgroup (TAC1), from the rift shoulder to the early syn-rift infill of the western Lomas de Olmedo sub-basin. Characterization of these samples highlights differences in provenance and provides implications for the tectonic development in the early stages of Mesozoic extension.

2.5.1 Las Breñas Formation

The southern rift shoulder of the Lomas de Olmedo sub-basin is represented by the Las Breñas Fm, a Cambrian–Ordovician sedimentary unit that is part of the Paleozoic pre-rift basement of the Central Andes (Agüera et al., 2019; Chebli et al., 1999; Russo et al., 1979). The middle to upper Cambrian MDA of the Las Breñas Fm (sample BREN1) agrees well with the proposed Cambrian–Ordovician depositional age and a stratigraphic placement below the Zapla Fm (Chebli et al., 1999; Rubinstein, 2005). Its depositional age implies that the Las Breñas Fm could have been recycled from the Precambrian–Cambrian Puncoviscana Fm or the Cambrian Mesón Group, which is also evident from the acceptable R^2 (cross-correlation) value compared with the Mesón Group (MESON; McBride, 2008). The relatively high likeness and R^2 (cross-correlation) values of the Las Breñas Fm compared to the Cambrian–Ordovician samples (Santa Victoria Group and Zapla Fm; samples LP-V6, ZU1; Aparicio González et al., 2020) (Table 2.3) may indicate a genetic correlation between these samples. However, the markedly high amount of Brasiliano-derived zircons with ages between 680–580 Ma suggests zircon sources for the Las Breñas Fm that are located farther east compared to the aforementioned Cambrian–Ordovician samples, which show prominent Pampean clusters. This is not surprising, given that the sampling location of BREN1 is located > 200 km east of the other samples. The lack of Famatinian zircon ages (< 3 grains) suggests that the Famatinian arc west of the Ordovician clastic platform did not provide a significant source of zircons. Instead, possible zircon sources for the Las Breñas Fm may have been located within the Pampia Terrane, Brasiliana Belt or Rio de la Plata Craton (proximal to distal in reference to the Las Breñas depositional environment; Ramos, 2008, 2018) (Figure 2.1c). Based on the very low R^2 and likeness values of the Las Breñas Fm, compared with Mesozoic strata of the Tacurú Group and Pirgua Subgroup, as well as the higher amount of Famatinian-aged zircons in these younger strata, it is unlikely that the Las Breñas Fm was a significant source of zircons for Mesozoic rocks in the westernmost Lomas de Olmedo sub-basin. Furthermore, the spatial relations between the Mesozoic samples, which were deposited in half-grabens near the northern rift margin, and the Las Breñas Fm in the southern rift shoulder of the sub-basin, also make it unlikely that early syn-rift strata from this part of the Lomas de Olmedo sub-basin contain zircons from far southeastern sediment sources. However, we cannot fully exclude the possibility that Mesozoic samples contain zircons reworked from the southern rift shoulder lithologies, because the large E–W offset between sampling locations in the northern Lomas de Olmedo sub-basin and its southern rift shoulder forms a major limitation for provenance interpretations. Sampling the southern rift shoulder within the Eastern Cordillera, more proximal to the Mesozoic samples, might form a better approach to unraveling its influence on Mesozoic sedimentary provenance.

2.5.2 Mesozoic strata

The detrital zircon U-Pb age signature of the Ocumazo conglomerate (Tacurú Group; sample TAC2) is markedly different from the underlying and overlying strata and does not show any strong correlation with Precambrian–Carboniferous source rocks (Table 2.3). Although the Mesón Group (MESON; McBride, 2008) and Mandiyuti Group (SM20070629-1; McBride, 2008) appear to form more likely sources of zircons (Table 2.3), based on R^2 and likeness values, Famatinian zircon ages clearly dominate the probability distribution, suggesting that the majority of the zircons is sourced from Ordovician rocks from the Famatinian arc that is now located west of the study area (Rapela et al., 2007). On the other hand, the eolian facies of the Tacurú Group interfinger with the Ocumazo conglomerate and recycling of these eolian sands may also have introduced more distal zircon sources. The Ocumazo conglomerate in the Cianzo syncline (see also Starck, 2008) is a very proximal deposit, as indicated by the angularity of the clasts. Moreover, the clast lithologies vary strongly depending on the lithologies exposed in the footwalls of adjacent normal faults, and the conglomerate generally has a large thickness proximal to normal faults, whereas it is absent in more distal areas. As such, the sandstones of the upper Cambrian–Ordovician Santa Victoria Group and, to a lesser extent, the Mesón Group directly west and/or north of Cianzo (Kley et al., 2005; Siks and Horton, 2011) could have formed proximal sources for the conglomerate clasts. The apparent discrepancy between the Ocumazo conglomerate clast composition and the prominent Famatinian cluster in the detrital zircon U-Pb record might be attributed to the sampled material: whereas field data was collected from conglomerate outcrops, we analyzed zircons from laminated, fine-grained sandstones that were intercalated in these conglomerates. Therefore, provenance interpretations based on detrital zircon U-Pb data might not be viable for clast-based data and vice versa. Furthermore, the major limitations of using first order alluvial deposits for provenance studies and tectonic interpretations should be considered. In cases of variable source rocks, first order deposits show highly variable compositions that directly reflect these sources. As a result, we can discriminate between individual source rock types in first (and second) order deposits (Ingersoll, 1990), but we might not be able to relate these strata to plate tectonic settings (Ingersoll et al., 1993). This is especially true for continental rifts, as Ingersoll et al. (1993) show. Therefore, we must consider that especially the Ocumazo conglomerate sample (TAC2), but also the basal Pirgua Subgroup sample (TAC1) compositions may not reflect the plate tectonic setting of NW Argentina in the Jurassic and Cretaceous.

It is intriguing that, although samples SM20070628-1, TAC2 and HOR1-297 form a continuous stratigraphic section across the Salta Group unconformity, from the eolian Tacurú Group to the basal Pirgua Subgroup, the Ocumazo conglomerate (sample TAC2) shows a very low correlation with the underlying and overlying strata (Table 2.3). In contrast, the basal Pirgua Subgroup in the Tilcara Range (TAC1) shows a high similarity to the Tacurú Group and Pirgua Subgroup samples of McBride (2008) (SM20070628-1, HOR1-297) (Table 2.3), although we sampled it > 15 km south of the Cianzo syncline. Based on field observations, both TAC2 and TAC1 were thought to be sampled from strata proximal to the basin-bounding normal faults of the Lomas de Olmedo sub-basin. For example, the sampling site of TAC1 is located directly above a basal breccia with angular clasts (Van Kooten et al., 2022b) and the Ocumazo conglomerate (TAC2) occurs only in the hanging walls of the Ocumazo and Hornocal normal faults (see also Figure 2.3a). However, the degree of rounding suggests that the Pirgua Subgroup in the Tilcara Range (TAC1) may have had a more distal source of sediment than the Ocumazo conglomerate (Tacurú Group) in the Cianzo syncline (TAC2). The R^2 and likeness values of the Pirgua Subgroup in the Tilcara Range (TAC1), and the eolian Tacurú Group and Pirgua Subgroup in the Cianzo syncline (SM20070629-1 and HOR1-297; McBride, 2008) are well correlated with each other, whereas the Ocumazo conglomerate (TAC2) generally shows a weak correlation with all other samples, which is probably related to the dominant Famatinian peak. This may indicate a genetic relationship between the Pirgua Subgroup in the Tilcara Range and the Cianzo syncline (HOR1-297; McBride, 2008), but it may also indicate strongly varying zircon sources between the Ocumazo conglomerate and the other units.

Although Ordovician YC1σ and YC2σ ages show a major offset between the Tacurú Group (TAC2, this study; SM20070628-1, McBride, 2008) and Pirgua Subgroup (HOR1-297; McBride, 2008), the YSG ages show a continuous upwards-younging trend of Middle to Late Jurassic ages. For the Tacurú Group (TAC2, SM20070628-1), a Middle–Late Jurassic MDA is in accordance with the proposed Jurassic depositional age of these strata in the Cianzo syncline (Starck, 1995, 2008) and the low discordance (0.8 %) of the youngest grain of TAC2 indicates that this U-Pb date is reliable. On the other hand, the overlying Pirgua Subgroup (HOR1-297, McBride, 2008) has a proposed Cretaceous depositional age (Marquillas et al., 2005, and references therein) that is younger than the Late Jurassic MDA provided by detrital zircon U-Pb data (McBride, 2008). Similarly, the basal Pirgua Subgroup in the Tilcara Range has a Permian MDA, even though from stratigraphic considerations its depositional age should be Cretaceous. Mesozoic grains generally seem to be scarce or absent, even in younger strata of NW Argentina (Carrapa et al., 2011; Carrapa et al., 2012; DeCelles et al., 2011; Pearson et al., 2012). McBride (2008) attributes the absence of Cretaceous grains within the detrital zircon U-Pb age signature of Pirgua Subgroup partly to a major divide between the magmatic arc and the Pirgua Subgroup during the Cretaceous period. However, we must also take into consideration the large distance (> 400 km) between the Jurassic and Cretaceous magmatic arc, located in the present-day Chilean Coastal Cordillera (Charrier and Muñoz, 1994; Scheuber and Gonzalez, 1999), and the Lomas de Olmedo sub-basin. Furthermore, given that basal volcanic complexes related to the Salta Rift occur in southern sub-basins and new volcanic zircons are only available in upper levels of the Pirgua Subgroup (Marquillas et al., 2005), it is not unlikely that the YSG age of the basal Pirgua Subgroup is older than its TDA. Similar objections can be found for the Tacurú Group MDA. The rounding of young zircons also attests to a certain transportation distance and thus an amount of time between zircon formation and deposition. Another limitation is the use of YSG ages for the MDA calculations, because these are generally more susceptible to external sources of error (Coutts et al., 2019). Using MLA to obtain an MDA is a statistically robust method, but in samples where the two youngest grains show a significant age difference, the MDA calculated from the MLA is identical to the YSG (Vermeesch, 2021) (Table 2.2) and thus has similar limitations.

2.5.3 Onset of extension

Although the continuity in U-Pb YSG ages within the Tacurú Group-Pirgua Subgroup section of the Cianzo syncline appears to suggest that the duration of the Salta Group unconformity is very short, we have outlined the limitations of this argument in Section 2.5.2. Moreover, the unconformity is strongly angular, showing changes in both dip and strike between the Tacurú Group and Pirgua Subgroup, and varying provenance also suggests a clear separation of these two units. Outcrop data showing poor sorting, footwall-dependent clast lithology, and angular to subangular clasts (see also TAC2; Figure 2.5a) strongly indicate a proximal origin of the Ocumazo conglomerate. Combined with rapid thickness changes and its occurrence near normal faults, the field evidence appears to support the idea that the Ocumazo conglomerate is a deposit related to extensional normal faults (see also Starck, 2008).

The Pirgua Subgroup is related to deposition in half-grabens that formed during the Salta Rift phase (Marquillas et al., 2005; Salfity and Marquillas, 1994), as is evident from rapid thickness changes toward Cretaceous normal faults (e.g., Amengual and Zanettini, 1973; Kley et al., 2005). In contrast to the Ocumazo conglomerate, the basal conglomerate of the Pirgua Subgroup is better sorted and contains clasts with a higher degree of rounding that are sourced from more distal lithologies (e.g., volcanic and granitic clasts). By back-rotating the Pirgua Subgroup and Tacurú Group strata, we might be able to better understand the basal Salta Group unconformity that separates these units. Assuming that tilting related to normal faulting occurs along listric faults, the strata are progressively tilted as the throw of the fault increases along a rotational axis that is parallel to the fault scarp (e.g., McClay and Buchanan, 1992). Therefore, by rotating the bedding orientation of the Tacurú Group (approximately 076/88; Figure 2.3a) with the Pirgua Subgroup, so that the Pirgua Subgroup bedding (approximately 107/60; Figure 2.3a) is again horizontal, we obtain the approximate orientation (055/41) of the Tacurú Group before deposition of the Salta Group (Figure 2.7a). This back-rotated orientation of the Tacurú Group could have been caused by the formation of Pirgua Subgroup half-grabens and the tilting of pre-Pirgua strata. In that case, the faults controlling these half-grabens would presumably have formed parallel to the Hornocal fault. However, if the Ocumazo conglomerate is indeed a deposit related to normal faulting, the faults responsible for the tilting of Tacurú Group strata should strike approximately NW–SE. This inferred fault orientation would be caused by SW–NE directed extension (Figure 2.7a), assuming that we ignore any pre-existing stratigraphic and structural heterogeneities. Interestingly, this conclusion is in agreement with a two-phase extension model proposed by Kley et al. (2005: their Figure 11d). A rotation of the direction of Mesozoic extension, as suggested by Kley et al. (2005), might be connected to a change in topography and hence a potential re-organization of paleoflow. McBride (2008) provides paleoflow indicators within the Pirgua Subgroup in the Cianzo syncline; these suggest that the lower section tentatively shows paleoflow toward the west (minor) and north, whereas the upper section shows stronger indicators of eastward paleoflow.

The eolian Tacurú Group (Figure 2.3d) near Cianzo has been correlated with lithologically similar, Jurassic units of the Chaco-Paraná and Paraná basins (Starck, 1995) that are interpreted as post-rift strata, deposited during a period of thermal sag (Sempere et al., 2002). Within the

Hornocal ranges, we relate the proximal character of the interfingering Ocumazo conglomerate (Figure 2.3e) to local extensional normal faults. The deposits of the Tacurú Group in the Cianzo syncline show marked similarities to early Pirgua Subgroup syn-rift deposits in the Sapagua area, a mere 35 kilometers NW of the Cianzo syncline, which are associated with normal fault activity during the Salta Rift phase (Monaldi et al., 2008). These strata were deposited unconformably on top of Paleozoic pre-rift strata and commence with an eolian section at their base, which interfingers with debris flow successions. The Sapagua sedimentary sequence correlates closely with the Tacurú Group deposits in the western limb of the Cianzo syncline, where predominantly eolian sandstones form the base of the Tacurú Group and are followed by a thick succession of coarse, proximal conglomerates (Ocumazo conglomerate; see also Figure 2.2). Although in the Cianzo syncline, the Tacurú Group is clearly separated from the Pirgua Subgroup by the basal Salta Group unconformity, the lithological correlation between the Sapagua early syn-rift succession (Monaldi et al., 2008) and the Tacurú Group in the Cianzo syncline suggests that the Ocumazo conglomerate in the Cianzo syncline is also a fault-bound deposit related to Mesozoic extension. This interpretation is largely in accordance with Starck (2008), who proposed a syn-tectonic, extensional origin for the Ocumazo conglomerate in the Cianzo syncline. Therefore, these sediments might indicate an early influence of extension predating the Salta Group syn-rift succession (Starck, 2008).

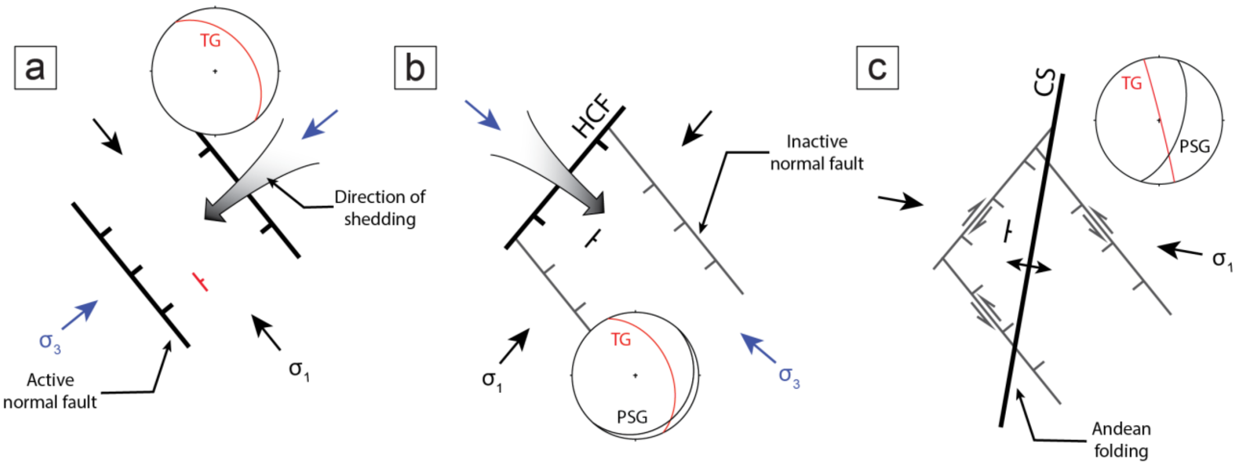

Figure 2.7 Proposed tectonic setting of the Cianzo area, showing direction of sediment shedding from structural highs bordering normal faults during (a) Jurassic deposition of the Ocumazo conglomerate (Tacurú Group), (b) Jurassic–Cretaceous deposition of the Pirgua Subgroup in a half-graben formed by the Hornocal fault (HCF), and (c) Miocene folding of the Cianzo syncline (CS). Black and blue arrows show the ideal orientation of σ_1 and σ_3, respectively. Stereonet insets show orientation of Tacurú Group (red; TG) and Pirgua Subgroup (black; PSG) during progressive rotation.

Jurassic extension is known from e.g., the Cordillera de Domeyko in Chile (Amilibia et al., 2008; Flint et al., 1993), where rifting is assumed to be closely related to the Salta Rift, and the Neuquén basin (Fennell et al., 2020; Vergani and Tankard, 1995), but the distance between the Tacurú Group in the Cianzo basin and these contemporaneous basins is too large for there to be a direct link between local extension and southern rifting events. Furthermore, the Jurassic–Cretaceous opening of the Atlantic ocean, which led to the Salta Rift phase in NW Argentina, caused a contractional regime in the location of the Neuquén basin (Fennell et al., 2020; Iannelli et al., 2020). Another extensional phase, related to Late Permian–Middle Jurassic rifting, has been recorded in Peru and Bolivia, where the main axis of the Peruvian-Bolivian rift basin runs along the present-day Eastern Cordillera and rifting propagated from north to south (Sempere et al., 1998; Sempere et al., 1999; Sempere et al., 2002). The Entre Ríos branch of this rift system runs south toward the Bolivian-Argentinian border. Nevertheless, a genetic relation between the Entre Ríos rift branch and the Ocumazo conglomerate seems unlikely, because the post-rift interpretation of the eolian Tacurú Group in Bolivia (Sempere et al., 2002) does not correlate with a syn-tectonic interpretation of the interfingering Ocumazo conglomerate in the Cianzo syncline (Starck, 2008).

Many studies have considered the earliest onset of Mesozoic extension in NW Argentina to be of Early Cretaceous age, mostly based on absolute dating of Pirgua Subgroup deposits, especially in southern sub-basins of the Salta Rift basin (e.g., Galliski and Viramonte, 1988; Marquillas et al., 2005; Salfity and Marquillas, 1994). Some authors (see Cristiani et al., 2003; Kley and Monaldi, 2002) have suggested a (Late) Jurassic onset of rifting, which is in accordance with K-Ar ages of alkaline lamprophyre dykes within the Eastern Cordillera, ascribed to the pre-rift stage (Hauser et al., 2010), zircon U-Pb and apatite fission track cooling ages of intrusions within the Puna plateau (Insel et al., 2012), and low-temperature thermochronology data from the Eastern Cordillera (Deeken et al., 2006; Zapata et al., 2019a). As we show here, in the western Lomas de Olmedo sub-basin, a Jurassic MDA for the Tacurú Group (Ocumazo conglomerate) within the Cianzo syncline correlates with Jurassic ZHe cooling ages from the footwall block of the Hornocal fault (Van Kooten et al., 2021) and Late Triassic–Early Cretaceous cooling ages within the Los Blancos well (Table 2.4), suggesting early exhumation of the rift shoulder and a Jurassic onset of extension. However, whether or not the deposition of the Ocumazo conglomerate is related to the Salta Rift extension cannot be determined from the subset of samples in this study. More detailed analysis of stratigraphic and structural relations is needed to investigate a possible link between the Jurassic extensional fault-related Ocumazo deposits and the onset of the Salta Rift extensional phase.

2.6 Conclusions

Detrital zircon U-Pb, ZHe analyses and point-counting data from three samples within the western Lomas de Olmedo sub-basin provide new information about the earliest extension and syn-rift infill of the Salta Rift in NW Argentina. The Jurassic Tacurú Group within the westernmost Lomas de Olmedo sub-basin is characterized by eolian and proximal alluvial fan facies, deposited on top of the upper Cambrian–lower Ordovician Santa Victoria Group. The conglomerates found in the Tacurú Group are connected to the earliest manifestation of extension in the Jurassic, also documented in ZHe cooling ages from the southern and northern rift shoulder of the Lomas de Olmedo sub-basin (Van Kooten et al., 2021), which are in agreement with data from Insel et al. (2012), Hauser et al. (2010) and Deeken et al. (2006). Maximum depositional ages from strata below and above the Salta Group unconformity (see Table 2.2 and Starck, 1995, 2008) suggest that the hiatus between the Tacurú Group and Pirgua Subgroup was short, but these units are clearly separated from each other by an angular unconformity. Together with the change in strike between units, the varying detrital zircon U-Pb age signatures and the different provenance signals, the major angularity of this unconformity may indicate a rotation of the extensional structures controlling the sediment fluxes in the Late Jurassic and a paleoflow re-organization in the western Lomas de Olmedo sub-basin (Figure 2.7).

Chapter 3. Constraining Andean propagation of exhumation at the limit of the Eastern Cordillera, NW Argentina, using low-temperature thermochronology in a structural context

This chapter was published in Tectonics (Vol. 41, e2022TC007342, 10.1029/2022TC007342), by W. S. M. T. van Kooten, E. R. Sobel, C. E. Del Papa, P. A. Payrola, and J. Glodny (2022).

Abstract

Within the Central Andes of NW Argentina, the spatiotemporal distribution and style of deformation is strongly influenced by pre-Cenozoic heterogeneities, mostly related to the Salta rift extension in the Cretaceous. At the enigmatic junction of the thin-skinned Subandean belt and the thick-skinned Santa Barbara System, the Tilcara Range and adjacent San Lucas block, located within the Eastern Cordillera, show thermochronological and field evidence of multiple exhumation events. Mesozoic (140–115 Ma), pre-Andean exhumation of basement highs is constrained by unconformities between basement and syn-rift strata, as well as zircon (U-Th-Sm)/He cooling ages. Cenozoic Andean exhumation is quantified by apatite (U-Th-Sm)/He and fission track cooling ages, which were reset between the Late Cretaceous and Miocene. These data show that the westernmost Tilcara Range began exhuming in the late Oligocene–early Miocene (26–16 Ma), after which exhumation propagated to the border of the Eastern Cordillera in the middle Miocene (22–10 Ma). The onset of rapid exhumation in the San Lucas block, which is located east of the Tilcara Range, occurred in the late Miocene (10–8 Ma) in its western part, and in the late Miocene–early Pliocene (6–4 Ma) in its eastern part. Internal deformation of the San Lucas block, disturbing zircon (U-Th-Sm)/He and apatite fission track age patterns, predates propagation of rapid exhumation. The low-temperature thermochronology data set presented here thus quantifies the multi-phase exhumation history of the Eastern Cordillera of NW Argentina and constrains the timing of Andean propagation of exhumation within the Eastern Cordillera and the adjacent structural transition zone.

3.1 Introduction

The Andean orogenic belt is commonly divided into morphotectonic provinces (e.g., Carrapa et al., 2011; Jordan et al., 1983; Kley, 1996; Strecker et al., 2007) that are characterized by their unique structural styles (Figure 3.1a). Especially the eastern limit of the Central Andes in southern Bolivia and NW Argentina shows rapid structural changes along-strike between the Inter-/Subandean Zone and the Santa Barbara System, which form the foreland of the Eastern Cordillera. Previous studies of the transition from the Eastern Cordillera to the Inter- and Subandean Zone, their structural characteristics and their exhumation history have focused heavily on the Bolivian part of the fold-and-thrust belt (Anderson et al., 2017; Anderson et al., 2018; Arriagada et al., 2008; Barnes et al., 2008; DeCelles and Horton, 2003; Echavarría et al., 2003; Eichelberger et al., 2013; Gubbels et al., 1993; Horton, 2005; Kley, 1996; McQuarrie, 2002; Müller et al., 2002; Rak et al., 2017; Roeder, 1988), where hydrocarbon exploration has provided a large data set for detailed structural modeling. In contrast, the limit of the Eastern Cordillera in Argentina and the transition from the Subandean Zone to the Santa Barbara System are poorly constrained; in particular, the cause for the abrupt termination of the Interandean and Subandean fold-and-thrust belt south of 23°S remains an enigma to be solved.

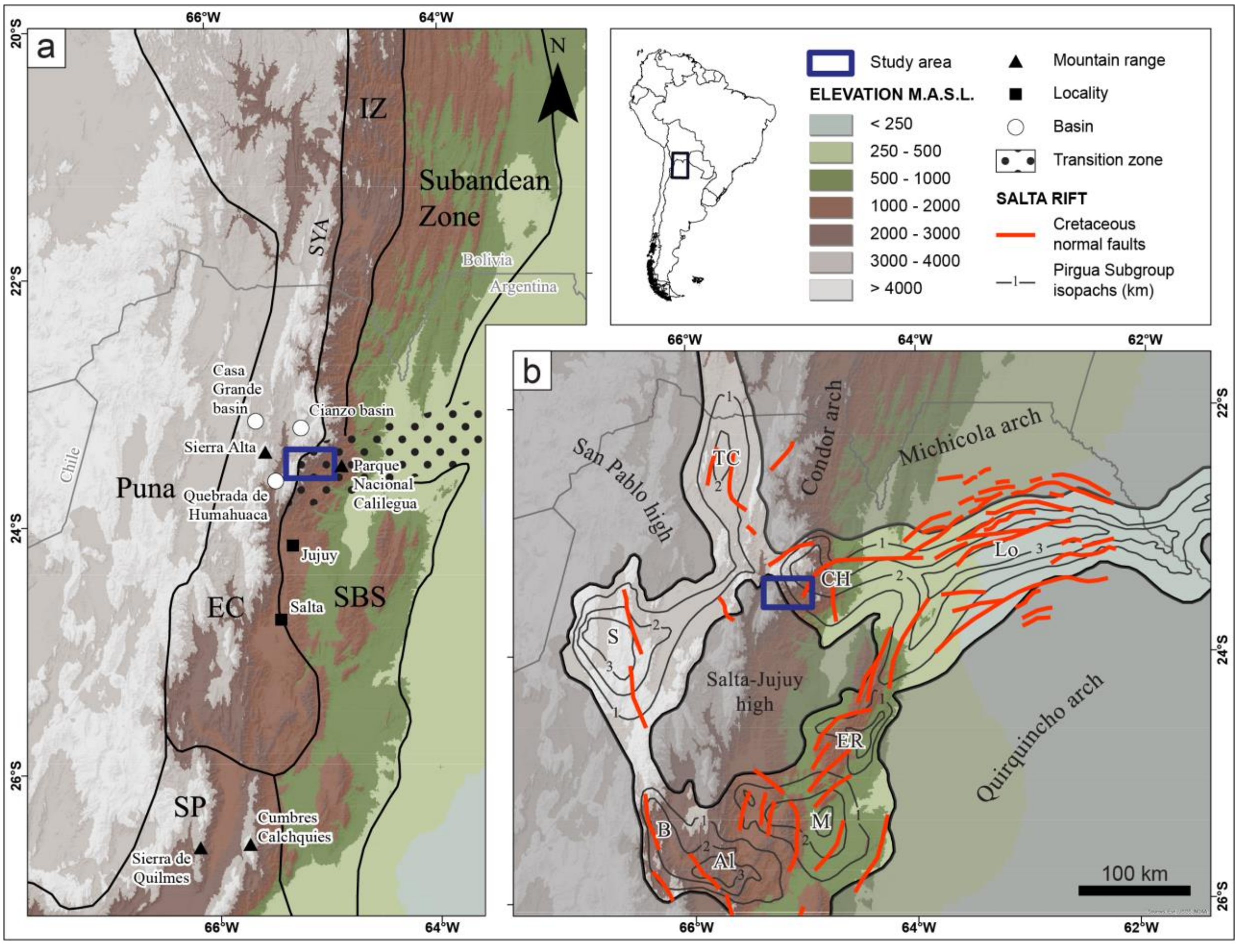

Figure 3.1 (a) Overview of the Central Andes between 20 and 27°S with its morphotectonic provinces, modified from Jordan et al. (1983). EC: Eastern Cordillera, IZ: Interandean Zone, SBS: Santa Barbara System, SP: Sierras Pampeanas. The transition zone between the Inter- and Subandean Zone, SBS and EC is marked. Sama-Yunchará anticlinorium (SYA) is indicated. (b) Overview of the Salta Rift basin including sub-basins (TC: Tres Cruces, CH: Cerro Hermoso, Lo: Lomas de Olmedo, S: Sey, ER: El Rey, M: Metán, Al: Alemanía, B: Brealito), showing syn-rift isopachs from Salfity and Marquillas (1994) and the location of structural highs (in grey). Locations of Cretaceous normal faults (in red) are taken from Starck (2011). The blue square represents the area shown in Figure 3.2.

The complex geologic history of the Central Andes, comprising multiple wide-reaching phases of contraction and extension (e.g., Carrera et al., 2006; Heredia et al., 2018; Ramos, 2008), is responsible for creating heterogeneities that were reactivated during Andean shortening and thus greatly influences the present structure of the Andean orogeny and the distribution of its morphotectonic provinces. Of all preceding phases, the widespread Salta Rift basin has played a major role in controlling the localization and characteristics of Andean deformation within the Eastern Cordillera. There are many excellent examples of reactivation and inversion of Cretaceous extensional faults within the Eastern Cordillera and Santa Barbara System (e.g., Carrera et al., 2006; Kley et al., 2005; Kley and Monaldi, 2002; Kortyna et al., 2019; Seggiaro et al., 2017), which have mostly been studied qualitatively using stratigraphic and structural relations based on field data. Complementing qualitative studies, low-temperature thermochronology, when placed in a structural context, is a powerful instrument to quantify both timing and magnitude of fault-related exhumation within fold-and-thrust belts and provides the opportunity to date multiple exhumation events related to the reactivation of pre-existing structures.

In this study we present a new robust data set of low-temperature thermochronology cooling ages constraining consecutive phases of exhumation within the Eastern Cordillera of NW Argentina. We performed apatite (U-Th-Sm)/He (AHe), apatite fission track (AFT) and zircon (U-Th-Sm)/He (ZHe) dating on 26 samples that are arranged in W–E vertical and horizontal transects crossing the Tilcara Range orographic barrier and adjacent Yungas lowlands. Using an improved structural framework and multi-sample thermal modeling, we reconstruct the reactivation of pre-Cenozoic heterogeneities in the course of the Andean orogeny. The resulting model focuses on the boundary of the Eastern Cordillera and the transition zone between the Subandean Zone and Santa Barbara System at 23.5°S, and sheds new light on propagation of deformation in time and space at the limit of this major Andean fold-and-thrust belt.

3.2 Geological setting

The Eastern Cordillera of NW Argentina is bordered by the Inter- and Subandean Zone to the east and the Altiplano-Puna plateau to the west (Figure 3.1a). Whereas the Interandean Zone is increasingly integrated into the Eastern Cordillera, the Subandean Zone abruptly terminates at 23°S and is replaced by the Santa Barbara System south of 23.5°S (Kley and Monaldi, 2002). The Eastern Cordillera and Santa Barbara System transition into the Sierras Pampeanas toward the south (Figure 3.1a). Concurrently, the structural style changes rapidly from a classic thin-skinned fold-and-thrust belt in the Bolivian Subandean Zone (Dunn et al., 1995; Eichelberger et al., 2013; McQuarrie, 2002) to the thick-skinned broken foreland basins of the Santa Barbara System and the Sierras Pampeanas, where basement blocks are uplifted along reactivated, pre-existing faults (e.g., Kley et al., 1999; Kley and Monaldi, 2002; Zapata et al., 2019b). Although Jordan et al. (1983) proposed a correlation between tectonic disparities and the transition from steep (~30°) to flat (~5–10°) subduction, more recent studies (Anderson et al., 2007; Gans et al., 2011; Horton, 2018b; Linkimer et al., 2020; Ramos et al., 2002) show that this transition zone is narrower and located further south, and that there is a poor correlation between changes in structural style and slab angle. Kley and Monaldi (2002) argue that the sharp boundaries of the Santa Barbara System form a pronounced contrast to the smooth variation of slab inclination and suggest that stratigraphic disparities might instead have a major impact on the current structural segmentation of the Andes. Similarly, McGroder et al. (2015) propose a strong influence of inherited crustal elements within the South American plate on structural styles and hydrocarbon resources within the Central Andes. Indeed, many authors (e.g., Carrera et al., 2006; Grier et al., 1991; Kley et al., 2005; Kley and Monaldi, 2002; Kortyna et al., 2019; McGroder et al., 2015) have demonstrated that inherited anisotropies from Paleozoic and Cretaceous tectonism strongly influenced the present-day deformational pattern in the Eastern Cordillera between 23 and 24°S.

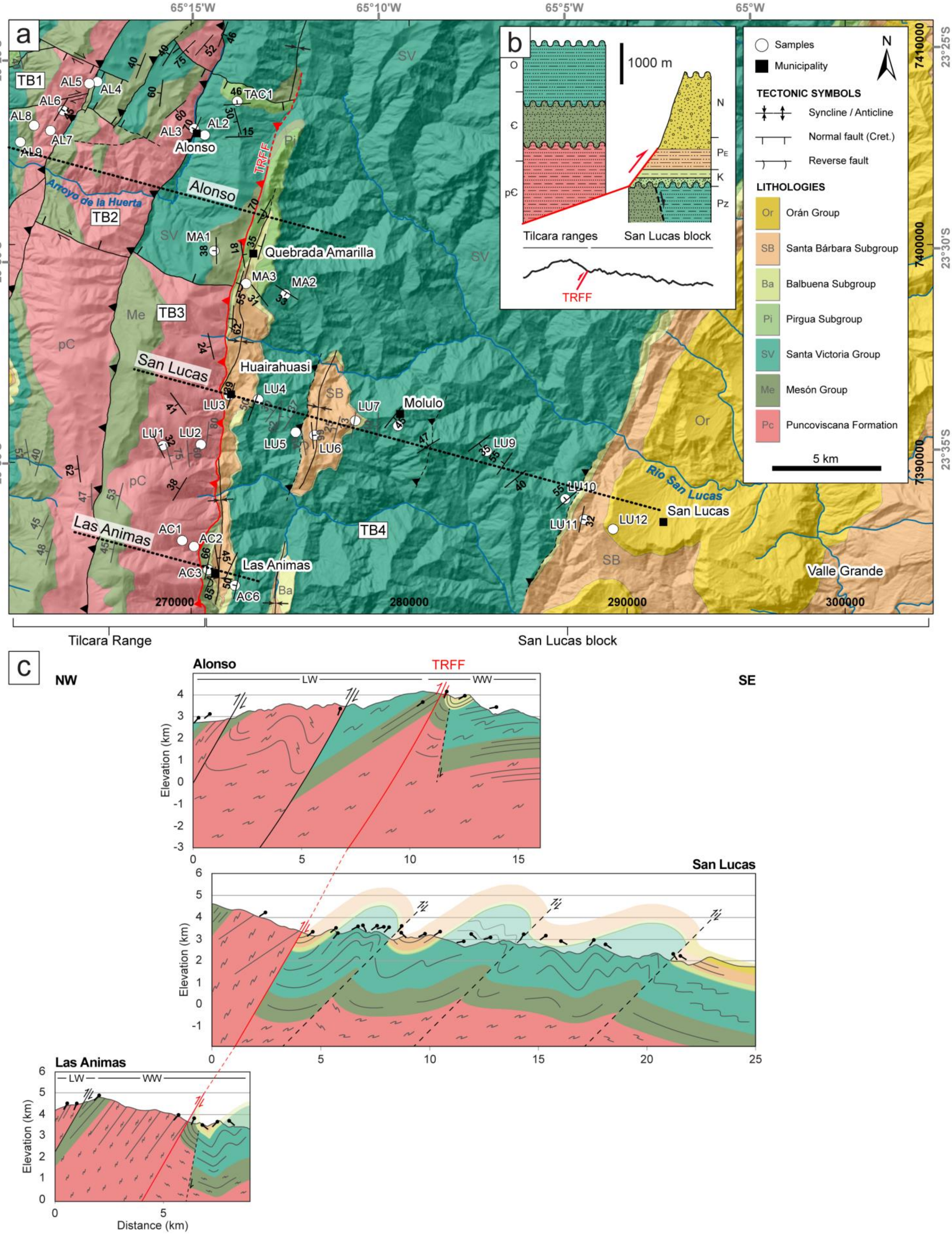
a
b
c
65°15'W
65°10'W
65°5'W
65°W
23°25'S
23°30'S
23°35'S
7410000
7400000
7390000
270000
280000
290000
300000
Tilcara Range
San Lucas block
Alonso
San Lucas
Las Animas
TRFF
TB1
TB2
TB3
TB4
Arroyo de la Huerta
Río San Lucas
Quebrada Amarilla
Huairahuasi
Molulo
Valle Grande
Samples
Municipality
TECTONIC SYMBOLS
Syncline / Anticline
Normal fault (Cret.)
Reverse fault
LITHOLOGIES
Orán Group
Santa Bárbara Subgroup
Balbuena Subgroup
Pirgua Subgroup
Santa Victoria Group
Mesón Group
Puncoviscana Formation
5 km
1000 m
Tilcara ranges
San Lucas block
NW
SE
LW
WW
Elevation (km)
Distance (km)

Figure 3.2 (a) Geologic map of the Tilcara Range and San Lucas block revised from González and Tchilinguirian (2003) and Jiron (2015). Coordinates are shown as UTM WGS84 zone 20K (inside frame) and degree-minutes-seconds (outside frame). TB1–TB4 mark tectonic blocks. Dotted lines depict Alonso, San Lucas and Las Animas transects. The Tilcara Range Frontal Fault (TRFF) is marked in red. Measurements marked in grey are from Jiron (2015). (b) Schematic overview of structural and stratigraphic relationships between the basement and Cretaceous–Paleogene strata within the Tilcara Range and San Lucas block (TB4). Topographic section shows the difference in altitude between the Tilcara Range and San Lucas block. (c) Schematic cross-sections of the Alonso, San Lucas and Las Animas transects. The Tilcara Range Frontal Fault is marked in red. The leeward (LW) and windward (WW) sides of the Tilcara Range are indicated. Folding in Precambrian–Paleozoic strata is shown schematically.

At the far eastern limit of the Eastern Cordillera, the Tilcara Range strikes N–S, showing high topography with peak elevations just below 5000 m. The Tilcara Range is bounded to the east by a high-angle, north-striking, east-vergent reverse fault that is hereafter referred to as the Tilcara Range Frontal Fault (Figure 3.2). The San Lucas block is located directly east of this reverse fault. The basement of the Tilcara Range consists of the late Ediacaran–early Cambrian Puncoviscana Formation (Fm), deposited in the Puncoviscana foreland basin bordering the Pampean orogen (Aceñolaza, 2003; Einhorn et al., 2015; Escayola et al., 2011; Pearson et al., 2012). It encompasses weakly metamorphosed (Escayola et al., 2011; Pearson et al., 2012) alternating claystones, siltstones and sandstones with an estimated total thickness of > 2000 m (Aceñolaza, 2003). The Pampean-Tilcaric unconformity (Escayola et al., 2011; Turner and Mendez, 1975) separates the Puncoviscana Fm from the overlying middle–late Cambrian Mesón Group and marks the end of the Pampean cycle (Adams et al., 2011).

The Mesón Group consists of up to 3000 m thick marine siliciclastic rocks (Aceñolaza, 2003; Moya, 1998; Sanchéz and Salfity, 1999), with thickness varying locally, and is divided into upper and lower coarse-grained, cliff-forming quartzite units, and the middle, finer-grained Campanario Fm. An unconformity exists between the Mesón Group and the overlying upper Cambrian–lower Ordovician Santa Victoria Group (Rahl et al., 2018; Vaucher et al., 2020). The Santa Victoria Group consists of alternating quartz-rich sandstones and shales with a thickness of a few thousands meters (Aceñolaza, 2003; Moya, 2015). Within the Tilcara Range, large parts were eroded and the preserved Ordovician strata can locally be as thin as 500 m (Buatois et al., 2006).

The Precambrian to Ordovician sedimentary basement strata were deformed during the Ocloyic phase (middle Ordovician–middle Silurian or Devonian) (Bahlburg et al., 2000; Heredia et al., 2018; Otamendi et al., 2020; Ramos, 2008; Seggiaro et al., 2017). The Ocloyic phase induced uplift in the area of the present-day Puna and Eastern Cordillera (Starck et al., 1992) and led to an eastward migration of foreland basins. Alonso et al. (2012) consider the Eastern Cordillera the “non-metamorphic part of the Ocloyic foreland thrust belt”. Structures in the Eastern Cordillera that were formed during the Ocloyic orogeny show a dominant north-strike and east vergence (Hongn et al., 2010a) and are thus positioned favorably for Andean reactivation (Heredia et al., 2018; Seggiaro et al., 2017). Salfity and Marquillas (1994) propose that compressional deformation related to the Ocloyic orogeny also affected the Tilcara Range. However, Ordovician normal faulting has also been recorded in the Eastern Cordillera (Seggiaro et al., 2008; Seggiaro et al., 2017; Villagrán et al., 2015) and not in all cases the original geometry and slip of Paleozoic structures is clearly defined. Although Silurian to Carboniferous strata have been deposited (González and Tchilinguirian, 2003; Starck, 1995), they were largely eroded prior to Cretaceous sedimentation (Salfity and Marquillas, 1994; Starck, 1995) and the majority of Cretaceous–Paleogene strata were deposited unconformably on top of Ordovician rocks (Figure 3.2b).

From the Late Jurassic to Early Cretaceous, the opening of the South Atlantic Ocean caused extension in the location of the Cenozoic Central Andes and the development of the Salta Rift basin, which covered most of NW Argentina (Marquillas et al., 2005; Salfity and Marquillas, 1994). The Salta Rift basin hosts a thick succession of syn- and post-rift sediments of the Salta Group (Turner, 1959) that were deposited from the lower Cretaceous up to the middle Eocene (Marquillas et al., 2005; Salfity and Marquillas, 1994). The Salta Group is divided into the syn-rift Pirgua Subgroup (Reyes and Salfity, 1973) and the post-rift Balbuena and Santa Barbara Subgroups (Moreno, 1970). Further subdivisions and their spatial distribution vary regionally, depending on the specific depocenter.

One of the Salta rift depocenters is the NW–SE striking Lomas de Olmedo sub-basin. It is delimited to the north by the Michicola arch and to the south by the Quirquincho arch. The Condor arch and the Salta-Jujuy high confine the basin to the west (Figure 3.1b). The area of the Tilcara Range was part of the westernmost Lomas de Olmedo sub-basin during the late syn-rift and post-rift stages. However, Salfity and Marquillas (1994) suggest that the very first sedimentary infill, consisting of the lowermost Pirgua Subgroup, was shed into a separate depocenter known as Cerro Hermoso (Figure 3.1b). Within the Tilcara Range, the Pirgua Subgroup is relatively thin, especially compared with its thickness of > 2500 m within the Cianzo syncline farther north (Boll et al., 1989). The post-rift strata were mainly accommodated by thermal subsidence (Marquillas et al., 2005; Viramonte et al., 1999) and possibly early flexural loading from the Altiplano-Puna plateau (Becker et al., 2015). Seismic sections show that normal fault activity related to rifting in the Lomas de Olmedo sub-basin commenced no later than the Cretaceous and continued up to the Paleocene (Starck, 2011). Some authors argue that local conglomerate levels, NE-directed paleoflow and the extraordinarily large spatial distribution of the Santa Barbara Subgroup indicate an early influence of the Andean orogenic wedge in the late Paleocene–Eocene (e.g., DeCelles et al., 2011). Ultimately, the late Eocene–early Oligocene onset of Andean shortening in the Puna and Eastern Cordillera ended the deposition of the Salta Group (Carrapa et al., 2011; Coutand et al., 2001; Marquillas et al., 2005; Salfity and Marquillas, 1994).

Following the uplift in the Puna and Eastern Cordillera during the late Eocene or early Oligocene (Carrapa et al., 2011; Carrapa and DeCelles, 2008; Coutand et al., 2001; DeCelles et al., 2007; DeCelles et al., 2011; Henríquez et al., 2020; Henríquez et al., 2023), the Salta Group was buried by foreland deposits of the Orán Group (Boll and Hernández, 1986; Salfity and Marquillas, 1994). Whereas most studies agree that its lower part (Metán Subgroup) was deposited in a widespread basin (Coutand et al., 2001; DeCelles et al., 2011; Siks and Horton, 2011), the younger tectonosedimentary history has been debated. Some authors conclude that from the late Oligocene–late Miocene on, clastic sediments were deposited in smaller, fully or partly isolated depocenters generated during the uplift of the Eastern Cordillera (Becker et al., 2015; Siks and Horton, 2011; Strecker et al., 2007). Thus, the Orán Group directly documents the propagation of Andean deformation from the Puna to the Eastern Cordillera (Becker et al., 2015). Other authors (Carrapa et al., 2012; DeCelles et al., 2011) argue that upper Miocene–Quaternary sediments represent wedge-top accumulations that were deposited in a connected regional foreland basin system.

3.2.1 Timing of uplift

Tectonic shortening related to Andean mountain building in the Puna and Eastern Cordillera (between 23.5 and 24°S) began in the early Paleogene with the inversion of extensional Salta Rift structures. Relief formation commenced in the middle–late Eocene (Montero-López et al., 2021). Although the proto-Sierra Alta (Figure 3.1), west of the Tilcara Range, started uplifting in the Paleogene (Montero-López et al., 2021), Pingel et al. (2013) (with data from Deeken et al., 2006; Reynolds et al., 2000; 2001; Siks and Horton, 2011) show that uplift was most pronounced at ~15 Ma. Undeformed deposits that unconformably overlie folded Ordovician to Miocene strata above the San Juan de Oro geomorphic surface, south of the Bolivian border, indicate that major deformation in the western Eastern Cordillera terminated at 9 Ma (Allmendinger and Zapata, 2000). In contrast, Streit et al. (2017) show that fluvial incision at the Casa Grande basin outlet (Figure 3.1) was only outpaced by the rate of uplift of the Sierra Alta, bounding this basin to the east, between 3.8–0.8 Ma, which they attribute to increased sediment supply connected to enhanced precipitation and increased uplift rates. This implies that range uplift west of the Humahuaca valley continued during Pliocene–Pleistocene times. Deformation in general propagated eastward (Anderson et al., 2017; Anderson et al., 2018; DeCelles et al., 2007; DeCelles et al., 2011; Deeken et al., 2006; Henríquez et al., 2019; Henríquez et al., 2020), with proposed periods of out-of-sequence deformation (e.g., Henríquez et al., 2023), and reached the Tilcara Range at ~10–4 Ma (Henríquez et al., 2023; Pingel et al., 2013; Pingel et al., 2014; Siks and Horton, 2011). Early uplift of the Tilcara Range and its northern continuation is well documented in the Cianzo basin, ~20 km east of Humahuaca, where the Orán Group records a changing geological setting from a widespread foreland basin to a restricted intermontane basin in the late Miocene (Siks and Horton, 2011). Uplift of the Tilcara Range formed an orographic barrier, disrupting drainage patterns within the Humahuaca basin west of the Tilcara Range after 4.2 Ma, based on changes in paleoflow directions and increasingly proximal facies (Pingel et al., 2013). Consequently, surface uplift of the Tilcara Range before 4.2 Ma was not sufficient to disrupt fluvial connectivity (Streit et al., 2017). These results clearly suggest Pliocene or younger uplift of the Tilcara Range. Pingel et al. (2019) show that an abrupt decrease of denudation rates is in agreement with the establishment of an orographic barrier after 3 Ma: whereas pre-3 Ma rates were similar to modern-day denudation rates (0.49 and 0.58 mm/a) on the wet side of the Tilcara Range (Bookhagen and Strecker, 2012; Schildgen et al., 2016), post-3 Ma rates show a tenfold decrease (Pingel et al., 2019), indicating dryer conditions on the leeward side of the orographic barrier and a strong erosional gradient, which might affect low-temperature thermochronology cooling ages.

3.3 Methods

3.3.1 Mapping and cross-section construction

The revised geologic map (Figure 3.2a) was constructed based on field data from our 2019 and 2021 campaigns, existing measurements by Jiron (2015) and descriptions and interpretations from González and Tchilinguirian (2003). We used satellite imagery (Google Earth Pro Imagery, Esri World Imagery Basemap) to interpolate geological boundaries in areas where no field-based data was available. The revised map was digitized using the Esri ArcGIS® software ArcMap™ v10.5.1 on a scale of 1:5,000. Three parallel, WNW–ESE striking, unbalanced cross-sections were constructed in the software MOVE v2019.1 (Petroleum Experts, 2020), hereafter referred to as the Alonso, San Lucas and Las Animas transects (Figure 3.2c). We used the kink band method (Suppe, 1983) to create horizons whenever viable. Parallel formation boundaries were created, assuming constant thickness and a negligible angular relationship between the Santa Barbara and the Balbuena subgroups. We used thickness measurements for Cretaceous–Paleogene strata from nearby stratigraphic sections (Boll et al., 1989) to estimate the viability of the sections. Because movement planes of major faults do not crop out, we qualitatively inferred the most probable fault orientation from the approximate intersection of major faults from satellite imagery with the digital elevation model (Copernicus WorldDEM-30).

3.3.2 Sample selection and preparation

We collected 26 samples along three W–E transects crossing the Tilcara Range from the Quebrada de Humahuaca to Valle Grande (Figure 3.2c). The aim was to sample vertical transects for thermochronologic analysis and to access different structural positions within the tectonic blocks. Preliminary mineral separates (i.e., crushing, sieving, magnetic separation with strong hand magnet) were conducted at the National University of Salta. Further processing at the University of Potsdam included 1) magnetic separation, using a Frantz® magnetic separator with a frontal angle of 10°, a side angle of 10° and a current of 1.2 A, 2) treatment of the non-magnetic fraction with 10 % acetic acid to remove carbonate and 3 % H_2O_2 to remove clay and organic matter, and 3) density separation using Sodium Polytungstate (SPT; ρ = 2.86 g/cm^3) and Diiodomethane (DI; ρ = 3.3 g/cm^3).

3.3.3 Single-grain (U-Th-Sm)/He thermochronology

Low-temperature (U-Th-Sm)/He apatite and zircon (AHe, ZHe, respectively) thermochronology is based on α-particle ejection associated with the decay of U, Th and Sm parent isotopes. He atoms (α particles) are retained within apatite on geological timescales at temperatures below 40 °C and are emitted at temperatures above 85 °C (Wolf et al., 1998). This temperature interval "where helium is neither quantitatively retained nor lost by diffusion" (Wolf et al., 1998, p. 105) is called the apatite partial retention zone (APRZ). The closure temperature (T_c) for the (U-Th-Sm)/He system varies with cooling rate, crystal size and radiation damage; a typical T_c is approximately 68 °C for apatite (Farley, 2000). For zircons, the partial retention zone (ZPRZ) is between 170 and 190 °C with an average experimental closure temperature of 183 °C (Reiners et al., 2004). Ideal crystals for (U-Th-Sm)/He thermochronology should be euhedral with a diameter of > 60 μm and free of inclusions, fractures and zoning.

We analyzed 26 samples from the basement and sedimentary strata of the Tilcara Range and San Lucas block using AHe and/or ZHe thermochronology. Aliquots were carefully hand-picked with a binocular polarizing microscope to eliminate grains with visible inclusions and/or fractures. Due to the detrital nature of the sandstone samples, the majority of the grains have a rounded geometry with frosted surfaces, potentially obscuring small inclusions and hairline fractures within the crystal. Although grains were carefully picked, we cannot fully exclude this cause of dispersion in detrital samples. Grain dimensions (width, length of prism and total length) and the number of terminations were recorded for all grains. Aliquots were packed in Pt (for apatite) or Nb (for zircon) tubes and loaded into the Australian Scientific Instruments (ASI) Alphachron He extraction and analysis system at the University of Potsdam. Aliquots were heated twice with a 978 nm diode laser at 8 A for 5 minutes for apatite, or at 12 A for 10 minutes for zircon to achieve full He degassing. Two zircon aliquots were heated four times (see Table B.1 in Appendix B), because of residual He in the first re-extract. The resulting gas was purified using a SAES AP10N hot getter and analyzed using a Pfeiffer Prisma 200 Quadrupole mass spectrometer. The aliquots were then transferred to the German Research Center for Geosciences (GFZ) Potsdam for analysis of U, Th and Sm abundances by isotope dilution. The grains were spiked with ^{235}U, ^{230}Th and ^{149}Sm, dissolved, and then analyzed on a Thermo Element 2 XR ICP-MS. Additional analytical data are provided in Zhou et al. (2016) and Galetto et al. (2021). (U-Th-Sm)/He ages were calculated following the equations in Meesters and Dunai (2005) using the He, U, Th and Sm abundances, an alpha-ejection correction factor (F_T; Farley et al., 1996; Ketcham et al., 2011) obtained from the measured grain dimensions, and the alpha-particle stopping distance from Ketcham et al. (2011). We report (U-Th-Sm)/He ages with a weighted error (Table B.1), which considers the relative contribution of each parent isotope to the total He production.

Weighted mean ages (Table 3.1) excluding outliers were calculated in IsoplotR using a random effects model that considers both the analytical uncertainty and an overdispersion term as sources of uncertainty (Vermeesch, 2018). AHe outliers are defined as aliquots that show Th/^{238}U > 100, or a combination of U < 2 ppm and 2σ (of corrected age) > 1.5 Ma. Furthermore, AHe aliquots are considered outliers if the single-grain age ± 2σ is greater than the sample's AFT age ± 1σ or if the single-grain ages show an exceptionally large amount of He compared to the amount of U, pointing toward the presence of an undissolved inclusion. ZHe outliers were defined by re-assessing grain geometry and characteristics and comparing these with single-grain ages. Excluded aliquots are marked in Table B.1 (Appendix B) and are ignored for both the weighted mean age calculation and further thermal history modeling. None of the AHe samples showed a positive age-eU trend corresponding to Flowers et al. (2009), although two samples showed a positive age-F_T and age-equivalent sphere radius (ESR) trend. Three ZHe samples showed positive age-eU trends, characteristic of zircons with < 1500 ppm eU according to the radiation damage model of Guenthner et al. (2013). One sample showed a negative age-eU trend with high overall eU, which can be attributed to increasing He diffusivity due to the interconnection of damage zones in the zircons (Guenthner et al., 2013). Age-F_T and age-ESR relationships are seen in two ZHe samples. For samples with age-eU and/or age-F_T relationships, all single-grain ages were included in QTQt models. Although we routinely used the RDAAM and ZRDAAM radiation damage models (Flowers et al., 2009; Guenthner et al., 2013) to model the age-eU spread, we did not apply the concept of inheritance envelopes (e.g., Guenthner et al., 2015), because of the relatively low overall spread in (U-Th-Sm)/He ages and eU. Age-eU, age-ESR and age-F_T plots are included in Figure B.1 in Appendix B and samples showing an age-eU and/or age-F_T trend are marked in Table 3.1.

3.3.4 Apatite fission track thermochronology

Apatite fission track thermochronology (AFT) is based on the spontaneous fission of ^{238}U, which creates charged particles that form linear damage zones in the crystal lattice called fission tracks. Through quantification of fission tracks and the abundance of the remaining parent isotope in apatite, a cooling age is generated for the sample. The temperature interval between 60 and 120 °C marks the apatite partial annealing zone (APAZ; Wagner et al., 1989) in which tracks can be partially annealed. The exact temperature interval of the APAZ varies with cooling rate and kinetic characteristics, which can be quantified using the diameter of the etch pits (Carlson et al., 1999; Donelick, 1993; Donelick et al., 1999; Ketcham et al., 1999).

We analyzed 19 samples for AFT thermochronology using the external detector method (Gleadow, 1981). The sample fraction containing apatites ($2.96 < \rho < 3.3$ g/cm^3) was mounted on a glass slide with epoxy, ground and polished. Apatite mounts were then etched using 5.5 N HNO_3 at 21 °C for 20 seconds (Donelick et al., 2005), packed with a mica detector on top and sent to Oregon State University for thermal neutron irradiation. After irradiation, the mica detectors were etched in 40 % HF at 21 °C for 45 minutes.

All samples were analyzed at the University of Potsdam using a Leica DMRM microscope at 1250X magnification and the FTStage software (Dumitru, 1994). For calculation of AFT ages a zeta correction factor (Hurford and Green, 1983) of 380.5 ± 7.5 (WvK) was applied. We measured the diameter of the etch pits *Dpar* (Donelick et al., 2005; Sobel and Seward, 2010) as a proxy for kinetic characteristics of the crystal, which strongly influence annealing (Barbarand et al., 2003; Carlson et al., 1999; Ketcham et al., 1999). Dpar measurements were calibrated by correlating individual Dpar measurements for Fish Canyon Tuff and Durango apatite with those by Donelick et al. (1999), yielding a correction factor of 1.07. For the full calibration procedure see Sobel and Seward (2010). It was not possible to measure a statistically relevant number of track-in-track (TINT) lengths. Although due to the low number of spontaneous track measurements (N_s) the sample size according to standard criteria (Yates et al., 1999) was too small for calculating viable chi-square statistics, we performed a chi-square test of independence on all samples. For samples that passed the chi-square test ($P(\chi^2) > 5$ %), we calculated a pooled age and one sigma error (Galbraith and Laslett, 1993); for samples that exhibited multiple age components and thus did not pass, we calculated a central age in IsoplotR. These samples were also checked for a possible correlation between Dpar and single-grain ages, which would explain larger-than-normal age scatter. Non-passing samples were generally excluded from modeling procedures. AFT data is summarized below (Table 3.2). Radial plots from RadialPlotter (Vermeesch, 2009) can be found in Figure B.2.

Table 3.1 (U-Th-Sm)/He ages for apatite and zircon grains. Lithologies range from Puncoviscana Fm (PRC), Mesón Group (CAM), Santa Victoria Group (ORD), Pirgua (PIR), Balbuena (BAL) and Santa Barbara (SAB) subgroups to Orán Group (ORA). Full (U-Th-Sm)/He data is provided in Table B.1.

Apatite (U-Th-Sm)/He data									
TB[a]	Sample	Aliquots[b]	Lithology	UTM E[c]	UTM N[c]	Z (m)	WM (Ma)[d]	SE (Ma)[e]	%[f]
1	AL5	3	PRC	265330	7407390	3732	9.0	0.4	3.9 %
	AL6	4	PRC	264129	7406152	3509	6.9	0.5	6.8 %
	AL7	4	PRC	263544	7405230	3306	11.7	0.6	5.1 %
	AL8	4	CAM	262789	7405469	3112	35.7	2.6	7.3 %
	AL9	3	ORD	262168	7404701	2820	10.0	0.1	1.2 %
2	AL4*	3	ORD	265693	7407476	3761	9.4	3.3	35.6 %
3	LU1	5	PRC	268703	7390777	4142	9.8	1.1	11.2 %
	AC1*	3	PRC	269588	7386416	4123	7.7	0.4	5.5 %
	TAC1	5	PIR	272118	7406576	4033	7.3	0.8	11.0 %
	AC2	3	PRC	270123	7386139	3894	4.3	0.3	7.9 %
	AL2	5	ORD	270624	7405026	3670	6.3	0.5	7.2 %
	LU2	4	PRC	270443	7390822	3607	6.8	0.6	8.1 %
4	MA3	3	SAB	272520	7398204	3863	6.4	0.4	6.6 %
	AC6	5	BAL	272000	7384350	3769	3.5	0.2	4.6 %
	AC3	4	CAM	270778	7385071	3574	4.1	0.8	19.4 %
	MA2	4	ORD	274321	7397718	3477	5.1	0.6	11.1 %
	LU5	3	ORD	274792	7391378	3415	6.3	0.4	5.7 %
	LU4	3	ORD	273074	7392891	3385	5.2	0.8	15.5 %
	LU6	3	SAB	275647	7391245	3297	4.2	0.2	5.7 %
	LU7	4	SAB	277533	7391911	3263	3.4	0.3	7.3 %
	LU3	4	SAB	271736	7393079	3220	3.5	0.3	7.5 %
	LU9	3	ORD	283558	7390518	2787	4.1	0.3	6.1 %
	LU12	4	ORA	289357	7386938	2375	3.5	0.4	10.3 %
	LU11	4	SAB	288034	7387380	2159	4.3	1.8	41.7 %
Zircon (U-Th-Sm)/He data									
TB[a]	Sample	Aliquots[b]	Lithology	UTM E[c]	UTM N[c]	Z (m)	WM (Ma)[d]	SE (Ma)[e]	%[f]
1	AL5	4	PRC	265330	7407390	3732	178.5	5.3	3.0 %
	AL8*†	4	CAM	262789	7405469	3112	313.9	15.5	4.9 %
2	AL3*	3	PRC	270128	7405319	3631	27.0	1.9	6.9 %
3	LU1	3	PRC	268703	7390777	4142	125.3	5.7	4.5 %
	AC1†	3	PRC	269588	7386416	4123	78.3	5.5	7.0 %
	TAC1	6	PIR	272118	7406576	4033	339.2	62.6	18.5 %
	MA1	2	CAM	271055.1	7399705	3960	50.6	1.1	2.2 %
	LU2†	3	PRC	270443	7390822	3607	67.2	6.9	10.2 %
4	AC6	5	BAL	272000	7384350	3769	415.4	35.7	8.6 %
	LU4	5	ORD	273074	7392891	3385	153.6	13.1	8.5 %
	LU3	4	SAB	271736	7393079	3220	314.7	23.7	7.5 %
	LU9†	3	ORD	283558	7390518	2787	110.6	10.7	9.7 %

[a]Corresponding tectonic block, for numbers see Figure 3.2

[b]Number of aliquots used, excluding outliers

[c]UTM zone 20K

[d]Weighted mean age calculated in IsoplotR, excluding outliers

[e]Standard error (1σ) of the weighted mean age

[f]Percentage of SE of the weighted mean age

*Samples with age-F_T relationship

†Samples with age-eU relationship

Table 3.2 Apatite fission track data. For lithology abbreviations see caption of Table 3.1.

TB[a]	Sample	Lithology	UTM E[b]	UTM N[b]	Z (m)	N[c]	Ns	Ni	Nd	RhoS (x10^5)	RhoI (x10^5)	RhoD (x10^5)[d]	Age (Ma)[e]	± 1σ (Ma)	P(χ^2) (%)[f]	Dpar (µm)[g]	SD (µm)[h]
1	AL5	PRC	265330	7407390	3732	17	44	708	4076	10.746	172.906	9.924	11.7	1.8	61.1 %	2.5	0.3
	AL6	PRC	264129	7406152	3509	10	72	1427	4076	24.454	484.667	9.879	9.5	1.2	31.6 %	2.6	0.2
	AL7	PRC	263544	7405230	3306	10	27	455	4076	9.080	153.016	9.849	11.1	2.2	73.5 %	2.1	0.2
	AL9	ORD	262168	7404701	2820	16	178	3132	4076	24.087	423.818	9.820	10.6	0.8	55.4 %	2.3	0.3
2	AL3	PRC	270128	7405319	3631	20	41	633	4076	7.417	114.511	9.984	12.3	2.0	97.7 %	2.3	0.7
3	AC1	PRC	269588	7386416	4123	13	49	978	4076	12.259	244.670	10.164	9.7	1.4	27.2 %	2.3	0.3
	AC2	PRC	270123	7386139	3894	12	36	911	4076	8.607	217.815	10.119	7.6	1.3	80.9 %	2.3	0.2
	AL2	ORD	270624	7405026	3670	15	56	1087	4076	17.950	348.422	10.029	9.8	1.4	30.6 %	2.6	0.2
	LU2	PRC	270443	7390822	3607	15	58	1346	5187	9.028	209.501	12.904	10.6	1.4	76.5 %	2.3	0.2
4	AC3	CAM	270778	7385071	3574	12	38	914	4076	12.335	296.678	10.089	9.2	1.9	*2.4 %*	2.4	0.2
	AC6	BAL	272000	7384350	3769	12	39	1284	4076	7.477	246.172	10.059	6.9	1.6	*1.1 %*	2.4	0.3
	LU12	ORA	289357	7386938	2375	26	171	1242	5187	11.404	82.831	12.517	32.7	2.7	30.7 %	3.2	0.5
	LU3	SAB	271736	7393079	3220	15	34	782	5187	8.569	197.078	12.839	10.6	1.9	92.5 %	2.3	0.4
	LU4	ORD	273074	7392891	3385	16	37	1503	5187	8.286	336.605	12.796	6.0	1.0	64.0 %	2.3	0.3
	LU5	ORD	274792	7391378	3415	21	66	2328	5187	11.080	390.812	12.753	6.9	0.9	88.8 %	2.4	0.2
	LU6	SAB	275647	7391245	3297	9	39	1629	5187	6.173	257.853	12.710	5.8	0.9	82.2 %	2.6	0.3
	LU7	SAB	277533	7391911	3263	5	12	381	5187	5.889	186.984	12.646	7.6	2.2	78.9 %	2.3	0.3
	LU9	ORD	283558	7390518	2787	17	111	4034	5187	8.528	309.943	12.582	8.3	1.6	*0.0 %*	2.4	0.2
	MA2	ORD	274321	7397718	3477	7	10	206	5187	8.692	179.065	12.432	11.5	3.7	32.7 %	2.6	0.5

$\zeta = 380.5 \pm 7.5$

[a]Corresponding tectonic block, for numbers see Figure 3.2

[b]UTM zone 20K

[c]Number of individual crystals dated

[d]CN5 standard glasses monitored thermal neutron fluences

[e]Central age for samples that did not pass chi-square test, pooled age for all other samples

[f]P(χ^2) (%) is the chi-square probability (Gailbraith and Laslett, 1993; Green, 1981)

[g]Corrected Dpar calculated after Sobel and Seward (2010)

[h]Standard deviation of measured Dpars

3.3.5 QTQt modeling

To better constrain pre-Cretaceous and Andean phases of exhumation we conducted thermal modeling in the QTQt software v5.8.0 (Gallagher, 2021) using data from Table 3.1 and Table 3.2. This software is able to take into account kinematic characteristics of single-grain ages. AHe and ZHe samples exclude outliers as discussed above. For AHe samples, we used the radiation damage model of Flowers et al. (2009). For ZHe samples, we used the radiation damage model of Guenthner et al. (2013). For one ZHe sample (TAC1), where an inheritance component was considered, we modeled ZHe age populations as two separate samples. The annealing model of Ketcham et al. (2007) was used for AFT samples. AFT data also included mean Dpar measurements to implement compositional control in the models.

Models were run for single tectonic blocks, because QTQt currently does not allow for a tectonic offset in the thermal history modeling. We modeled spatially offset elevation profiles separately, because the lateral offset and the presence of faults between W–E elevation profiles disrupt age-elevation or age-stratigraphy relationships. Furthermore, samples located at the leeward side of the Tilcara Range were modeled separately from samples located at the windward side, because post-3 Ma denudation rates indicate a strong erosional gradient across the Tilcara Range (Pingel et al., 2019; see Section 3.2.1) that might have affected pre-3 Ma cooling rates. For models run using age-elevation relationships (Table 3.3), we used the sampling elevation as input. For models using age-stratigraphy relationships, we calculated a "stratigraphic elevation" relative to the stratigraphically deepest sample by projecting samples onto cross-sections. We then measured the stratigraphic offset between samples, using the basement-Salta Group unconformity as a zero offset line. The resulting values were normalized, so that the stratigraphically deepest sample is located at zero meters pseudo-elevation. This correction was conducted separately for all three sections to account for irregularities in unit thicknesses within the Tilcara Range and San Lucas block. In cases where the basement-Salta Group uconformity has been eroded, the base of the Mesón Group was used as a zero offset line. Furthermore, variations in burial depth due to varying thickness of Cenozoic strata and erosion of basement strata before deposition of the Salta Group have not been taken into account.

Models were consistently run with ≥ 100,000 repetitions post burn-in, to ensure strong likelihood and posterior chains. In cases where 100,000 iterations was an insufficiently large sampling size, we increased the number of iterations to 200,000 (Table 3.3). AFT-only models were regularly run with 200,000 iterations because of the increase in model fit with comparatively low extra computing time. We used a maximum bounding box of 275 ± 275 Ma and 70 ± 70 °C, 80 ± 80 °C or 150 ± 150 °C (AHe, AFT and ZHe models, respectively). The present-day temperature offset of the samples was set to a maximum of 10 ± 10 °C, because all samples were sampled at the surface. Additional time-temperature constraints based on depositional age are documented in Table 3.3. In all cases, we present the expected model, which is a weighted mean model using the posterior probability for weighting (see Gallagher et al. (2009) for further information). A complete summary of QTQt models and their respective parameters and constraints is given in Table 3.3. Models that are not discussed in detail in the results can be found in Figure B.3.

Table 3.3 QTQt modeling parameters and stratigraphic and sample constraints. Stratigraphic constraints describe broad time-temperature conditions at which the included samples were at the surface, and are used as additional modeling constraints. Sample constraints describe the samples, low-temperature thermochronology methods and trends (age-elevation or age-stratigraphy, see Figure 3.4) included in the corresponding model.

General constraints

Modeling interval[a]	0–550 Ma, 0–300 °C	Maximum cooling rate	1000 °C/Ma
eU resampling	No	Reheating	Allowed
Iterations[b]	≥ 100000/≥ 100000	Gradient variation	Allowed
Present day offset[c]	≤ 10 ± 10 °C	Surface temperature	10 ± 10 °C

Model-specific constraints

	Stratigraphic constraints		*Sample constraints*					
Run	Time (Ma)	Temp. (°C)	AHe	AFT	ZHe	Trend[d]	Offset (°C)[e]	Iterations
5a	500 ± 50	0–20			AL3	S	35.01	200000
	510 ± 30	0–20			AL5			
					AL8			
5b	500 ± 50	0–20		AL5		E	27.36	200000
	465 ± 20	0–20		AL7				
				AL9				
5c	500 ± 50	0–20	AL5			S	24.21	100000
	510 ± 30	0–20	AL6					
	465 ± 20	0–20	AL7					
			AL8					
			AL9					
5d	500 ± 50	0–20			AL3	S	36.81	100000
	510 ± 30	0–20	AL5		AL5			
	465 ± 20	0–20	AL6					
			AL7	AL7				
			AL8		AL8			
			AL9					
5e	500 ± 50	0–20		AL5	AL5	E	27.36	100000
	510 ± 30	0–20		AL7				
	465 ± 20	0–20		AL9				
6a	510 ± 30	0–20			MA1	E	2.19	100000
	115 ± 15	0–20			TAC1			
6b	465 ± 20	0–20	AL2			E	10.89	100000
	115 ± 15	0–20	TAC1					
6c	465 ± 20	0–20	MA2			E	11.58	100000
	60 ± 2	0–20	MA3					
6d	465 ± 20	0–20	AL2			E	16.68	100000
	115 ± 15	0–20	MA2					
	60 ± 2	0–20	MA3					
			TAC1					
6e	465 ± 20	0–20		AL2		E	-	200000
6f	465 ± 20	0–20		MA2		E	-	200000

6g	510 ± 30	0–20	AL2	AL2		E	10.89	100000
	465 ± 20	0–20			MA1			
	115 ± 15	0–20	TAC1		TAC1			
6h	465 ± 20	0–20	MA2	MA2		E	11.58	100000
	60 ± 2	0–20	MA3					
7a	500 ± 50	0–20			LU1	S	48.21	100000
					LU2			
7b	465 ± 20	0–20			LU4	E	17.94	100000
					LU9			
7c	465 ± 20	0–20			LU4	S	27.99	100000
					LU9			
7d	500 ± 50	0–20	LU1			E	27.66	100000
	465 ± 20	0–20	LU2					
	60 ± 2	0–20	LU3					
	44 ± 6	0–20	LU4					
			LU5					
			LU6					
			LU7					
7e	500 ± 50	0–20	LU1			E	16.05	100000
			LU2					
7f	465 ± 20	0–20	LU9			E	18.84	200000
	60 ± 2	0–20	LU11					
	23 ± 15	0–20	LU12					
7g	500 ± 50	0–20		LU2		E	-	200000
7h	465 ± 20	0–20		LU3		S	84.87	200000
	60 ± 2	0–20		LU4				
	44 ± 6	0–20		LU5				
	23 ± 15	0–20		LU6				
				LU7				
				LU12				
7i	500 ± 50	0–20	LU1		LU1	E	16.05	100000
			LU2	LU2	LU2			
7j	465 ± 20	0–20		LU3	LU3	S	116.55	100000
	60 ± 2	0–20		LU4	LU4			
	44 ± 6	0–20		LU5				
	23 ± 15	0–20		LU6				
				LU7				
					LU9			
				LU12				
7k	465 ± 20	0–20	LU9		LU9	E	18.84	200000
	60 ± 2	0–20	LU11					
	23 ± 15	0–20	LU12	LU12				
8a	500 ± 50	0–20	AC1			E	16.47	100000
	510 ± 30	0–20	AC2					
	70 ± 2	0–20	AC3					
			AC6					

8b	500 ± 50	0–20	AC1 AC2			E	6.87	100000
8c	510 ± 30 70 ± 2	0–20 0–20	AC3 AC6			E	5.85	100000
8d	500 ± 50	0–20		AC1 AC2		E	6.87	200000
8e	500 ± 50	0–20		AC1 AC2		S	17.82	200000
8f	500 ± 50 510 ± 30 70 ± 2	0–20 0–20 0–20	AC1 AC2 AC3 AC6	AC1 AC2	AC1	E	16.47	100000
8g	500 ± 50	0–20	AC1 AC2	AC1 AC2	AC1	E	6.87	100000
8h	500 ± 50	0–20		AC1 AC2	AC1	S	17.82	100000

[a]Temperature interval for AHe-, AFT- and ZHe-only models 0–140 °C, 0–160 °C and 0–300 °C, respectively
[b]Number of iterations burn-in and post-burn-in
[c]Present-day offset maximum 10 ± 10 °C, unless original offset was lower
[d]Age-elevation (E) or age-stratigraphy (S)
[e]Thermal offset between the hottest and coldest sample, based on a geothermal gradient of 30 °C/km

3.4 Results

3.4.1 Field geology

From west to east, the study area is divided into four tectonic blocks (TB1–TB4), of which TB1–TB3 are located within the Tilcara Range and TB4 (San Lucas block) encompasses the area east of the Tilcara Range Frontal Fault. TB1 to TB3 consist of mostly Precambrian to Ordovician basement rocks that generally dip to the WSW–WNW (Figure 3.2). We found large domains of upper Cambrian–lower Ordovician rocks, identified by their characteristic lithological assemblage, fossils and trace fossils. Discrepancies between existing maps (e.g., González and Tchilinguirian, 2003; Rodríguez-Fernández et al., 1999) can be explained by the improved accessibility of the Tilcara Range outcrops along newly-built roads, the increasing quality of satellite imagery used for interpolation of formation boundaries and the large-scale character of the aforementioned maps. Both the Puncoviscana Fm and Santa Victoria Group show a strong lithological contrast to the intervening Mesón Group. This contrast is further accentuated by the Tilcaric unconformity, which is strongly angular near Huacalera. The alternating lithologies in the Puncoviscana Fm and Santa Victoria Group allowed the accommodation of intensive small-scale folding in these units (Figure 3.2, 3.3a). In contrast, the competent sandstones and quartzites of the Mesón Group are less deformed and form excellent markers for large-scale deformation in the basement blocks of the Tilcara Range. Within the Tilcara Range there are also small, locally restricted outcrops of the Pirgua Subgroup (see also Kley et al., 2005).

NW–SE striking high-angle faults divide TB1–TB3 internally, as seen from offsets within the Precambrian to Ordovician basement. In some cases, they show an apparent strike-slip movement, as indicated in Figure 3.2a. Kley et al. (2005) suggest that these apparent strike-slip faults within the basement blocks of the Tilcara Range are in fact Cretaceous normal faults that were tilted during block rotation linked to fault activity along NNE–SSW striking reverse faults. Evidence supporting this is found within TB3, where one of the faults cuts off syn-rift strata of the Pirgua Subgroup against upper Cambrian–lower Ordovician rocks, suggesting a half-graben setting. The syn-rift strata consist of locally confined, proximal breccia grading into conglomerates and cross-bedded sandstones that unconformably overlie the Santa Victoria Group.

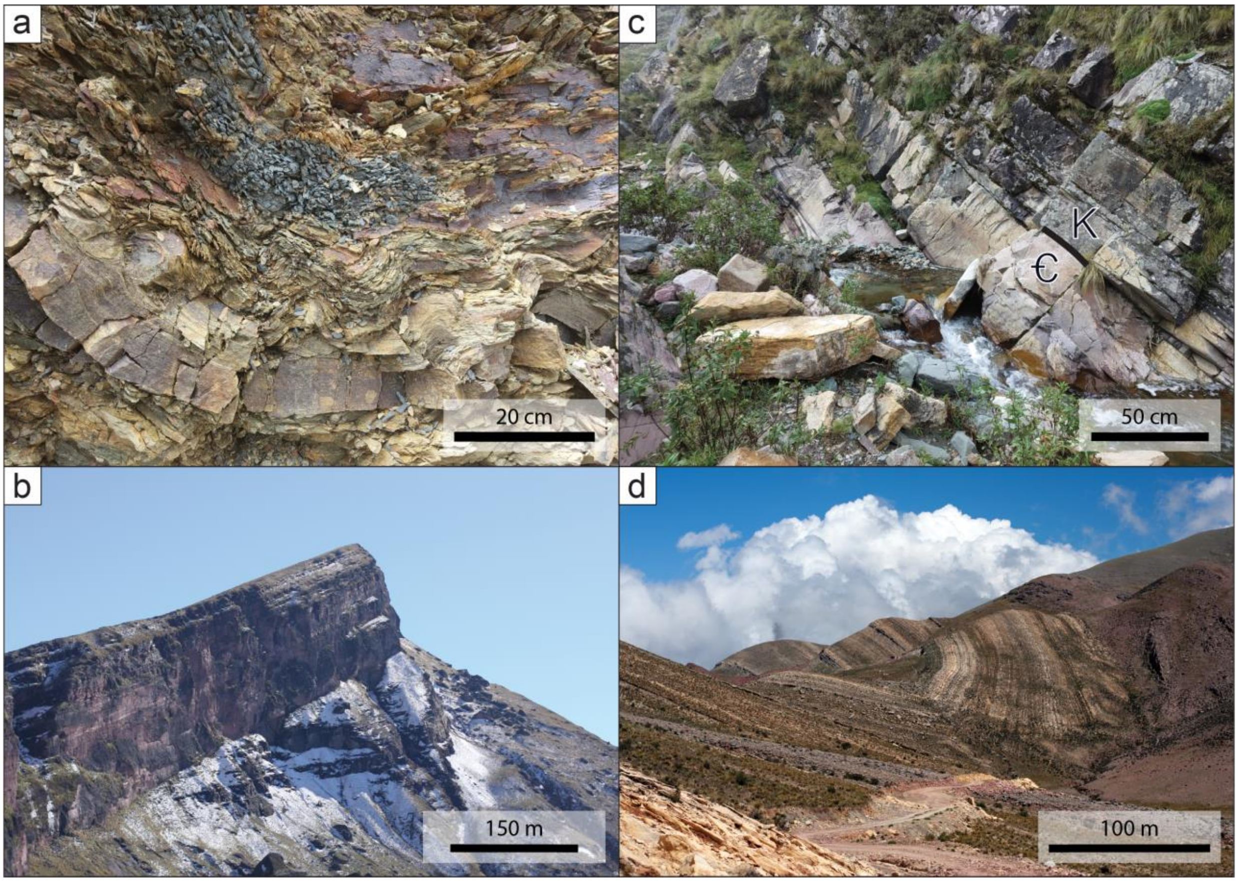

Figure 3.3 (a) Small-scale folding in the Santa Victoria Group east of Alonso. Due to alternating competent and incompetent lithologies, the Santa Victoria Group strata can easily accommodate strain. (b) Angular unconformity (30°) between the Santa Victoria Group and the Cretaceous Pirgua Subgroup at Quebrada Amarilla. (c) Paraconformity between the Mesón Group and the Cretaceous–Paleogene Yacoraite Fm near Las Animas. (d) Footwall syncline in the Cretaceous–Paleogene succession. The Yacoraite Fm and Pirgua Subgroup show an overturned western limb.

The tectonic blocks of the Tilcara Range are tilted along and separated by NNE–SSW high-angle, east-vergent reverse faults (Figure 3.2c, Alonso transect), recognized also by previous authors (Alonso et al., 2012; González and Tchilinguirian, 2003; Rodríguez-Fernández et al., 1999). A minor reverse fault with a similar orientation occurs west of Alonso (Figure 3.2a) and accommodates shortening within TB2. These faults appear to cut NW–SE striking faults (Figure 3.2a), suggesting that the most recent Andean shortening was accommodated by thrusting along the NNE–SSW fault system. Although we can only speculate about its timing and mechanism of formation, the existence of approximately north-striking, east-vergent Paleozoic reverse faults that have been reactivated during Andean shortening has been proven in the Eastern Cordillera and specifically within the Tilcara Range (e.g., Barrabino et al., 2015). The NNE–SSW striking fault system continues up to the Tilcara Range Frontal Fault, which marks a transition in structural elevation and outcropping lithologies, and forms the boundary between the Tilcara Range and the San Lucas block. A direct fault contact between basement strata of the Tilcara Range and syn-rift strata of the San Lucas block (Figure 3.2a) is not visible in the field, but the fault is causally linked to the formation of a close (interlimb angle ~35°), east-verging footwall syncline within the Salta Group of the San Lucas block, which can be traced along the Tilcara Range Frontal Fault for several kilometers (Figure 3.2a). The western limb of this syncline bordering the reverse fault has been overturned (Figure 3.2c, Alonso and Las Animas transect). Similar folds showing an identical NE–SW to NNE–SSW trend can be observed farther east, suggesting the presence of possibly blind reverse or thrust faults within TB4 (Figure 3.2c, San Lucas transect). Toward the east, the Salta Group and the overlying Orán Group form increasingly open, upright folds. The presence of the Lumbrera Fm, with a middle–late Eocene depositional age known from the vertebrates fossil record assigned to the Riochican–Casamayoran (Pascual et al., 1981) and U-Pb dating of a tuff layer near its top (Del Papa et al., 2010), within the synclines shows that fault activity along the Tilcara Range Frontal Fault, and in general shortening within the San Lucas block, must be younger than the late Eocene.

Within the Tilcara Range, most of the Salta Group has been eroded and is only present in small outcrops related to synclines. In contrast, east of the Tilcara Range Frontal Fault, a full succession of the Salta Group is preserved, from basal conglomerates of the Pirgua Subgroup to the transition of the Santa Barbara Subgroup into the overlying Orán Group close to San Lucas. Both in the northern and middle part of the area, the Pirgua Subgroup unconformably overlies the Santa Victoria Group (Figure 3.2a). In the north, we observed a strong angular unconformity (30°, Figure 3.3b), whereas at Huairahuasi the angle is significantly smaller (< 11°). We attribute this angular variety to folding of the Santa Victoria Group before deposition of the Salta Group, also shown in other locations within the Eastern Cordillera (e.g., Alonso et al., 2012). Short wavelength folding is also clear from rapidly changing bedding orientations within the Puncoviscana Fm and Santa Victoria Group (Figure 3.2). However, large-scale folding with NE–SW to NNE–SSW trending fold axes also occurs in the Santa Victoria Group (Figure 3.2a), suggesting that Andean deformation has affected these rocks as well as the Salta Group strata.

The thickness of the Salta Group varies from north to south and west to east, and is largely controlled by thickness changes of the Pirgua Subgroup. Transects in Figure 3.2c and sections from Boll et al. (1989), 5 km south of the Alonso transect, document a rapidly decreasing thickness of the Pirgua Subgroup from 413 m in the north to 10 m at Huairahuasi (compare sections in Figure 3.2c). South and east of Huairahuasi, the Pirgua Subgroup is not preserved, leaving the Yacoraite Fm resting paraconformably on top of the Mesón and Santa Victoria Groups (Figure 3.3c) near Las Animas and San Lucas. Whereas the Balbuena Subgroup retains a relatively stable thickness from north to south and west to east, the thickness of the Santa Barbara Subgroup varies from > 487 m in the north (Boll et al., 1989) to > 206 m in the south, and > 650 m in the west to 492 m in the east. The latter strongly contrasts with the measured thickness of > 198.8 m at the Rio San Lucas by Boll et al. (1989).

The relatively large thickness of the Pirgua Subgroup north of Quebrada Amarilla, its rapid thinning toward the south and the presence of breccias and proximal conglomerate levels at its base suggest the presence of a remnant NW–SE striking Cretaceous normal fault north of Quebrada Amarilla, compatible with the data of Kley et al. (2005). Combined with locally confined and fault-bound outcrops of syn-rift strata within the Tilcara Range, this supports the general idea that at the margins of the Lomas de Olmedo sub-basin, the thickness of the Pirgua Subgroup varies dramatically due to its deposition in local half-graben settings (Marquillas et al., 2005; Salfity and Marquillas, 1994).

3.4.2 Thermochronology

Thermochronological data were plotted in age-elevation and age-stratigraphy diagrams to analyse trends (Figure 3.4). We calculated regression lines using a linear fit based on weighted mean cooling ages that exclude outliers. Visual guides were traced by hand (Figure 3.4, dashed lines) whenever sample statistics were not robust enough to calculate a fit (i.e., for trends with only two samples or for samples with high dispersion), but visually a trend could be seen. AHe ages range from 1.7 ± 0.5 Ma to 43.5 ± 1.8 Ma (excluding one outlier) and show a decrease from west to east, concordant with sampling elevation (Figure 3.4 and B.1). AHe ages at the leeward side of the Tilcara Range are generally older than ages at similar elevations at the windward side. Within coherent NW–SE transects, there is a pervasive positive age-elevation trend across the Tilcara Range Frontal Fault (Figure 3.4), indicating a lack of significant fault activity after exhumation beyond the APRZ. Within the AL9-AL5 vertical profile of TB1, AHe ages range from 43.5 ± 1.8 Ma to 8.4 ± 0.2 Ma and show a disperse but positive age-stratigraphy trend (Figure 3.4a). Assuming the lower, stratigraphically younger samples were only partially reset, this could explain the increasingly scattered ages in these samples. Similarly, the overdispersion of single-grain AHe ages within sample AL4 (TB2) could be caused by partial resetting. However, fully reset AFT ages and burial of the samples to > 4.5 km (e.g., Siks and Horton, 2011) suggest that AHe ages should be fully reset. For sample AL4, an age-ESR trend could provide an alternative explanation for dispersion, but the small absolute difference in ESR and rapid exhumation also make this an unlikely solution. AHe ages show no offset across faults and between TB2 and TB3 there is a positive age-elevation trend. Within the San Lucas transect, samples LU1–LU7 and LU9–LU12 form continuous age-elevation trends, although the latter shows a slight offset toward older ages. This might suggest that minor thrust or reverse faults disturb the basement strata internally. In theory, partial resetting of AHe cooling ages could also explain a deviation from the general age-elevation trend. However, the samples show late Miocene to Pleistocene cooling ages, whereas the depositional ages of the source rocks range from the upper Cambrian to the Miocene. Furthermore, samples LU9–LU12 show a continuous age-elevation trend with a similar slope as the trend seen in samples LU1–LU7.

AFT ages range from 5.8 ± 0.9 Ma to 12.3 ± 2.0 Ma for reset ages. Coinciding with the AHe age distribution, spatial relationships between samples are disrupted within tectonic blocks. We attribute this to disruption of the age pattern due to fault activity and propagation of fault activity from north to south. AFT ages from the leeward side show a positive, near-vertical age-elevation trend, contrasting with the negative trend seen in the AHe data (Figure 3.4a). Again, there is no evidence for fault activity between the tectonic blocks, suggesting that late Miocene exhumation of these fault blocks occurred homogeneously and fault activity along the NNE–SSW fault system ceased before exhumation through the APAZ.

At the windward side of the Tilcara Range, AFT cooling ages do not show a general age-elevation trend, contrary to the AHe data. (Figure 3.4). Instead, the samples adhere to an overall positive age-stratigraphy trend (Figure 3.4 and B.1). We attribute the lack of an age-elevation relationship to the interplay of both absolute sampling elevation and Cenozoic burial depth, and suggest that the majority of folding and faulting within TB4 must have taken place after cooling through the APAZ, placing an important constraint on deformation in this block. The stratigraphically highest sample LU12 has an age of 32.7 ± 2.7 Ma: this comparatively old age likely results from the limited thickness of foreland strata to the east, which cannot have buried the sample deeply enough to cause resetting prior to a Miocene–Pliocene exhumation event. Several samples from the Santa Barbara Subgroup also show ages that are older than expected for the general age-stratigraphy trend and might only be partially reset. AFT ages show a subtle age offset across the Tilcara Range Frontal Fault in all three transects, with slightly younger ages in the hanging wall (Figure 3.4). The minor offset indicates that fault-related exhumation beyond the APAZ was limited.

ZHe ages range from 24.1 ± 0.2 Ma to 560.8 ± 10.0 Ma (excluding one young and one old outlier). The highest sample in TB3 within the Alonso transect shows two age populations: one Early–Middle Jurassic and one late Cambrian–early Silurian. We cannot exclude either of these based on ICP-MS data, grain geometry or impurities within the grain and there is no age-eU or age-F_T relationship. Because both populations are older than the Cretaceous depositional age, we argue that the sample is partially reset and that the ZHe ages show an age distribution that reflects the detrital provenance – and as such the radiation damage history – of the single aliquots. ZHe single-grain ages do not show an overall age-elevation trend, nor an overall age-eU trend (Figure B.1). However, ZHe samples within TB1 show a positive age-stratigraphy trend, similar to the AHe data. Within TB4, there is a positive age-elevation and/or age-stratigraphy trend, neither confirming nor rejecting the hypothesis that deformation in this block took place after cooling beyond the APAZ. The sample LU3 shows ZHe ages that are older than its depositional age (Figure 3.4b), and was not fully reset. Similar to sample LU3, the TB4 sample in the Las Animas transect is non-reset and reflects detrital provenance rather than Paleogene exhumation. Since sample LU3 fits only on an age-stratigraphy trend (Figure 3.4b) it is likely that deformation took place after cooling through the ZPRZ.

ZHe samples were collected from both sides of the reverse faults dividing the tectonic blocks (Figure 3.4). Although from TB2 to TB3, ages appear to be offset (Figure 3.4a), age-elevation plots across the fault show that there is a continuous positive age-elevation trend from TB2 to TB3. Within the windward side of the Tilcara Range, ZHe data across the Tilcara Range Frontal Fault show a clear offset toward younger ages in the hanging wall block (Figure 3.4b–c), indicating that there has been fault activity after the samples cooled through the ZPRZ.

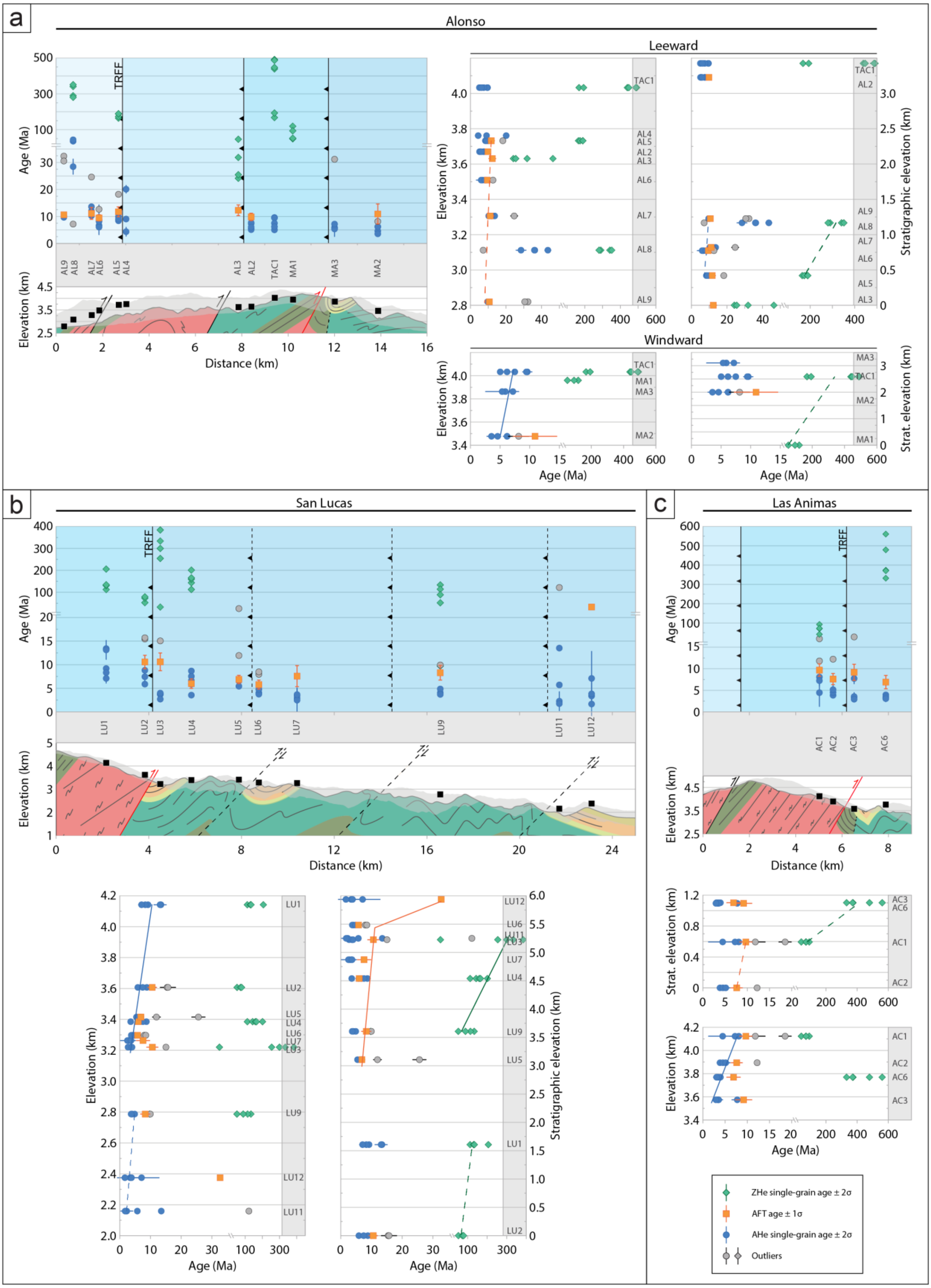

a
Alonso
Leeward
Windward
TREFF
Age (Ma)
Elevation (km)
Distance (km)
Stratigraphic elevation (km)
Strat. elevation (km)
Age (Ma)
b
San Lucas
c
Las Animas
ZHe single-grain age ± 2σ
AFT age ± 1σ
AHe single-grain age ± 2σ
Outliers

Figure 3.4 Diagrams of the (a) Alonso transect, (b) San Lucas transect, and (c) Las Animas transect showing single-grain AHe and ZHe ages, as well as AFT ages plotted against the distance along the section. Schematic geological sections (see also Figure 3.2c) with swath profiles show the location and elevation of the samples. Samples are projected onto the section and the location of faults and formation boundaries are drawn relative to the samples. Transects are accompanied by age-elevation and age-stratigraphy plots, including calculated regression lines (solid) and visual guides (dashed). Note the breaks in the y- and x-axes.

3.4.3 QTQt modeling

Based on the different trends for AHe, AFT and ZHe samples described above, we initially created single-method QTQt models. Depending on the trend seen in the thermochronological data (Figure 3.4), models were run in age-elevation and/or age-stratigraphy space. Age-elevation models use the sampling elevation, whereas age-stratigraphy models use the stratigraphic pseudo-elevation of samples, measured from the cross-sections in Figure 3.2c (see Section 3.3.5 for full methodology). Age-elevation models are based on the assumption that deformation processes, which change spatial relationships between samples, terminated before cooling through the APRZ, APAZ or ZPRZ. In contrast, age-stratigraphy models assume deformation has not yet occurred. Single-method models (see Figure B.3 in Appendix B) that showed robust results were combined into multi-method models, which were preferably used for interpretation of thermal histories (Figure 3.5–3.8). For age-elevation (age-stratigraphy) models where single-grain ages of one method are incompatible with an age-elevation (age-stratigraphy) trend, we still used at least one sample of that method to impose better time and temperature constraint. Cooling rates are calculated from the visual inflection points of the hot sample 95 % confidence interval, obtaining a lowest and highest cooling rate for the most recent exhumation phase. We report these as average cooling rates with standard deviation.

Alonso transect (leeward)

Early exhumation within TB1 and TB2 is constrained by a multi-sample age-stratigraphy ZHe model (model 5a; Figure B.3) that we modeled following the age-stratigraphy relationship seen in Figure 3.4a. Predicted ZHe ages are generally slightly older than observed ages. Although the model suggests an early, pre-Salta Group exhumation of the Tilcara Range between the Carboniferous and the Early Cretaceous (330–140 Ma), ZHe ages cannot constrain the Miocene–Pliocene exhumation well, suggesting an onset of exhumation between 16 and 2 Ma.

Andean exhumation is constrained by single- and multi-method models using AHe and AFT samples. An age-elevation AFT model for TB1 (model 5b; Figure 3.5b; see also Figure 3.4a), shows an onset of rapid exhumation between 24 and 16 Ma. In contrast, an AHe model for TB1 (model 5c; Figure B.3) using an age-stratigraphy relationship (see also Figure 3.4a) proposes an early, Cretaceous exhumation with an onset between 135 and 114 Ma, as well as a Miocene exhumation starting between 13 to 10 Ma with a decreasing exhumation rate < 9 Ma. For both models, predicted ages show a fairly good fit with the observed ages. The discrepancy in the onset of exhumation between the models can be explained by the different temperature intervals that AHe and AFT cooling ages document. As such, AFT ages are better suited to document early cooling and the earliest onset of exhumation.

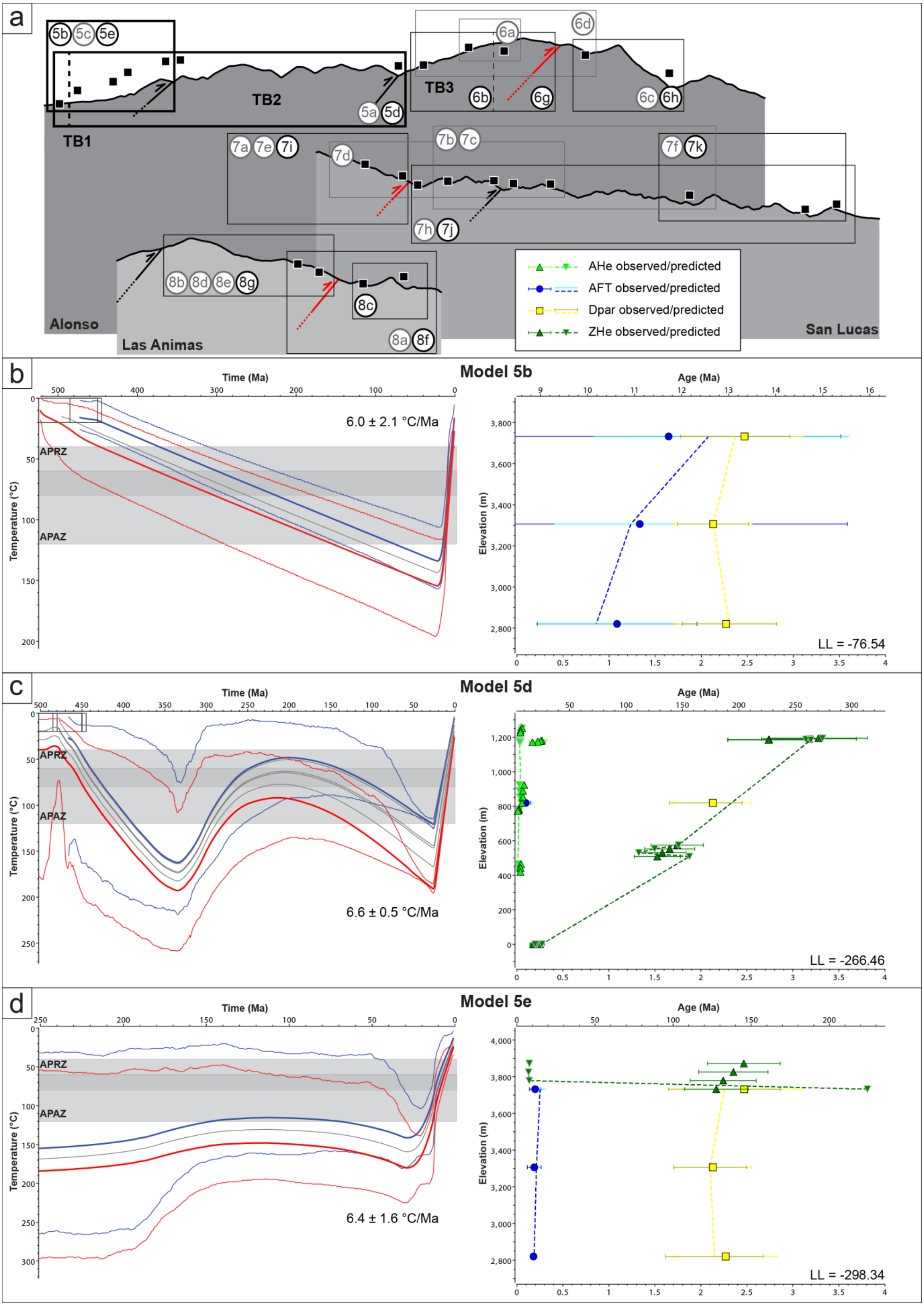
a
5b 5c 5e
TB1
TB2
5a 5d
TB3
6a 6d
6b 6g
6c 6h
7a 7e 7i
7d
7b 7c
7f 7k
7h 7j
8b 8d 8e 8g
8c
8a 8f
Alonso
Las Animas
San Lucas
AHe observed/predicted
AFT observed/predicted
Dpar observed/predicted
ZHe observed/predicted
b
Model 5b
Time (Ma)
Temperature (°C)
APRZ
APAZ
6.0 ± 2.1 °C/Ma
Age (Ma)
Elevation (m)
LL = -76.54
c
Model 5d
Time (Ma)
Temperature (°C)
APRZ
APAZ
6.6 ± 0.5 °C/Ma
Age (Ma)
Elevation (m)
LL = -266.46
d
Model 5e
Time (Ma)
Temperature (°C)
APRZ
APAZ
6.4 ± 1.6 °C/Ma
Age (Ma)
Elevation (m)
LL = -298.34

Figure 3.5 Modeling results for the leeward side of the Alonso section. (a) shows the subset of samples used for individual models (see also Table 3.3) and its location on the section. Models marked in grey are shown in Figure B.3. The Tilcara Range Frontal Fault is marked in red. Models (b) 5b, (c) 5d and (d) 5e are shown as the expected t-T-path and 95 % confidence interval of the hot and cold sample. Average cooling rates with standard deviation are shown for the most recent exhumation phase. All models show the predicted and observed single-aliquot ages and the log likelihood (LL) to the right.

We ran one multi-method age-stratigraphy model (model 5d; Figure 3.5c) for TB1 and TB2, using five AHe, one AFT and three ZHe ages. The model shows an early pulse of exhumation from the Mississippian to the Early Jurassic (335–200 Ma), which is roughly within the timeframe given by model 5a. The samples were re-buried below the APAZ between 245 and 26 Ma. Late Oligocene to Miocene exhumation is well-constrained in this model and started at approximately 26 Ma, slightly earlier than in model 5b. An age-elevation model for TB1 (model 5e; Figure 3.5d) that excludes AHe ages shows Andean rapid exhumation starting in the early Miocene (21–16 Ma) and slowing down in the middle Miocene (13–12 Ma). Although both multi-sample models agree on a late Oligocene to middle Miocene (26–16 Ma) onset of rapid exhumation, model 5d shows a much tighter constraint on the timing of exhumation, which could also be connected to the larger number of samples modeled. Furthermore, observed ages are more in accordance with predicted ages in model 5d, suggesting a higher reliability.

Alonso transect (windward)

Pre-Cretaceous exhumation of the windward side of the Tilcara Range is constrained by a ZHe model for TB3 (model 6a; Figure B.3). Samples were modeled in age-elevation space, based on the small amount of internal deformation of TB3 after the onset of cooling. Predicted ages match the observed ages well. The model shows an early exhumation from the Late Jurasic to the Early Cretaceous (150–117 Ma) to bring upper Cambrian–lower Ordovician basement to the surface. Although it is clear that the samples were again buried below the APAZ until 60–47 Ma, the timing of Andean exhumation is poorly constrained. Some iterations show an onset of exhumation between 62 and 47 Ma, but a large number of iterations suggest the final pulse of exhumation may have started between 26 and 15 Ma. The latter seems to be more in agreement with the AHe and AFT models.

Miocene–Pliocene exhumation is constrained by AHe, AFT and multi-method models. AHe age-elevation models were run separately for TB3 and TB4 to compare the timing of deformation on both sides of the Tilcara Range Frontal Fault. The TB3 model (model 6b; Figure 3.6b) shows exhumation starting between 21 and 11 Ma with a slightly decreasing rate of exhumation at approximately 6 Ma. The TB4 model suggests an onset of rapid exhumation between 16 and 15 Ma, within the same interval seen in model 6b (model 6c; Figure B.3), but no decrease of the exhumation rate. We also ran a model across the Tilcara Range Frontal Fault (model 6d; Figure B.3), which proposes an onset of exhumation between 18 and 12 Ma, in between the TB3 and TB4 model. In all cases, the majority of the predicted AHe ages is older than the corresponding observed ages.

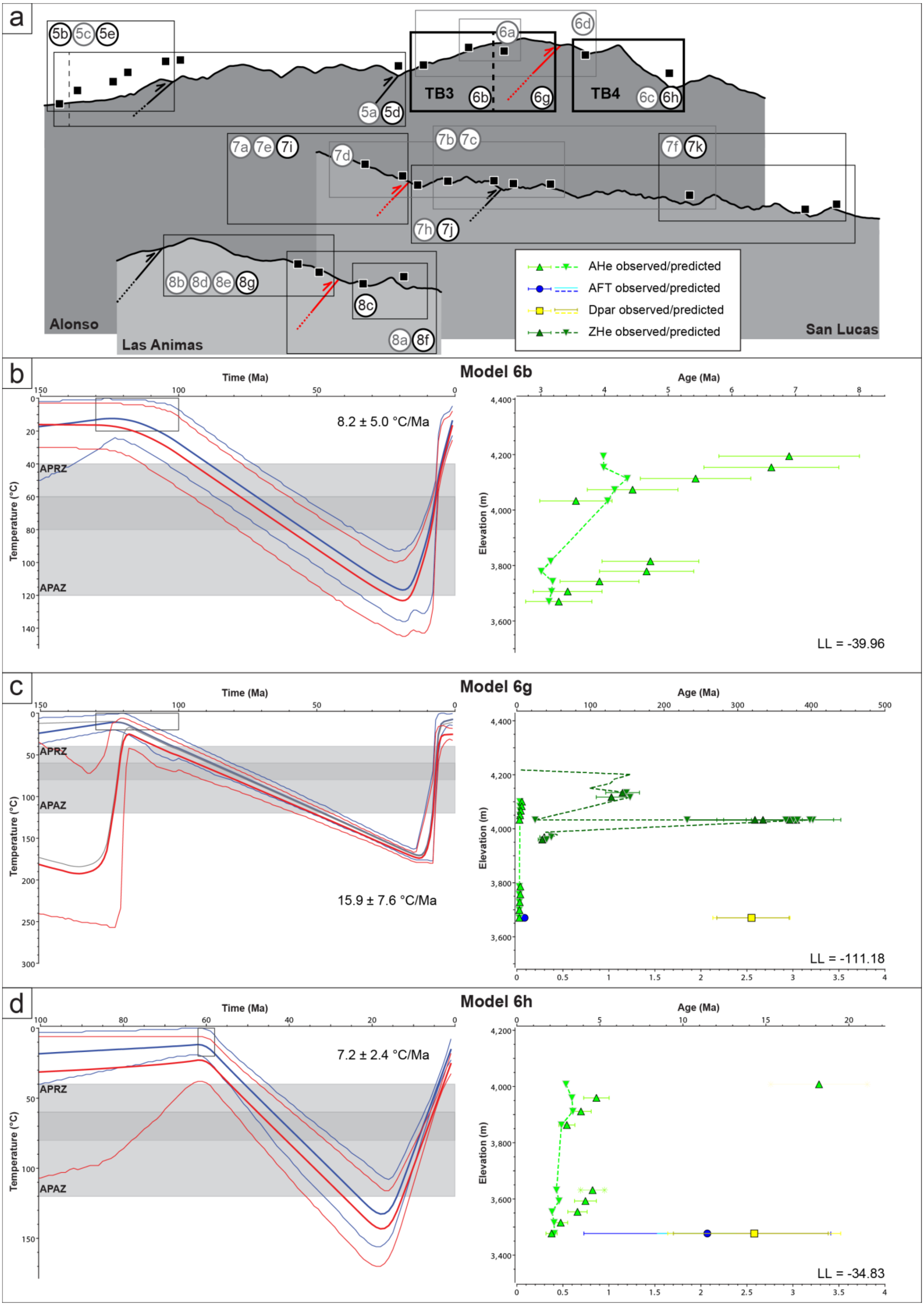

a
Alonso
Las Animas
San Lucas
TB3
TB4
AHe observed/predicted
AFT observed/predicted
Dpar observed/predicted
ZHe observed/predicted
b
Model 6b
8.2 ± 5.0 °C/Ma
LL = -39.96
c
Model 6g
15.9 ± 7.6 °C/Ma
LL = -111.18
d
Model 6h
7.2 ± 2.4 °C/Ma
LL = -34.83
Time (Ma)
Age (Ma)
Temperature (°C)
Elevation (m)
APRZ
APAZ

Figure 3.6 Modeling results for the windward side of the Alonso section. (a) shows the subset of samples used for individual models (see also Table 3.3) and its location on the section. Models marked in grey are shown in Figure B.3. The Tilcara Range Frontal Fault is marked in red. Models (b) 6b, (c) 6g and (c) 6h are shown as the expected t-T-path and 95 % confidence interval of the hot and cold sample. Average cooling rates with standard deviation are shown for the most recent exhumation phase. All models show the predicted and observed single-aliquot ages and the LL to the right.

We ran separate single-sample AFT models for TB3 and TB4 (model 6e and 6f, respectively). The model for TB3 (model 6e; Figure B.3) suggests an onset of exhumation between 17 and 14 Ma, whereas the model for TB4 (model 6f; Figure B.3) shows continuous exhumation starting between 22 and 17 Ma. The predicted vs. observed fit is better for model 6f. The AFT models do not add any significant constraint on the timing of exhumation.

TB3 and TB4 were modeled separately in multi-method, multi-sample models. The TB3 model uses two AHe, one AFT and two ZHe ages in age-elevation space, based on the AHe and ZHe single-method models (model 6g; Figure 3.6c). It suggests a first pulse of rapid exhumation for the hot sample starting in the Early Cretaceous (133–123 Ma). This is within the exhumation timeframe given by model 7a. From 118 Ma, the samples were buried well below the APAZ (> 160 °C). Andean exhumation started between 14 and 8 Ma and slowed down between 8 and 7 Ma, coinciding with model 6b. The TB4 model uses two AHe ages in age-elevation space and one AFT age for better constraint (model 6h; Figure 3.6d). It proposes burial > 100 °C after deposition of the Santa Barbara Subgroup at approximately 62 Ma. The onset of continuous exhumation occurred between 18 and 16 Ma, slightly earlier than in AHe model 6c. Again, predicted AHe cooling ages are slightly older than observed ages, but the model fit for AFT and ZHe data is good. Similar to the single-sample AFT models, the onset of exhumation occurred earlier in TB4 than in TB3.

San Lucas transect

Early pre-Salta Group exhumation was inferred from ZHe models that were run in both age-stratigraphy and age-elevation space. Based on the assumption that folding and block rotation happened after the samples cooled through the ZPRZ, age-stratigraphy trends are theoretically more accurate. However, the effect of the deformation on inter-sample relationships and thermal gradients for the ZHe samples might be too small to notice. The TB3 age-stratigraphy model (model 7a; Figure B.3), although better than the age-elevation model, does not provide good constraints on pre-Salta Group exhumation. Furthermore, predicted ZHe ages are much older than the observed ages. For TB4, the age-elevation (model 7b; Figure B.3) and age-stratigraphy model (model 7c; Figure B.3) yield very similar results with a well-constrained onset of exhumation between 136 and 121 Ma (138 and 112 Ma for model 7c). For these models, ZHe ages show a better observed vs. predicted fit. Using a third, Paleogene sample for the TB4 models does not increase the model fit. Unfortunately, none of the models provide good constraints on the timing of Miocene exhumation.

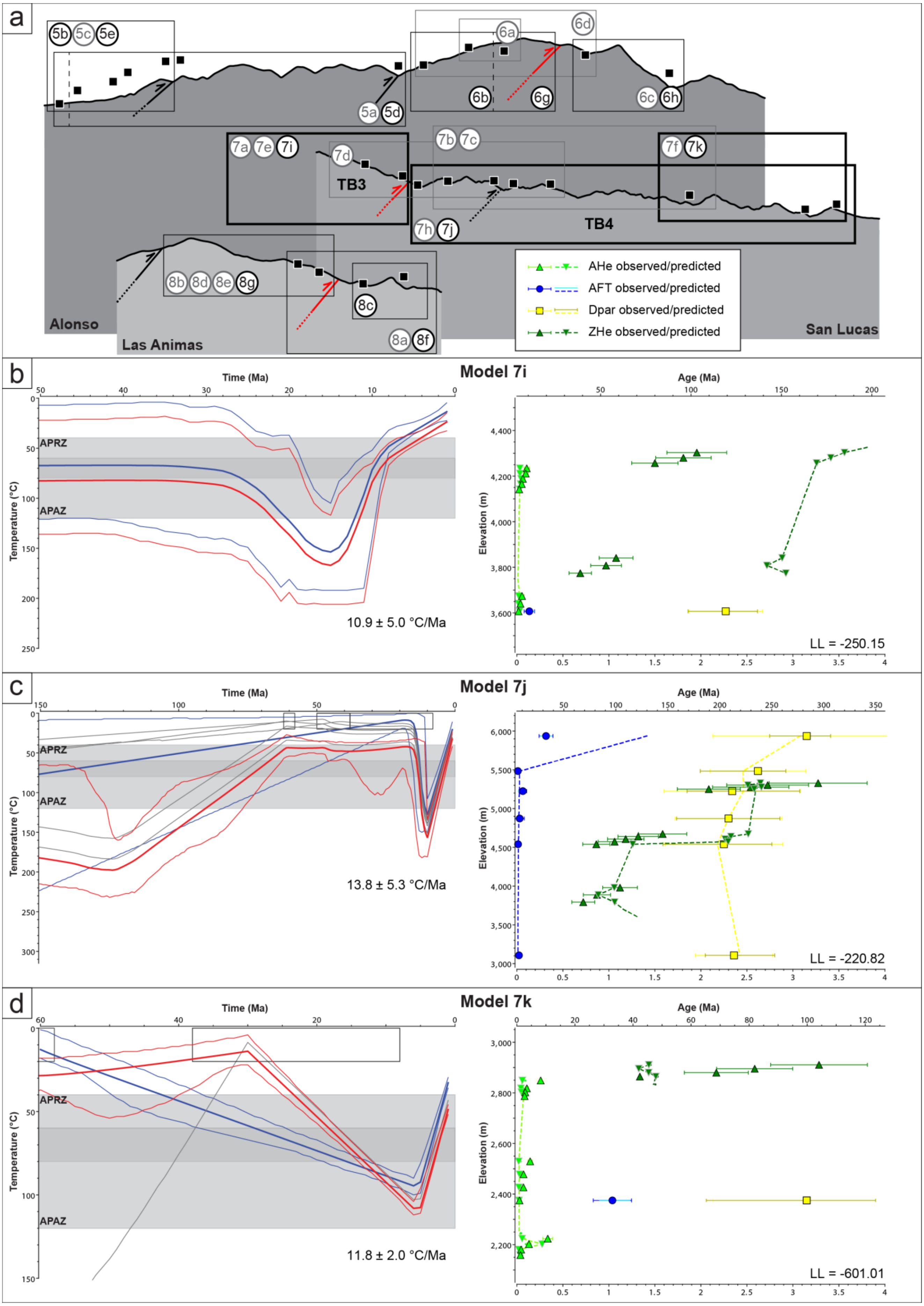

a
Alonso
Las Animas
San Lucas
TB3
TB4
AHe observed/predicted
AFT observed/predicted
Dpar observed/predicted
ZHe observed/predicted
b
Model 7i
10.9 ± 5.0 °C/Ma
LL = -250.15
c
Model 7j
13.8 ± 5.3 °C/Ma
LL = -220.82
d
Model 7k
11.8 ± 2.0 °C/Ma
LL = -601.01
Time (Ma)
Temperature (°C)
Age (Ma)
Elevation (m)
APRZ
APAZ

Figure 3.7 Modeling results for the San Lucas section. (a) shows the subset of samples used for individual models (see also Table 3.3) and its location on the section. Models marked in grey are shown in Figure B.3. The Tilcara Range Frontal Fault is marked in red. Models (b) 7i, (c) 7j and (c) 7k are shown as the expected t-T-path and 95 % confidence interval of the hot and cold sample. Average cooling rates with standard deviation are shown for the most recent exhumation phase. All models show the predicted and observed single-aliquot ages and the LL to the right.

To constrain the Andean exhumation, we ran a multi-sample AHe model (model 7d; Figure B.3) that crosses the Tilcara Range Frontal Fault because of the age-elevation relationship for AHe samples in TB3 and TB4. The model suggests burial at < 44 Ma, based on the Santa Barbara Subgroup depositional age. Miocene exhumation started between 14 and 11 Ma and slowed down after 9 Ma, which is similar to model 5c but earlier than model 6b and 6g. A separate model for TB3 (model 7e; Figure B.3) yields a similar timing of exhumation, starting between 11 and 10 Ma and slowing down between 9 and 8 Ma. In contrast, the easternmost part of TB4 (samples LU9–LU12, model 7f) shows a badly-constrained phase of burial below the APRZ between 30 and 5 Ma and an onset of exhumation between 5 and 4 Ma, much later than models 7d and 7e.

Similar to model 7e, a single-sample AFT model from TB3 (model 7g; Figure B.3) shows an onset of exhumation between 22 and 16 Ma. A multi-sample age-stratigraphy AFT model for TB4, which assumes that most of the block-internal deformation happened after cooling through the APAZ (model 7h; Figure B.3), suggests burial of the cold sample from ~27 Ma, followed by rapid exhumation that started between 10 and 8 Ma. This shows that in the San Lucas transect the onset of exhumation in TB4 occurred later than in TB3. Although the model predicts ages that are too old for the upper three samples, it obtains a good Dpar fit throughout the sample column.

We also modeled TB3 and TB4 separately for multi-method models. The age-elevation model for TB3 (model 7i; Figure 3.7b), using two AHe, one AFT and two ZHe ages with an age-elevation relationship, shows burial below the APAZ from approximately 45 Ma. Exhumation started between 15 and 13 Ma, and slowed down < 8 Ma. Similar to the ZHe models, predicted ZHe ages are too old compared to the observed ages, which might be connected to a too-shallow modeled Cenozoic burial of the samples. Although we also ran an age-stratigraphy model with one AFT and two ZHe ages, we prefer the age-elevation model (7i) because of the larger number of constraints placed by the sampling and the resulting constraints on the Miocene exhumation. The use of AFT and ZHe ages in an age-elevation model should not result in major errors, because TB3 is not folded internally and inter-sample relationships are preserved. For TB4 we used age-stratigraphy space, because the AFT samples do not adhere to an age-elevation trend. The model (model 7j; Figure 3.7c) yields an onset of exhumation at 10 Ma. Even though the uppermost AFT sample shows a predicted age that is too old, the other AFT samples, Dpar values and ZHe ages show a good fit. An age-elevation model of the far eastern part of TB4 (model 7k; Figure 3.7d) yields an onset of exhumation for the hot sample < 6 Ma, roughly coinciding with model 7f. ZHe predicted ages are again too old in this model, for similar reasons as described above.

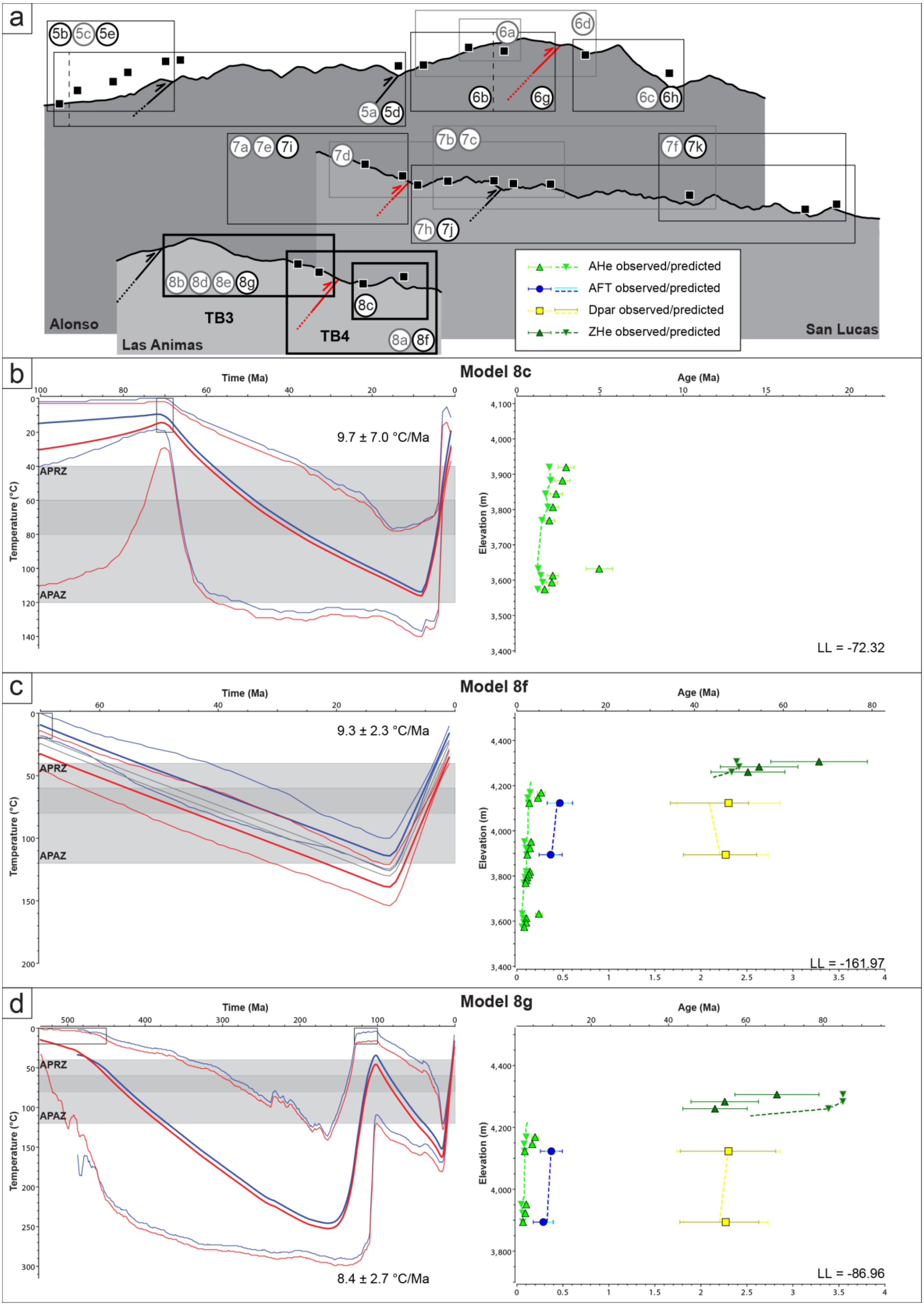

a
5b 5c 5e
5a 5d
6a 6d
6b 6g
6c 6h
7a 7e 7i
7d
7b 7c
7f 7k
7h 7j
8b 8d 8e 8g
8c
8a 8f
TB3
TB4
Alonso
Las Animas
San Lucas
AHe observed/predicted
AFT observed/predicted
Dpar observed/predicted
ZHe observed/predicted
b
Model 8c
Time (Ma)
Temperature (°C)
9.7 ± 7.0 °C/Ma
APRZ
APAZ
Age (Ma)
Elevation (m)
LL = -72.32
c
Model 8f
Time (Ma)
Temperature (°C)
9.3 ± 2.3 °C/Ma
APRZ
APAZ
Age (Ma)
Elevation (m)
LL = -161.97
d
Model 8g
Time (Ma)
Temperature (°C)
APRZ
APAZ
8.4 ± 2.7 °C/Ma
Age (Ma)
Elevation (m)
LL = -86.96

Figure 3.8 Modeling results for the Las Animas section. (a) shows the subset of samples used for individual models (see also Table 3.3) and its location on the section. Models marked in grey are shown in Figure B.3. The Tilcara Range Frontal Fault is marked in red. Models (b) 8c, (c) 8f and (c) 8g are shown as the expected t-T-path and 95 % confidence interval of the hot and cold sample. Average cooling rates with standard deviation are shown for the most recent exhumation phase. All models show the predicted and observed single-aliquot ages and the LL to the right.

Las Animas transect

Although pre-Cretaceous exhumation cannot be constrained well by ZHe models of the Las Animas transect, single- and multi-sample models are able to constrain Miocene exhumation. We ran one AHe model crossing the Tilcara Range Frontal Fault (model 8a; Figure B.3) that suggests exhumation started before 9 Ma, but the model does not give any hard constraints for the minimum age of onset. The separate age-elevation model for TB3 (model 8b; Figure B.3) yielded exhumation beginning between 11 and 10 Ma. The TB4-specific model (model 8c; Figure 3.8b) shows burial < 70 Ma, constrained by the depositional age of the Santa Barbara Subgroup, and exhumation starting around 15 Ma at the earliest, with the exhumation rate increasing slightly at approximately 4 Ma. The separate models for TB3 and TB4 both constrain the onset of exhumation better than the combined model and are not affected by fault motion. Furthermore, predicted AHe cooling ages match the observed ages quite well.

Multi-sample age-elevation and age-stratigraphy AFT models for TB3 (model 8d and 8e: Figure B.3) both show similar t-T-paths with an early–middle Miocene onset of exhumation (17–12 Ma and 19–13 Ma, respectively). Unfortunately, both AFT samples in TB4 did not pass the chi-square test and were thus not considered for modeling.

We ran a multi-sample age-elevation model across the Tilcara Range Frontal Fault (model 8f; Figure 3.8c), which yielded an onset of rapid exhumation at 11 Ma, corresponding to the AHe model for TB3. An age-elevation model for TB3 (model 8g; Figure 3.8d) shows Late Jurassic–Early Cretaceous exhumation (165–102 Ma), burial at < 102 Ma below the APAZ and rapid exhumation beginning between 18 and 16 Ma, coinciding with the earliest timeframe given by the AFT model 8d. Although we ran an age-stratigraphy model, which excluded AHe ages, the Tertiary history of that model is badly constrained whereas the Miocene history is very similar to model 8g. Thus, the age-elevation and age-stratigraphy models show great similarities, indicating that internal deformation after cooling through the ZPRZ and APAZ did not affect the modeling interval for Miocene exhumation.

Summary of modeling results

The timing of pre-Salta Group exhumation is well-constrained for both the leeward and windward side of the Tilcara Range. ZHe models from the western Alonso transect show an early phase of exhumation from the Carboniferous to the Early Cretaceous (335–140 Ma), which is confirmed by the multi-method model. However, north of the Alonso transect, the Salta Group rests unconformably on top of upper Cambrian–lower Ordovician (Santa Victoria Group) basement, indicating that the samples may have been close to the surface as late as the Cretaceous (115 ± 15 Ma). The latter is also suggested by ZHe and multi-method models from the windward side, which consistently show a Late Jurassic to Early Cretaceous phase of exhumation (between 150 and 110 Ma), with most of the models showing an onset of exhumation between 140 and 115 Ma.

Cooling related to Andean exhumation began earlier in TB1 and TB2, compared to TB3 and TB4 (Alonso transect), and the cooling rate also shows an earlier decrease in the westernmost tectonic blocks. Furthermore, cooling rates for the most recent Andean exhumation phase are notably lower for the leeward side of the Tilcara Range than for the windward side. Models from the leeward side of the Tilcara Range show an onset of exhumation in the late Oligocene–middle Miocene (26–16 Ma) and two models show a decrease of cooling rates after 13 Ma. In contrast, the windward side of the Alonso transect shows an onset of exhumation between 21 to 11 Ma for TB3 and 22–15 Ma for TB4, with a decrease in cooling rate for TB3 around 7 Ma. Models from the San Lucas transect also show a decreasing rate around 7 Ma for TB3. Models from the Alonso, San Lucas and Las Animas transects all show a similar onset of cooling for TB3 (21–11 Ma, 22–10 Ma and 18–11 Ma, respectively). Although for the Alonso and Las Animas transect the onset of exhumation for TB3 and TB4 is rougly contemporaneous, models from the San Lucas transect show a younger onset between 10 and 8 Ma. The San Lucas transect models are considered more reliable, because the larger number of samples within this transect encompass a broader swath of stratigraphy and structure. Models for the far eastern part of TB4 (San Lucas transect) show an onset of exhumation between 6–4 Ma, younger than the decrease in exhumation rate in TB3 at approximately 7 Ma. This suggests that propagation of fault-related exhumation across the Tilcara Range Frontal Fault occurred in the latest Miocene–earliest Pliocene.

3.5 Discussion

3.5.1 Pre-Andean exhumation

Although the apatite low-temperature thermochronology is only able to show exhumation related to the Andean orogeny, ZHe samples have not received a sufficiently large overprint to erase earlier exhumation events. The majority of ZHe samples from TB1–TB4 record an early period of exhumation within the lower Cretaceous (140–115 Ma), showing an earlier onset than rift shoulder exhumation in the Brealito basin (130–80 Ma; Deeken et al., 2006), the Sierra de Quilmes (105–76 Ma; Carrapa et al., 2014) or at the Cumbres Calchaquíes (Sobel and Strecker, 2003) to the south. Stratigraphic relations of basal Salta Group units directly overlying basement show that Cambrian–Ordovician strata were at the surface during deposition of syn-rift strata. Farther north, the Salta Group overlies Jurassic, Carboniferous and Silurian–Devonian basement (e.g., Siks and Horton, 2011). Whereas the absence of Jurassic and Carboniferous strata in the Tilcara Range is related to the southern boundary of the Tarija basin, which was located along the Michicola arch north of the study area (Starck, 1995), the absence of Silurian–Devonian strata within the Tilcara Range and the San Lucas block shows a marked pre-rift exhumation gradient from north to south (Kley et al., 2005; Starck, 1995). Although the depositional age of the Salta Group was used as a constraint in many models, thus fixing the upper limit of pre-Cretaceous exhumation, several models show an upper limit of cooling in the Cretaceous, regardless of further post-depositional constraints, strongly suggesting a pre-rift exhumation of the Tilcara Range, which we link to to normal movement along NW–SE striking faults associated with Salta rift extension (see also Kley et al., 2005). These faults segment the basement uplifts of the Tilcara Range lithologically, but do not offset NNE–SSW striking reverse faults, indicating that these particular pre-existing faults might not have been activated during the most recent phase of the Andean orogeny. In contrast, there is evidence of major inverted normal faults within the Cianzo basin directly north of the study area, (Kley et al., 2005; Siks and Horton, 2011; Starck, 2011).

3.5.2 Andean uplift of the Tilcara Range

The Tilcara Range and the San Lucas block were buried by up to 4.5 kilometers of Neogene foreland strata (Siks and Horton, 2011), sourced from the Andean orogenic wedge to the west (DeCelles et al., 2011). However, this burial was not deep enough to reset the ZHe system; therefore, ZHe data from the Precambrian–Ordovician basement units are unable to document Andean exhumation. Fortunately, low-temperature apatite thermochronology is able to constrain the Miocene–Pliocene history of the Tilcara Range and the San Lucas block. Thermal modeling shows that exhumation of the leeward TB1–TB3 related to the propagation of the Andean wedge started in the late Oligocene–early Miocene (26–16 Ma; Figure 3.9). Multi-method models also provide a tentative upper constraint for rapid exhumation of TB1 between 13 and 12 Ma, presumably driven by fault activity. AHe cooling ages are not able to constrain the earliest phase of the exhumation, but record a decrease of the exhumation rate < 9 Ma, in the late Miocene. Although the latter is in agreement with data from Reynolds et al. (2000), constraining pronounced deformation within the Tilcara Range to 10–4 Ma, reconstructions of Henríquez et al. (2023) suggest shortening and exhumation within the Tilcara Range < 6.5 Ma. We propose an earlier onset of exhumation based on thermal modeling. Results from other studies, which propose a propagation of deformation from the Puna to the Eastern Cordillera in the late Eocene or early Oligocene (Coutand et al., 2001; Elger et al., 2005; Hongn et al., 2007), also indicate that an early Miocene onset of exhumation at the eastern border of the Eastern Cordillera is plausible.

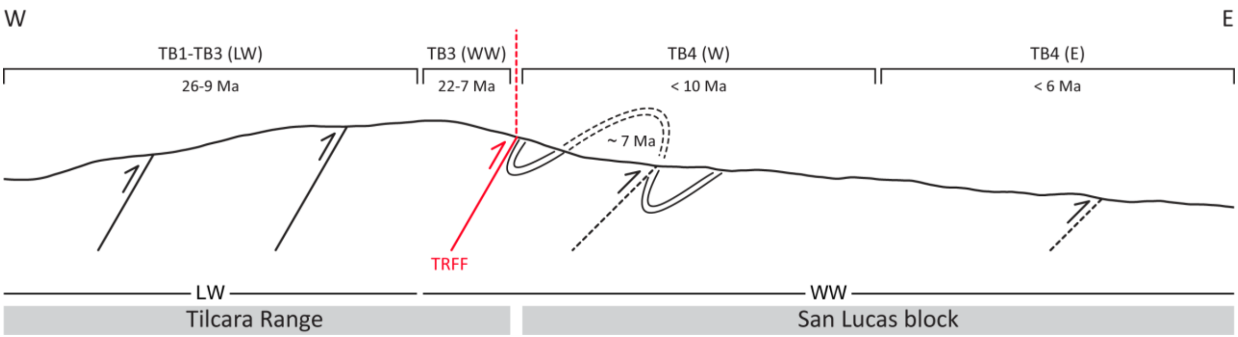

Figure 3.9 Schematic section showing the timeframe of rapid exhumation for different parts of the Tilcara Range and San Lucas block, inferred from thermal models. Tectonic blocks TB1–TB4, leeward (LW) and windward (WW) side of the Tilcara Range are marked. The Tilcara Range Frontal Fault (TRFF) is shown in red. Detachment(s) in the subsurface (see discussion) are not shown due to scaling issues.

At the windward side of the Tilcara Range, a general decrease of AHe cooling ages from west to east coincides with lower elevation toward the east and the transition from a high orographic barrier to the Andean foreland. AHe cooling ages in all transects show age-elevation relationships that persist across the Tilcara Range Frontal Fault and NNE–SSW striking intrablock faults. Thermal models for TB3 along all transects indicate a coeval onset of exhumation along-strike.

In general, the models suggest that the onset of exhumation for the windward side of the Tilcara Range occurs at a slightly later stage than for the leeward side (leeward: 26–16 Ma; windward: 22–10 Ma). This is in agreement with a systematic younging of cooling ages toward the east (Reiners et al., 2015), as well as an overall eastward propagation of deformation and uplift within the Puna and Eastern Cordillera (Carrapa et al., 2011; Deeken et al., 2006; Gubbels et al., 1993; Henríquez et al., 2023). Furthermore, many models show a decrease of exhumation at ~7 Ma, which might serve as an upper constraint for fault-related exhumation of TB3 (Figure 3.9). Although this disagrees with data from the central part of the Eastern Cordillera, showing that deformation within the Eastern Cordillera ceased at 9–10 Ma (Allmendinger and Zapata, 2000; Gubbels et al., 1993), other studies (Henríquez et al., 2023; Pingel et al., 2013; Reynolds et al., 2000; Reynolds et al., 2001; Siks and Horton, 2011) suggest that the easternmost border of the Eastern Cordillera was active also in the late Miocene. Rahl et al. (2018) attribute provenance changes in Neogene foreland basin sediments at 23°S to growing topography at the eastern border of the Eastern Cordillera. Similar to the results of Siks and Horton (2011) from the Cianzo basin, they find evidence for blocking of far western sediment sources through the uplift of mountain ranges bounding the Eastern Cordillera by the late Miocene, between 12 and 7 Ma. This is consistent with increasing sedimentation rates in the foreland strata by 9 Ma, because of orographic barrier uplift and increased localization of erosion at the orogenic front (Echavarría et al., 2003). Concurrently, average cooling rates for models at the leeward side of the Tilcara Range are notably lower than cooling rates for the windward side (6.0–6.6 °C/Ma leeward vs. 7.2–15.9 °C/Ma windward), also indicating more effective erosion at the wet side of the range and the establishment of an orographic barrier during the most recent phase of Andean exhumation in the Miocene–Pliocene. Although denudation rates determined from cosmogenic nuclides (^{10}Be from fluvial sands; Pingel et al., 2019) show a strong variation from 3 Ma, the thermal models show that the uplift of the Tilcara Range must have affected the erosional gradient pre-3 Ma.

3.5.3 Exhumation along the Tilcara Range Frontal Fault

The uplift and exhumation of TB1–TB3 was presumably driven by fault activity along the Tilcara Range Frontal Fault, which shows a major change in the structural elevation of the Tilcara Range and San Lucas block. Evidence of fault-related exhumation comes from a structural offset of approximately 400 m between the Pirgua Subgroup in TB3 and TB4, east of Alonso. Furthermore, ZHe cooling ages that are younger than the Salta rift-related exhumation phase show a consistent and pronounced offset across the Tilcara Range Frontal Fault in all transects with younger ages in the hanging wall. They indicate fault movement after ~50 Ma, coinciding with the stratigraphic and structural lower constraints, which are given by the youngest stratigraphic unit in its footwall. AFT ages record only a slight offset across the fault and we therefore propose that these ages document the final stages of fault activity along the Tilcara Range Frontal Fault. This is supported by the continuous AHe age-elevation trend across the Tilcara Range Frontal Fault, proving that fault activity mostly ceased before cooling through the APRZ at ≥ 7 Ma. We thus propose that the upper limit of fault activity along the Tilcara Range Frontal Fault coincides with the decrease in exhumation rate at approximately 7 Ma, and might also mark the propagation of fault activity to the east. Late Miocene–early Pliocene AFT cooling ages from the northern continuation of the Tilcara Range suggest that fault-related exhumation might continue < 7 Ma in parts of the range (Henríquez et al., 2023), although inherited Cretaceous normal faults could be responsible for a segmentation between the Tilcara Range and its northern counterpart. Furthermore, continued exhumation of upper thrust sheets might also be related to an inferred step-down of the basal décollement in the most recent (6.5–0 Ma) time step of Henríquez et al. (2022: their Figure 12). In any case, the propagation of exhumation in Argentina from the Eastern Cordillera to its foreland at 23.5°S occurred at a later stage than in Bolivia, where propagation from the Eastern Cordillera into the Interandean Zone happened after 30–25 Ma (Anderson et al., 2018; Ege et al., 2007; McQuarrie et al., 2008; Müller et al., 2002) and propagation from the Interandean Zone into the Subandean Zone occurred between ~11–8 Ma (Anderson et al., 2018).

3.5.4 Uplift of the San Lucas block

Thermal models from the San Lucas block imply an onset of exhumation between 10 and 8 Ma, slightly earlier than the proposed upper limit of fault activity along the Tilcara Range Frontal Fault. However, thermal models from the Alonso and Las Animas transects suggests that TB4 started exhuming earlier than TB3, indicating an out-of-sequence propagation of exhumation. The idea of in-sequence eastward propagation of the Andean thrust belt has recently been challenged (Del Papa et al., 2013; Montero-López et al., 2018; Payrola et al., 2020). Instead, it was proposed that deformation has been spatially widespread and disparate in a broken-foreland style (Del Papa et al., 2013; Montero-López et al., 2018). Pearson et al. (2013) suggest that, even though the Andean thrust belt overall propagated toward the east, every eastward pulse prompted a local westward migration of deformation. Out-of-sequence pulses have also been proposed in a very recent study by Henríquez et al. (2023). Our data also suggests that local out-of-sequence uplift of tectonic blocks is possible.

The continuous AHe age-elevation trend within TB4 indicates that internal faulting and folding has transpired before cooling of the samples through the APRZ at ≥ 7 Ma. The timing of deformation within the San Lucas block and final activity along the Tilcara Range Frontal Fault suggests that the competent Tilcara Range acted as a backstop, not dissimilar to the situation at the Eastern Cordillera and Inter-/Subandean Zone, close to the Bolivian border. In contrast, AFT and ZHe ages exhibit approximate age-stratigraphy relationships for TB4, indicating a timing of block-internal deformation during or after cooling through the APAZ. Since the youngest AFT cooling ages in TB4 are approximately 6–7 Ma, deformation within the westernmost San Lucas block occurred before the onset of rapid exhumation in the easternmost part of TB4, suggesting that deformation was still active in the west. Therefore, faulting and folding could have been coeval with the youngermost cooling through the APAZ.

Pleistocene AHe cooling ages within the easternmost part of the area show that TB4 was exhumed until very recently. Thermal models show an onset of cooling around 6–4 Ma, coinciding with a decrease of the exhumation rate in TB3, the upper limit of uplift for the Tilcara Range proposed by Reynolds et al. (2000) and recent AFT results from Henríquez et al. (2023). It is again evident that, along-strike to the north, exhumation occurred earlier than in corresponding morphotectonic provinces to the south. For example, the Bolivian Subandean Zone started exhuming < 12 Ma (Anderson et al., 2018; Uba et al., 2007; Uba et al., 2009) and the far eastern part of the Bolivian Subandean Zone shows late Miocene–Pliocene AHe ages (Anderson et al., 2018) that are similar to the San Lucas block ages. Similarly, exhumation in the Puna at 23–24°S and in the Bolivian Eastern Cordillera at 21°S was coeval (Anderson et al., 2017; Anderson et al., 2018; Elger et al., 2005; Henríquez et al., 2020; Henríquez et al., 2023; Müller et al., 2002). More recent Pliocene–Pleistocene exhumation of TB4 may be explained by uplift along underlying, potentially blind thrust faults that nucleate from a basal detachment. On the other hand, González and Tchilinguirian (2003) show inferred reverse or thrust faults cropping out east of the Calilegua National Park (Figure 3.1a). Along-strike to the north, these outcrops appear to coincide with the easternmost border of the Interandean Zone in Bolivia (Kley, 1996). Furthermore, close to the Calilegua National Park, a 2009 earthquake recorded thrust faulting in an ESE (104°) direction at the shallow depth of 5 km (Heidbach et al., 2016; Heidbach et al., 2018), suggesting that the thrusts driving exhumation of TB4 continue to be active.

3.5.5 Structural implications

East-vergent, high-angle reverse faults within Precambrian to Ordovician strata that segment the basement blocks of the Tilcara Range are associated with rotation of the blocks along a N–S oriented, (sub)horizontal axis, causing a tilting of the strata toward the west. The high-angle character of the faults suggests that these might be reactivated and possibly related to pre-existing structures from the Ocloyic phase, which also affect the present-day structure of the Eastern Cordillera (Alonso et al., 2012; Hongn et al., 2010a; Salfity and Marquillas, 1994; Starck et al., 1992). For example, in the westernmost part of the study area, retrodeformation of Andean east-vergent thrusting reveals Paleozoic east-vergent shortening in the Precambrian–Ordovician basement (Barrabino et al., 2015). Regional evidence of Paleozoic inherited structures is found e.g., west of the Quebrada de Humahuaca (Alonso et al., 2012; Mon et al., 1993; Seggiaro and Gallardo, 2002) and east of Salta (Seggiaro et al., 2014). In general, Paleozoic folding shows a higher amplitude and shorter wavelength than Andean deformation (see also Barrabino et al., 2015), which is highlighted by the angular unconformity between the Salta Group and previously folded Santa Victoria Group strata. Although many of the aforementioned Paleozoic structures relate to a convergent setting, an influence of early to middle Ordovician normal faulting has also been debated (see Figure 3.2c in this study and discussion in Seggiaro et al., 2017).

East of the Tilcara Range Frontal Fault, the San Lucas block shows close, in part overturned folds within the Cretaceous to Paleogene strata, forming east-vergent footwall synclines (Figure 3.2c). The amount of shortening decreases toward the east, as is evident from the increasing open fold geometry observed from Huairahuasi to San Lucas (see also Henríquez et al., 2023). Coinciding with the structural change from high-angle uplifts of deeper basement rocks within the Tilcara Range to a more fold-dominated style and lower-angle reverse faults within the San Lucas block is a marked exhumation gradient: the Salta Group overlies the deformed Santa Victoria Group sedimentary basement directly both west and east of the Tilcara Range, but the range itself is mainly built of the Precambrian–Cambrian Puncoviscana Fm and Mesón Group (see also González and Tchilinguirian, 2003; Salfity and Marquillas, 1994) with locally constricted, small outcrops of the Salta Group. The absence of syn-rift and foreland basin deposits within the Tilcara Range indicates that major exhumation has taken place after the establishment of an orographic barrier in the Andean phase. However, the sharp contacts between the Puncoviscana Fm and the Santa Victoria Group along NE–SW striking faults, which coincidentally form the local half-grabens in which the syn-rift deposits were shed, also suggest a high amount of pre-Cretaceous exhumation.

The structural elevation and lithological contrast between the Tilcara Range and the San Lucas block show similarities to the transition between the Eastern Cordillera and Interandean Zone in southern Bolivia (Kley, 1996), where the thick-skinned Eastern Cordillera fold-and-thrust belt exhibits high-angle, east-vergent basement faults that ultimately root in a detachment at 8–10 km depth (Kley, 1996). This shallow detachment level continues to the east, underneath the Interandean Zone (Allmendinger and Zapata, 2000; Kley, 1996). A frontal, high-angle reverse fault separates the Eastern Cordillera from the Interandean Zone, which at the surface shows characteristics of a thin-skinned fold-and-thrust belt but rides on top of a basement thrust sheet (Kley, 1996; McQuarrie, 2002). In NW Argentina, the detachment below the Puna and part of the Eastern Cordillera is located at a similar depth of ~10 km, ramping upwards to ultimately form the northern continuation of the Tilcara Range Frontal Fault at the surface (Henríquez et al., 2023). Based on all of the aforementioned, the Tilcara Range Frontal Fault and its apparent northern continuation, the Cianzo thrust (reverse fault) (Siks and Horton, 2011), may very well be the along-strike equivalent of the frontal reverse fault of the Sama-Yunchará anticlinorium (Figure 3.1a, SYA), forming the boundary of the Eastern Cordillera in Bolivia. However, toward the south, the Interandean Zone located east of the Sama-Yunchará anticlinorium increasingly disappears and structures east of the Tilcara Range are generally considered to belong to the Eastern Cordillera (see e.g., Henríquez et al., 2023).

Although thermochronological cooling ages from the San Lucas block and its northern continuation (Henríquez et al., 2023) are similar to the easternmost Subandean Zone of Bolivia, we cannot consider the San Lucas block to be the direct equivalent of the Subandean Zone from a structural point of view. The boundary between the Eastern Cordillera and Interandean Zone in Bolivia is marked by the transition at the basement-cover interface from competent Cambrian quartzite into incompetent Silurian shales (Anderson et al., 2018; Kley, 1996). Consequently, the main detachment level within the thin-skinned Subandean Zone (Dunn et al., 1995; Echavarría et al., 2003; Gubbels et al., 1993; Kley, 1996) is located within these Silurian shales, dipping gently (2–3°) toward the west (see e.g., Anderson et al., 2017; Echavarría et al., 2003; McQuarrie, 2002). The termination of thin-skinned deformation at 23°S, coinciding with the margin of the Lomas de Olmedo sub-basin, is attributed to the increased erosion of the Silurian–Devonian section toward the south (Starck, 1995) and the removal of these incompetent, potential detachment horizons (Kley and Monaldi, 2002), which are absent within the San Lucas block (Figure 3.2). Furthermore, although it was proposed that the Subandean detachment is located at depths of > 24 km beneath the Santa Barbara System (Allmendinger and Zapata, 2000), the slip recorded by earthquake focal mechanisms east of the study area (Figure 3.1a) cannot be related to this detachment, because it occurred at too shallow depth (Heidbach et al., 2016; Heidbach et al., 2018). Solving this problem is beyond the scope of this work, but previous studies have presented various solutions for the crustal structure of the Central Andes at this longitude. In one model, Cahill et al. (1992) propose an upward ramping of the detachment below the Santa Barbara System, based on seismicity patterns and focal mechanism solutions. In a more recent study, McFarland et al. (2017) infer a basal thrust belt detachment at approximately 15 km depth beneath the Eastern Cordillera, with a freely slipping portion to the west, showing no microseismicity, and a fully locked portion below the San Lucas block, showing microseismicity (data from Cahill et al., 1992). A very recent study by Henríquez et al. (2023) proposes a detachment at the base of the Ordovician strata, at ~10 km depth beneath the Puna, which reaches the surface as the along-strike continuation of the Tilcara Range Frontal Fault. They propose a second detachment beneath the northern continuation of the San Lucas block, located at ~18 km depth, but ramping upwards to shallower levels beneath the eastern part of the study area.

South of 23.5°S, the Subandean Zone is replaced by the thick-skinned Santa Barbara System, which is characterized by basement uplifts along pre-existing faults and sparse low-angle Tertiary faults (Kley and Monaldi, 2002). Based on the thickness of the Cambrian–Ordovician strata and the inferred high-angle (> 30°) geometry of block-internal faults, deformation of the San Lucas block also shows involvement of Precambrian–Cambrian, weakly metamorphosed basement rocks. However, footwall synclines within Tertiary strata, which are classically related to thrusting (McNaught and Mitra, 1993), and short-wavelength folds in general are more widespread. Furthermore, the main detachment level within a thick-skinned fold-and-thrust belt is generally at greater depth than recorded by the 2009 earthquake east of Calilegua (Pfiffner, 2017). Simple geometric extrapolation of a 5° west-dipping detachment located at 5 km depth below the Calilegua National Park toward the west shows that this detachment would be located at approximately 12 km depth below the Tilcara Range and the San Lucas block, similar to the depth of the Eastern Cordillera/Interandean Zone detachment in the Bolivian fold-and-thrust belt (Kley, 1996) and the detachment beneath the Eastern Cordillera and Puna in NW Argentina (Henríquez et al., 2023). Such a shallow detachment is able to invoke thrust faults, relatively low-angle reverse faults and short-wavelength folding at the surface. At the same time, a deeper detachment may be responsible for crustal thickening and propagation of deformation into the Andean foreland, but might also be able to influence exhumation in shallower crustal levels. Hybrid models showing a combination of thick- and thin-skinned deformation have been documented by e.g., Giambiagi et al. (2008; 2009) and Parker and Pearson (2021). To study their application to the Tilcara Range and San Lucas block, more detailed structural mapping and modeling, especially of the Santa Victoria Group and its relationship to the overlying Salta Group, is needed.

3.6 Conclusions

Thermal modeling within a structural context provides quantitative constraints on the deformation and exhumation history of the Tilcara Range and San Lucas block. Placed within a broader reference frame, the low-temperature AHe, AFT and ZHe data set imposes new constraints on the multi-phase exhumation history of the Eastern Cordillera in NW Argentina (Figure 3.9). We extract four key conclusions from our study:

1. Thermal models using ZHe single-grain ages record a cooling event between approximately 140 and 115 Ma, corresponding to pre-Salta Group exhumation of basement highs in the early stages of the Salta Rift. In particular, the lower limit is newly constrained by thermal models in this study.

2. Exhumation related to the Andean orogeny began in the latest Oligocene–early Miocene (26–16 Ma) at the westernmost border of the Tilcara Range and propagated toward the east, reaching the eastern part of the range in the early–middle Miocene (22–10 Ma), the western San Lucas block in the late Miocene (10–8 Ma) and the eastern San Lucas block in the early Pliocene (6–4 Ma). Individual thermal models indicate out-of-sequence deformation at a local scale, although at a larger scale, deformation appears to occur in-sequence.

3. The Tilcara Range Frontal Fault forms the structural boundary between the thick-skinned Tilcara Range and the San Lucas block, which is characterized by short-wavelength folds and lower-angle reverse faults. Thermal models indicate that rapid exhumation of the easternmost Tilcara Range began in the early Neogene and ended around 7 Ma. AHe cooling ages show continuous age-elevation relationships across the Tilcara Range Frontal Fault, confirming that major fault-related exhumation ceased in the late Miocene (≥ 7 Ma) and rapid exhumation in the western San Lucas block began coevally.

4. Internal faulting and folding of the San Lucas block predates final fault-related exhumation at the Tilcara Range Frontal Fault and disturbs age-elevation relationships between ZHe and AFT samples. Thermochronologically, the San Lucas block is the equivalent of the Subandean Zone, with cooling ages showing that its western part started exhuming in the late Miocene (10–8 Ma), while its eastern part started exhuming in the late Miocene–early Pliocene (5–4 Ma). Recent earthquake focal mechanisms show that faults east of Valle Grande, which may drive exhumation of the San Lucas block, have been active recently.

Chapter 4. Structural inheritance in the Eastern Cordillera, NW Argentina: Low-temperature thermochronology of the Cianzo Basin

This chapter is currently under review for Tectonics, by W. S. M. T. van Kooten, M. Vallati, E. R. Sobel, C. E. del Papa, P. Payrola, D. Starck, A. Bande, M. F. Wayar Córdoba, A. T. Lapiana and J. Glodny.

Abstract

The present-day deformation style of the Eastern Cordillera in NW Argentina is strongly influenced by the inversion of pre-existing Paleozoic and Mesozoic structures. In particular, the basin-bounding normal faults and lithologic contrasts from the Cretaceous–Paleogene Salta Rift phase form heterogeneities that were preferentially reactivated during the Andean orogeny. Constraining the timing and characteristics of reactivation is a key to understanding the interplay between tectonics and inherited crustal anisotropies. In this study, we combine structural and sedimentological field observations with a low-temperature thermochronology data set from the area surrounding the Cianzo basin. The southeastern basin boundary is formed by the inverted Hornocal fault, which was the basin-bounding normal fault of the Lomas de Olmedo sub-basin. Lacustrine deposits of the Yacoraite Formation overspill on the footwall of this fault and mark the post-rift phase. Apatite (U-Th-Sm)/He and fission track ages from the Cianzo syncline in its hanging wall show an onset of rapid exhumation related to fault inversion between the late Oligocene and Miocene (24–15 Ma). Structural relationships between thermochronology cooling ages, sampling elevation and stratigraphic position constrain the timing of major folding in the eastern limb of the Cianzo syncline to the middle Miocene, whereas the western limb did not start tilting before the upper Miocene. Quantification of fault-related exhumation patterns surrounding the Cianzo basin emphasizes the influence of the pre-existing structural framework on deformation in fold-and-thrust belts.

4.1 Introduction

Inherited heterogeneities greatly affect the localization, style and dimension of deformation during the structural development of an orogen (Butler et al., 2006). Inversional structures are known from many mountain chains, including the Alps (e.g., Boutoux et al., 2014; Coward et al., 1991; Zerlauth et al., 2014), the Apennine (Di Domenica et al., 2012; Scisciani, 2009) and the High Atlas (Beauchamp et al., 1999; Teixell et al., 2003). In the case of the Argentinian Andes, its structural framework holds a key to understanding the many phases of deformation that have affected Earth's longest mountain range. One of the most influential pre-Andean phases of deformation is the formation of the Salta Rift basin in the Cretaceous, which covered large parts of the present-day Eastern Cordillera of NW Argentina (Marquillas et al., 2005; Salfity, 1994) and southern Bolivia (Martinez et al., 1995). Its multiple sub-basins (Figure 4.1a), bounded by normal faults and filled with the km-thick Salta Group sedimentary sequence, provide crustal heterogeneities, which are reactivated and inverted during Andean orogeny (e.g., Grier et al., 1991; Hongn et al., 2010a; Kley et al., 2005; Starck, 1995). The structural and stratigrahic framework of the Salta Rift sub-basins is also of economic interest: the carbonate and clastic rocks of the Yacoraite Formation (post-rift Salta Group; Moreno, 1970) are well known in Argentina for their economic importance and the stunning outcrops in Salta and Jujuy provinces. The unit is both the main source rock of the Lomas de Olmedo sub-basin and one of the main reservoir rocks. Hydrocarbon production reached its peak during the 70–80s and nowadays has a marginal contribution. Moreover, the basin is in exploratory maturity stage, with more than 90 % of the reserves already produced (Starck, 2011).

The Cianzo basin in NW Argentina is a prominent example of an Andean basin bound in part by pre-Andean faults. Its geometry is largely controlled by an inherited Cretaceous normal fault, which was inverted during the Andean orogeny. The availability of 1) suitable lithologies for low-temperature thermochronology, 2) major elevation gradients, and 3) changes in structural elevation since the Cretaceous make the Cianzo basin and its surrounding ranges an excellent natural laboratory to examine the reactivation of pre-existing heterogeneities in the context of Andean shortening. In this study, we investigate the northern margin of the Lomas de Olmedo sub-basin (Salta Rift basin; Figure 4.1a). We use the case of the Cianzo basin as an example for inversion processes that play a key role in the timing and distribution of exhumation during the Andean orogeny. Our new model is based on 28 apatite fission track samples, 146 apatite (U-Th-Sm)/He and 57 zircon (U-Th-Sm)/He aliquots, and describes the evolution of the Lomas de Olmedo sub-basin margin, from its initial Mesozoic formation to its Cenozoic inversion.

4.2 Geological overview

4.2.1 Tectonic setting

The Eastern Cordillera of the Central Andes is an approximately N–S striking morphotectonic province that is bordered to the west by the Puna (in the south) and Altiplano Plateau (in the north) and, to the east, the Inter- and Subandean Zone. Whereas the latter is a prime example of a thin-skinned fold-and-thrust belt (e.g., Dunn et al., 1995; Echavarría et al., 2003; Eichelberger et al., 2013; McQuarrie, 2002) that is facilitated by a gently-dipping (2–3°) main detachment level in relatively weak Silurian–Devonian shales (Anderson et al., 2017; Echavarría et al., 2003; McQuarrie, 2002), the predominantly thick-skinned style of deformation of the Eastern Cordillera is governed by pre-existing heterogeneities from Paleozoic and Mesozoic tectonic events (e.g., Carrera et al., 2006; Grier et al., 1991; Kley et al., 2005; Kley and Monaldi, 2002; Kortyna et al., 2019; McGroder et al., 2015). Evidence of these earlier phases can be found in unconformities between folded Paleozoic strata and overlying rift-related sediments, high-angle reverse faults and normal faults that have been inverted during the propagation of the Andean orogenic wedge (Kley et al., 2005; Kley and Monaldi, 2002). Precambrian and Paleozoic structural inheritance is also seen in many locations along the Andean orocline (e.g., Carrera and Muñoz, 2013; Giambiagi et al., 2014; Hongn et al., 2010a; Perez et al., 2016).

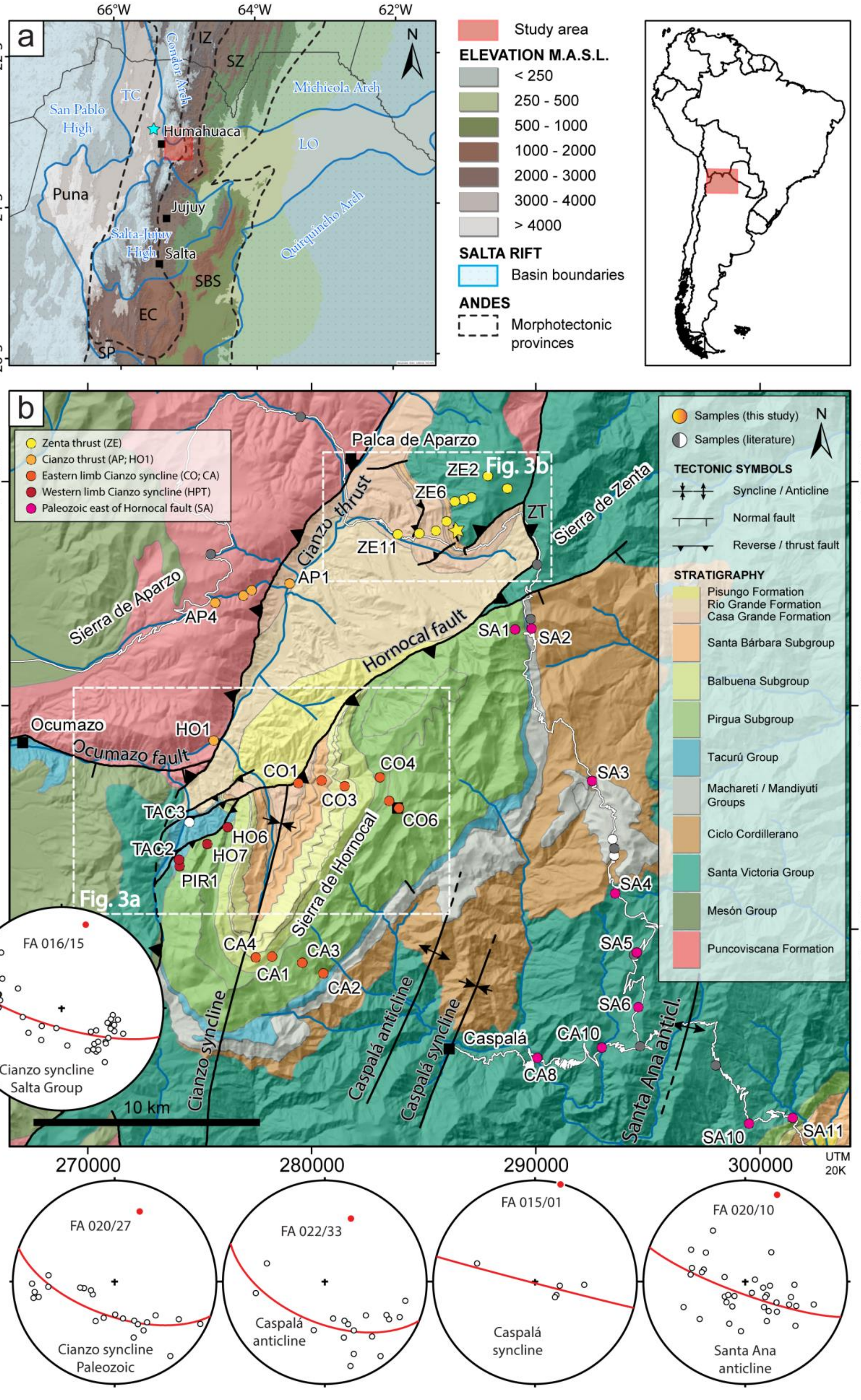
a
b
Study area
ELEVATION M.A.S.L.
SALTA RIFT
Basin boundaries
ANDES
Morphotectonic provinces
Samples (this study)
Samples (literature)
TECTONIC SYMBOLS
Syncline / Anticline
Normal fault
Reverse / thrust fault
STRATIGRAPHY
Pisungo Formation
Rio Grande Formation
Casa Grande Formation
Santa Bárbara Subgroup
Balbuena Subgroup
Pirgua Subgroup
Tacurú Group
Macharetí / Mandiyutí Groups
Ciclo Cordillerano
Santa Victoria Group
Mesón Group
Puncoviscana Formation
Zenta thrust (ZE)
Cianzo thrust (AP; HO1)
Eastern limb Cianzo syncline (CO; CA)
Western limb Cianzo syncline (HPT)
Paleozoic east of Hornocal fault (SA)
Palca de Aparzo
Cianzo thrust
Hornocal fault
Sierra de Aparzo
Sierra de Zenta
Sierra de Hornocal
Ocumazo fault
Cianzo syncline
Caspalá anticline
Caspalá syncline
Santa Ana anticl.
Caspalá
Fig. 3a
Fig. 3b
10 km
UTM 20K
FA 016/15
Cianzo syncline Salta Group
FA 020/27
Cianzo syncline Paleozoic
FA 022/33
Caspalá anticline
FA 015/01
Caspalá syncline
FA 020/10
Santa Ana anticline

Figure 4.1 (a) Overview map of the Salta Rift basin showing location of highs and basin boundaries from Salfity and Marquillas (1994). The Lomas de Olmedo (LO) and Tres Cruces (TC) depocenters are marked. Blue star marks the location of the Sapagua half-graben. Dashed lines outline morphotectonic provinces (IZ: Interandean Zone; SZ: Subandean Zone; EC: Eastern Cordillera; SBS: Santa Barbara System; SP: Sierras Pampeanas). Red rectangle marks location of b. (b) Geologic map of the Cianzo basin and Hornocal fault hanging wall. Sample colors show association with different modeling sections (see legend in upper left corner and Section 4.4.2). Yellow star marks location of measured Yacoraite section (Section 4.4.1). Grey and white samples are from Henríquez et al. (2023) and Reiners et al. (2015), respectively. Insets show locations of Figure 4.3a–b. The map is based on own field data and existing data of Kocks (1999), González and Tchilinguirian (2003), Kley et al. (2005), Siks and Horton (2011) and Starck (2011).

In the Mesozoic, the opening of the Atlantic Ocean caused far-reaching extension in the South-American plate. As a result, the Salta Rift formed a major extensional basin in present-day NW Argentina, Chile, Bolivia and Paraguay, consisting of several sub-basins radiating from the central Salta-Jujuy high (Figure 4.1a). The Tres Cruces and Lomas de Olmedo sub-basins form the northern arms of the Salta Rift basin and are bounded by the Condor, Michicola and Quirquincho arches. The Cerro Hermoso depocenter formed an individual basin in the early stages (Salfity and Marquillas, 1994), but was later integrated into the Lomas de Olmedo sub-basin. Rift shoulder exhumation (Deeken et al., 2006; Zapata et al., 2019a) and deposition of clastic strata related to nearby fault activity (Van Kooten et al., 2022a) in NW Argentina is suggested to have started in the Jurassic. Syn- and post-rift sediments of the Salta Group (Boll et al., 1989; Marquillas et al., 2005; Moreno, 1970; Reyes and Salfity, 1973; Salfity and Marquillas, 1994) were deposited during the Cretaceous–Paleogene and show evidence of normal fault activity in the Paleogene post-rift succession (Starck, 2011: his Figure 5).

Uplift and exhumation during the Andean orogeny has changed the structural elevation of Salta Group strata within the Eastern Cordillera. Pre-Andean inverted and non-inverted normal faults (Kley et al., 2005; Kley and Monaldi, 2002; Monaldi et al., 2008) are now located at 3–5 km above sealevel. A prominent example of an inverted normal fault is the SW–NE striking Hornocal fault (Amengual and Zanettini, 1973; Kley et al., 2005; Siks and Horton, 2011), which bounds the Cianzo basin to the SE (Figure 4.1b). Across the Hornocal fault, the Salta Group thickness changes: its hanging wall shows > 2000 m of syn-rift strata (McBride, 2008), whereas the footwall only shows a condensed post-rift succession (Kocks, 1999; Siks and Horton, 2011), characteristic of an extensional basin-bounding fault (Horton and Folguera, 2022). The Cianzo syncline (Figure 4.1b) occurs in the hanging wall of the Hornocal fault (Amengual and Zanettini, 1973). The Zenta thrust (Figure 4.1b) bounds the Cianzo basin to the NE (e.g., Kley et al., 2005; Kocks, 1999; Siks and Horton, 2011). The east-vergent Cianzo “thrust” (i.e., Cianzo reverse fault, designation “thrust” from literature; e.g., Kley et al., 2005) bounds the basin to the west. Both faults emplaced Paleozoic rocks onto the Eocene–Miocene basin infill. Although the high-angle character of the Cianzo thrust was recognized early on (Amengual and Zanettini, 1973), there is no conclusive evidence that it is a reactivated structure. It roots in a detachment at ~10 km depth beneath the Eastern Cordillera, whereas the NW-vergent Hornocal fault connects to the east with east-vergent faults that root in a detachment at ~18 km depth (Henríquez et al., 2023).

Andean shortening has a two-stage history in the Eastern Cordillera, with an earlier ESE-WNW oriented thrust regime, and a more recent NE-SW oriented thrust regime since ~4 Ma (Allmendinger, 1986; Marrett et al., 1994; Marrett and Strecker, 2000). Fault kinematic analyses and fold axes orientations show that Neogene shortening directions in the southern Central Andes are rotated clockwise by ~40° compared to the general plate convergence direction (Marrett et al., 1994). However, the present-day velocity field and the velocity fields of the past 25 Ma, as derived from geological data, are similar in magnitude and direction (Hindle et al., 2002; Kley, 1999; Lamb, 2001), which seems to contradict a rotation of the shortening direction. The Andean thrust front was located within the Puna plateau between 45–25 Ma. It then moved to the Eastern Cordillera in the late Eocene–early Oligocene (Coutand et al., 2001; Elger et al., 2005; Hongn et al., 2007) with active uplift of the Sierra Alta around 25–20 Ma (Henríquez et al., 2023). Other authors date pronounced uplift of the Sierra Aguilar to ~24–17 Ma and Sierra Alta to 15 Ma (Deeken et al., 2006; Pingel et al., 2013).

North of 22°S, major deformation in the western Eastern Cordillera ceased at 9–10 Ma, based on undeformed strata that overlie folded Miocene sediments above a geomorphic surface (Allmendinger and Zapata, 2000; Gubbels et al., 1993). To the south, the Sierra Alta shows increased uplift rates during the Pliocene–Pleistocene (Streit et al., 2017). The Andean thrust front moved to the east of the Humahuaca valley by at least 15–10 Ma (Henríquez et al., 2023; Pingel et al., 2013; Pingel et al., 2014; Siks and Horton, 2011). Inversion of the Hornocal fault is proposed to have commenced in the middle to late Miocene (Henríquez et al., 2023; Lapiana, 2021; Siks and Horton, 2011), based on growth strata in upper Miocene syntectonic deposits (Siks and Horton, 2011). Propagation of the thrust front and exhumation of the ranges east of the Cianzo basin occurred after ~6.5 Ma (Henríquez et al., 2023). Pliocene and Pleistocene AHe cooling ages in the easternmost part of the Eastern Cordillera (Van Kooten et al., 2022b) and recent earthquake focal mechanisms (Heidbach et al., 2018) show that shortening and exhumation are ongoing in this part of the Central Andes.

4.2.2 Stratigraphic framework

The Ediacarian–early Cambrian (e.g., Adams et al., 2011; Aparicio González et al., 2014; Lork et al., 1990) Puncoviscana Formation (Fm; Figure 4.2) forms the low-grade metamorphic basement of the Central Andes and crops out in a narrow N–S striking band within the Puna and Eastern Cordillera. It consists of green to purple metamorphosed sandstones, siltstones and claystones with a thickness > 2000 m, which were deposited as submarine fans (Aceñolaza, 2003). K-Ar ages show evidence of two metamorphic events at 535–540 Ma and 565–568 Ma (Adams et al., 1990), caused by the collision of the Arequipa-Antofalla block and the Córdoba or Pampia terrane (Escayola et al., 2011; Ramos et al., 2010). The middle–late Cambrian Mesón Group (Figure 4.2) succeeds the Puncoviscana Fm. It consists of conglomerates, sandstones/quartzites and shales that were deposited in a shallow marine environment over the strongly angular Tilcaric unconformity (Aceñolaza, 2003; Moya, 1998; Sanchéz and Salfity, 1999) and can reach a thickness of up to 3000 m. Cambrian magmatism constrains the base of the Mesón Group to approximately 526 ± 2 Ma (Tastil Batholith: Hongn et al., 2001a; Hongn et al., 2001b) and its detrital zircon U-Pb maximum depositional age is between 524.8 ± 4.1 and

502 ± 4 Ma (Adams et al., 2011; Aparicio González et al., 2014; Augustsson et al., 2011; Franceschinis et al., 2020a).

The upper Cambrian to lower Ordovician (Buatois et al., 2006; Zeballo and Tortello, 2005) Santa Victoria Group (Figure 4.2) overlies the Mesón Group and consists of alternating shales, sandstones and local volcaniclastic rocks, deposited in a marine environment. Late Ordovician–Devonian strata of the Ciclo Cordillerano (Figure 4.2) (Starck, 1995) overlie the Santa Victoria Group with an angular unconformity (Amengual and Zanettini, 1973). These units consist of cyclical alternations of shales and sandstones deposited in intracratonic basins, which were inverted during the Late Devonian–Early Carboniferous (Starck, 1995). The strata reach a combined thickness of 1132 m in the Hornocal region (Starck, 1995). Depositional ages range from the Late Ordovician (Monaldi & Boso, 1987) to the middle Devonian (Baldis et al., 1976; Noetinger et al., 2016). The Macharetí, Mandiyutí, and Tacurú Groups (Figure 4.2) overlie the Ciclo Cordillerano units with a low-angle unconformity. The decreasing thickness of these strata toward the SW from > 800 m to ~200 m is attributed to the geometry of the original Paleozoic Tarija basin (Starck, 1995, 2008). The Pennsylvanian (Aráoz et al., 2016; Di Pasquo, 2013; Di Pasquo and Azcuy, 1999) Macharetí and Mandiyutí Groups are separated by unconformities. Both groups contain braided fluvial and deltaic or subaqueous sediments, as well as glacigenic and postglacial diamictites (Starck, 1995; Starck and Del Papa, 2006).

The Tacurú Group overlies the Santa Victoria Group (Ordovician) in the west and the Mandiyutí Group (Carboniferous) in the east of the Cianzo syncline. The unconformity in between has an angular character (~37–40°; Starck, 2008; Van Kooten et al., 2022a). In the Cianzo area, the Tacurú Group consists of eolian sandstones, which have been correlated with upper Jurassic strata in Bolivia (Sempere, 1995; Starck, 2008; Tomezzoli, 1996). The strata have a thickness of up to 400 m in the eastern limb of the Cianzo syncline (Starck, 2008). Locally, the eolian facies inter-finger with the proximal Ocumazo conglomerate, which is a poorly sorted, angular to sub-angular conglomerate that is attributed to early extensional movement and fault formation in NW Argen-tina (Starck, 2008; Van Kooten et al., 2022a). The Ocumazo conglomerate has a Middle Jurassic detrital zircon maximum depositional age (McBride, 2008; Van Kooten et al., 2022a). In the Cianzo area, the Tacurú Group forms an intermediate succession between Paleozoic sedimentary units and the overlying Salta Group that is unique in the Eastern Cordillera. To the west, east and south of the Cianzo area, the Salta Group directly overlies Precambrian to Devonian strata.

The Salta Group (Turner, 1959) was deposited onto Precambrian to Jurassic strata. In the north-eastern part of the Salta Rift basin, the Salta Group succession reaches over 5 km in thickness (Boll et al., 1989). It is divided into the Pirgua, Balbuena and Santa Barbara subgroups (Figure 4.2) based on the tectono-stratigraphic evolution (Moreno, 1970). The syn-rift Pirgua Subgroup forms the lower part (Reyes and Salfity, 1973) and largely consists of clastic redbeds with variable thickness, depending on the proximity to the controlling normal faults. In the Cianzo syncline, the thickness varies from approximately 2150 m in the west (McBride, 2008) to > 2500 m in the southeast (Boll et al., 1989). Here, the Pirgua Subgroup follows a typical rift-filling sequence, with a basal unit composed of clast-supported conglomerates with gravel- to cobble-sized subangular to rounded clasts sourced from the Mesón Group, as well as more distal volcanic and magmatic sources (Van Kooten et al., 2022a). Massive to cross-bedded red sandstones overlie the basal conglomerate and make up the majority of the Pirgua Subgroup (Figure 4.2). The middle part is characterized by dark red siltstones that are alternated and intercalated with sandstones, and become progressively more abundant upwards. The upper part consists of massive sandstones with carbonate nodules (rhizoliths), paleosols and burrows (see also McBride, 2008).

The Pirgua Subgroup in the Lomas de Olmedo sub-basin is divided into two tectonosedimentary units (Boll et al., 1989). Its depositional age is estimated from four volcanic episodes: in the southern and central sub-basins of the Salta Rift basin, the Alto de las Salinas volcanism (128–112 Ma; K-Ar, whole rock; Bossi and Wampler, 1969), the Isonza basalt (96 ± 5 to 99 ± 5 Ma; K-Ar, whole rock; Valencio et al., 1976) and the Las Conchas basalt (78 ± 5 Ma and 76.4 ± 3.5 Ma; Reyes et al., 1976; Valencio et al., 1976) show Cretaceous ages. The upper Cretaceous (70 ± 5 Ma, K-Ar; Gómez Omil et al., 1989) Palmar Largo volcanic complex in the Lomas de Olmedo sub-basin is stratigraphically located at the top of the Pirgua Subgroup and is intercalated with the overlying Balbuena Subgroup. Deposition of the Pirgua Subgroup was predominantly controlled by tectonic activity, expressed by active rifting and extension along half-grabens, as suggested by the marked variability of thickness of the sedimentary units. Normal fault activity continued up to the Paleocene (see seismic section in Starck, 2011).

The post-rift succession of the Salta Group consists of the mixed carbonate-siliclastic Balbuena Subgroup (Figure 4.2) and siliciclastic-dominated fluvial-lacustrine Santa Barbara Subgroup (Moreno, 1970). The Balbuena Subgroup is subdivided into the Lecho, Yacoraite and Olmedo formations. The Lecho Fm is predominanly composed of well-sorted, cross-bedded aeolian to fluvial sandstones. The Yacoraite Fm is a mixed carbonate-siliciclastic succession, characterized by prevalent carbonate-dominated facies such as oolitic-bioclastic grainstones-packstones and frequent stromatolite levels (Deschamps et al., 2020; Marquillas et al., 2005). In the Lomas de Olmedo sub-basin, it forms both the main hydrocarbon source rock and one of the main reservoir rocks. Reservoir facies correspond to naturally fractured limestone, intercalated sandstone intervals and limestone with primary and secondary porosity (Disalvo et al., 2002). There is no consensus on the depositional environment of the Yacoraite Fm, although more recent studies propose a lacustrine, rather than a marine environment (e.g., Deschamps et al., 2020; Gomes et al., 2020). The Olmedo Fm is represented in parts of the Lomas de Olmedo sub-basin by black and grey to greenish shales and siltstones representing mudflats deposited in an hypersaline lacustrine environment (Gómez Omil et al., 1989; Marquillas et al., 2005). In the Cianzo syncline all three formations of the Balbuena Subgroup are present and show an overall thickness of > 285.5 m (Boll et al., 1989). In the footwall of the Hornocal fault, only the Yacoraite Fm is present with a highly reduced thickness when compared to an average 150–200 meters measured in other sections in the Tres Cruces and Lomas de Olmedo sub-basins (Kocks, 1999; Marquillas et al., 2005). The overlying Santa Barbara Subgroup is subdivided into the Mealla, Maíz Gordo and Lumbrera Fms (Del Papa, 1999; Del Papa and Quattrocchio, 2002; Del Papa and Salfity, 1999; Hernández et al., 2008; Starck, 2011). The Mealla Fm is represented by a package of dark red to purple and pinkish-white medium- to coarse-grained sandstones, locally intercalated with conglomerates at the base. The Maíz Gordo Fm consists of medium- to coarse-grained, well-channelized reddish-grey sandstones. The Lumbrera Fm mainly consists of bright red, thick mudstones with thin levels of fine-grained sandstones intercalated with thick, white, fine- to medium-grained sandstones. Within the footwall of the Hornocal fault, the Santa Barbara succession is characterized by superimposed paleosol horizons rich in carbonate nodules, root-traces and bioturbation features indicating low rates of deposition. This paleosol package could be equivalent to the "supersol zone" identified in the Cianzo syncline by DeCelles et al. (2011). Within the footwall of the Hornocal fault, the Santa Barbara Subgroup shows a reduced thickness of approximately 200 m (Kocks, 1999), although a later study reported a thickness of approximately 400 m (Siks and Horton, 2011), which correlates more closely with the increased thickness of the Santa Barbara Subgroup in the Cianzo syncline (Section 4.1). The post-rift succession was mainly accommodated by thermal subsidence (Marquillas et al., 2005; Viramonte et al., 1999). However, the wide distribution of the Santa Barbara Subgroup, local conglomerate intercalations and a general NE paleoflow also suggest early flexural loading (Becker et al., 2015) and sediment deposition from the Andean orogenic wedge in the late Paleocene–Eocene (DeCelles et al., 2011). Some authors propose that the middle Eocene upper Lumbrera Fm already shows a foreland basin signature, as opposed to the syn-rift signature of the lower Lumbrera, Maíz Gordo and Mealla Fm (Del Papa et al., 2010; Starck and Vergani, 1996).

The onset of Andean shortening and uplift in the Puna and Eastern Cordillera during the late Eocene–early Oligocene (e.g., Coutand et al., 2001; DeCelles et al., 2007; Henríquez et al., 2020) terminated the post-rift thermal subsidence-controlled deposition of the Salta Group. In the Andean foreland basin, the upper Eocene–upper Miocene Orán Group (Boll and Hernández, 1986; Salfity and Marquillas, 1994) overlies the Salta Group sediments and shows an increasingly proximal signature with respect to the approaching Andean wedge. Siks and Horton (2011) divide Orán Group-equivalent strata in the Cianzo basin into the Casa Grande, Río Grande (Metán Subgroup) and Pisungo formations (Jujuy Subgroup), following the division of the Tres Cruces sub-basin to the west. The Casa Grande Fm consists of bright red claystones, siltstones and fine-grained sandstones with a thickness of 1400 m (Siks and Horton, 2011). The overlying Río Grande Fm consists of > 3000 m of fine- to coarse-grained massive and cross-bedded sandstones with intercalated claystones and clast-supported pebble conglomerates (Siks and Horton, 2011). The Pisungo Fm represents the youngest sedimentary cover in the Cianzo basin. It consists of clast- and matrix-supported, pebble to boulder conglomerates that are part of the syn-tectonic sedimentary succession directly related to the Hornocal fault inversion (Siks and Horton, 2011). The lower unit was deposited in a widespread foreland basin (Coutand et al., 2001; DeCelles et al., 2011). The upper units show an overall coarsening-upward trend and increasingly proximal sediment sources, documenting the approaching Andean orogenic wedge. In that context, depocenters became partially or fully isolated from the late Oligocene–late Miocene (Becker et al., 2015; Siks and Horton, 2011). Some studies conclude that the upper Miocene to Quaternary strata may also represent wedge-top accumulations from a regional, connected foreland basin prior to formation of a broken foreland (e.g., Carrapa et al., 2012; DeCelles et al., 2011).

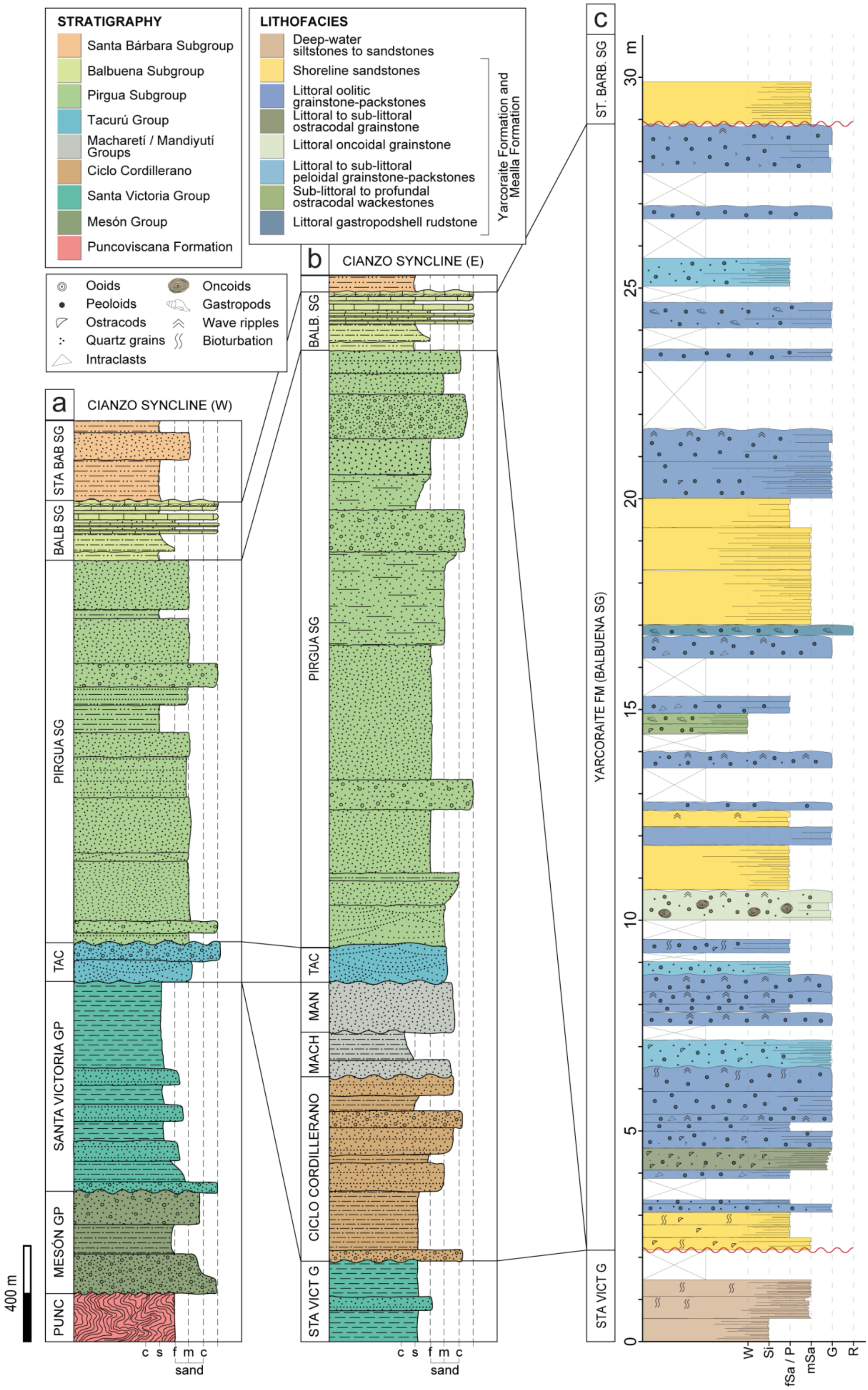

STRATIGRAPHY
Santa Bárbara Subgroup
Balbuena Subgroup
Pirgua Subgroup
Tacurú Group
Macharetí / Mandiyutí Groups
Ciclo Cordillerano
Santa Victoria Group
Mesón Group
Puncoviscana Formation
LITHOFACIES
Deep-water siltstones to sandstones
Shoreline sandstones
Littoral oolitic grainstone-packstones
Littoral to sub-littoral ostracodal grainstone
Littoral oncoidal grainstone
Littoral to sub-littoral peloidal grainstone-packstones
Sub-littoral to profundal ostracodal wackestones
Littoral gastropodshell rudstone
Yarcoraite Formation and Mealla Formation
Ooids
Peloids
Ostracods
Quartz grains
Intraclasts
Oncoids
Gastropods
Wave ripples
Bioturbation
a
CIANZO SYNCLINE (W)
STA BAB SG
BALB SG
PIRGUA SG
TAC
SANTA VICTORIA GP
MESÓN GP
PUNC
400 m
c s f m c
sand
b
CIANZO SYNCLINE (E)
BALB. SG
PIRGUA SG
TAC
MAN
MACH
CICLO CORDILLERANO
STA VICT G
c s f m c
sand
c
ST. BARB. SG
YARCORAITE FM (BALBUENA SG)
STA VICT G
m
30
25
20
15
10
5
0
W
Si
fSa / P
mSa
G
R

Figure 4.2 Proterozoic–Paleocene stratigraphy of (a) the western and (b) eastern limb of the Cianzo syncline (Hornocal fault hanging wall), and (c) the Hornocal fault footwall (measured section in Zenta range). Compiled from Moya (1988), Boll et al. (1989), Starck (1995), Sanchéz and Salfity (1999) and McBride (2008).

4.3 Methodology

4.3.1 Structural and sedimentological fieldwork

This study is based on structural observations and sedimentological fieldwork in the Cianzo area (Province of Jujuy, Argentina; Figure 4.1b), where we measured a high-resolution stratigraphic log. The section was measured at the centimeter-scale. Carbonate facies were classified according to the revised classification of Dunham (1962) and clastic strata were classified based on the Udden-Wentworth grain-size scale (Udden, 1914; Wentworth, 1922).

4.3.2 Single-grain (U-Th-Sm)/He thermochronology

Natural decay of U, Th and Sm isotopes leads to the production of ^{4}He atoms (α particles), which are retained within apatite and zircon at low temperatures and lost by diffusion at higher temperatures (e.g., Farley, 2002). Low-temperature (U-Th-Sm)/He thermochronology utilizes this natural phenomenon to obtain cooling ages of apatite and zircon crystals, which give information about burial and exhumation processes at upper crustal levels. Within the temperature interval of the partial retention zone, "helium is neither quantitatively retained nor lost by diffusion" (Wolf et al., 1998, p. 105). The apatite partial retention zone (APRZ) is located approximately between 40 and 80 °C (Wolf et al., 1998) with a typical closure temperature (T_c) of ~68 °C (Farley, 2000), whereas the zircon partial retention zone (ZPRZ) is located approximately between 170 and 190 °C with an experimental T_c of 183 °C (Reiners et al., 2004). The exact temperature interval of the APRZ and ZPRZ depends on cooling rate and kinetic characteristics of the sample, such as radiation damage and grain size. Crystals that are analyzed for apatite (AHe) or zircon (ZHe) (U-Th-Sm)/He thermochronology are ideally euhedral, free of inclusions, fractures and zoning, and have a diameter > 60 µm. We carefully selected aliquots without visible inclusions and/or fractures from 36 samples of Precambrian to Miocene rocks using a binocular polarizing microscope. Many samples contained detrital grains with a rounded geometry and frosted surfaces, which may hide small inclusions and hairline fractures within the grain, and could potentially cause age dispersion. We recorded grain dimensions (width, prism length, total length) and the number of terminations for calculation of the alpha-ejection correction factor F_T (Farley et al., 1996; Ketcham et al., 2011). The aliquots were packed in Pt or Nb tubes (for apatite and zircon, respectively) and degassed at the University of Potsdam using the Australian Scientific Instruments (ASI) Alphachron He extraction and analysis system. Analysis of U, Th and Sm abundances by isotope dilution was conducted at GFZ Potsdam. For detailed analytical data and procedures see Zhou et al. (2016) and Galetto et al. (2021). (U-Th-Sm)/He age calculation follows the equations in Meesters and Dunai (2005). Cooling ages are reported with a weighted 2σ error calculated using the relative contribution of each parent isotope to the total He production.

Table 4.1 Apatite and zircon (U-Th-Sm)/He cooling ages.

Apatite (U-Th-Sm)/He data							
Sample	Aliquots[a]	Stratigraphic unit	UTM E[b]	UTM N[b]	Z (m)	WM (Ma)[c]	SE (Ma)[d]
AP1†	2	PRC	278998	7435444	3487	10.6	1.7
CA1	2	UPI	278228	7418767	4414	6.8	0.2
CA2*	2	LPI	279564	7418488	4079	5.5	0.4
CA3	4	LPI	280501	7418016	3894	6.2	0.4
CA4	3	CAR	277480	7418741	4606	7.3	0.8
CA10	3	ORD	292930	7414695	3348	4.3	0.1
CO1	5	CGR	279398	7426515	3669	4.8	0.7
CO2*	5	MEA	280434	7426637	3985	27.8	19.0
CO3	4	YAC	281464	7426391	4368	5.7	0.4
CO4	4	UPI	283020	7426783	4668	11.3	3.1
CO5	3	LPI	283450	7425718	4886	6.4	0.4
CO6	3	LPI	283881	7425413	5093	6.5	0.1
HO1	5	PRC	275622	7428427	3329	10.8	2.1
HO6	4	LPI	276232	7424548	3604	7.3	0.3
HO7	5	LPI	275315	7423806	3604	6.2	0.4
PIR1	3	LPI	274082	7422808	3819	5.9	0.3
SA1	4	LPI	289076	7433384	4716	6.7	0.3
SA2†	5	CAR	289808	7433432	4525	10.4	1.2
SA4*	4	ORD	293534	7421603	4280	4.6	0.7
SA5*	5	ORD	294499	7418946	3972	4.3	1.8
SA6	3	ORD	294566	7416508	3606	4.4	0.8
SA10	4	ORD	299523	7411307	2760	2.8	0.3
TAC2	4	JUR	274077	7423106	3771	5.2	0.7
TAC3	5	JUR	274525	7424769	3468	6.5	0.5
ZE2	3	ORD	287856	7440249	4795	5.9	0.2
ZE3	5	ORD	288733	7439679	4547	17.7	1.3
ZE4	4	ORD	287123	7439286	4469	10.0	1.6
ZE6	5	ORD	286380	7439116	4279	16.8	3.3
ZE8	5	SAB	286011	7438216	4014	4.4	0.7
ZE9	5	CGR	285526	7437805	3833	11.3	3.3
ZE10	5	CGR	284804	7437689	3832	8.0	0.7
ZE11	5	CGR	283832	7437649	3739	7.7	1.1
Zircon (U-Th-Sm)/He data							
Sample	**Aliquots[a]**	**Stratigraphic Unit**	**UTM E[b]**	**UTM N[b]**	**Z (m)**	**WM (Ma)[c]**	**SE (Ma)[d]**
AP2	4	PRC	277302	7435139	3866	119.0	3.3
CA3	3	LPI	280501	7418016	3894	404.9	0.7
CA8	4	ORD	290050	7414244	2765	107.5	39.6
CA10	6	ORD	292930	7414695	3348	15.6	6.5
HO1	3	PRC	275622	7428427	3329	175.1	11.8
HO5*	3	UPI	276734	7424820	3730	512.8	71.6
PIR1†	4	LPI	274082	7422808	3819	469.1	72.6
SA3*	3	CAR	292502	7426625	4468	310.5	16.1
SA10	2	ORD	299523	7411307	2760	258.0	79.6
SA11	3	UPI	301469	7411570	2446	368.9	4.9
TAC2	2	JUR	274077	7423106	3771	452.7	2.4
TAC3†	2	JUR	274525	7424769	3468	485.4	1.8
ZE3	6	ORD	288733	7439679	4547	35.7	19.0
ZE11	3	CGR	283832	7437649	3739	352.6	68.0

[a]Number of aliquots used, excluding outliers
[b]UTM zone 20K
[c]Weighted mean age calculated in IsoplotR, excluding outliers
[d]Standard error of the weighted mean age
*Samples with age-F_T relationship

We calculated weighted mean ages in IsoplotR, applying the random effects model that considers the analytical uncertainty and an overdispersion term as sources of uncertainty (Vermeesch, 2018). We used the IsoplotR algorithm for detecting outliers in AHe and ZHe data, which uses a modified version of Chauvenet's criterion. Outliers were excluded from the weighted mean age calculation and are ignored for thermal history modeling procedures, except for two cases: 1) the aliquot age overlaps within a 2σ error with other aliquots of the sample, and 2) the sample is partially or non-reset for Mesozoic and Neogene exhumation, in which case the cooling ages reflect e.g., the detrital composition of the sample. In case of reset samples with outliers that do not overlap within a 2σ error with other aliquots, but that exhibit an age-eU or age-F_T trend, we did not model these.

Two AHe samples show a positive age-eU trend, attributed to the formation of an increasing number of "traps" within the apatite crystal caused by increasing radiation damage (Flowers et al., 2009). Three samples show a negative and one sample a positive age- F_T (and coincidentally an age-ESR) trend. For ZHe, two samples show a negative age-eU trend at low overall eU. According to the radiation damage model of Guenthner et al. (2013), zircons with < 1500 ppm eU may show a positive age-eU trend; negative trends are seen in zircons with high overall eU and are related to increasing He diffusivity due to connection of damage zones within the zircon crystal (Guenthner et al., 2013). One sample shows a positive and one sample a negative age- F_T and age-ESR trend. All trends are plotted on age-eU, age- F_T and age-ESR diagrams and are included in Appendix C (Figure C.1). Samples showing such a relationship are marked in Table 4.1. Full single-grain (U-Th-Sm)/He data can be found in Table C.1 (Appendix C).

4.3.3 Apatite fission track thermochronology

Charged particles are created through spontaneous fission of ^{238}U, producing linear damage zones (fission tracks) in the crystal lattice of apatite (e.g., Donelick et al., 2005). The fission track density and the abundance of their remaining parent isotopes in the crystal is used to calculate a cooling age, thus forming the basis for apatite fission track thermochronology. Fission tracks can be partially annealed within the apatite partial annealing zone (APAZ; Wagner et al., 1989), which is located approximately between 60 and 120 °C, although the exact temperature interval varies with cooling rate and kinetic characteristics of the sample. The latter can be quantified by measurement of the etch pit diameter (Dpar).

We analyzed 24 samples for AFT thermochronology using the external detector method (Gleadow, 1981). Etching conditions of the apatite mounts were 20 s in 5.5 N HNO3 at 21 °C (Donelick et al., 2005). The mounts were packed with mica detectors and CN5 dosimetry glasses and sent to Oregon State University for thermal neutron irradiation. The mica detectors were then etched for 45 min in 40 % HF at 21 °C. AFT samples were analyzed at the University of Potsdam using a Leica DMRM microscope at 1250X magnification and the FTStage software (Dumitru, 1994). Dpar sample measurements were calibrated using the Dpar standard measurements of Donelick et al. (1999) for Fish Canyon Tuff and Durango apatite (correction factor 1.07), applying the calibration procedure of Sobel and Seward (2010). Dpar is used as a proxy for kinetic characteristics that influence annealing behavior of apatite (Barbarand et al., 2003; Carlson et al., 1999; Ketcham et al., 1999). Low track density prevented the measurement of a statistically relevant number of track-in-track (TINT) lengths, except for sample AP4, for which 17 lengths were measured with values between 7–14 µm. A chi-square test of independence was performed on all samples; for passing samples a pooled age ± 1σ error was calculated (Galbraith and Laslett, 1993), whereas for non-passing samples we calculated a central age in IsoplotR (Vermeesch, 2018). These samples do not show clear age-Dpar relationships and were generally excluded from modeling procedures. Analytical data and AFT cooling ages are summarized in Table 4.2. Radial plots created in RadialPlotter (Vermeesch, 2009) are included in Appendix C.

4.3.4 QTQt modeling

AHe, AFT and ZHe data were used for multi-sample thermal modeling in QTQt v5.8.0 (Gallagher, 2021). The RDAAM radiation damage model of Flowers et al. (2009) was used for AHe samples, whereas the ZRDAAM model of Guenthner et al. (2013) was used for ZHe samples. We used the annealing model of Ketcham et al. (2007) for AFT samples and included average Dpar measurements for compositional control in models. AHe and ZHe aliquots with zero terminations and rounded aliquots were modeled as spheres.

Samples were divided into blocks or sections, based on their location relative to major faults, to avoid across-fault modeling. Depending on whether cooling ages positively correlate with sampling elevation or "stratigraphic" elevation, we ran models using either the sampling elevation (-AE models) or a calculated stratigraphic pseudo-elevation (-AS models) as input. This stratigraphic pseudo-elevation was obtained by projecting the samples onto cross-sections, measuring their stratigraphic offset and normalizing the values so that the stratigraphically deepest sample is located at zero meters pseudo-elevation. We did not place time-temperature constraints on the model, apart from the depositional age of the samples and the present-day temperature range, to avoid unnecessary constraint that may bias model results. Models were run with ≥ 100,000 repetitions burn-in and post burn-in to achieve stable log likelihood (LL) and posterior chains. The number of repetitions was increased to 200,000 for models where these chains were visually unstable (i.e., too much structure and not enough sampling between different dimensions; see Gallagher, 2012). We calculated average cooling rates for the most recent exhumation phase based on the visual inflection points of the hot sample 95 % confidence interval. A detailed summary of QTQt modeling parameters for individual models is given in Table 4.3. For all models, we present the expected model, which uses the posterior probability to calculate a weighted mean model (Gallagher et al., 2009).

The quality of the model depends on the structure of the likelihood and posterior chains in QTQt (Gallagher, 2012), the LL value, which describes the fit of observed vs. predicted cooling ages, and the geological plausibility of the thermal history. LL values above -100 are considered "good", values between -100 and -200 are considered "acceptable" and we attempt to avoid values below -200. Because we impose minimal constraints on the models, geologically unlikely thermal histories can result. The plausibility of a thermal history was determined by comparing it to the cooling ages, the general geologic history of the Andes and age-elevation and/or age-stratigraphy trends that indicate which model (-AE, -AS) is better suited.

Table 4.2 Apatite fission track data. Samples with less than 12 individual crystals dated are printed in italics.

Sample	Lithology	UTM E[a]	UTM N[a]	Z (m)	N[b]	Ns	Ni	Nd	RhoS	RhoI	RhoD [c]	Age (Ma)[d]	± 1σ (Ma)	P(χ^2) (%)[e]	Dpar (µm)[f]	SD (µm)[g]
AP1*	PRC	278998	7435444	3662	23	43	865	8096	6.26E+05	1.13E+06	1.31E+06	11.2	1.9	6 %	1.66	0.10
AP2*	PRC	277302	7435139	3866	15	20	573	8096	4.71E+04	1.35E+06	1.31E+06	7.7	1.8	82 %	1.70	0.20
AP3*	PRC	276941	7434905	4015	17	21	445	8096	4.94E+04	1.05E+06	1.31E+06	10.5	2.4	60 %	1.65	0.20
AP4*	PRC	275688	7434582	4205	17	211	790	8096	3.76E+05	1.41E+06	1.30E+06	58.6	5.8	49 %	1.70	0.20
CA1	UPI	278228	7418767	4414	18	61	1399	5117	1.11E+05	2.54E+06	9.27E+06	11.2	1.5	42 %	2.22	0.32
CA3	LPI	280501	7418016	3894	15	65	1178	5117	1.21E+05	2.20E+06	1.32E+06	14.2	2.8	1 %	2.43	0.40
CA4	UPI	277480	7418741	4606	7	26	633	5117	1.23E+05	3.01E+06	2.43E+07	10.2	2.1	89 %	2.32	0.50
CA10	ORD	292930	7414695	3348	22	41	1191	5117	9.24E+04	2.68E+06	1.15E+07	8.4	1.4	27 %	2.14	0.29
CO1	CGR	279398	7426515	3669	13	110	452	4401	2.10E+05	8.63E+05	8.41E+06	46.5	9.0	0 %	2.62	0.88
CO3	BAL	281464	7426391	4368	6	62	569	4401	2.59E+05	2.37E+06	1.84E+07	21.5	6.1	0 %	2.31	0.28
CO5	LPI	283450	7425718	4886	12	66	1082	4401	1.68E+05	2.75E+06	1.12E+07	14.0	2.7	0 %	2.26	0.26
CO6	LPI	283881	7425413	5093	6	26	427	4401	1.77E+05	2.90E+06	2.99E+07	12.0	2.4	35 %	2.06	0.29
HO1	PRC	275622	7428427	3329	15	150	375	4076	2.49E+05	6.21E+05	6.75E+06	74.1	7.3	100 %	2.41	0.30
HO7	LPI	275315	7423806	3604	14	36	464	4076	1.08E+05	1.40E+06	1.23E+07	14.4	2.5	100 %	2.32	0.26
SA1	LPI	289076	7433384	4716	12	61	1360	5117	1.66E+05	3.70E+06	1.39E+07	10.7	1.4	69 %	2.33	0.26
SA2	CAR	289808	7433432	4525	14	127	3295	5117	2.07E+05	5.37E+06	8.34E+06	9.0	0.8	14 %	2.39	0.28
SA4	ORD	293534	7421603	4280	12	18	594	5117	6.52E+04	2.15E+06	1.85E+07	6.9	1.7	62 %	2.22	0.20
SA5	ORD	294499	7418946	3972	12	28	1000	5117	1.17E+05	4.17E+06	2.13E+07	6.3	1.2	14 %	2.24	0.40
SA10	ORD	299523	7411307	2760	9	9	334	5117	5.46E+04	2.03E+06	3.11E+07	5.7	2.0	14 %	2.57	0.60
ZE2	ORD	287856	7440249	4795	11	30	366	4401	1.63E+05	1.99E+06	2.39E+07	17.4	3.3	34 %	2.54	0.48
ZE3	ORD	288733	7439679	4547	15	37	844	4401	1.41E+05	3.21E+06	1.67E+07	9.2	1.6	63 %	2.29	0.28
ZE4	ORD	287123	7439286	4469	17	26	869	4401	8.80E+04	2.94E+06	1.49E+07	6.3	1.3	99 %	2.46	0.38
ZE5	ORD	286784	7439187	4397	11	8	232	4401	8.29E+04	2.40E+06	4.56E+07	7.2	2.6	59 %	2.26	0.25
ZE6	ORD	286380	7439116	4279	19	60	1291	4401	1.79E+05	3.86E+06	1.32E+07	11.2	2.5	0 %	2.36	0.18
ZE8	SAB	286011	7438216	4014	7	13	321	4401	6.54E+04	1.61E+06	2.21E+07	8.3	2.4	83 %	2.29	0.12
ZE9	CGR	285526	7437805	3833	6	31	118	4401	1.11E+05	4.23E+05	1.58E+07	51.5	16.7	2 %	3.15	0.66
ZE10	CGR	284804	7437689	3832	18	74	509	4401	1.46E+05	1.01E+06	8.70E+06	29.4	3.7	43 %	2.34	0.28
ZE11	CGR	283832	7437649	3739	11	61	321	4401	1.80E+05	9.46E+05	1.30E+07	38.3	5.4	50 %	2.30	0.22

ζ = 380.5 ± 7.5 (WvK) and 339.5 ± 21.7 (ATL)

[a]UTM zone 20K

[b]Number of individual crystals dated

[c]CN5 standard glasses monitored thermal neutron fluences

[d]Central age for samples that did not pass chi-square test, pooled age for all other samples

[e]P(χ2) (%) is the chi-square probability (Gailbraith and Laslett, 1993; Green, 1981)

[f]Corrected Dpar calculated after Sobel and Seward (2010)

[g]Standard deviation of measured Dpars

*Samples and counting data from Lapiana (2021)

Table 4.3 QTQt modeling parameters.

General constraints			
Modeling interval	0–600 Ma, 0–300 °C	**Maximum cooling rate**	1000 °C/Ma
eU resampling	No	**Reheating**	Allowed
Iterations[a]	≥ 100000/≥ 100000	**Gradient variation**	Allowed
Present day offset[b]	≤ 10 ± 10 °C	**Surface temperature**	10 ± 10 °C

Model-specific constraints and data									
		Sample set-up				*Expected model*			
Run	**Samples location**	**AHe**	**AFT**	**ZHe**	**Z-axis**[c]	**LL**	**Onset of exhumation**	**Exhumation rate (mm/a)**
CO_AE	E limb Cianzo syncline	CO1 CO3 CO5 CO6	CO6		AE	-85.78	24–15 Ma	0.29 ± 0.10
CO_AS*	E limb Cianzo syncline	CO6	CO1 CO3 CO5 CO6		AS	-135.79	32–20 Ma	0.20 ± 0.06
CA_AE	E limb Cianzo syncline	CA1 CA2 CA3 CA4	CA1 CA4	CA3	AE	-78.92	21–17 Ma	0.24 ± 0.06
CA_AS*	E limb Cianzo syncline	CA1 CA2 CA3 CA4	CA4		AS	-31.57	> 18 Ma	0.37 ± 0.29
SA_AE	Basement E Cianzo syncline	SA1 SA4 SA6 SA10	SA1 SA2 SA4 SA5 SA10	SA11	AE	-241.12	14–9 Ma	0.42 ± 0.06
SA_AE_ AFT	Basement E Cianzo syncline		SA2 SA4 SA5 SA10		AE	-82.37	28–13 Ma	0.33 ± 0.12
SA_AE_ AFTZ	Basement E Cianzo syncline		SA1 SA2 SA4 SA5 SA10	SA3 SA11	AE	-166.11	13–11 Ma	0.33 ± 0.13
HPT_AS*	W limb Cianzo syncline	HO6 HO7 PIR1 TAC2	HO7	TAC2	AS	-112.78	19–16 Ma	0.25 ± 0.04
AP_AE*	Hanging wall Cianzo thrust		AP1 AP2 AP3 AP4	AP2	AE	-190.21	14–13 Ma	0.23 ± 0.09
HO1*	Hanging wall Cianzo thrust	HO1	HO1	HO1	---	-105.51	12–10 Ma	0.27 ± 0.18

[a]Number of iterations burn-in and post-burn-in
[b]Present-day offset maximum 10 ± 10 °C, unless original offset was lower
[c]Age-elevation (AE) or age-stratigraphy (AS) trend
*200000 iterations burn-in and post-burn-in

4.4 Results

Field observations (Section 4.4.1) and results from thermochronology (Section 4.4.2) are presented in subsections in the context of the three main faults delimiting the Cianzo basin: the Cianzo thrust, the Hornocal (and Ocumazo) fault, and the Zenta thrust.

4.4.1 Field observations

Cianzo thrust

The east-vergent Cianzo thrust (Figure 4.1b, 4.3) strikes approximately N–S and forms the western delimitation of the Cianzo basin. The thrust separates the Precambrian-lower Cambrian Puncoviscana Fm in its hanging wall from Eocene to Miocene foreland basin strata that have been tilted to steep and overturned orientations near the thrust. The thrust itself shows a high-angle character, especially seen in outcrops near the Cianzo community. It cuts into into Precambrian–Ordovician strata to the south and may connect to N–S striking reverse faults bounding the Tilcara Range (e.g., Amengual and Zanettini, 1973; González and Tchilinguirian, 2003; Rodríguez-Fernández et al., 1999), although its trace is lost in the Paleozoic strata SW of the Cianzo syncline. Extrapolation of the Cianzo thrust trace shows that it likely cuts both the Hornocal and Ocumazo faults. The E–W strike of the Ocumazo fault rotates slightly counter clockwise toward the intersection with the Cianzo thrust and correlates well with the ENE–WSW strike of the Hornocal fault in the SW corner of the Cianzo syncline.

Hornocal and Ocumazo faults

The Hornocal fault is marked by an erosional and topographic trace that is visible on satellite imagery and maps. This coincides with the contrast between younger, less indurated and thus more easily eroded Cenozoic strata (Rio Grande and Pisungo formations) in the footwall and cohesive, compacted Salta Group strata in the hanging wall. While in its central part, the Hornocal fault shows a single, well-defined trace, toward the SW it splays into multiple, approximately parallel-striking splay faults (Figure 4.3a; H1–H3). The northernmost splay fault (H1) mostly offsets Cenozoic strata. The central splay fault (H2) shows the largest stratigraphic offset of Jurassic Ocumazo conglomerates (hanging wall) against Miocene Rio Grande Fm (footwall). The southernmost fault (H3) marks the transition from a full, > 1600 m thick section of the Pirgua Subgroup in the hanging wall (McBride, 2008), to a 430 m thin section in the footwall. The northern splay fault is accompanied by a footwall syncline in Neogene strata, with a steeply NE-plunging fold axis (029/62) and a near-vertical, NW-dipping axial surface (Figure 4.3a). In the north, the Zenta thrust connects to the Hornocal fault, whereas the latter maintains its Cretaceous normal offset NE of the junction (Figure 4.1b) (Kley et al., 2005).

The hanging wall block of the Hornocal fault is formed by the Cianzo syncline, which has a near-vertical, NW-dipping axial plane and a NNE-plunging fold axis (016/15) in the Cretaceous–Neogene strata (Figure 4.1b). Bedding in the underlying Silurian–Jurassic succession shows a fold axis with a slightly steeper plunge (020/27; Figure 4.1b). The eastern limb of the Cianzo syncline rotates clockwise toward the north, from WNW-dipping to NW-dipping, where it approaches the Hornocal fault. Below the Salta Group, the Tacurú Group forms an intermediate succession, overlying Carboniferous strata in the eastern limb and the Santa Victoria Group (upper Cambrian–Ordovician) in the western limb. There is an angular unconformity of ~37–40° between the Santa Victoria Group and the Tacurú Group. The Pirgua Subgroup overlies the Tacurú Group with an angular unconformity of 41–42° in both fold limbs, characterized by a change in dip and strike (see also Van Kooten et al., 2022a).

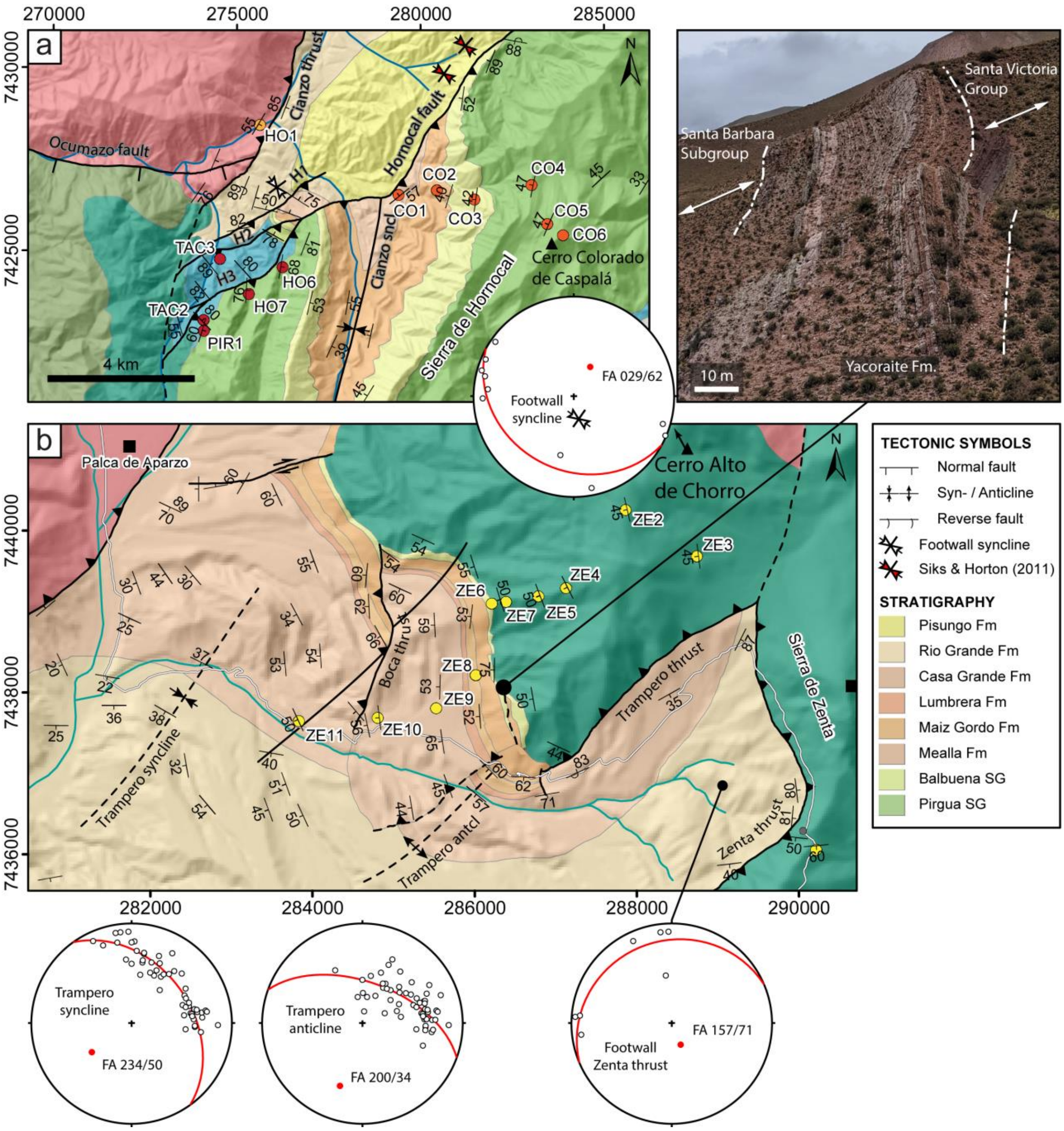

Figure 4.3. Detailed geologic map of (a) the Hornocal fault, and (b) the Sierra de Zenta. Stereograms show poles of measured bedding, calculated pi plots and fold axes. Photo (top right) shows the measured Yacoraite Fm section (Figure 4.2c). Footwall synclines (Siks and Horton, 2011) are marked with symbols in (a). The legend shows Cretaceous–Neogene lithologies. For legend of Paleozoic lithologies, see Figure 4.1b. Maps include own field data and existing data and measurements of Kocks (1999), González and Tchilinguirian (2003), Kley et al. (2005), Siks and Horton (2011) and Starck (2011).

The pre-rift base of the Cianzo syncline is formed by upper Cambrian–Carboniferous strata. Within these Paleozoic strata (Hornocal fault hanging wall), the Caspalá anticline-syncline pair (Fold axis plunging 022/33 and 015/01, respectively) and Santa Ana anticline (Fold axis plunging 020/10) form open folds with fold axes trending approximately parallel to the Cianzo syncline (Figure 4.1b). The upper Cambrian–Silurian succession shows small-scale (meter-scale wavelength) folding, favored by a mechanically heterogeneous sedimentary succession. The Devonian–Jurassic strata consists of a more homogeneous, competent succession, so that small-scale folding is less pronounced.

Stratigraphic thicknesses of the Salta Group change rapidly within the Cianzo syncline. In the western limb, the stratigraphic thickness of the Pirgua Subgroup, measured in MOVE cross-sections, amounts to 1630 m. McBride (2008) measured a thickness of 2147 m using a Jacob's staff, but the base of this measured section is located below the Salta Group unconformity, thus overestimating the thickness of the lower Pirgua Subgroup by approximately 425 m. A stratigraphic section in Boll et al. (1989) from the SE limb, along the Rio Caspalá, shows a thickness of 2525 m for the Pirgua Subgroup. Closer to the Hornocal fault, the thickness rapidly increases to 4030 m (measured in MOVE) within the eastern limb. The post-rift Balbuena Subgroup shows a decreasing thickness toward the fault trace, from > 285.5 m in the southern part of the syncline (Boll et al., 1989) to ~165 m closer to the fault trace (measured in MOVE).

Zenta thrust

The Zenta thrust and a number of minor faults bound the Cianzo basin to the north and emplaced the Ordovician Santa Victoria Group onto the Cenozoic Casa Grande and Rio Grande formations. The Zenta thrust itself dips gently toward the east and connects to the Hornocal fault south of Abra de Zenta (Figure 4.1b). Its footwall geometry consists of an anticline with laterally rotated limbs that strike approximately parallel to the trace of the Zenta thrust (Figure 4.3b). Whereas Miocene–Pliocene activity along the Hornocal fault is evident from syntectonic growth strata within the Pisungo Fm, these sediments only crop out south of the Hornocal fault-Zenta thrust junction with a thickness > 1500 m (Siks and Horton, 2011). Whether the strata were not deposited, or eroded north of the junction is unclear. West of the Zenta thrust, the SW–NE striking, SE-vergent Trampero thrust (Kocks, 1999) juxtaposed the Santa Victoria Group onto the Lumbrera and Casa Grande formations. The Trampero thrust eventually runs into the Zenta thrust to the north, but its fault trace is lost east of Cerro Alto de Chorro, where it is covered by Quaternary sediments. Small faults and the Trampero anticline-syncline pair with SSW- to SW-plunging fold axes (200/34, 234/50; Figure 4.3b) dissect the hanging wall of the Trampero thrust.

A condensed succession of the Yacoraite Fm, with a thickness of 27 m (measured section in Figure 4.2c), and Santa Barbara Subgroup unconformably overlie the Santa Victoria Group. In the measured section, the Yacoraite Fm presents a reduced thickness (compared to the average 200 meters observed in other localities; Marquillas et al., 2005), suggesting that this section is incomplete. The outcrops have a limited areal extent and are laterally covered by debris and soil, moreover the section itself is heavily structurally deformed and weathered (Figure 4.3). The base of the Yacoraite Fm is characterized by a meter-scale succession of sandstone beds, overlying an interval of dark grey to brown, thinly-bedded metamorphozed siltstones and sandstones of the Ordovician Santa Victoria Group. The top of the Yacoraite Fm is represented by an interval of brecciated limestones, with crackle to mosaic breccias.

The Yacoraite Fm is a mixed carbonate-siliciclastic succession. In the study area it is characterized by a limited number of facies, showing little variability in their expression. Siliciclastic-dominated facies are exclusively represented by sandstones. Sandstone beds show predominantly tabular morphologies, with sub-meter-scale thicknesses, and are commonly thinly stratified (1–8 cm). Plane parallel laminations have rarely been observed, whereas the bed tops are marked with wave ripples. Bioturbation is frequently observed, generally constrained to the bed tops, and represented by common *Psilonichnus* and *Skolithos* centimeter-scale vertical or y-shaped burrows. The sandstones range in grain size from fine to coarse and are almost entirely composed by moderately to poorly sorted quartz grains, with sub-angular morphologies. Feldspars and rock fragments are present in minor quantities, as are ostracods, turriculate gastropods, reworked ooids and rip-up clasts.

The carbonate-dominated facies are represented by common oolitic grainstone-packstones, peloidal and ostracodal grainstones, and minor occurrences of ostracodal wackestones and gastropod shell rudstones. Oolitic grainstone-packstones show tabular to lenticular morphologies, with frequent wave ripples at bed tops and occasionally erosive bases. Beds are generally massive, but centimeter-scale stratification and occasional faint plane parallel to slightly wavy lamination have been observed. Ooids are generally small in size (< 400 μm) and show spherical morphologies with a good degree of sorting. Ooids are typically associated with peloids, ostracods and gastropods (various turriculate gastropods and *Planorbis* sp.), and rarely with centimeter-scale sub-spherical oncoids. Oolitic grainstones are frequently heavily cemented and show a high degree of recrystallization, to the point that in several cases the texture resembles more that of a cementstone (Wright, 1992). Peloidal and ostracodal grainstone-packstones are less common and show typically thinly stratified beds (1–5 cm), with overall tabular geometries. Plane parallel lamination is common. Ostracods form tight and chaotic shell accumulations, and are associated with common peloids and sparse ooids. Wackestones are rarely observed and show thin, tabular beds with faint plane parallel lamination and centimeter-scale alternances with ostracod packstones. Only sparse and poorly sorted peloids, ooids and turriculate gastropods have been observed within the wackestones. One bed of gastropod rudstone was observed (meter 17.2 on the stratigraphic log; Figure 4.2c), characterized by chaotic shell accumulations, with centimeter-scale *Turritella sp.* gastropods showing a poor degree of sorting and common shell fragments. The rudstone bed is characterized by an erosive base and common intraclasts in the lower part of the bed.

4.4.2 Thermochronology

We conducted AHe, AFT and ZHe thermochronology on samples collected within the hanging wall blocks of major faults bounding the Cianzo basin to quantify Mesozoic rift shoulder exhumation, as well as Neogene fault inversion related to the Andean orogeny. The resulting data set contains 28 AFT samples, 146 AHe and 57 ZHe aliquots. As a first step, we plotted single-grain cooling ages against sampling elevation and stratigraphic pseudo-elevation (see Section 4.3.3). Single-grain ages were then modeled in QTQt v5.8.0 (Gallagher, 2021) according to the age-elevation or age-stratigraphy trends deducted from these diagrams. Plotting and then modeling samples along both trends allows us to interpret when tilting associated with folding or faulting occurred. We ran various preliminary models based on only AHe or AFT ages, after which we gradually increased the amount of AHe and ZHe samples to reach a final model.

Cianzo thrust

ZHe single-grain ages (Table C.1 in Appendix C) from the Puncoviscana Formation in the hanging wall of the Cianzo thrust (AP and HO1 samples; Figure 4.1b) range from 110.5 ± 1.8 to 197.8 ± 4.2 Ma. Although these cooling ages are markedly younger than the Precambrian–lower Cambrian depositional age of the strata. AFT ages range from 7.7 ± 1.8 to 74.1 ± 7.3 Ma. Wheres the AP samples (Lapiana, 2021) show a positive age-elevation trend with a break-in-slope, sample HO1 does not fit on this trend (Figure 4.4a). AHe single-grain cooling ages range from 5.8 ± 0.7 to 21.3 ± 2.1 Ma. Sample AP1 is excluded from further modeling, because it is overdispersed and there are no coherent aliquots to model.

Model AP-AE indicates an onset of cooling between 160–140 Ma. From > 25 Ma the Cianzo thrust hanging wall underwent reheating of up to 120 °C. The onset of the most recent, rapid cooling took place between 14–13 Ma. The model fit is acceptable, with a LL of -190.21. The average exhumation rate for the final exhumation phase is 0.23 ± 0.09 mm/a (assuming a geothermal gradient of 30 °C/km). Single-sample model HO shows an onset of Mesozoic cooling interpreted to be a result of exhumation before 190 Ma. Miocene cooling started between 12 and 10 Ma, with a poorly constrained average exhumation rate of 0.27 ± 0.18 mm/a. AHe and ZHe cooling ages show an acceptable, bordering on good observed versus predicted fit (Figure 4.4b).

Hornocal fault

We analyzed exhumation interpreted to be related to fault activity along the Hornocal fault using samples from the western and eastern limbs of the Cianzo syncline. In the western limb of the Cianzo syncline, Neoproterozoic–Paleozoic ZHe cooling ages are older than the respective Cretaceous–Paleogene depositional ages and thus reflect the detrital provenance of the Tacurú and Salta Groups. One ZHe aliquot from sample TAC3 (location in Figure 4.1b) shows a Jurassic cooling age of 154.6 ± 1.2 Ma, which coincides with Jurassic cooling ages in the hanging wall of the Cianzo thrust. Given that sample TAC3 was located in an intermediate fault block between splay faults (H2 and H3; Figure 4.3a), we calculated the stratigraphic pseudo-elevation of this sample relative to the base of the Balbuena Subgroup. We chose this reference because we assume that the post-rift section shows less rapid lateral thickness variations than the syn-rift section. A single AFT cooling age of 14.4 ± 2.5 Ma is available (Sample HO7; Table 4.2). AHe ages range between 3.5 ± 0.5 Ma and 8.5 ± 0.9 Ma and show a steep positive age-stratigraphy trend (Figure 4.5). In age-elevation space these samples show a vertical to negative trend, due to tilting of the strata. Therefore, we chose to model the samples with their stratigraphic pseudo-elevation (see Section 4.3).

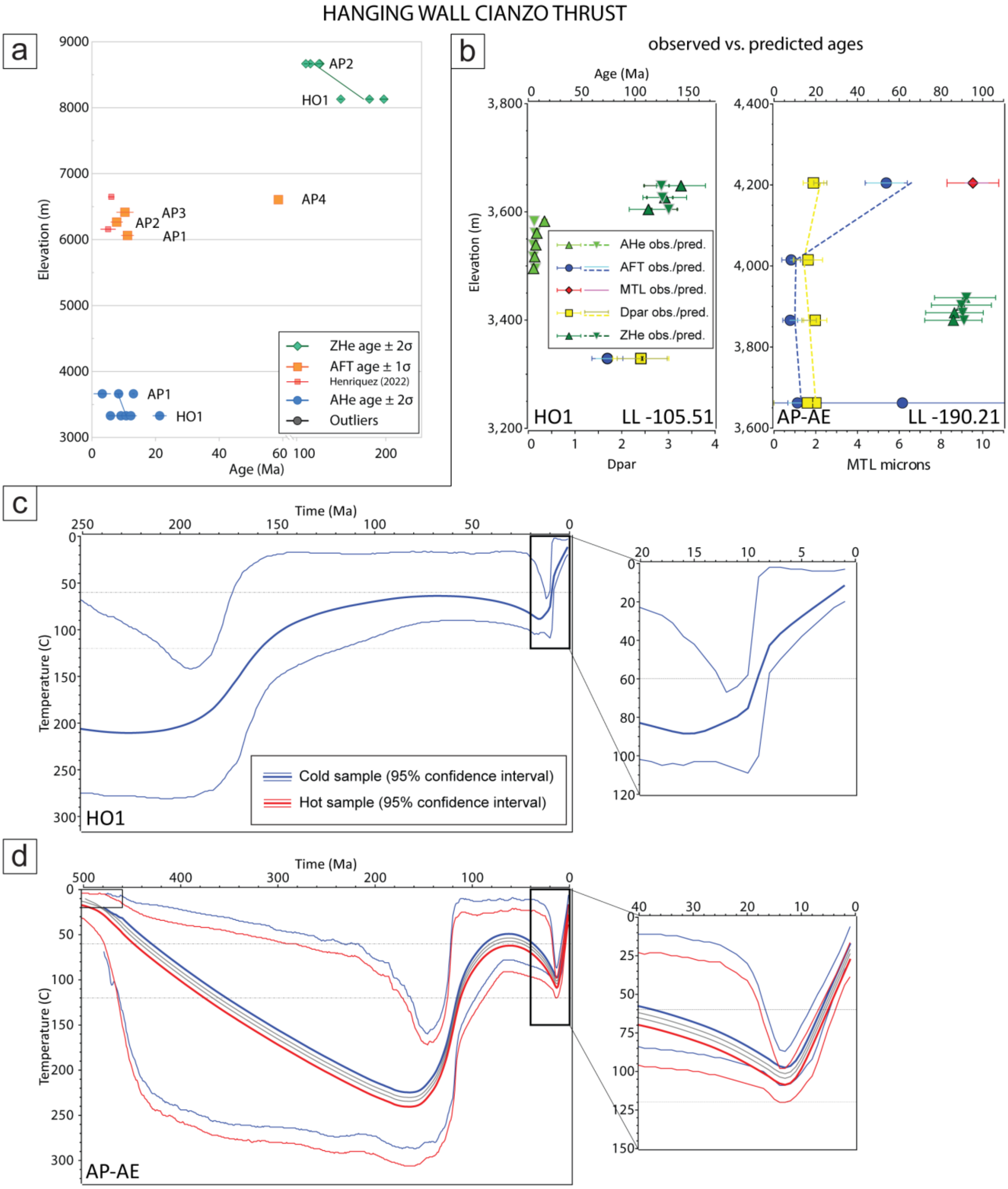

Figure 4.4 Thermochronological data for the hanging wall of the Cianzo thrust (including two data points of Henríquez et al., 2023), plotted against (a) sampling elevation. QTQt modeling results show the observed vs. predicted single-grain ages (b) and the expected t-T-path for model HO1 (c) and AP-AE (d).

For the multi-sample age-stratigraphy model HPT-AS we chose to exclude sample TAC3 to avoid across-fault modeling. The model shows an onset of cooling interpreted to be related to exhumation between 19 and 16 Ma, with an average exhumation rate of 0.25 ± 0.04 mm/a. All of the samples show an acceptable observed versus predicted fit, with a LL of -112.78 (see Section 3.4).

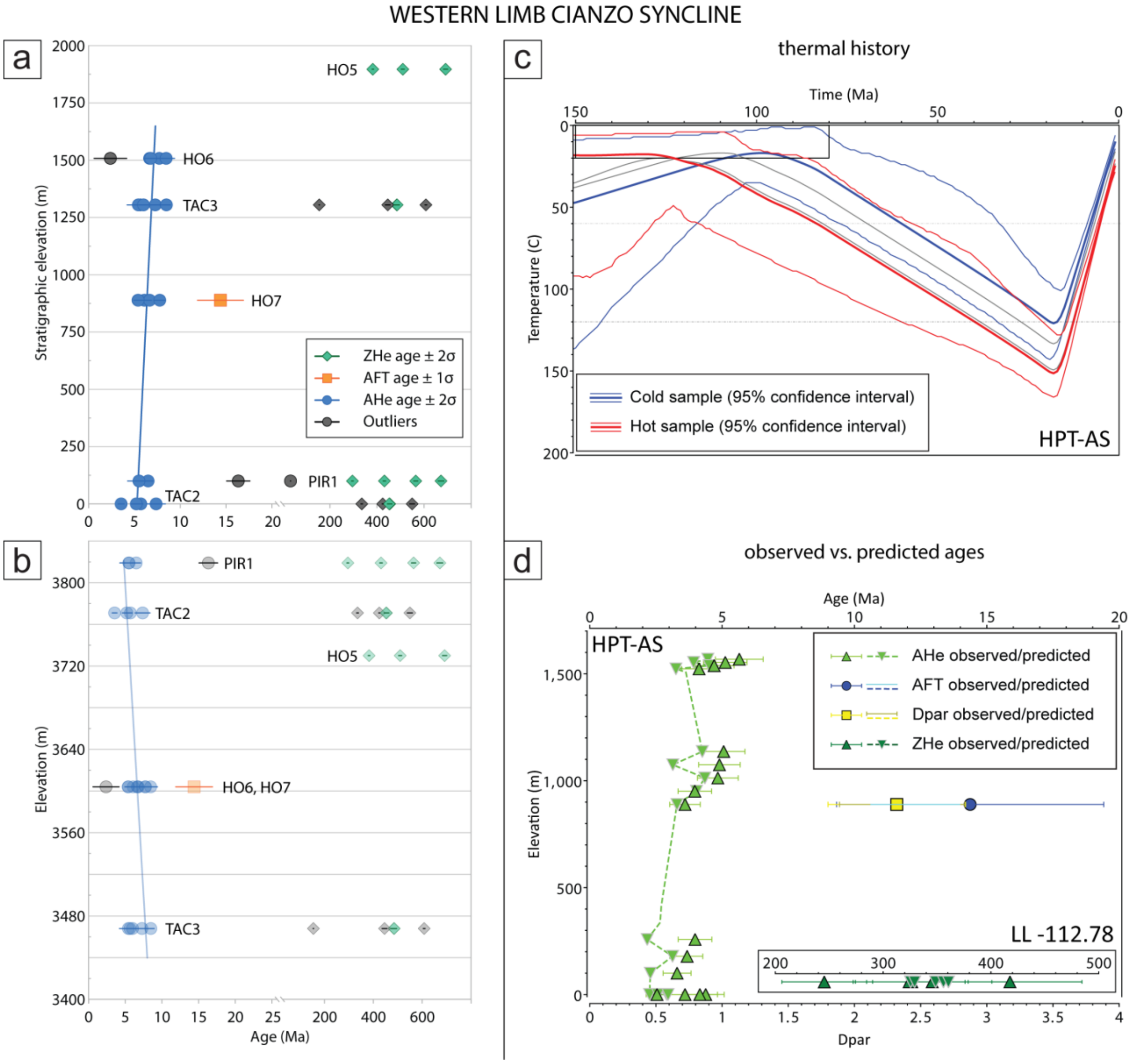

Figure 4.5 Thermochronological data for the western limb of the Cianzo syncline, plotted against (a) stratigraphic pseudo-elevation and (b) sampling elevation. QTQt modeling results of HPT-AS show (c) the expected t-T-path and (d) observed vs. predicted single-grain ages. LL stands for log likelihood. AS denotes the age-stratigraphy model.

In the eastern limb of the Cianzo syncline, Salta Group ZHe single-grain ages are non-reset for Mesozoic and Neogene cooling events. In the underlying Santa Victoria Group, ZHe ages become younger with increasing stratigraphic depth. In general, the ZHe samples show a positive age-stratigraphy trend. AFT ages range from 8.4 ± 1.4 Ma to 46.5 ± 9.0 Ma. Samples with cooling ages older than ~14 Ma consistently fail the chi-square test, which we attribute to partial annealing toward the top of the stratigraphic column. CO samples (Figure 4.1b) show a negative age-elevation, but positive age-stratigraphy trend with a clear break-in-slope (Figure 4.6a–b). CA samples (Figure 4.1b) show both a negative age-elevation and age-stratigraphy trend, but ages overlap within error (Figure 4.7a–b). Different trends are interpreted to be a result of the present-day ~45° inclination of the strata toward the west, leading to an inverse elevation-stratigraphy relationship for the CO samples, due to a west-dipping relief, and a normal relationship for the

CA samples, due to their location on the east-dipping slope of the Hornocal range. AHe ages range from 2.7 ± 1.7 Ma to 157.4 ± 2.1 Ma. AHe samples from the W-dipping slope (CO) show a positive age-elevation, but negative age-stratigraphy trend. AHe samples from the E-dipping slope (CA) show a positive age-elevation trend, coinciding with the W-dipping slope. Due to the orientation of the slope, the age-stratigraphy trend is positive as well, but markedly steeper.

We ran separate models for the CO and CA sections, due to the spatial offset between the sections and the varying trends observed. CO samples were modeled in age-elevation space (Model CO-AE; Figure 4.6). The model shows an onset of rapid cooling interpreted to be a result of exhumation between 24–15 Ma. The age-stratigraphy model CO-AS shows an onset of rapid cooling between 32–20 Ma. Three of four AFT samples did not pass the chi-square test; therefore, we interpret that these are partially annealed. However, predicted ages do not match observed ages for these samples, which may be attributed to the lack of length data. This results in an acceptable fit for model CO-AS, as opposed to a good fit for model CO-AE. The age-elevation model CA-AE shows an onset of cooling between 21–17 Ma (Figure 4.7). The corresponding age-stratigraphy model CA-AS shows a loosely-constrained onset of rapid cooling by 18 Ma. For all CO and CA models the onset of cooling overlaps. Based on the positive age-elevation trend for CO AHe samples, the CA-AE model is more likely to show the correct thermal history for AHe samples than the CA-AS model. Both models show a good observed vs. predicted fit.

Approximate exhumation rates, based on a geothermal gradient of 30°C/km, overlap within error for all models in the western and eastern limbs of the Cianzo syncline at approximately 0.25 mm/a. Most of the models show a well-constrained average exhumation rate, with the exception of model CA-AS (Table 4.3).

SA samples (Figure 4.1b) form both a vertical and horizontal section in the hanging wall of the Hornocal-Zenta fault. ZHe ages range from 166.8 ± 3.4 Ma to 457.5 ± 6.6 Ma and form a near-vertical age-elevation and age-stratigraphy trend (Figure 4.8a). AFT ages range from 5.7 ± 2.0 Ma to 10.7 ± 1.4 Ma, forming a positive age-elevation and age-stratigraphy trend, with a break-in-slope for the age-elevation diagram. AHe cooling ages show high dispersion and range from 0.9 ± 0.5 Ma to 9.0 ± 0.1 Ma, forming a positive age-elevation trend. The highest sample, SA1, is located north of the Hornocal fault trace and is therefore excluded to avoid across-fault modeling. AFT samples plot along an extrapolated, positive age-elevation trend (Figure 4.8). The higher effective closure temperature of the AFT system is thus interpreted to suggest that the majority of deformation in the Paleozoic strata of the Hornocal fault hanging wall occurred before cooling through the APAZ and APRZ.

The age-elevation model SA-AE has a LL that is higher than for the other models and is out of the range deemed "acceptable" (Section 3.4). This is attributed to the relatively high dispersion of AHe cooling ages. The model shows an onset of rapid cooling that we interpret to result from exhumation between 13–9 Ma. If run with AFT and ZHe ages only (SA-AE-AFTZ), the model fit is good and the onset of cooling (13–11 Ma) still overlaps with model SA-AE, as do the exhumation rates of 0.42 ± 0.06 and 0.33 ± 0.12 mm/a, respectively (Table 4.3). Compared to models from the Cianzo syncline, the onset of cooling occurs later.

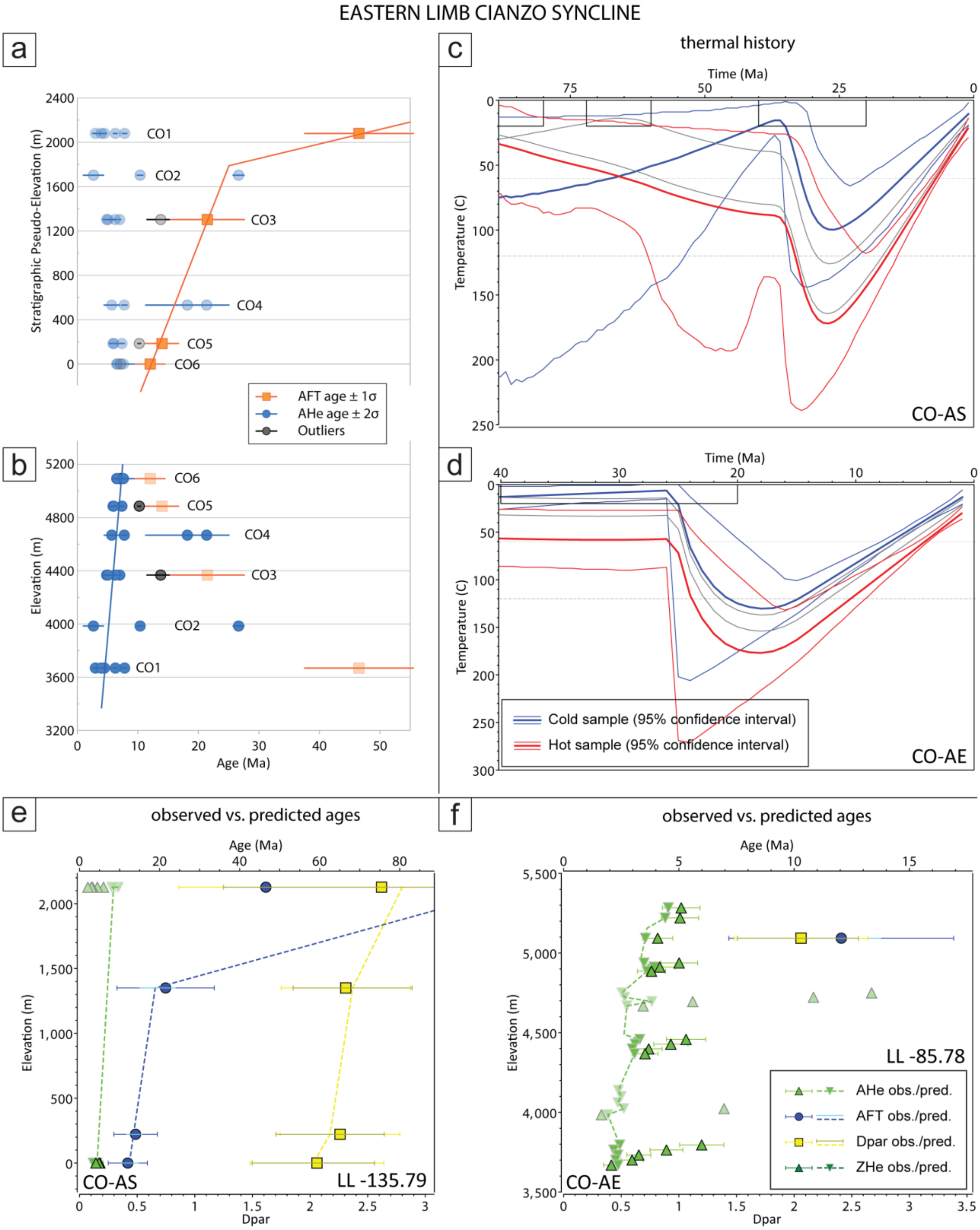

Figure 4.6 Thermochronological data for the eastern limb of the Cianzo syncline (CO section), plotted against (a) stratigraphic pseudo-elevation and (b) sampling elevation. (c) and (d) show the expected t-T-path for model CO-AS and CO-AE, respectively. (e) and (f) show observed vs. predicted single-grain ages for model CO-AS and CO-AE, respectively. LL stands for log likelihood. AE and AS denote age-elevation and age-stratigraphy model.

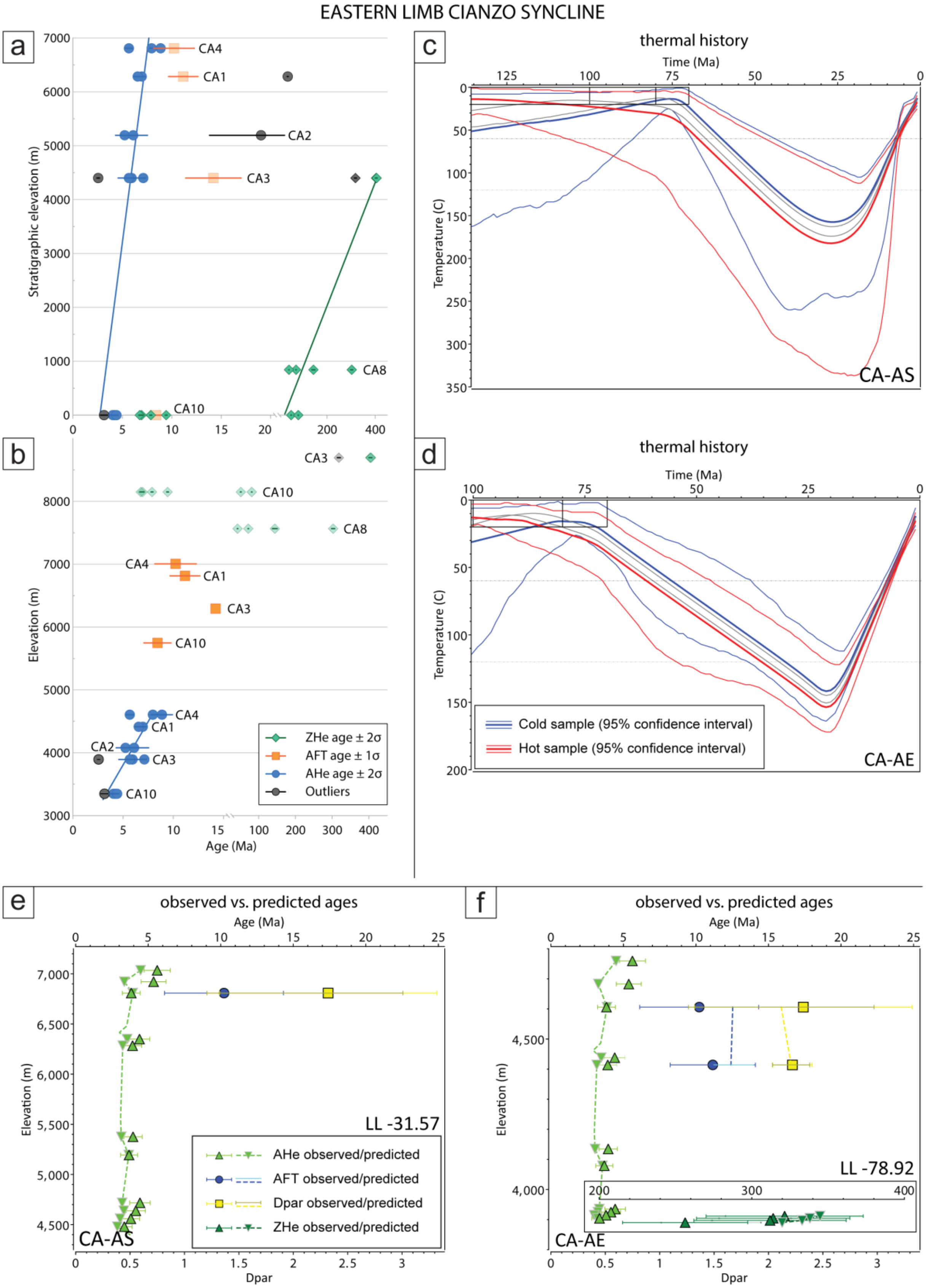

Figure 4.7 Thermochronological data for the eastern limb of the Cianzo syncline, plotted against (a) stratigraphic pseudo-elevation and (b) sampling elevation. (c) and (d) show the expected t-T-path for model CA-AS and CA-AE. (e) and (f) show observed vs. predicted single-grain ages for model CA-AS and CA-AE. LL stands for log likelihood. AE and AS denote age-elevation and age-stratigraphy model.

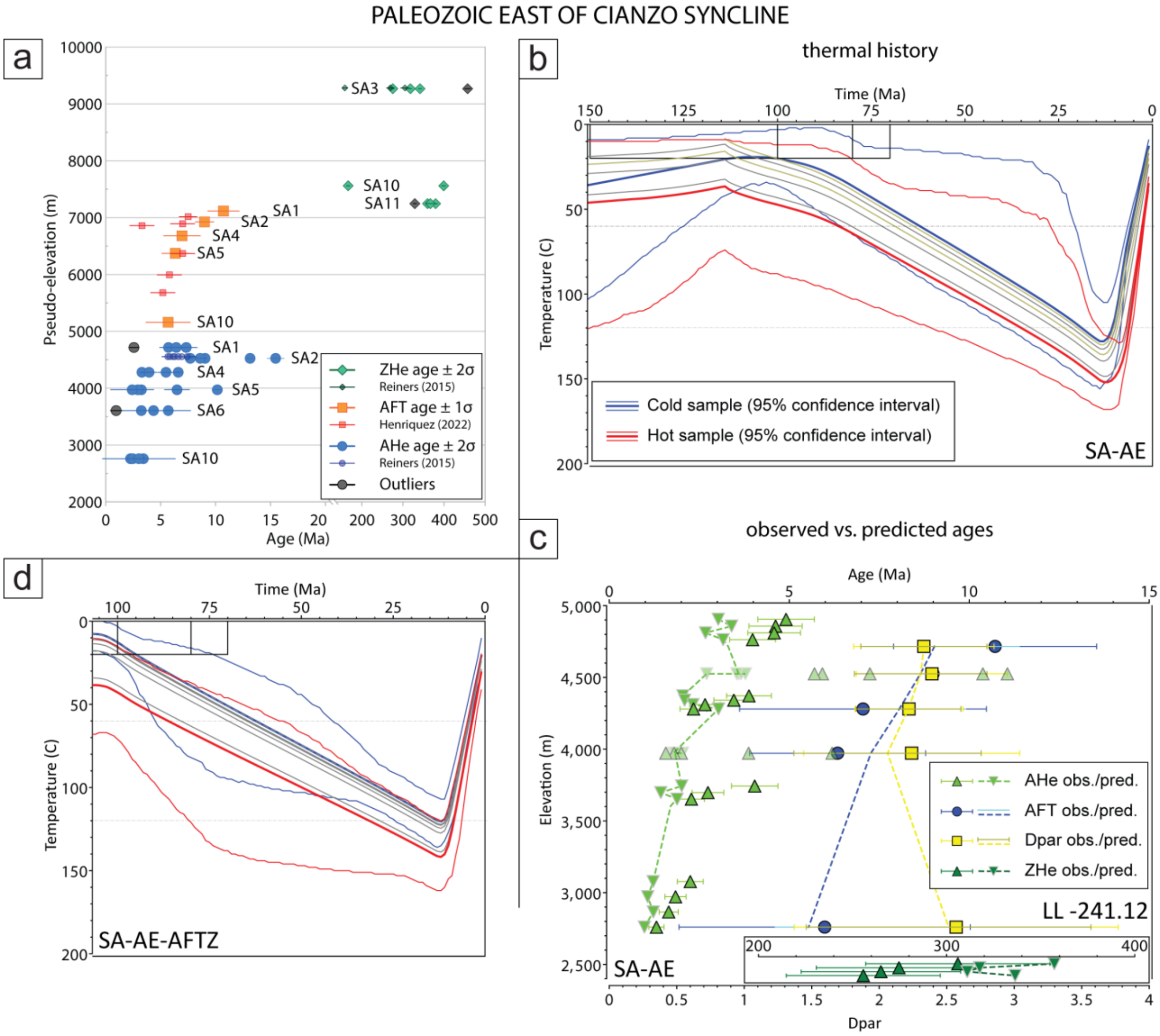

Figure 4.8 Thermochronological data for the eastern hanging wall of the Hornocal fault, plotted in (a) an age-elevation diagram. AFT ages from Henríquez et al. (2023), as well as AHe and ZHe from Reiners et al. (2015). Modeling results for SA-AE show (c) the expected t-T-path and (d) observed vs. predicted single-grain ages. (e) shows the expected t-T-path for model SA-AE-AFTZ. LL stands for log likelihood. AE denotes the age-elevation model.

Zenta thrust

ZHe ages from the ZE section are partially- and non-reset, with cooling ages ranging between 5.9 ± 0.1 Ma and 552.3 ± 9.3 Ma. AFT cooling ages range between 6.3 ± 1.3 Ma and 51.5 ± 16.7 Ma, whereas AHe ages range between 2.9 ± 0.4 Ma and 33.5 ± 2.3 Ma. AHe and AFT samples show ambiguous trends with AFT samples from the Casa Grande Fm being non-reset for Miocene exhumation, whereas the rest of the AFT samples show an overall positive age-elevation trend (Figure 4.9). AHe samples may either show a positive age-elevation trend with three partially-reset samples, or a positive age-stratigraphy trend on which sample ZE3 does not plot due to post-exhumational deformation. Due to the large amount of dispersion and the lack of clear age-elevation or age-stratigraph trends, we chose to not conduct thermal modeling for these samples at this point in time.

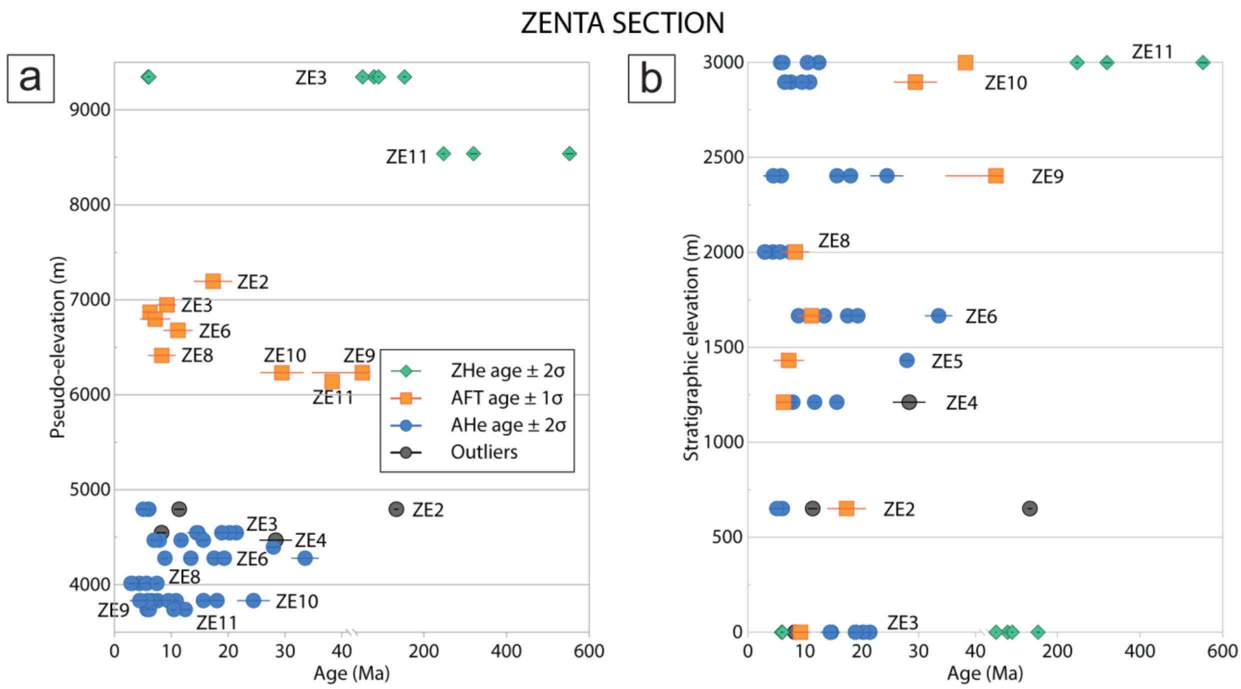

Figure 4.9 Thermochronological data for the Zenta section, plotted in (a) age vs. pseudo-elevation, and (b) age-stratigraphy diagrams.

4.5 Discussion

The fault-bounded Cianzo basin is delimited by 1) reactivated and inverted Cretaceous structures with orientations oblique to Andean shortening, and 2) Cenozoic structures with orientations resulting from Andean shortening. In the following sections we discuss the Salta Rift phase and subsequent Andean phase, as well as their corresponding structures and exhumation processes.

4.5.1 Salta Rift

The Hornocal fault, delimiting the Cianzo basin to the SE, is a prime example of an inverted Cretaceous normal fault, as is evident from rapid changes in the thicknesses of syn-rift sediments adjacent to the fault (Kley et al., 2005; Starck et al., 1993; Starck, 1995). Multiple splay faults in the SW part of the Hornocal fault cut off fault blocks, which show strong variations in sedimentary thickness of Mesozoic strata. The proximal, fault-related Ocumazo conglomerates (Tacurú Group), present in the hanging wall blocks of the Hornocal and Ocumazo faults (Figure 4.3a), are the earliest strata that are connected to fault activity (Van Kooten et al., 2022a). Pirgua Subgroup deposits similar to the Tacurú Group in the Cianzo area have been described at the base of the Sapagua half-graben, west of the Cianzo basin (Figure 4.1a) (Monaldi et al., 2008). These deposits are composed of eolian and fluvial sandstones, and non-channelized debris flows, which thicken toward the fault. While the succession in the Cianzo area was ascribed to Tacurú Group pre-rift strata, the deposits in the Sapagua half-graben have been connected to the early phases of the Salta Rift (Monaldi et al., 2008). The Tacurú Group in the Cianzo area has a Jurassic detrital zircon U-Pb maximum depositional age, pointing toward pre-Salta Rift extension (Van Kooten et al., 2022a). The distribution of the Ocumazo conglomerate south of the northernmost Hornocal fault splay (H1; Figure 4.3a) suggests that normal faulting was initiated along this fault plane.

ZHe samples from the Aparzo range consistently document Jurassic and Cretaceous cooling ages, although dispersion is high (Table 4.1 and Table C.1, Appendix C). Single sample models do not allow for good constraints on Cretaceous exhumation, although all models appear to predict an onset of cooling interpreted to be related to rift shoulder exhumation after 200 Ma. Although the Salta Rift has generally been assigned a Cretaceous age based on the syn-rift succession (e.g., Marquillas et al., 2005), a Jurassic onset of rifting has also been discussed previously (Cristiani et al., 2003; Kley and Monaldi, 2002). Thermochronology data from the Eastern Cordillera correspond to a pre-Cretaceous onset of rifting (Deeken et al., 2006; Van Kooten et al., 2022a; Zapata et al., 2019a). However, with few reset ZHe samples available from the rift shoulder and a high dispersion of cooling ages, we have limited possibilities to constrain the onset of rifting in this part of the Lomas de Olmedo sub-basin. AFT and AHe ages have been reset or partially reset through burial by several kilometers of Cretaceous–Miocene strata and thus mostly document Andean rather than Salta Rift exhumation.

The Salta Rift phase is marked by the deposition of thick syn-rift strata south of the Hornocal fault. The strong variation in sedimentary thickness of the Salta Group north and south of the fault, with an absence of syn-rift strata in the footwall, has been discussed in previous studies (e.g., Amengual and Zanettini, 1973; Kley et al., 2005). Thickness variations of the Pirgua Subgroup within the Cianzo syncline show that subsidence increased toward the NE, with a maximum thickness of > 4000 m near Cerro Colorado de Caspalá. In the SW, where the Hornocal fault splays into multiple faults (Figure 4.3a), the thickness of the Pirgua Subgroup is reduced from > 1600 m in the hanging wall, to 430 m in the intermediate block. This variations suggests that, while the northernmost and central splay faults (H1, H2; Figure 4.3a) formed during the initial stages of rifting, the southernmost splay fault (H3) formed the main basin boundary during the Cretaceous.

4.5.2 Post-rift phase

The post-rift units of the Salta Group start with the Lecho Fm, which is absent in the footwall of the Hornocal fault, as well as the lower part of the overlying Yacoraite Fm. Where the Lecho Fm is absent, the upper part of the Yacoraite Fm unconformably overlies the Ordovician Santa Victoria Group. Facies of the Yacoraite Fm can be mostly ascribed to the littoral and sub-littoral facies associations, a zonation introduced by Renaut and Gierlowski-Kordesch (2010) for lacustrine depositional systems. Oolitic grainstones were deposited in upper littoral and marginal areas of the Yacoraite paleo-lake, forming extensive shoals within moderate to high energy wave-influenced conditions, as indicated by the clean grain supported fabrics, a good degree of sorting and common wave ripples and wavy bedding. Rare storm-weather events resulted in the deposition of chaotic shell accumulations (gastropod shell rudstones), forming storm-beds characterized by distinctive erosive bases, chaotic shell accumulations and common intraclasts. Peloidal and ostracodal grainstone-packstones were deposited in a low to moderate energy environment, likely in the sheltered areas in the back-shoals of the littoral zone or alternatively, in more distal settings within the sub-littoral zone. In more distal settings, ostracod wackestones were deposited through settling within the water column, only occasionally influenced by weak currents in a low-energy and relatively deep water environment. Siliciclastic-dominated facies were deposited in proximity to fluvial sources and formed shallow-water low-relief deltas, reworked by currents and waves into shoreline sandstones. Alternatively, the thin and tabular sandstone beds represent sheet-like sandflats and bars deposited in proximity to river inputs (McLane, 1995; Tänavsuu-Milkeviciene et al., 2017). The facies associations and stratigraphic architecture observed suggest that deposition of the lower post-rift section in the Cianzo area likely occurred in a highly fluctuating, restricted depositional environment. Our observations are in line with hypotheses from other authors (Deschamps et al., 2020; Gomes et al., 2020; Hernández et al., 2008; Llorens et al., 2022; Palma, 2000; Rohais et al., 2019), who interpreted the Yacoraite Fm as being deposited in a lacustrine environment. The common presence of lacustrine ostracods (Ceolin et al., 2022), the rapid facies transitions and high vertical heterogeneity of the succession also lend support to this interpretation, together with the absence of any common marine fossil.

The Yacoraite paleo-lake corresponds to a balanced-fill lake basin type, characterized by facies comparable to the “Fluctuating Profundal” association described by Carroll and Bohacs (1999), suggesting a perennial and relatively stable lake system. The predominance of littoral facies and the depositional geometries represented by thin, tabular beds suggest deposition in a shallow-water lake, likely with a low-relief ramp-like profile. Extensive wave-dominated littoral areas allowed the development of oolitic grainstone shoals as seen in other lake systems (Chidsey et al., 2015; Sarg et al., 2013).

The Yacoraite Fm in the measured section on the Hornocal fault footwall presents marked differences in the facies expression and stratigraphic thickness when compared to other outcrops from different Salta Rift sub-basins (e.g., northern Tres Cruces sub-basin, southern Metán-Alemania; Figure 4.1a). In Cianzo, sub-aerial exposure features were not observed, whereas tepees, desiccation cracks and paleosol are common in sections measured in other localities (Boll et al., 1989). In contrast to the section found in the Cianzo syncline (Figure 4.2b), the condensed Yacoraite Fm section was deposited on an erosive contact to the Santa Victoria Group below. Furthermore, the facies and lithological succession described are characteristic for the upper Yacoraite Fm, suggesting the lower part of the formation was either not deposited or eroded. We propose that the condensed Yacoraite Fm section found in the Hornocal fault footwall represents the overspill of the Lomas de Olmedo sub-basin due to decreasing subsidence rates and a filling of the accommodation space. This is in line with a reducing thickness from the southern Cianzo syncline toward the Hornocal fault trace (Boll et al., 1989 and Section 4.2) and suggests that the Lecho Fm and lower part of the Yacoraite Fm were not deposited on the footwall.

4.5.3 Andean orogeny

Structural framework

Inversion of the Hornocal fault is evident from the differential structural elevation of syn- and post-rift strata (Kley et al., 2005). In the northern segment of the Hornocal fault, Siks and Horton (2011) document growth strata in a footwall syncline in the Pisungo Fm (upper Miocene). The southern segment of the Hornocal fault is also marked by a footwall syncline within the Rio

Grande Fm (upper Oligocene–Miocene) (Figure 4.3a). The NNE–SSW trending fold axis of this syncline plunges oblique to the trace of the fault. Folds in the hanging wall of the Hornocal fault (i.e., Cianzo syncline, Caspalá folds) are oriented similarly, with less steeply plunging axes. In a previously undeformed pile of sediments, newly formed folds will form perpendicular to the direction of shortening (e.g., Ortner and Gruber, 2011). Therefore, in the absence of pre-Andean shortening, NNE–SSW striking folds in Neogene strata would likely form due to ESE-directed shortening. This direction of shortening corresponds to the earlier thrust regime in the southern Central Andes (Allmendinger, 1986; Marrett et al., 1994; Marrett and Strecker, 2000). Analogue models of obliquely inverted basin margins show that, although deformed zones are preferentially reactivated, the orientation of newly formed thrusts is perpendicular to the maximum shortening direction and contractional structures rotate toward pre-existing oblique faults in the vicinity of the fault plane (Almilibia et al., 2005). On the other hand, Payrola et al. (2012) demonstrate that the inversion of normal faults may lead to the formation of fault-propagation folds oblique to the direction of shortening. In the case of the Cianzo syncline, the strike of the eastern limb is rotated clockwise toward the Hornocal fault. This corresponds to a “dextral strike-slip component of motion on the Hornocal fault during reactivation” (Kley et al., 2005, p. 166), which resulted from the obliquity of the Hornocal fault relative to the Andean direction of shortening.

In contrast to the Hornocal fault, there is no conclusive evidence whether the Cianzo thrust is a reactivated structure or formed during Andean orogenesis. Paleozoic, inherited structures occur regionally (Alonso et al., 2012; Mon et al., 1993; Seggiaro and Gallardo, 2002). There are N–S striking, east-vergent reactivated Paleozoic faults in the Tilcara Range (Barrabino et al., 2015). The high-angle, reverse fault character of the Cianzo thrust is a conspicuous marker of an inherited structure, given that in external parts of orogens thrust faults are amongst the first structures to form in the upper crustal levels (Ramsay and Huber, 1987). Fault activity since the Miocene has led to tilting and overturning of Miocene strata (Rio Grande Fm) in the footwall. However, this does not offer a minimum age for shortening.

Timing of uplift, deformation and exhumation

AHe and AFT samples from the Cianzo syncline document the timing of inversion of the Hornocal fault. The negative age-elevation trend for AHe samples in the western limb (Figure 4.5) suggests that the strata were tilted during or after cooling through the APRZ, whereas the data from the eastern limb (Figure 4.6, 4.7) suggest that the samples were exhumed through the APRZ in a tilted position. Henríquez et al. (2023), based on their balanced cross-section and retrodeformation, suggest that the western limb of the Cianzo syncline was tilted during Hornocal fault inversion, while at a later stage the formation of a major anticline to the east led to tilting of the eastern limb. Our thermal models show an overlapping Oligocene to middle Miocene onset of exhumation, as well as similar exhumation rates of ~0.25 mm/a for both limbs (Table 4.3, Figure 4.5–4.7). However, the resolution of these models is not high enough to resolve a difference in the timing of exhumation of the individual limbs. An Oligocene to middle Miocene onset of exhumation for the Hornocal fault matches the timing suggested for the Tilcara Range (Van Kooten et al., 2022b), located south of the Cianzo basin. Growth strata in the footwall of the Hornocal fault (Figure 4.3a) provides a middle–late Miocene age constraint for fault activity, based on $^{40}Ar/^{39}Ar$ analyses (Siks and Horton, 2011). While this appears to be slightly younger than the thermal models, it is possible that not all segments of the fault were reactivated at the same time. Henríquez et al. (2023) suggest a Late Miocene–Pliocene timeframe (6.5–2.1 Ma) for main activity of both the Cianzo thrust and Hornocal fault, much younger than what our data suggests. The data set of Henríquez et al. (2023) does not provide data points within the Cianzo syncline (Figure 4.1b). Consequently, our data set includes higher elevation samples with older cooling ages than provided by Henríquez et al. (2023) and thus is able to record an earlier onset of exhumation.

Published AFT data from the Cianzo thrust hanging wall (2 samples; Henríquez et al., 2023) in part fit on the age-elevation trend set by our AP samples (Figure 4.4a). Both samples are reset for Andean exhumation, whereas our upper samples are partially reset. Therefore, the upper sample of Henríquez et al. (2023), which was collected north of our section (Figure 4.1b), is younger than e.g., sample AP4 from a similar elevation. As a consequence, our thermal models predict an earlier onset of cooling than the exhumation time step proposed by Henríquez et al. (2023). Our thermal models show an onset of cooling interpreted to be related to exhumation in the middle to late Miocene. This suggests that initial fault activity along the Cianzo thrust occurred at a later stage than along the Hornocal fault, but both faults were active at one point in time during their multiple episodes of reactivation. It has been proposed that fault activity along the Cianzo thrust succeeds activity along the Hornocal fault (Henríquez et al., 2023; Siks and Horton, 2011), with the Cianzo thrust decapitating the latter. Our thermal models are not able to resolve this, given that cooling in all models is continuous. Simple thermal histories with continuous cooling are favored by the Bayesian approach taken by QTQt (Gallagher, 2012) and thus the modeling results may not exactly reflect the structural observations. Although the Andes experienced an overall eastward propagation of deformation (Pearson et al., 2013), out-of-sequence deformation has been recorded in the NW Argentina (e.g., Del Papa et al., 2013; Montero-López et al., 2018; Payrola et al., 2020) and has been proposed for the Eastern Cordillera between 23 and 24°S (Henríquez et al., 2023).

Within the Paleozoic strata east of the Cianzo syncline, existing AFT cooling ages (Henríquez et al., 2023) mostly plot on the same trend as the ages in our data set (Figure 4.8). One sample from Henríquez et al. (2023) is younger than the rest, but was sampled north of the Hornocal fault (Figure 4.1b). Nine single-grain AHe ages are slightly younger than our data (Reiners et al., 2015), but fit well on the overall trend (Figure 4.8). Four published single-grain ZHe ages (Reiners et al., 2015) appear to be non- or partially-reset for Cenozoic exhumation, corresponding to our results. In the underlying Santa Victoria Group, young (upper Miocene) ZHe ages occur with increasing stratigraphic depth. These ages may reflect partial resetting due to burial, as well as inherited kinematic properties of the crystals (i.e., high eU and hence radiation-damage control on young ages, corresponding to Guenthner et al., 2013). At the same time, the positive age-stratigraphy trend suggests that tilting of the samples due to folding occurred at the earliest during cooling through the ZPRZ (~170–190 °C, ignoring specific kinetic characteristics). Thermal modeling results show that the onset of exhumation, although in part overlapping with exhumation of the Cianzo syncline, generally youngs toward the east. This is in agreement with the model of Henríquez et al. (2023), as well as the observed eastward younging of cooling ages (Reiners et al., 2015) and general propagation of deformation (e.g., Anderson et al., 2017; Anderson et al., 2018; Carrapa et al., 2011; DeCelles et al., 2007; DeCelles et al., 2011; Deeken et al., 2006; Gubbels et al., 1993). Our youngest (Pliocene) AHe cooling ages, located at the eastern margin of the study area, overlap with cooling ages of Van Kooten et al. (2022b) and fall into the 6.5–2.1 Ma time step of Henríquez et al. (2023). These data suggest that, although uplift and exhumation have occurred since at least the Miocene, it has been ongoing until very recently in this part of the Eastern Cordillera.

4.6 Conclusions

Based on our field observations, sedimentological and thermochronological studies, we propose the following timeline for the Cianzo area:

1) Salta Rift phase (Cretaceous–Paleogene): With increasing accommodation space along the Hornocal fault, a thick syn-rift succession (Pirgua Subgroup) was deposited with a maximum subsidence in the present-day Cerro Colorado de Caspalá area. Maximum normal movement occurred along the southernmost splay of the Hornocal fault. During the post-rift phase, lacustrine strata (Yacoraite Fm) filled up the basin. On lake margins on the northern rift shoulder, condensed successions were deposited.

2) Andean phase 1 (Oligocene?–middle Miocene): ESE-directed shortening during Andean orogeny led to the reactivation of the Hornocal fault, the formation of NNE–SSW striking synclines in its footwall and folding of the Cianzo syncline in the hanging wall. Low-temperature thermochronology suggests that an onset of exhumation occurred between the Oligocene and middle Miocene. Structural evidence of fault activity (Siks and Horton, 2011) has been observed from the middle–late Miocene.

3) Andean phase 2 (middle Miocene–Pliocene): Exhumation propagated to the Paleozoic strata east of the Cianzo syncline. West of the Hornocal fault, the Cianzo thrust was active and the western limb of the Cianzo syncline was tilted. Pliocene AHe cooling ages from the easternmost part of the Eastern Cordillera show that exhumation was recent.

Although thermal modeling using QTQt cannot perform across-fault-modeling, our data set and results offer a solid basis for future 3D thermal modeling. This could increase the resolution and further improve exhumation constraints for the Eastern Cordillera.

Chapter 5. Discussion and conclusions

The aim of this study is to offer new insights into exhumation patterns in the Eastern Cordillera between 23 and 24°S, where extensional structures and stratigraphic anisotropies of the Mesozoic Lomas de Olmedo sub-basin in part control the localization and timing of compressional deformation. To this goal, the earliest onset of extension and rift shoulder exhumation in NW Argentina, and the structural and sedimentary development of the Lomas de Olmedo sub-basin margin were analyzed using sedimentary analyses (point counting, facies analysis from field data), detrital zircon U-Pb geochronology and ZHe thermochronology. To constrain Andean deformation, reactivation and inversion of pre-existing structures, structural field observations combined with low-temperature AHe, AFT and ZHe thermochronology were used. Resulting from this is a comprehensive data set of cooling ages and corresponding thermal models that describes two consecutive phases of exhumation and provides a deeper understanding of the influence of pre-existing heterogeneities on exhumation patterns in the Eastern Cordillera between 23 and 24°S.

In this chapter I provide an interpretation of the main results from Chapter 2, 3 and 4 in a broader geological context. The implications of these results are discussed in the framework of the research questions stated in the introduction and compared to existing literature to highlight their contribution to the reconstruction of the Central Andes geological evolution. Furthermore, I address the limitations of the research methods used in this study and discuss future research questions and the methodology that may be used to answer these.

5.1 Mesozoic evolution of the Lomas de Olmedo rift shoulder

The history of Cretaceous extension in NW Argentina has often been described from a sedimentary point of view by characterizing the syn-rift Pirgua Subgroup (Salta Group; e.g., Marquillas et al., 2005; McBride, 2008). Low-temperature thermochronology cooling ages documenting rift shoulder exhumation are scarce (see compilation in Stalder et al., 2020), because AHe and AFT ages are mostly reset for Andean exhumation and ZHe ages often show the detrital provenance signature of the Proterozoic and Paleozoic strata (Table 3.1, 4.1, B.1 and C.1). In this section, I address the onset of extension and rift shoulder exhumation in the southern Central Andes and the subsequent evolution of the Lomas de Olmedo rift basin, using thermochronological and sedimentological data.

Samples from the southern and northern rift shoulder of the Lomas de Olmedo sub-basin display a spectrum of Late Triassic to Early Cretaceous ZHe cooling ages (see also Figure 5.1). Single-grain cooling ages are highly dispersed between and within samples, which may be attributed to the Proterozoic–Paleozoic depositional age and long thermal history of the samples. Thermal models allow to constrain the onset of rift shoulder exhumation to the Early Cretaceous (140–115 Ma) in the Tilcara Range (Chapter 3) and show a loose Jurassic–earliest Cretaceous constraint in the Aparzo Range (> 190 Ma for model HO1; 160–140 Ma for model AP-AE; Chapter 4). On the southern rift shoulder (Sample BREN1), cooling ages range from the Late

Triassic to Early Cretaceous (Chapter 2). Although these ages are older than the timeframe proposed for more southern parts of the Central Andes (Carrapa et al., 2014; Deeken et al., 2006; Sobel and Strecker, 2003), it is clear that based solely on low-temperature thermochronology, rift shoulder exhumation cannot be constrained more tightly. However, the interpolation of ZHe dates over the study area shows a clear distribution of older, non-reset cooling ages in the depocenter south of the Hornocal fault (Figure 5.1).

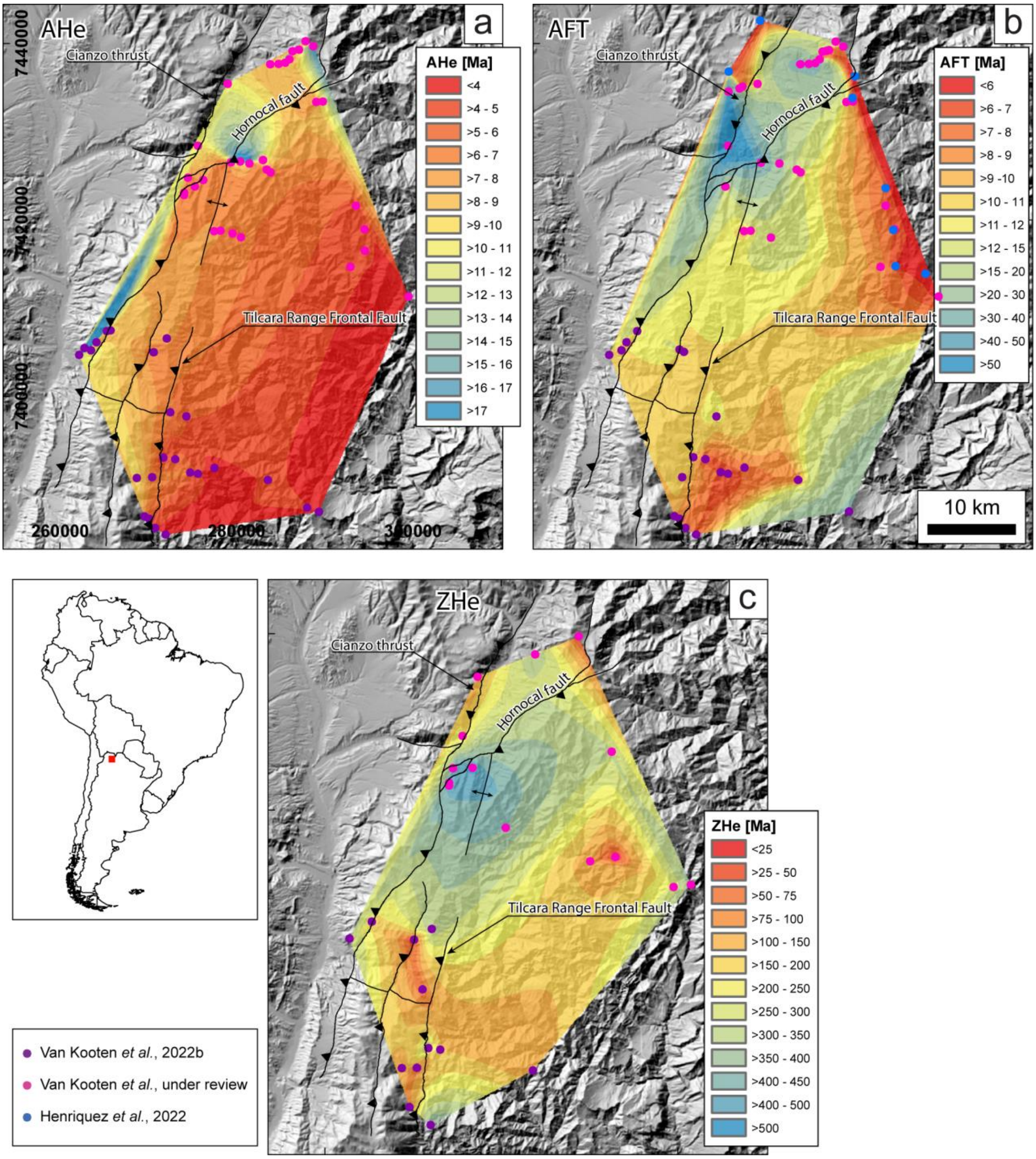

Figure 5.1 Interpolation of low-temperature thermochronology cooling ages in the Eastern Cordillera between 23 and 24°S. (a) Distribution of AHe, (b) AFT and (c) ZHe cooling ages within the Tilcara, Aparzo and Hornocal ranges in relation to major structural elements. For AHe and ZHe ages, the weighted mean age (calculated in IsoplotR; Vermeesch, 2018) was used. The data were interpolated using a nearest neighbor algorithm. AFT dates from Henríquez et al. (2023) are included.

Whereas in most localities between 23 and 24°S the Salta Group was deposited on top of Paleozoic strata (e.g., González and Tchilinguirian, 2003; Rodríguez-Fernández et al., 1999), the Tacurú Group forms a local transitional unit in the Cianzo basin. Starck (2008) correlates the strata found in the Cianzo basin with upper Jurassic eolian deposits in Bolivia (Kusaik, 2008; Sempere, 1995; Tomezzoli, 1996). In Cianzo, widespread eolian sandstones alternate with the very local Ocumazo conglomerate, which shows major thickness variations relative to normal faults (Chapter 2.5). Both the Ocumazo conglomerate and the overlying Pirgua Subgroup show an upper Jurassic MDA (155 ± 2 Ma and 150 ± 1 Ma, respectively; see also McBride, 2008). The stratigraphy of the basal Pirgua Subgroup in the Sapagua half-graben, located ~30 km NW of Cianzo (Monaldi et al., 2008), demonstrates that there are lithological similarities between the local basal succession of eolian sandstones and debris flow deposits of the Pirgua Subgroup and strata of the Tacurú Group in the Cianzo basin. At the same time, the Bolivian strata, with which the Tacurú Group in the Cianzo basin is correlated (Starck, 2008), are interpreted to reflect post-rift deposition (Sempere et al., 2002). The Tacurú Group and Pirgua Subgroup are separated by a major angular unconformity and marked differences in sediment provenance (Chapter 2.4). Furthermore, the Pirgua Subgroup is widely distributed throughout the Salta Rift basin (Marquillas et al., 2005) and shows rapid thickness variations in relation to structures such as the Hornocal fault (Chapter 4; see also Amengual and Zanettini, 1973; Kley et al., 2005), whereas the Ocumazo conglomerate was deposited in local depocenters. In summary, although both units represent fault-related syn-tectonic strata in the Cianzo area (Starck, 2008), the Tacurú Group and Pirgua Subgroup mark separate stages in the evolution of the Central Andes. Backtilting of the strata shows that the direction of extension may have rotated between deposition of the Tacurú Group conglomerates and the basal Salta Group (Figure 2.7). Kley et al. (2005) have suggested a similar multi-phase extension history to explain variable orientations of Salta Rift faults.

The debate surrounding the timing of extension in NW Argentina has been ongoing, with an Early Cretaceous onset of extension described that is based on the depositional age of the syn-rift Pirgua Subgroup (e.g., Galliski and Viramonte, 1988; Marquillas et al., 2005; Salfity and Marquillas, 1994 and references therein), whereas other data suggest a pre-Cretaceous onset of extension for the Salta Rift (e.g., Cristiani et al., 2003; Deeken et al., 2006; Hauser et al., 2010; Insel et al., 2012; Kley and Monaldi, 2002). The data in this study suggest that the onset of extension in the southern Central Andes may have begun during the (Late) Jurassic.

The deposition of the Pirgua Subgroup in the western Lomas de Olmedo sub-basin is especially related to the formation of accommodation space along the basin-bounding Hornocal fault (Kley et al., 2005). The present-day architecture of this now inverted fault, with several splay faults in its southwestern part, has previously been recognized (e.g., Siks and Horton, 2011). However, whether these splay faults have been present since the Mesozoic, or are a feature of the Andean orogeny has not been addressed. Field observations show that the thickness of the Pirgua Subgroup increases from the northernmost splay fault (H1) to the hanging wall of the southern fault (H3; Chapter 4.4). The deposition of the Tacurú Group conglomerates also appears to be related to the position of these faults. No syn-rift strata have been deposited on the rift shoulder (Kocks, 1999). Therefore, the faulting must have initiated along the northern Hornocal splay fault

(H1). The thickness increase for the Pirgua Subgroup suggests that the central (H2) and southern (H3) splay faults were formed during the initial stages of rifting. These thickness variations furthermore show that the local depocenter was located near the present-day Cerro Colorado de Caspalá (Chapter 4.4; see also Boll et al., 1989; Kocks, 1999; McBride, 2008). In contrast, the post-rift sediments show a decreasing thickness from the sub-basin depocenter toward the fault trace (Chapter 4.4; see also Boll et al., 1989) and a condensed succession on the rift shoulder (Zenta Range; Figure 4.2). The rapid decrease of thickness toward the rift shoulder and the facies variations record the infill of the Lomas de Olmedo basin by lacustrine sediments that, through lack of accommodation space, eventually overspilled onto the rift shoulder (Starck, 2011). This marks the beginning of the Cenozoic history of the Lomas de Olmedo sub-basin.

5.2 Cenozoic deformation and exhumation history

The low-temperature thermochronology data set in this study comprises AHe, AFT and ZHe data from the Eastern Cordillera between 23 and 24°S, including samples from the Tilcara Range and adjacent San Lucas block, and the basin-bounding Aparzo, Hornocal and Zenta Ranges. In this section, I address the interpretation of this data set and its implications for the timing of fault initiation and reactivation, deformation and exhumation in the Eastern Cordillera.

In the Tilcara Range, cooling that is interpreted to result from exhumation started in the easternmost fault blocks in the late Oligocene–early Miocene (26–16 Ma). In the windward part of the range, the onset of exhumation is coeval along-strike and is slightly shifted toward younger ages (22–10 Ma) compared to the leeward side (26–16 Ma). Leeward cooling rates are lower (6.0–6.6 °C/Ma; 0.20–0.22 mm/a assuming a geothermal gradient of 30 °C/km) than windward cooling rates (7.2–15.9 °C/Ma; 0.24–0.53 mm/a). This may be attributed to the more humid climate on the windward side of the Tilcara Range and the enhanced erosion that impacts exhumation rates (Pingel et al., 2014; Sobel and Strecker, 2003). The easternmost Tilcara Range is uplifted along a frontal fault (Tilcara Range Frontal Fault), with a structural offset of 400 m (based on the offset Salta Group unconformity). ZHe ages consistently record an offset across this fault, with young (Cretaceous–early Paleogene) ages in the hanging wall block and Paleozoic to Jurassic ages in the footwall block. AFT cooling ages document little offset and AHe ages show a continuous age-elevation relationship. Thus, AFT dates record the final stages of fault activity before the samples cooled through the apatite partial retention zone at ≥ 7 Ma (see Chapter 3.5). Thermal models show that cooling of the Mesozoic and Paleozoic units east of the Tilcara Range (San Lucas block) started between 10–8 Ma and continued at least until the Pleistocene. Within these units, ZHe and AFT ages are aligned on an age-stratigraphy trend, whereas AHe ages form an age-elevation trend, showing that internal deformation of the San Lucas block commenced ≥ 7 Ma.

In the Cianzo basin, cooling interpreted to be a result of Andean exhumation is mostly documented by AHe and AFT cooling ages (Table 4.1, 4.2, Figure 5.1). Thermal models show a late Oligocene to middle Miocene (~24–15 Ma) onset of cooling of the Hornocal Range, with average exhumation rates of ~0.25 mm/a (assuming a geothermal gradient of 30 °C/km). Exhumation rates for the late Miocene and the Eastern Cordillera, calculated by Stalder et al.

(2020), are similar to our exhumation rates inferred from thermal models. The timing of exhumation in the Hornocal Range corresponds to the onset of exhumation for the western Tilcara Range (Chapter 3), with slightly lower cooling rates. However, it does not overlap with the late Miocene–Pliocene timeslot that was recently proposed for the main uplift along the Hornocal fault (Henríquez et al., 2023). Growth strata in the footwall of the Hornocal fault record pronounced uplift of the Hornocal Range in the middle–late Miocene (Siks and Horton, 2011), which does not exclude an earlier onset of exhumation in the late Oligocene to middle Miocene. Both the Aparzo Range and Paleozoic units east of the Hornocal Range show a middle Miocene onset of exhumation (14–9 Ma). Whether activity along the Cianzo thrust and uplift of the Aparzo Range outlasts Hornocal fault activity, as has been suggested (Henríquez et al., 2023; Siks and Horton, 2011), cannot be resolved by the thermal models. Cooling rates of the Aparzo Range are similar to those of the Hornocal Range, whereas the Paleozoic units east of Hornocal show higher rates. This may be attributed to the eastward increase in humidity caused by the Hornocal Range forming an orographic barrier. Pingel et al. (2013) ascribe a Pliocene–Pleistocene age to aridification west of the Tilcara Range. In the Hornocal Range, substantial relief may have formed by the late Miocene (Siks and Horton, 2011).

Comparisons of cooling ages in this study with the sparse data available for the Eastern Cordillera between 23 and 24°S (see figures in Stalder et al., 2020 and Chapter 4) show that published AHe, ZHe (Reiners et al., 2015) and AFT (Henríquez et al., 2023) ages from samples collected in Paleozoic strata mostly plot on the trends reflected in our samples. Individual ages that do not overlap with our data and trends are often located in different fault blocks, or horizontally offset relative to the sections in this study.

The interplay of uplift and deformation is exemplified in various relationships between structures, cooling ages and sampling elevation or stratigraphic elevation (Chapter 4.4.2). These relationships demonstrate that while the western limb of the Cianzo syncline in the hanging wall of the Hornocal fault was tilted during or after cooling through the apatite partial retention zone, the eastern limb was tilted before and exhumed in a tilted position. In a recent publication, however, Henríquez et al. (2023) suggest that the western limb was tilted before the eastern limb. Pliocene AHe cooling ages at the eastern margin of the study area overlap with AHe data from the eastern San Lucas block, showing recent (Pliocene–Pleistocene) deformation in this area (see also Henríquez et al., 2023). Cooling ages and results from thermal modeling show a general younging-eastward trend (Figure 5.1) corresponding to in-sequence propagation of the Andean wedge (e.g., Anderson et al., 2017; Anderson et al., 2018; DeCelles et al., 2007; DeCelles et al., 2011; Gubbels et al., 1993; Reiners et al., 2015). Out-of-sequence movement of the Cianzo thrust is in line with data from other parts of NW Argentina (e.g., Del Papa et al., 2013; Montero-López et al., 2018; Payrola et al., 2020).

Although the timing of exhumation is quite similar along-strike N–S, the Tilcara Range and the Cianzo basin show a different structural framework, which can be ascribed to varying influence of pre-Andean anisotropies and their orientation. The Tilcara Range is internally dissected by high-angle, N–S striking, east-vergent reverse faults (González and Tchilinguirian, 2003;

Rodríguez-Fernández et al., 1999) that may or may not be attributed to the reactivation of Paleozoic crustal heterogeneities. The faults are oriented approximately perpendicular to Andean shortening and are thus easily reactivated. Salta Rift-related faults in the Tilcara Range (Chapter 3) do not show signs of reactivation due to unfavorable orientations (Kley et al., 2005). The Cianzo thrust shows an orientation and dip similar to the N–S faults bounding the Tilcara Range (Amengual and Zanettini, 1973; Siks and Horton, 2011). The Hornocal fault, in contrast to the Salta Rift faults in the Tilcara Range, strikes NE–SW (Amengual and Zanettini, 1973; Kley et al., 2005) and is thus oriented more suitably for inversion.

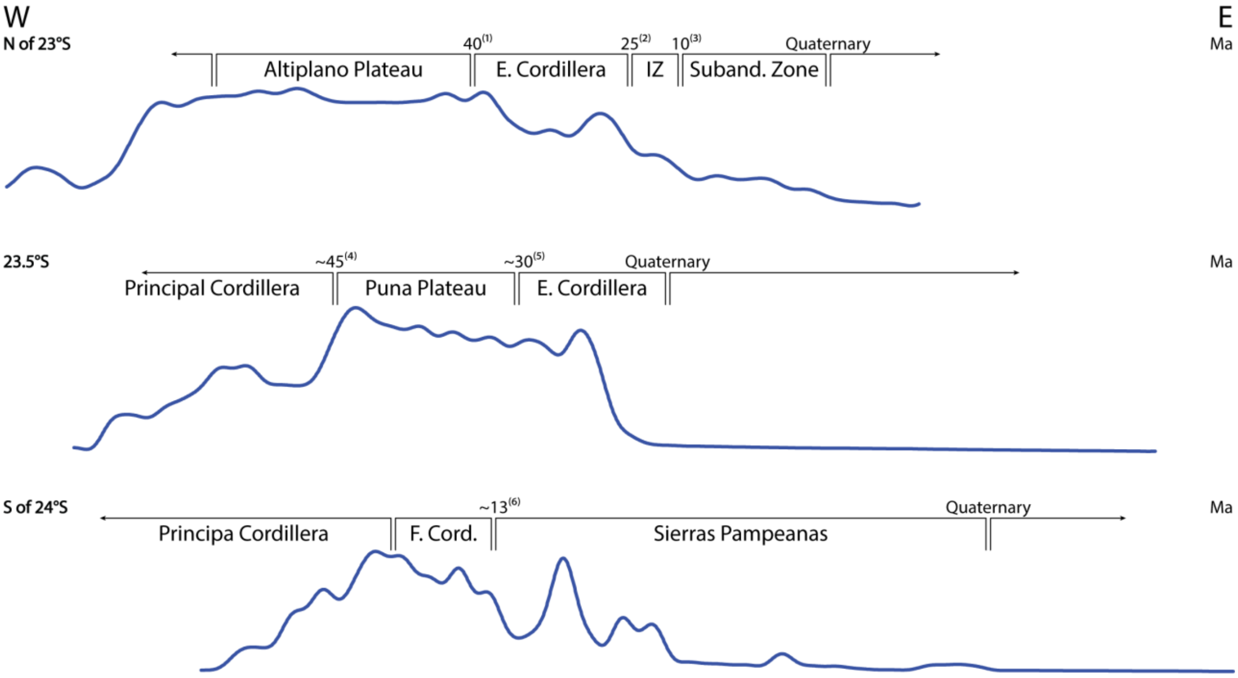

Figure 5.2 Schematic compilation of the timing of exhumation for various ~W–E sections across the Central Andes. (1) McQuarrie et al., 2008; (2) Anderson et al., 2018; Ege et al., 2007; McQuarrie et al., 2008; Müller et al., 2002; (3) Anderson et al., 2018; (4) Henríquez et al., 2020; (5) Coutand et al., 2001; Henríquez et al., 2023; (6) Zapata et al., 2019b.

Compared to sections north and south of the study area, the propagation of exhumation from the western to the eastern margin of the Eastern Cordillera occurred at different points in time. North of 23°S, exhumation propagated from the eastern border of the Eastern Cordillera into the Interandean Zone around 25 Ma (Anderson et al., 2018; Ege et al., 2007; McQuarrie et al., 2008; Müller et al., 2002) (Figure 5.2). Contemporaneous exhumation at 23.5°S occurred at the western border of the Eastern Cordillera (Chapter 3; Coutand et al., 2001; Henríquez et al., 2023 and references therein). Uplift has been disparate South of 24°S, but propagated to the Sierras Pampeanas no earlier than ~ 13 Ma (Zapata et al., 2019b). Recent (Quaternary) deformation has occurred at the eastern margin of the Subandean Zone in Bolivia, whereas it was located at the eastern margin of the Eastern Cordillera at 23.5°S, where the Subandean Zone is terminated.

5.3 Limitations

Within the multi-method approach chosen for this study, each method has its own limitations. The detrital zircon U-Pb ages obtained from Mesozoic strata show a skewed distribution of U-Pb ages, with a very small number of younger grains. This limits the possibilities of using statistically more robust methods for maximum depositional age calculations. In cases where the age difference between the youngest grains of a sample is large, the maximum likelihood age will simply be identical to the youngest single grain age (Vermeesch, 2021). The latter in particular is susceptible to external sources of error (Coutts et al., 2019). For samples from the Tacurú Group and Pirgua Subgroup, however, where an approximate depositional age is known, applying the youngest 1σ or 2σ grain cluster would lead to a very conservative age estimation. Measuring a much larger number of grains may resolve this problem, although there appears to be a general scarcity or absence of Mesozoic grains in the younger sediments of NW Argentina (e.g., Carrapa et al., 2012; DeCelles et al., 2011; Pearson et al., 2012).

For low-temperature apatite and zircon thermochronology, a major limitation has been the lack of geometrically ideal zircon and apatite grains. Although grains picked for AHe or ZHe dating were generally within an acceptable size range (> 60 µm width), larger crystals would have been preferred because these have a smaller surface area compared to the total size and are thus less affected by boundary effects of He diffusion. In addition, apatite crystals for AHe dating often had a frosted surface and a rounded geometry, caused by e.g., abrasion and chemical erosion. Frosting makes it more difficult to see inclusions and cracks, which can impact cooling ages, and furthermore increases the surface area of a grain. Rounding impairs F_T calculations, which generally assume an ideal crystal geometry. Dispersion in (U-Th-Sm)/He ages was highest in the stratigraphically oldest units. While this may be attributed to radiation damage that accumulates in these grains, correlations between e.g., eU, F_T or ESR are generally lacking. Dispersion within the AHe and ZHe data has affected thermal modeling whenever these correlations were absent. Significant dispersion can be an effect of long residence within the partial annealing or partial retention zone (e.g., Flowers et al., 2007; Guenthner et al., 2013). Furthermore, the geometrical and surface quality of the grains was lower for the Paleozoic units than for the Mesozoic units. AFT analyses were mostly impaired by the lack of suitable grains to count and dislocations within the grains, in particular in Neoproterozoic–Paleozoic units. As a consequence of the young cooling ages, there was a lack of a significant number of confined track length measurements. This has impaired thermal modeling procedures, since track lengths provide important information for the models.

For thermal modeling we consistently used the expected model, rather than the maximum likelihood, maximum posterior or maximum mode model, as recommended by Gallagher (2012). The expected model represents a range of models. Therefore, the data fit is not as good and the constraints produced by these models are less tight compared to e.g., the maximum likelihood model. It is tempting to use maximum likelihood or maximum posterior thermal models to constrain exhumation. However, the expected model is favored in the Bayesian approach because the maximum likelihood and maximum mode models contain more time-temperature points and are thus more complex (Gallagher, 2012). The maximum posterior model, in contrast, is in most cases too simple to represent the geologic history of the samples. Independent of the model, the resolution of QTQt models for the Eastern Cordillera is not high enough to resolve differential exhumation in smaller-scale structures. In the case of the Cianzo syncline, both fold limbs show overlapping constraints on the onset of exhumation in thermal models, even though the trends in cooling ages suggest that there was a differential exhumation across the syncline.

5.4 Outlook

The data set presented in this study provides new constraints for the exhumation patterns of the Eastern Cordillera between 23 and 24°S. However, some questions remain unanswered and various questions have emerged.

Although the nature of the Ocumazo conglomerate (Tacurú Group) as a fault-related, syn-tectonic deposit has been described in Chapter 2, a link between Jurassic and Salta Rift extension could not be confirmed based on the data in this study. To answer the question, whether these phases are connected, detailed structural and stratigraphic analyses of field relations must be conducted. Potential methods include measuring detailed stratigraphic sections across unconformities and on various fault blocks, conglomerate clast counting in the Tacurú Group and basal Pirgua Subgroup, and the analysis of flow directions. McBride (2008) has measured a section across the basal Salta Group unconformity, but assigned the Ocumazo conglomerate (Tacurú Group) to the syn-rift section. Correlations between eolian strata in Bolivia (Kusaik, 2008; Sempere, 1995; Tomezzoli, 1996) and the eolian Tacurú Group in the Cianzo syncline (see Starck, 2008) may also further constrain the Mesozoic development of the depositional realm in this part of the Central Andes.

From a methodological point of view, the causes for the dispersion of AHe and ZHe cooling ages, in particular in the Neoproterozoic–Paleozoic strata, may provide an interesting research topic. Although this dispersion has been a limitation for thermal modeling in this study, it also is an opportunity to investigate how provenance and thermal inheritance of basement strata affects cooling ages produced by recent rapid exhumation. Studies that describe and attempt to explain intrasample dispersion have been conducted by e.g., Hueck et al. (2018) and Powell et al. (2020).

The structural framework of the Cianzo basin lends itself for 3D structural modeling. The recent (2D) balanced cross-section by Henríquez et al. (2023) provides a solid basis for this kind of study. Structural measurements are available for the Cianzo basin, but a closer coverage is needed for the Aparzo, Hornocal and Zenta ranges, where roads are scarce and access is difficult. By combining 3D structural forward modeling with across-fault thermal modeling, we may resolve the kinematic and exhumation history of the northern Lomas de Olmedo sub-basin margin in greater detail than thermal models for single fault blocks are able to. Combinations of this kind, using e.g., Pecube (Braun, 2003) and MOVE (Petroleum Experts, 2020) have been explored in recent studies (e.g., Eizenhöfer et al., 2023; Helfrich, 2020). The exhaustive thermochronologic data set presented in this study, combined with existing cooling ages from Reiners et al. (2015) and Henríquez et al. (2023), and available structural and sedimentological data (e.g., Kley et al., 2005; Kocks, 1999; McBride, 2008; Siks and Horton, 2011) forms the basis for future studies, especially in the realm of thermokinematic modeling.

References

Aceñolaza, G.F. (2003). The Cambrian System in Northwestern Argentina: stratigraphical and palaeontological framework. *Geologica Acta* 1, 23–39.

Adams, C.J., Miller, H., Aceñolaza, G.F., Toselli, A.J., Griffin, W.L. (2011). The Pacific Gondwana margin in the late Neoproterozoic–early Paleozoic: Detrital zircon U–Pb ages from metasediments in northwest Argentina reveal their maximum age, provenance and tectonic setting. *Gondwana Research* 19 (1), 71–83.

Adams, C.J., Miller, H., Toselli, A.J. (1990). Nuevas edades de metamorfismo por el método K-Ar de la Formación Puncoviscana y equivalentes, NW de Argentina. In: Aceñolaza, G.F., Miller, H., Toselli, A.J. (Eds.) *El Ciclo Pampeano en el Noreste Argentino. Serie Correlación Geológica*, vol. 4, pp. 209–219.

Adams, C.J., Miller, H., Toselli, A.J., Griffin, W.L. (2008). The Puncoviscana Formation of northwest Argentina: U-Pb geochronology of detrital zircons and Rb-Sr metamorphic ages and their bearing on its stratigraphic age, sediment provenance and tectonic setting. *Neues Jahrbuch für Geologie und Paläontologie - Abhandlungen* 247 (3), 341–352.

Agüera, M., Belotti, H., Cavalleri, P., Naides, C., Porras, J. (2019). Oil Discovery in Ordovician Prerift Sequences Las Breñas Formation, Lomas de Olmedo Sub-Basin, Northwestern Argentina. *AAPG ICE 2019*, 1234.

Allmendinger, R.W. (1986). Tectonic development, southeastern border of the Puna Plateau, northwestern Argentine Andes. *Geological Society of America Bulletin* 97 (9), 1070–1082.

Allmendinger, R.W., Gubbels, T.L. (1996). Pure and simple shear plateau uplift, Altiplano-Puna, Argentina and Bolivia. *Tectonophysics* 259 (1-3), 1–13.

Allmendinger, R.W., Ramos, V.A., Jordan, T.E., Palma, M., Isacks, B.L. (1983). Paleogeography and Andean structural geometry, northwest Argentina. *Tectonics* 2 (1), 1–16.

Allmendinger, R.W., Zapata, T.R. (2000). The footwall ramp of the Subandean decollement, northernmost Argentina, from extended correlation of seismic reflection data. *Tectonophysics* 321 (1), 37–55.

Almilibia, A., Clay, K.M., Montserrat, F., Muñoz, J.A., Roca, E. (2005). Analogue Modelling of Inverted Oblique Rift Systems. *Geologica Acta* 3, 251–272.

Alonso, J.L., Seggiaro, R.E., Quintana, L., Gallastegui, J., Bulnes, M., Poblet, J., Heredia, N., Rodríguez-Fernández, L.R. (2012). Deformaciones paleozoicas en la Cordillera Oriental de los Andes a los 23°S (NO de Argentina). *Actas 8° Congreso Geológico de España* 13, 1844–1847.

Amengual, A., Zanettini, J.C.M. (1973). Geologíca de la comarca de Cianzo y Caspalá (Provincia de Jujuy). *Revista de la Asociación Geológica Argentina* 28, 341–352.

Amilibia, A., Sàbat, F., McClay, K.R., Muñoz, J.A., Roca, E., Chong, G. (2008). The role of inherited tectono-sedimentary architecture in the development of the central Andean mountain belt: Insights from the Cordillera de Domeyko. *Journal of Structural Geology* 30 (12), 1520–1539.

Anderson, M., Alvarado, P., Zandt, G., Beck, S.L. (2007). Geometry and brittle deformation of the subducting Nazca Plate, Central Chile and Argentina. *Geophysical Journal International*

171 (1), 419–434.
Anderson, R.B., Long, S.P., Horton, B.K., Calle, A.Z., Ramirez, V. (2017). Shortening and structural architecture of the Andean fold-thrust belt of southern Bolivia (21°S): Implications for kinematic development and crustal thickening of the Central Andes. *Geosphere* 13 (2), 538–558.
Anderson, R.B., Long, S.P., Horton, B.K., Thomson, S.N., Calle, A.Z., Stockli, D.F. (2018). Orogenic Wedge Evolution of the Central Andes, Bolivia (21°S): Implications for Cordilleran Cyclicity. *Tectonics* 37 (10), 3577–3609.
Aparicio González, P.A., Pimentel, M.M., Hauser, N., Moya, M.C. (2014). U–Pb LA-ICP-MS geochronology of detrital zircon grains from low-grade metasedimentary rocks (Neoproterozoic – Cambrian) of the Mojotoro Range, northwest Argentina. *Journal of South American Earth Sciences* 49, 39–50.
Aparicio González, P.A., Uriz, N., Arnol, J., Dopico, C.M., Cayo, L.E., Cingolani, C., Impiccini, A., Stipp Basei, M.A. (2020). Sedimentary provenance analysis of the Ordovician to Devonian siliciclastic units of the Subandean Ranges and Santa Barbara System, northwestern Argentina. *Journal of South American Earth Sciences* 101, 102629.
Aráoz, L., Noetinger, S., Vergel, M., Di Pasquo, M. (2016). Bioestratigrafía, paleogeografía y paleoecología del Paleozoico de Sierra de Zenta, Cordillera Oriental Argentina. *Serie Correlación Geológica* 32, 43–64.
Arriagada, C., Cobbold, P.R., Roperch, P. (2006). Salar de Atacama basin: A record of compressional tectonics in the Central Andes since the mid-Cretaceous. *Tectonics* 25 (1), TC1008.
Arriagada, C., Roperch, P., Mpodozis, C., Cobbold, P.R. (2008). Paleogene building of the Bolivian Orocline: Tectonic restoration of the Central Andes in 2-D map view. *Tectonics* 27 (6), TC6014.
Augustsson, C., Rusing, T., Adams, C.J., Chmiel, H., Kocabayoglu, M., Buld, M., Zimmermann, U., Berndt, J., Kooijman, E. (2011). Detrital Quartz and Zircon Combined: The Production of Mature Sand with Short Transportation Paths Along the Cambrian West Gondwana Margin, Northwestern Argentina. *Journal of Sedimentary Research* 81 (4), 284–298.
Baby, P., Hérail, G., Salinas, R., Sempere, T. (1992). Geometry and kinematic evolution of passive roof duplexes deduced from cross section balancing: Example from the foreland thrust system of the southern Bolivian Subandean Zone. *Tectonics* 11 (3), 523–536.
Bahlburg, H., Berndt, J., Gerdes, A. (2016). The ages and tectonic setting of the Faja Eruptiva de la Puna Oriental, Ordovician, NW Argentina. *Lithos* 256-257, 41–54.
Bahlburg, H., Moya, M.C., Zimmermann, U., Bock, B., Hervé, F. (2000). Paleozoic Plate Tectonic Evolution of the Western Gondwana Margin in Northern Chile and Northwestern Argentina. *Zeitschrift für Angewandte Geologie* Sonderheft 1, 345–353.
Baldis, B., Benedetto, J., Blasco, G., Martel, M. (1976). Trilobites Silúrico-Devónicos de la Sierra de Zapla (Noroeste de Argentina). *Ameghiniana* 13 (3-4), 185–225.
Barazangi, M., Isacks, B.L. (1976). Spatial distribution of earthquakes and subduction of the Nazca plate beneath South America. *Geology* 4 (11), 686–692.

Barbarand, J., Carter, A., Wood, I., Hurford, A.J. (2003). Compositional and structural control of fission-track annealing in apatite. *Chemical Geology* 198 (1-2), 107–137.

Barnes, J.B., Ehlers, T.A., McQuarrie, N., O'Sullivan, P.B., Tawackoli, S. (2008). Thermochronometer record of central Andean Plateau growth, Bolivia (19.5°S). *Tectonics* 27 (3), TC3003.

Barrabino, E., Seggiaro, R.E., Ramos, J.J., Villagrán, C., Celedón, M. (2015). Análisis estructural del valle de Alfarcito-Punta Corral, Quebrada de Humahuaca, Provincia de Jujuy. *Actas 16° Reunión de Tectónica*, 70–71.

Beauchamp, W., Allmendinger, R.W., Barazangi, M., Demnati, A., El Alji, M., Dahmani, M. (1999). Inversion tectonics and the evolution of the High Atlas Mountains, Morocco, based on a geological-geophysical transect. *Tectonics* 18 (2), 163–184.

Becker, T.P., Summa, L.L., Ducea, M.N., Karner, G.D. (2015). Temporal growth of the Puna Plateau and its bearing on the post–Salta Rift system subsidence of the Andean foreland basin at 25°30′S. In: DeCelles, P.G., Ducea, M.N., Carrapa, B., Kapp, P.A. (Eds.) *Geodynamics of a Cordilleran Orogenic System: The Central Andes of Argentina and Northern Chile*. Geological Society of America.

Boll, A., Gómez Omil, R.J., Hernández, R., 1989. Síntesis Estratigráfica del Grupo Salta: Informe inédito YPF, Buenos Aires.

Boll, A., Hernández, R. (1986). Interpretación estructural del área Tres Cruces. *Boletín de Informaciones Petroleras* 7, 2–14.

Bookhagen, B., Strecker, M.R. (2012). Spatiotemporal trends in erosion rates across a pronounced rainfall gradient: Examples from the southern Central Andes. *Earth and Planetary Science Letters* 327-328, 97–110.

Bossi, G.E., Wampler, M. (1969). Edad del Complejo Alto de Las Salinas y Formación El Cadillal segun el metodo K-Ar. *Acta Geológica Lilloana* 10, 141–160.

Boutoux, A., Bellahsen, N., Lacombe, O., Verlaguet, A., Mouthereau, F. (2014). Inversion of pre-orogenic extensional basins in the external Western Alps: Structure, microstructures and restoration. *Journal of Structural Geology* 60, 13–29.

Braun, J. (2003). Pecube: a new finite-element code to solve the 3D heat transport equation including the effects of a time-varying, finite amplitude surface topography. *Computers & Geosciences* 29 (6), 787–794.

Breitkreuz, C., van Schmus, W.R. (1996). Geochronology and significance of Late Permian ignimbrites in Northern Chile. *Journal of South American Earth Sciences* 9 (5-6), 281–293.

Buatois, L.A., Mángano, M.G. (2003). La icnofauna de la Formación Puncoviscana en el noroeste Argentino: La colonización de fondos oceánicos y reconstrucción de paleoambientes y paleoecosistemas de la transición Precámbrica-Cámbrica. *Ameghiniana* 40, 103–117.

Buatois, L.A., Zeballo, F.J., Albanesi, G.L., Ortega, G., Vaccari, N.E., Mángano, M.G. (2006). Depositional environments and stratigraphy of the upper Cambrian-lower Ordovician Santa Rosita Formation at the Alfarcito area, Cordillera Oriental, Argentina: Integration of biostratigraphic data within a sequence stratigraphic framework. *Latin American Journal of Sedimentology and Basin Analysis* 13, 1–29.

Butler, R.W.H., Tavarnelli, E., Grasso, M. (2006). Structural inheritance in mountain belts: An Alpine–Apennine perspective. *Journal of Structural Geology* 28 (11), 1893–1908.

Cahill, T., Isacks, B.L. (1992). Seismicity and shape of the subducted Nazca Plate. *Journal of Geophysical Research: Solid Earth* 97 (B12), 17503.

Cahill, T., Isacks, B.L., Whitman, D., Chatelain, J.-L., Perez, A., Chiu, J.M. (1992). Seismicity and tectonics in Jujuy Province, northwestern Argentina. *Tectonics* 11 (5), 944–959.

Carlson, W.D., Donelick, R.A., Ketcham, R.A. (1999). Variability of apatite fission-track annealing kinetics; I, Experimental results. *American Mineralogist* 84 (9), 1213–1223.

Carrapa, B., Bywater-Reyes, S., DeCelles, P.G., Mortimer, E., Gehrels, G.E. (2012). Late Eocene-Pliocene basin evolution in the Eastern Cordillera of northwestern Argentina (25°-26°S): regional implications for Andean orogenic wedge development. *Basin Research* 24 (3), 249–268.

Carrapa, B., DeCelles, P.G. (2008). Eocene exhumation and basin development in the Puna of northwestern Argentina. *Tectonics* 27 (1), TC1015.

Carrapa, B., Reyes-Bywater, S., Safipour, R., Sobel, E.R., Schoenbohm, L.M., DeCelles, P.G., Reiners, P.W., Stockli, D.F. (2014). The effect of inherited paleotopography on exhumation of the Central Andes of NW Argentina. *Geological Society of America Bulletin* 126 (1-2), 66–77.

Carrapa, B., Trimble, J.D., Stockli, D.F. (2011). Patterns and timing of exhumation and deformation in the Eastern Cordillera of NW Argentina revealed by (U-Th)/He thermochronology. *Tectonics* 30 (3), TC3003.

Carrera, N., Muñoz, J.A. (2008). Thrusting evolution in the southern Cordillera Oriental (northern Argentine Andes): Constraints from growth strata. *Tectonophysics* 459 (1-4), 107–122.

Carrera, N., Muñoz, J.A. (2013). Thick-skinned tectonic style resulting from the inversion of previous structures in the southern Cordillera Oriental (NW Argentine Andes). *Geological Society, London, Special Publications* 377 (1), 77–100.

Carrera, N., Muñoz, J.A., Sàbat, F., Mon, R., Roca, E. (2006). The role of inversion tectonics in the structure of the Cordillera Oriental (NW Argentinean Andes). *Journal of Structural Geology* 28 (11), 1921–1932.

Carroll, A.R., Bohacs, K.M. (1999). Stratigraphic classification of ancient lakes: Balancing tectonic and climatic controls. *Geology* 27 (2), 99–102.

Casquet, C., Fanning, C.M., Galindo, C., Pankhurst, R.J., Rapela, C.W., Torres, P. (2010). The Arequipa Massif of Peru: New SHRIMP and isotope constraints on a Paleoproterozoic inlier in the Grenvillian orogen. *Journal of South American Earth Sciences* 29 (1), 128–142.

Ceolin, D., Filho, S., Terra, G., Fragoso, D., Bunevich, R.B., Fauth, G., Hernandez, J., Hernández, R. (2022). Ostracods from upper Yacoraite Formation (Danian), Salta Basin, Western Argentina: Taxonomy and paleoenvironmental indicators of climatic signals in lacustrine deposits. *Journal of South American Earth Sciences* 116, 103836.

Charrier, R., Muñoz, N. (1994). Jurassic-Cretaceous Palaeogeographic Evolution of the Chilean Andes at 23°–24°S Latitude and 34°–35°S Latitude: A Comparative Analysis. In: Reutter, K.-J., Scheuber, E., Wigger, P.J. (Eds.) *Tectonics of the Southern Central Andes*. Springer,

Berlin, Heidelberg, pp. 233–242.
Chebli, G.A., Mozetic, M.E., Rossello, E.A., Buhler, M. (1999). Cuencas sedimentarias de la Llanura Chacopampeana. *Geología Argentina* 29, 627–644.
Chen, Y.-W., Wu, J., Suppe, J. (2019). Southward propagation of Nazca subduction along the Andes. *Nature* 565 (7740), 441–447.
Chidsey, T.C., Vanden Berg, M.D., Eby, D.E. (2015). Petrography and characterization of microbial carbonates and associated facies from modern Great Salt Lake and Uinta Basin's Eocene Green River Formation in Utah, USA. *Geological Society, London, Special Publications* 418 (1), 261–286.
Coira, B.L.L., Zapettini, E.O., Ferpozzi, F.J. (2008). *Mapa Geológico de la Provincia de Jujuy*. Secretaría de Industria, Comercio y Minería. Subsecretaría de Minería. Servicio Geológico Minero Argentino. Instituto de Geología y Recursos Minerales, Argentina.
Coutand, I., Carrapa, B., Deeken, A., Schmitt, A.K., Sobel, E.R., Strecker, M.R. (2006). Propagation of orographic barriers along an active range front: insights from sandstone petrography and detrital apatite fission-track thermochronology in the intramontane Angastaco basin, NW Argentina. *Basin Research* 18 (1), 1–26.
Coutand, I., Cobbold, P.R., Urreiztieta, M. de, Gautier, P., Chauvin, A., Gapais, D., Rossello, E.A., López-Gamundí, O. (2001). Style and history of Andean deformation, Puna plateau, northwestern Argentina. *Tectonics* 20 (2), 210–234.
Coutts, D.S., Matthews, W.A., Hubbard, S.M. (2019). Assessment of widely used methods to derive depositional ages from detrital zircon populations. *Geoscience Frontiers* 10 (4), 1421–1435.
Coward, M.P., Gillcrist, R., Trudgill, B. (1991). Extensional structures and their tectonic inversion in the Western Alps. *Geological Society, London, Special Publications* 56 (1), 93–112.
Cristiani, C., Matteini, M., Mazzouli, R., Omarini, R.H. (2003). Petrological study of interaction processes between crustal and mantle magmas for reconstructing the geotectonic setting of a continental rift: the case of Jurassic-Cretaceous Tusaquillas Plutonic complex in Central Andes (NW Argentina). *EGS-AGU-EUG Joint Assembly Abstracts*.
DeCelles, P.G., Carrapa, B., Gehrels, G.E. (2007). Detrital zircon U-Pb ages provide provenance and chronostratigraphic information from Eocene synorogenic deposits in northwestern Argentina. *Geology* 35 (4), 323–326.
DeCelles, P.G., Carrapa, B., Horton, B.K., Gehrels, G.E. (2011). Cenozoic foreland basin system in the Central Andes of northwestern Argentina: Implications for Andean geodynamics and modes of deformation. *Tectonics* 30 (6), TC6013.
DeCelles, P.G., Giles, K.A. (1996). Foreland basin systems. *Basin Research* 8 (2), 105–123.
DeCelles, P.G., Horton, B.K. (2003). Early to middle Tertiary foreland basin development and the history of Andean crustal shortening in Bolivia. *Geological Society of America Bulletin* 115 (1), 58–77.
Deeken, A., Sobel, E.R., Coutand, I., Haschke, M., Riller, U., Strecker, M.R. (2006). Development of the southern Eastern Cordillera, NW Argentina, constrained by apatite fission track thermochronology: From early Cretaceous extension to middle Miocene

shortening. *Tectonics* 25 (6), TC6003.

Del Papa, C.E. (1999). Sedimentation on a ramp type lake margin: Paleocene–Eocene Maíz Gordo Formation, northwestern Argentina. *Journal of South American Earth Sciences* 12, 389–400.

Del Papa, C.E., Hongn, F.D., Powell, J., Payrola, P.A., Do Campo, M., Strecker, M.R., Petrinovic, I., Schmitt, A.K., Pereyra, R. (2013). Middle Eocene-Oligocene broken-foreland evolution in the Andean Calchaqui Valley, NW Argentina: insights from stratigraphic, structural and provenance studies. *Basin Research* 25 (5), 574–593.

Del Papa, C.E., Kirschbaum, A., Powell, J., Brod, A., Hongn, F.D., Pimentel, M.M. (2010). Sedimentological, geochemical and paleontological insights applied to continental omission surfaces: A new approach for reconstructing an Eocene foreland basin in NW Argentina. *Journal of South American Earth Sciences* 29 (2), 327–345.

Del Papa, C.E., Quattrocchio, M. (2002). Sedimentary facies and palynofacies assemblages in an Eocene perennial lake, Lumbrera formation, northwest Argentina. *Journal of South American Earth Sciences* 15, 553–569.

Del Papa, C.E., Salfity, J.A. (1999). Non-marine Paleogene sequences, Salta Group, Northwest Argentina. *Acta Geológica Hispanica* 34 (2-3), 105–121.

Deschamps, R., Rohais, S., Hamon, Y., Gasparrini, M. (2020). Dynamic of a lacustrine sedimentary system during late rifting at the Cretaceous–Palaeocene transition: Example of the Yacoraite Formation, Salta Basin, Argentina. *The Depositional Record* 6 (3), 490–523.

Di Domenica, A., Turtù, A., Satolli, S., Calamita, F. (2012). Relationships between thrusts and normal faults in curved belts: New insight in the inversion tectonics of the Central-Northern Apennines (Italy). *Journal of Structural Geology* 42, 104–117.

Di Pasquo, M. (2013). Avances sobre palinología bioestratigrafía y correlación de los Grupos Macharetí y Manduyutí Neopaleozoico de la Cuenca Tarija provincia de Salta Argentina. *Ameghiniana* 40 (1), 3–32.

Di Pasquo, M., Anderson Folnagy, H.J., Isaacson, P.E., Grader, G.W. (2019). Late Paleozoic Carbonates and Glacial Deposits in Bolivia and Northern Argentina: Significant Paleoclimatic Changes. In: Fraticelli, C.M., Markwick, P.J., Martinius, A.W., Suter, J.R. (Eds.) *Latitudinal Controls on Stratigraphic Models and Sedimentary Concepts*. SEPM (Society for Sedimentary Geology), pp. 185–203.

Di Pasquo, M., Azcuy, C.L. (1999). Interpretación paleoambiental del Grupo Mandiyutí (Carbonífero Superior), provincia de Salta, Argentina. Evidencias palinológicas, sedimentológicas y tafonómicas. *Ameghiniana* 36 (4), 453–463.

Di Pasquo, M., Carlos L. Azcuy, Daniel Starck (2014). Palinología de la formación San Telmo (Carbonífero superior) en la sierra San Antonio, provincia de Salta, Argentina. *Ameghiniana* 38, 85–98.

Di Pasquo, M., Vergel, M. (2008). Primer registro palinológico del Pennsylvaniano del Norte de la Sierra de Zenta, provincia de Jujuy, Argentina. *Actas XII Simpósio de Paleobotânicos e Palinólogos*, 51.

Dickinson, W.R., Beard, S.L., Brakenridge, R.G., Erjavec, J.L., Ferguson, R.C., Inman, K.F., Knepp, R.A., Lindberg, F.A., Ryberg, P.T. (1983). Provenance of North American

Phanerozoic sandstones in relation to tectonic setting. *Geological Society of America Bulletin* 94 (2), 222–235.

Dickinson, W.R., Gehrels, G.E. (2009). Use of U–Pb ages of detrital zircons to infer maximum depositional ages of strata: A test against a Colorado Plateau Mesozoic database. *Earth and Planetary Science Letters* 288 (1-2), 115–125.

Dickinson, W.R., Suczek, C.A. (1979). Plate Tectonics and Sandstone Compositions. *AAPG Bulletin* 63 (12), 2164–2182.

Disalvo, A., Rodríguez Schelotto, M., Gómez Omil, R.J., Hoffman, C., Benítez, J., Hurtado, S. (2002). Los reservorios de la Formación Yacoraite. In: Schiuma, M., Hinterwimmer, G., Vergani, G.D. (Eds.) *Rocas Reservorio delas Cuencas productivas de la Argentina - Actas V Congreso de Exploración y Desarrollo de Hidrocarburos*, pp. 717–738.

Do Campo, M., Nieto, F. (2003). Transmission electron microscopy study of very low-grade metamorphic evolution in Neoproterozoic pelites of the Puncoviscana formation (Cordillera Oriental, NW Argentina). *Clay Minerals* 38 (4), 459–481.

Donelick, R.A. (1993). A method of fission track analysis utilizing bulk chemical etching of apatite (Patent no. 5,267,274): Patent.

Donelick, R.A., Ketcham, R.A., Carlson, W.D. (1999). Variability of apatite fission-track annealing kinetics; II, Crystallographic orientation effects. *American Mineralogist* 84 (9), 1224–1234.

Donelick, R.A., O'Sullivan, P.B., Ketcham, R.A. (2005). Apatite Fission-Track Analysis. *Reviews in Mineralogy and Geochemistry* 58 (1), 49–94.

Dumitru, T., 1994. FTStage (Software).

Dunham, R.J. (1962). Classification of Carbonate rocks according to depositional texture. *AAPG Memoir* 1, 108–121.

Dunn, J.F., Hartshorn, K.G., Hartshorn, P.W. (1995). Structural Styles and Hydrocarbon Potential of the Sub-Andean Thrust Belt of Southern Bolivia. In: Tankard, A.J., Suárez-Soruco, R., Welsink, H.J. (Eds.) *Petroleum Basins of South America*. American Association of Petroleum Geologists.

Echavarría, L., Hernández, R., Allmendinger, R.W., Reynolds, J.H. (2003). Subandean thrust and fold belt of northwestern Argentina: Geometry and timing of the Andean evolution. *AAPG Bulletin* 87 (6), 965–985.

Ege, H., Sobel, E.R., Scheuber, E., Jacobshagen, V. (2007). Exhumation history of the southern Altiplano plateau (southern Bolivia) constrained by apatite fission track thermochronology. *Tectonics* 26 (1), TC1004.

Eichelberger, N., McQuarrie, N., Ehlers, T.A., Enkelmann, E., Barnes, J.B., Lease, R.O. (2013). New constraints on the chronology, magnitude, and distribution of deformation within the central Andean orocline. *Tectonics* 32 (5), 1432–1453.

Einhorn, J.C., Gehrels, G.E., Vernon, A., DeCelles, P.G. (2015). U-Pb zircon geochronology of Neoproterozoic–Paleozoic sandstones and Paleozoic plutonic rocks in the Central Andes (21°S–26°S). In: DeCelles, P.G., Ducea, M.N., Carrapa, B., Kapp, P.A. (Eds.) *Geodynamics of a Cordilleran Orogenic System: The Central Andes of Argentina and Northern Chile*. Geological Society of America.

Eizenhöfer, P.R., Glotzbach, C., Kley, J., Ehlers, T.A. (2023). Thermo-Kinematic Evolution of the Eastern European Alps Along the TRANSALP Transect. *Tectonics* 42 (4), e2022TC007380.

Elger, K., Oncken, O., Glodny, J. (2005). Plateau-style accumulation of deformation: Southern Altiplano. *Tectonics* 24 (4), TC4020.

Erdős, Z., Huismans, R.S., Van der Beek, P., Thieulot, C. (2014). Extensional inheritance and surface processes as controlling factors of mountain belt structure. *Journal of Geophysical Research: Solid Earth* 119 (12), 9042–9061.

Escayola, M.P., Van Staal, C.R., Davis, W.J. (2011). The age and tectonic setting of the Puncoviscana Formation in northwestern Argentina: An accretionary complex related to Early Cambrian closure of the Puncoviscana Ocean and accretion of the Arequipa-Antofalla block. *Journal of South American Earth Sciences* 32 (4), 438–459.

Farley, K.A. (2000). Helium diffusion from apatite: General behavior as illustrated by Durango fluorapatite. *Journal of Geophysical Research: Solid Earth* 105 (B2), 2903–2914.

Farley, K.A. (2002). (U-Th)/He Dating: Techniques, Calibrations, and Applications. *Reviews in Mineralogy and Geochemistry* 47 (1), 819–844.

Farley, K.A., Wolf, R.A., Silver, L.T. (1996). The effects of long alpha-stopping distances on (U-Th)/He ages. *Geochimica et Cosmochimica Acta* 60 (21), 4223–4229.

Fennell, L.M., Naipauer, M., Borghi, P., Sagripanti, L., Pimentel, M.M., Folguera, A. (2020). Early Jurassic intraplate extension in west-central Argentina constrained by U-Pb SHRIMP dating: Implications for the opening of the Neuquén basin. *Gondwana Research* 87, 278–302.

Fielding, E.J., Jordan, T.E. (1988). Active deformation at the boundary between the Precordillera and Sierras Pampeanas, Argentina, and comparison with ancient Rocky Mountain deformation. Interactions of the Rocky Mountain Foreland and the Cordilleran Thrust Belt. *Geological Society of America Memoirs* 171, 143–163.

Flint, S., Turner, P., Jolley, E.J., Hartley, A.J. (1993). Extensional tectonics in convergent margin basins: An example from the Salar de Atacama, Chilean Andes. *Geological Society of America Bulletin* 105 (5), 603–617.

Flowers, R.M., Ketcham, R.A., Shuster, D.L., Farley, K.A. (2009). Apatite (U–Th)/He thermochronometry using a radiation damage accumulation and annealing model. *Geochimica et Cosmochimica Acta* 73 (8), 2347–2365.

Flowers, R.M., Shuster, D.L., Wernicke, B.P., Farley, K.A. (2007). Radiation damage control on apatite (U-Th)/He dates from the Grand Canyon region, Colorado Plateau. *Geology* 35 (5), 447–450.

Folk, R.L. (1980). *Petrology of sedimentary rocks,* 4th ed. Hemphill Pub Co, Texas.

Franceschinis, P.R., Escayola, M.P., Rapalini, A.E., Rodríguez Piceda, C. (2020a). Age constraints on the Cambrian Mesón Group (NW Argentina) based on detrital zircons U–Pb geochronology and magnetic polarity bias. *Journal of South American Earth Sciences* 104, 102835.

Franceschinis, P.R., Rapalini, A.E., Escayola, M.P., Rodríguez Piceda, C. (2020b). Paleogeographic and tectonic evolution of the Pampia Terrane in the Cambrian: New

paleomagnetic constraints. *Tectonophysics* 779, 228386.
Galbraith, R.F., Laslett, G.M. (1993). Statistical models for mixed fission track ages. *Nuclear Tracks and Radiation Measurements* 21 (4), 459–470.
Galetto, A., Georgieva, V., García, V., Zattin, M., Sobel, E.R., Glodny, J., Bordese, S., Arzadún, G., Bechis, F., Caselli, A.T., Becchio, R. (2021). Cretaceous and Eocene Rapid Cooling Phases in the Southern Andes (36°–37°S): Insights From Low-Temperature Thermochronology, U-Pb Geochronology, and Inverse Thermal Modeling From Domuyo Area, Argentina. *Tectonics* 40 (6), e2020TC006415.
Gallagher, K. (2012). Transdimensional inverse thermal history modelling for quantitative thermochronology. *Journal of Geophysical Research: Solid Earth* 117, B02408.
Gallagher, K., 2021. QTQt (Software).
Gallagher, K., Charvin, K., Nielsen, S., Sambridge, M., Stephenson, J. (2009). Markov chain Monte Carlo (MCMC) sampling methods to determine optimal models, model resolution and model choice for Earth Science problems. *Marine and Petroleum Geology* 26 (4), 525–535.
Galliski, M.A., Viramonte, J.G. (1988). The Cretaceous paleorift in northwestern Argentina: A petrologic approach. *Journal of South American Earth Sciences* 1 (4), 329–342.
Gans, C.R., Beck, S.L., Zandt, G., Gilbert, H., Alvarado, P., Anderson, M., Linkimer, L. (2011). Continental and oceanic crustal structure of the Pampean flat slab region, western Argentina, using receiver function analysis: new high-resolution results. *Geophysical Journal International* 186 (1), 45–58.
Gautheron, C., Espurt, N., Barbarand, J., Roddaz, M., Baby, P., Brusset, S., Tassan-Got, L., Douville, E. (2013). Direct dating of thick- and thin-skin thrusts in the Peruvian Subandean zone through apatite (U-Th)/He and fission track thermochronometry. *Basin Research* 25 (4), 419–435.
Gehrels, G.E. (2014). Detrital Zircon U-Pb Geochronology Applied to Tectonics. *Annual Review of Earth and Planetary Sciences* 42 (1), 127–149.
Giambiagi, L., Bechis, F., García, V., Clark, A.H. (2008). Temporal and spatial relationships of thick- and thin-skinned deformation: A case study from the Malargüe fold-and-thrust belt, southern Central Andes. *Tectonophysics* 459 (1-4), 123–139.
Giambiagi, L., Ghiglione, M., Cristallini, E., Bottesi, G. (2009). Kinematic models of basement/cover interaction: Insights from the Malargüe fold and thrust belt, Mendoza, Argentina. *Journal of Structural Geology* 31 (12), 1443–1457.
Giambiagi, L., Mescua, J., Heredia, N., Farías, P., García-Sansegundo, J., Fernández, C., Stier, S., Pérez, D., Bechis, F., Moreiras, S.M., Lossada, A.C. (2014). Reactivation of Paleozoic structures during Cenozoic deformation in the Cordón del Plata and Southern Precordillera ranges (Mendoza, Argentina). *Journal of Iberian Geology* 40 (2), 309–320.
Giambiagi, L., Tassara, A., Echaurren, A., Julve, J., Quiroga, R., Barrionuevo, M., Liu, S., Echeverría, I., Mardónez, D., Suriano, J., Mescua, J., Lossada, A.C., Spagnotto, S., Bertoa, M., Lothari, L. (2022). Crustal anatomy and evolution of a subduction-related orogenic system: Insights from the Southern Central Andes (22-35°S). *Earth-Science Reviews* 232, 104138.

Gleadow, A. (1981). Fission-track dating methods: What are the real alternatives? *Nuclear Tracks* 5 (1-2), 3–14.

Gomes, J.P.B., Bunevich, R.B., Tonietto, S.N., Alves, D.B., Santos, J.F., Whitaker, F.F. (2020). Climatic signals in lacustrine deposits of the Upper Yacoraite Formation, Western Argentina: Evidence from clay minerals, analcime, dolomite and fibrous calcite. *Sedimentology* 67 (5), 2282–2309.

Gómez Omil, R.J., Boll, A., Hernández, R. (1989). Cuenca cretácico terciaria del Noroeste argentino (Grupo Salta). In: Chebli, G.A., Spalletti, L.A. (Eds.) *Cuencas Sedimentarias Argentinas*. Universidad Nacional de Tucumán, pp. 43–64.

González, M.A., Tchilinguirian, P. (2003). *Hoja Geológica 2366-IV, San Martín. Ciudad de Libertador General San Martín.* Instituto de Geología y Recursos Minerales (Segemar), Buenos Aires, Argentina.

Grier, M.E., Salfity, J.A., Allmendinger, R.W. (1991). Andean reactivation of the Cretaceous Salta rift, northwestern Argentina. *Journal of South American Earth Sciences* 4 (4), 351–372.

Gubbels, T.L., Isacks, B.L., Farrar, E. (1993). High-level surfaces, plateau uplift, and foreland development, Bolivian central Andes. *Geology* 21 (8), 695–698.

Guenthner, W.R., Reiners, P.W., DeCelles, P.G., Kendall, J. (2015). Sevier belt exhumation in central Utah constrained from complex zircon (U-Th)/He data sets: Radiation damage and He inheritance effects on partially reset detrital zircons. *Geological Society of America Bulletin* 127 (3-4), 323–348.

Guenthner, W.R., Reiners, P.W., Ketcham, R.A., Nasdala, L., Giester, G. (2013). Helium diffusion in natural zircon: Radiation damage, anisotropy, and the interpretation of zircon (U-Th)/He thermochronology. *American Journal of Science* 313 (3), 145–198.

Hain, M.P., Strecker, M.R., Bookhagen, B., Alonso, R.N., Pingel, H., Schmitt, A.K. (2011). Neogene to Quaternary broken foreland formation and sedimentation dynamics in the Andes of NW Argentina (25°S). *Tectonics* 30 (2), TC2006.

Haschke, M., Günther, A., Melnick, D., Echtler, H., Reutter, K.-J., Scheuber, E., Oncken, O. (2006). Central and Southern Andean Tectonic Evolution Inferred from Arc Magmatism. In: Oncken, O., Chong, G., Franz, G., Giese, P., Götze, H.-J., Ramos, V.A., Strecker, M.R., Wigger, P.J. (Eds.) *The Andes*. *Active Subduction Orogeny*, 1st ed. Springer, Berlin, Heidelberg, pp. 337–353.

Hauser, N., Matteini, M., Omarini, R.H., Pimentel, M.M. (2010). Constraints on metasomatized mantle under Central South America: evidence from Jurassic alkaline lamprophyre dykes from the Eastern Cordillera, NW Argentina. *Mineralogy and Petrology* 100 (3), 153–184.

Heidbach, O., Rajabi, M., Cui, X., Fuchs, K., Müller, B., Reinecker, J., Reiter, K., Tingay, M., Wenzel, F., Xie, F., Ziegler, M.O., Zoback, M.-L., Zoback, M. (2018). The World Stress Map database release 2016: Crustal stress pattern across scales. *Tectonophysics* 744, 484–498.

Heidbach, O., Rajabi, M., Reiter, K., Ziegler, M.O., WSM Team, 2016. World Stress Map Database Release 2016.

Helfrich, A. (2020). *Testing interpretations of the displacement magnitude of the Teton Fault* *and uplift of the Teton Range, Wyoming with integrated flexural-kinematic and thermal modeling*. Master Thesis, Lexington, Kentucky, United States of America.

Henríquez, S., DeCelles, P.G., Carrapa, B. (2019). Cretaceous to Middle Cenozoic Exhumation History of the Cordillera de Domeyko and Salar de Atacama Basin, Northern Chile. *Tectonics* 38 (2), 395–416.

Henríquez, S., DeCelles, P.G., Carrapa, B., Hughes, A.N. (2023). Kinematic evolution of the central Andean retroarc thrust belt in northwestern Argentina and implications for coupling between shortening and crustal thickening. *Geological Society of America Bulletin* 135 (1-2), 81–103.

Henríquez, S., DeCelles, P.G., Carrapa, B., Hughes, A.N., Davis, G.H., Alvarado, P. (2020). Deformation history of the Puna plateau, Central Andes of northwestern Argentina. *Journal of Structural Geology* 140, 104133.

Heredia, N., García-Sansegundo, J., Gallastegui, G., Farías, P., Giacosa, R., Hongn, F.D., Tubía, J.M., Alonso, J.L., Busquets, P., Charrier, R., Clariana, P., Colombo, F., Cuesta, A., Gallastegui, J., Giambiagi, L., González-Menéndez, L., Limarino, O., Martín-González, F., Pedreira, D., Quintana, L., Rodríguez-Fernández, L.R., Rubio-Ordóñez, Á., Seggiaro, R.E., Serra-Varela, S., Spalletti, L.A., Cardó, R., Ramos, V.A. (2018). The Pre-Andean Phases of Construction of the Southern Andes Basement in Neoproterozoic–Paleozoic Times. In: Folguera, A., Contreras-Reyes, E., Heredia, N., Encinas, A., Iannelli, S.B., Oliveros, V., Dávila, F.M., Collo, G., Giambiagi, L., Maksymowicz, A., Iglesia Llanos, M.P., Turienzo, M., Naipauer, M., Orts, D., Litvak, V., Alvarez, O., Arriagada, C. (Eds.) *The evolution of the Chilean-Argentinean Andes*. Springer International Publishing, Cham, pp. 111–131.

Hernández, R., Gómez Omil, R.J., Boll, A. (2008). Estratigrafía, Tectónica y Potencial Petrolera del Rift Cretácico en la Provincia de Jujuy. *Relatorio del XVII Congreso Geológico Argentino, Jujuy*, 207–232.

Hernández, R., Jordan, T.E., Dalenz Farjat, A., Echavarría, L., Idleman, B.D., Reynolds, J.H. (2005). Age, distribution, tectonics, and eustatic controls of the Paranense and Caribbean marine transgressions in southern Bolivia and Argentina. *Journal of South American Earth Sciences* 19 (4), 495–512.

Herriott, T.M., Crowley, J.L., Schmitz, M.D., Wartes, M.A., Gillis, R.J. (2019). Exploring the law of detrital zircon: LA-ICP-MS and CA-TIMS geochronology of Jurassic forearc strata, Cook Inlet, Alaska, USA. *Geology* 47 (11), 1044–1048.

Hilley, G.E., Blisniuk, P.M., Strecker, M.R. (2005). Mechanics and erosion of basement-cored uplift provinces. *Journal of Geophysical Research: Solid Earth* 110, B12409.

Hindle, D., Kley, J., Klosko, E., Stein, S., Dixon, T., Norabuena, E. (2002). Consistency of geologic and geodetic displacements during Andean orogenesis. *Geophysical Research Letters* 29 (8), 29-1-29-4.

Hongn, F.D., Del Papa, C.E., Powell, J., Petrinovic, I., Mon, R., Deraco, V. (2007). Middle Eocene deformation and sedimentation in the Puna-Eastern Cordillera transition (23°-26°S): Control by preexisting heterogeneities on the pattern of initial Andean shortening. *Geology* 35 (3), 271–274.

Hongn, F.D., Mon, R., Petrinovic, I., Del Papa, C.E., Powell, J. (2010a). Inversión y reactivación tectónicas cretácico-cenozoicas en el noroeste argentino: Influencia de las heterogeneidades del basamento neoproteroico-paleozoico inferior. *Revista de la Asociación Geológica Argentina* 66 (1), 38–53.

Hongn, F.D., Tubía, J.M., Aranguren, A., Mon, R. (2001a). El batolito de Tastil (Salta, Argentina): un caso de magmatismo poliorogénico en el basamento andino. *Boletín Geológico y Minero* 112, 113-124.

Hongn, F.D., Tubía, J.M., Aranguren, A., Mon, R., Battaglia, R. (2001b). Intrusión del granito rojo del batolito de Tastil en areniscas Eopaleozoicas en el Angosto de la Quesera, Cordillera Oriental, Salta. *Revista de la Asociación Geológica Argentina* 56, 249–252.

Hongn, F.D., Tubía, J.M., Aranguren, A., Vegas, N., Mon, R., Dunning, G.R. (2010b). Magmatism coeval with lower Paleozoic shelf basins in NW-Argentina (Tastil batholith): Constraints on current stratigraphic and tectonic interpretations. *Journal of South American Earth Sciences* 29 (2), 289–305.

Horton, B.K. (2005). Revised deformation history of the central Andes: Inferences from Cenozoic foredeep and intermontane basins of the Eastern Cordillera, Bolivia. *Tectonics* 24 (3), TC3011.

Horton, B.K. (2018a). Sedimentary record of Andean mountain building. *Earth-Science Reviews* 178, 279–309.

Horton, B.K. (2018b). Tectonic Regimes of the Central and Southern Andes: Responses to Variations in Plate Coupling During Subduction. *Tectonics* 37 (2), 402–429.

Horton, B.K., Capaldi, T.N., Perez, N.D. (2022). The role of flat slab subduction, ridge subduction, and tectonic inheritance in Andean deformation. *Geology* 50 (9), 1007–1012.

Horton, B.K., DeCelles, P.G. (1997). The modern foreland basin system adjacent to the Central Andes. *Geology* 25 (10), 895–898.

Horton, B.K., Folguera, A. (2022). Tectonic inheritance and structural styles in the Andean fold-thrust belt and foreland basin. In: Zamora, G., Mora, A. (Eds.) *Andean Structural Styles*, 1 ed. Elsevier, pp. 3–28.

Hueck, M., Dunkl, I., Heller, B., Stipp Basei, M.A., Siegesmund, S. (2018). (U-Th)/He Thermochronology and Zircon Radiation Damage in the South American Passive Margin: Thermal Overprint of the Paraná LIP? *Tectonics* 37 (10), 4068–4085.

Hurford, A.J., Green, P.F. (1983). The zeta age calibration of fission-track dating. *Chemical Geology* 41, 285–317.

Iaffa, D.N., Sàbat, F., Muñoz, J.A., Mon, R., Gutierrez, A.A. (2011). The role of inherited structures in a foreland basin evolution. The Metán Basin in NW Argentina. *Journal of Structural Geology* 33 (12), 1816–1828.

Iannelli, S.B., Fennell, L.M., Fernández Paz, L., Litvak, V., Encinas, A., Folguera, A. (2020). Late Cretaceous to Oligocene Magmatic Evolution of the Neuquén Basin. In: Kietzmann, D., Folguera, A. (Eds.) *Opening and Closure of the Neuquén Basin in the Southern Andes*. Springer International Publishing, Cham, pp. 397–416.

Ingersoll, R.V. (1990). Actualistic sandstone petrofacies: Discriminating modern and ancient source rocks. *Geology* 18 (8), 733–736.

Ingersoll, R.V., Bullard, T.F., Ford, R.L., Grimm, J.P., Pickle, J.D., Sares, S.W. (1984). The

Effect of Grain Size on Detrital Modes: A Test of the Gazzi-Dickinson Point-Counting Method. *Journal of Sedimentary Research* 54 (1), 103–116.

Ingersoll, R.V., Kretchmer, A.G., Valles, P.K. (1993). The effect of sampling scale on actualistic sandstone petrofacies. *Sedimentology* 40 (5), 937–953.

Insel, N., Grove, M., Haschke, M., Barnes, J.B., Schmitt, A.K., Strecker, M.R. (2012). Paleozoic to early Cenozoic cooling and exhumation of the basement underlying the eastern Puna plateau margin prior to plateau growth. *Tectonics* 31 (6), TC6006.

Jackson, S.E., Pearson, N.J., Griffin, W.L., Belousova, E.A. (2004). The application of laser ablation-inductively coupled plasma-mass spectrometry to in situ U–Pb zircon geochronology. *Chemical Geology* 211 (1-2), 47–69.

Jammes, S., Huismans, R.S. (2012). Structural styles of mountain building: Controls of lithospheric rheologic stratification and extensional inheritance. *Journal of Geophysical Research: Solid Earth* 117, B10403.

Jiron, R. (2015). *Interactions of tectonics, climate, and deposition in intermontane basins on the margin of the Puna Plateau, NW Argentina*. PhD thesis, Santa Barbara, CA.

Jordan, T.E., Allmendinger, R.W. (1986). The Sierras Pampeanas of Argentina; a modern analogue of Rocky Mountain foreland deformation. *American Journal of Science* 286 (10), 737–764.

Jordan, T.E., Isacks, B.L., Allmendinger, R.W., Brewer, J.A., Ramos, V.A., Ando, C.J. (1983). Andean tectonics related to geometry of subducted Nazca plate. *Geological Society of America Bulletin* 94 (3), 341–361.

Ketcham, R.A., Carter, A., Donelick, R.A., Barbarand, J., Hurford, A.J. (2007). Improved modeling of fission-track annealing in apatite. *American Mineralogist* 92 (5-6), 799–810.

Ketcham, R.A., Donelick, R.A., Carlson, W.D. (1999). Variability of apatite fission-track annealing kinetics; III, Extrapolation to geological time scales. *American Mineralogist* 84 (9), 1235–1255.

Ketcham, R.A., Gautheron, C., Tassan-Got, L. (2011). Accounting for long alpha-particle stopping distances in (U–Th–Sm)/He geochronology: Refinement of the baseline case. *Geochimica et Cosmochimica Acta* 75 (24), 7779–7791.

Kleinert, K., Strecker, M.R. (2001). Climate change in response to orographic barrier uplift: Paleosol and stable isotope evidence from the late Neogene Santa María basin, northwestern Argentina. *Geological Society of America Bulletin* 113 (6), 728–742.

Kley, J. (1996). Transition from basement-involved to thin-skinned thrusting in the Cordillera Oriental of southern Bolivia. *Tectonics* 15 (4), 763–775.

Kley, J. (1999). Geologic and geometric constraints on a kinematic model of the Bolivian orocline. *Journal of South American Earth Sciences* 12 (2), 221–235.

Kley, J., Monaldi, C.R. (1998). Tectonic shortening and crustal thickness in the Central Andes: How good is the correlation? *Geology* 26 (8), 723–726.

Kley, J., Monaldi, C.R. (2002). Tectonic inversion in the Santa Barbara System of the central Andean foreland thrust belt, northwestern Argentina. *Tectonics* 21 (6), 11-1-11-18.

Kley, J., Monaldi, C.R., Salfity, J.A. (1999). Along-strike segmentation of the Andean foreland: causes and consequences. *Tectonophysics* 301 (1-2), 75–94.

Kley, J., Rossello, E.A., Monaldi, C.R., Habighorst, B. (2005). Seismic and field evidence for selective inversion of Cretaceous normal faults, Salta rift, northwest Argentina. *Tectonophysics* 399 (1-4), 155–172.

Kocks, H. (1999). *Geologie und Tektonik des Gebietes zwischen Palca de Aparzo und Abra de Zenta in der Ostkordillere der Zentralanden bei 23° Süd (Nordargentinien)*. Diploma Thesis, Karlsruhe, Germany.

Kortyna, C., DeCelles, P.G., Carrapa, B. (2019). Structural and thermochronologic constraints on kinematics and timing of inversion of the Salta rift in the Tonco-Amblayo sector of the Andean retroarc fold-thrust belt, northwestern Argentina. In: *Andean Tectonics*. Elsevier, pp. 429–464.

Kraemer, B., Adelmann, D., Alten, M., Schnurr, W., Erpenstein, K., Kiefer, E., Van den Bogaard, P., Görler, K. (1999). Incorporation of the Paleogene foreland into the Neogene Puna plateau: The Salar de Antofalla area, NW Argentina. *Journal of South American Earth Sciences* 12 (2), 157–182.

Kusaik, M.E. (2008). *Le mésozoïque du système Subandin de Bolivie : évolution sédimentaire et synthèse du bassin*. Thesis, Grenoble, France.

Lamb, S. (2001). Vertical axis rotation in the Bolivian orocline, South America: 2. Kinematic and dynamical implications. *Journal of Geophysical Research: Solid Earth* 106 (B11), 26633–26653.

Lana, C., Farina, F., Gerdes, A., Alkmim, A., Gonçalves, G.O., Jardim, A.C. (2017). Characterization of zircon reference materials via high precision U–Pb LA-MC-ICP-MS. *Journal of Analytical Atomic Spectrometry* 32 (10), 2011–2023.

Lapiana, A.T. (2021). *Evolución de los sistemas fluviales en la cuenca de antepaís paleógena-neógena en la región de Sierra de Aguilar-Tres Cruces, Noroeste Argentino*. Doctoral Thesis, Córdoba, Argentina.

Linkimer, L., Beck, S.L., Zandt, G., Alvarado, P., Anderson, M., Gilbert, H., Zhang, H. (2020). Lithospheric structure of the Pampean flat slab region from double-difference tomography. *Journal of South American Earth Sciences* 97, 102417.

Llorens, M., Perez Loinaze, V., Narváez, P., Zelaya, A., Pincheira, E., Gorustovich, S. (2022). A Mid-Latitude Maastrichtian Palynological Record From The Yacoraite Formation (Salta Group), Northwestern Argentina. *Cretaceous Research* 140, 105332.

Lork, A., Miller, H., Kramm, U., Grauert, B. (1990). Sistemática U-Pb de circones detríticos de la Formación Puncoviscana y su significado para la edad máxima de sedimentación en la Sierra de Cachi (prov. De Salta, Argentina). In: Aceñolaza, G.F., Miller, H., Toselli, A.J. (Eds.) *El Ciclo Pampeano en el Noreste Argentino. Serie Correlación Geológica*, vol. 4, pp. 199–208.

Lowell, J.D. (1995). Mechanics of basin inversion from worldwide examples. *Geological Society, London, Special Publications* 88 (1), 39–57.

Lucassen, F., Franz, G., Laber, A. (1999). Permian high pressure rocks—the basement of the Sierra de Limón Verde in Northern Chile. *Journal of South American Earth Sciences* 12 (2), 183–199.

Ludwig, K. (2012). Isoplot 4.15: a geochronological toolkit for Microsoft Excel. *Berkeley*

Geochronology Center Special Publication 5.
Mángano, M.G., Buatois, L.A. (2004). Integración de estratigrafía secuencial, sedimentología e icnología para un análisis cronoestratigráfico del Paleozoico inferior del noroeste argentino. *Revista de la Asociación Geológica Argentina* 59, 273–280.
Marquillas, R.A., Del Papa, C.E., Sabino, I.F. (2005). Sedimentary aspects and paleoenvironmental evolution of a rift basin: Salta Group (Cretaceous–Paleogene), northwestern Argentina. *International Journal of Earth Sciences* 94 (1), 94–113.
Marrett, R.A., Allmendinger, R.W., Alonso, R.N., Drake, R.E. (1994). Late Cenozoic tectonic evolution of the Puna Plateau and adjacent foreland, northwestern Argentine Andes. *Journal of South American Earth Sciences* 7 (2), 179–207.
Marrett, R.A., Strecker, M.R. (2000). Response of intracontinental deformation in the central Andes to late Cenozoic reorganization of South American Plate motions. *Tectonics* 19 (3), 452–467.
Marshak, S. (2004). Salients, recesses, arcs, oroclines, and syntaxesda review of ideas concerning the formation of map-view curves in fold-thrust belts. In: McClay, K.R. (Ed.) *Thrust Tectonics and Hydrocarbon Systems*. American Association of Petroleum Geologists, pp. 131–156.
Martinez, E., Aranibar, O., Welsink, H.J., Jarandilla, J. (1995). Structural Inversion of a Cretaceous Rift Basin, Southern Altiplano, Bolivia. In: Tankard, A.J., Suárez-Soruco, R., Welsink, H.J. (Eds.) *Petroleum basins of South America*. American Association of Petroleum Geologists.
McBride, S. (2008). *Sediment provenance and tectonic significance of the cretaceous Pirgua Subgroup, NW Argentina*. Master Thesis, Tucson, Arizona.
McClay, K.R., Buchanan, P.G. (1992). Thrust faults in inverted extensional basins. In: McClay, K.R. (Ed.) *Thrust Tectonics*. Springer, Dordrecht, pp. 93–104.
McFarland, P.K., Bennett, R.A., Alvarado, P., DeCelles, P.G. (2017). Rapid Geodetic Shortening Across the Eastern Cordillera of NW Argentina Observed by the Puna-Andes GPS Array. *Journal of Geophysical Research: Solid Earth* 122 (10), 8600–8623.
McGroder, M.F., Lease, R.O., Pearson, D.M. (2015). Along-strike variation in structural styles and hydrocarbon occurrences, Subandean fold-and-thrust belt and inner foreland, Colombia to Argentina. In: DeCelles, P.G., Ducea, M.N., Carrapa, B., Kapp, P.A. (Eds.) *Geodynamics of a Cordilleran Orogenic System: The Central Andes of Argentina and Northern Chile*. Geological Society of America.
McLane, M. (1995). *Sedimentology.* Oxford University Press, New York.
McNaught, M.A., Mitra, G. (1993). A kinematic model for the origin of footwall synclines. *Journal of Structural Geology* 15 (6), 805–808.
McQuarrie, N. (2002). The kinematic history of the central Andean fold-thrust belt, Bolivia: Implications for building a high plateau. *Geological Society of America Bulletin* 114 (8), 950–963.
McQuarrie, N., Barnes, J.B., Ehlers, T.A. (2008). Geometric, kinematic, and erosional history of the central Andean Plateau, Bolivia (15-17°S). *Tectonics* 27 (3), TC3007.
McQuarrie, N., DeCelles, P.G. (2001). Geometry and structural evolution of the central Andean

backthrust belt, Bolivia. *Tectonics* 20 (5), 669–692.

McQuarrie, N., Horton, B.K., Zandt, G., Beck, S.L., DeCelles, P.G. (2005). Lithospheric evolution of the Andean fold–thrust belt, Bolivia, and the origin of the central Andean plateau. *Tectonophysics* 399 (1-4), 15–37.

Meesters, A.G.C.A., Dunai, T.J. (2005). A noniterative solution of the (U-Th)/He age equation. *Geochemistry, Geophysics, Geosystems* 6 (4), Q04002.

Mon, R., Rahmer, S., Mena, R. (1993). Estructuras superpuestas en la Cordillera Oriental. *Actas XII Congreso Geológico Argentino y II Congreso de Exploración de Hidrocarburos* 2, 48–54.

Monaldi, C.R., Boso, M. (1987). Dalmanitina (Dalmanitina) subandina nov. Sp. (Trilobita) en la Formación Zapla del norte argentino. *Actas 4° Congreso Latinoamericano de Paleontología* 1, 149–157.

Monaldi, C.R., Salfity, J.A., Kley, J. (2008). Preserved extensional structures in an inverted Cretaceous rift basin, northwestern Argentina: Outcrop examples and implications for fault reactivation. *Tectonics* 27 (1), TC1011.

Montero-López, C., Del Papa, C.E., Hongn, F.D., Strecker, M.R., Aramayo, A. (2018). Synsedimentary broken-foreland tectonics during the Paleogene in the Andes of NW Argentine: new evidence from regional to centimetre-scale deformation features. *Basin Research* 30, 142–159.

Montero-López, C., Hongn, F.D., López Steinmetz, R.L., Aramayo, A., Pingel, H., Strecker, M.R., Cottle, J.M., Bianchi, C. (2021). Development of an incipient Paleogene topography between the present-day Eastern Andean Plateau (Puna) and the Eastern Cordillera, southern Central Andes, NW Argentina. *Basin Research* 33 (2), 1194–1217.

Moreno, J.A. (1970). Estratigrafía y paleogeografía del Cretácico superior en la cuenca del noroeste argentino, con especial mención de los Subgrupos Balbuena y Santa Bárbara. *Revista de la Asociación Geológica Argentina* 24, 9–44.

Moulin, M., Aslanian, D., Unternehr, P. (2010). A new starting point for the South and Equatorial Atlantic Ocean. *Earth-Science Reviews* 98 (1-2), 1–37.

Moya, M.C. (1988). Lower Ordovician in the southern part of the Argentine Eastern Cordillera. In: Bahlburg, H., Breitkreuz, C., Giese, P. (Eds.) *The Southern Central Andes*, vol. 17. Springer, Berlin/Heidelberg, pp. 55–69.

Moya, M.C. (1998). El Paleozoico Inferior en la Sierra de Mojotoro, Salta-Jujuy. *Revista de la Asociación Geológica Argentina* 53 (2), 219–238.

Moya, M.C. (2015). La "Fase Oclóyica Ordovícico Superior" en el noroeste argentine: Interpretación histórica y evidencias en contrario. *Contribuciones a la Geología Argentina: Serie Correlación Geológica* 31 (1), 73–110.

Müller, J.P., Kley, J., Jacobshagen, V. (2002). Structure and Cenozoic kinematics of the Eastern Cordillera, southern Bolivia (21°S). *Tectonics* 21 (5), 1-1-1-24.

Nakapelyukh, M., Bubniak, I., Bubniak, A., Jonckheere, R., Ratschbacher, L. (2018). Cenozoic structural evolution, thermal history, and erosion of the Ukrainian Carpathians fold-thrust belt. *Tectonophysics* 722, 197–209.

Nielsen, A. (1997). A review of Ordovician agnostid genera (Trilobita). *Transactions of the*

Royal Society of Edinburgh: Earth Sciences 87, 463–501.
Noetinger, S., Di Pasquo, M., Isaacson, P.E., Aceñolaza, G.F., Del Vergel, M.M. (2016). Integrated study of fauna and microflora from the Early Devonian (Pragian–Emsian) of northwestern Argentina. *Historical Biology* 28 (7), 913–929.
Omarini, R.H., Sureda, R.J., Götze, H.-J., Seilacher, A., Pflüger, F. (1999). Puncoviscana folded belt in northwestern Argentina: testimony of Late Proterozoic Rodinia fragmentation and pre-Gondwana collisional episodes. *International Journal of Earth Sciences* 88 (1), 76–97.
Oncken, O., Chong, G., Franz, G., Giese, P., Götze, H.-J., Ramos, V.A., Strecker, M.R., Wigger, P.J. (Eds.) (2006). *The Andes*. *Active Subduction Orogeny,* 1st ed. Springer, Berlin, Heidelberg.
Ortner, H., Gruber, A. (2011). 3D-Geometrie der Strukturen zwischen Karwendel-Synklinale und Thiersee-Synklinale. In: Gruber, A. (Ed.) *Arbeitstagung 2011 "Geologie des Achenseegebietes"*. *Geologisches Kartenblatt 88 Achenkirch*. Geologische Bundesanstalt, Wien, pp. 51–67.
Otamendi, J.E., Cristofolini, E.A., Morosini, A., Armas, P., Tibaldi, A.M., Camilletti, G.C. (2020). The geodynamic history of the Famatinian arc, Argentina: A record of exposed geology over the type section (latitudes 27°-33° south). *Journal of South American Earth Sciences* 100, 102558.
Palma, R.M. (2000). Lacustrine Facies in the Upper Cretaceous Balbuena Subgroup (Salta Group): Andina Basin, Argentina. In: *Lake Basins Through Space and Time*, vol. 46. American Association of Petroleum Geologists, pp. 323–328.
Parker, S.D., Pearson, D.M. (2021). Pre-thrusting stratigraphic control on the transition from a thin-skinned to thick-skinned structural style: An example from the double-decker Idaho-Montana Fold-Thrust Belt. *Tectonics* 40 (5), e2020TC006429.
Pascual, R., Bond, M., Vucetich, M. (1981). El Subgrupo Santa Bárbara (Grupo Salta) y sus vertebrados, cronología, paleoambientes y paleobiogeografía. *Actas VIII Congreso Geológico Argentino* 3, 743-758.
Paton, C., Hellstrom, J.C., Paul, B., Woodhead, J.D., Hergt, J.M. (2011). Iolite: Freeware for the visualisation and processing of mass spectrometric data. *Journal of Analytical Atomic Spectrometry* 26 (12), 2508–2518.
Paton, C., Woodhead, J.D., Hellstrom, J.C., Hergt, J.M., Greig, A., Maas, R. (2010). Improved laser ablation U-Pb zircon geochronology through robust downhole fractionation correction. *Geochemistry, Geophysics, Geosystems* 11 (3), Q0AA06.
Payrola, P.A., Del Papa, C.E., Aramayo, A., Pingel, H., Hongn, F.D., Sobel, E.R., Zeilinger, G., Strecker, M.R., Zapata, S., Cottle, J.M., Salado Paz, N., Glodny, J. (2020). Episodic out-of-sequence deformation promoted by Cenozoic fault reactivation in NW Argentina. *Tectonophysics* 776, 228276.
Payrola, P.A., Hongn, F.D., Cristallini, E., García, V., Del Papa, C.E. (2012). Andean oblique folds in the Cordillera Oriental – Northwestern Argentina: Insights from analogue models. *Journal of Structural Geology* 42, 194–211.
Pearson, D.M., Kapp, P.A., DeCelles, P.G., Reiners, P.W., Gehrels, G.E., Ducea, M.N., Pullen,

A. (2013). Influence of pre-Andean crustal structure on Cenozoic thrust belt kinematics and shortening magnitude: Northwestern Argentina. *Geosphere* 9 (6), 1766–1782.

Pearson, D.M., Kapp, P.A., Reiners, P.W., Gehrels, G.E., Ducea, M.N., Pullen, A., Otamendi, J.E., Alonso, R.N. (2012). Major Miocene exhumation by fault-propagation folding within a metamorphosed, early Paleozoic thrust belt: Northwestern Argentina. *Tectonics* 31 (4), TC4023.

Perez, N.D., Horton, B.K., Carlotto, V. (2016). Structural inheritance and selective reactivation in the central Andes: Cenozoic deformation guided by pre-Andean structures in southern Peru. *Tectonophysics* 671, 264–280.

Petroleum Experts, 2020. MOVE (Software).

Petrus, J.A., Kamber, B.S. (2012). VizualAge: A Novel Approach to Laser Ablation ICP-MS U-Pb Geochronology Data Reduction. *Geostandards and Geoanalytical Research* 36 (3), 247–270.

Pfiffner, A.O. (2017). Thick-skinned and thin-skinned tectonics: A global perspective. *Geosciences* 7 (3), 71.

Pingel, H., Alonso, R.N., Mulch, A., Rohrmann, A., Sudo, M., Strecker, M.R. (2014). Pliocene orographic barrier uplift in the southern Central Andes. *Geology* 42 (8), 691–694.

Pingel, H., Schildgen, T.F., Strecker, M.R., Wittmann, H. (2019). Pliocene–Pleistocene orographic control on denudation in Northwest Argentina. *Geology* 47 (4), 359–362.

Pingel, H., Strecker, M.R., Alonso, R.N., Schmitt, A.K. (2013). Neotectonic basin and landscape evolution in the Eastern Cordillera of NW Argentina, Humahuaca Basin (~24°S). *Basin Research* 25 (5), 554–573.

Powell, J.W., Issler, D.R., Schneider, D.A., Fallas, K.M., Stockli, D.F. (2020). Thermal history of the Mackenzie Plain, Northwest Territories, Canada: Insights from low-temperature thermochronology of the Devonian Imperial Formation. *Geological Society of America Bulletin* 132 (3-4), 767–783.

Rahl, J.M., Harbor, D.J., Galli, C.I., O'Sullivan, P.B. (2018). Foreland Basin Record of Uplift and Exhumation of the Eastern Cordillera, Northwest Argentina. *Tectonics* 37 (11), 4173–4193.

Rak, A.J., McQuarrie, N., Ehlers, T.A. (2017). Kinematics, Exhumation, and Sedimentation of the North Central Andes (Bolivia): An Integrated Thermochronometer and Thermokinematic Modeling Approach. *Tectonics* 36 (11), 2524–2554.

Ramos, V.A. (1988). Late Proterozoic-Early Paleozoic of South America - a collisional history. *Episodes* 11, 168–174.

Ramos, V.A. (2008). The basement of the Central Andes: the Arequipa and related terranes. *Annual Review of Earth and Planetary Sciences* 36 (1), 289–324.

Ramos, V.A. (2018). The Famatinian Orogen along the protomargin of western Gondwana: Evidence for a nearly continuous Ordovician magmatic arc between Venezuela and Argentina. In: Folguera, A., Contreras-Reyes, E., Heredia, N., Encinas, A., Iannelli, S.B., Oliveros, V., Dávila, F.M., Collo, G., Giambiagi, L., Maksymowicz, A., Iglesia Llanos, M.P., Turienzo, M., Naipauer, M., Orts, D., Litvak, V., Alvarez, O., Arriagada, C. (Eds.) *The evolution of the Chilean-Argentinean Andes*. Springer International Publishing, Cham, pp. 133–161.

Ramos, V.A., Cristallini, E., Pérez, D.J. (2002). The Pampean flat-slab of the Central Andes. *Journal of South American Earth Sciences* 15 (1), 59–78.

Ramos, V.A., Vujovich, G., Martino, R., Otamendi, J.E. (2010). Pampia: A large cratonic block missing in the Rodinia supercontinent. *Journal of Geodynamics* 50 (3-4), 243–255.

Ramsay, J.G., Huber, M.I. (1987). *The techniques of modern structural geology, Vol. 2. Folds and Fractures.* Pergamon Press, London.

Rapela, C.W., Pankhurst, R.J., Casquet, C., Baldo, E.G., Saavedra, J., Galindo, C., Fanning, M. (1998). The Pampean Orogeny of the southern proto-Andes: Cambrian continental collision in the Sierras de Córdoba. *Geological Society, London, Special Publications* 142 (1), 181–217.

Rapela, C.W., Pankhurst, R.J., Casquet, C., Fanning, M., Baldo, E.G., González-Casado, J.M., Galindo, C., Dahlquist, J.A. (2007). The Río de la Plata craton and the assembly of SW Gondwana. *Earth-Science Reviews* 83 (1-2), 49–82.

Rech, J.A., Currie, B.S., Michalski, G., Cowan, A.M. (2006). Neogene climate change and uplift in the Atacama Desert, Chile. *Geology* 34 (9), 761–764.

Rech, J.A., Currie, B.S., Shullenberger, E.D., Dunagan, S.P., Jordan, T.E., Blanco, N., Tomlinson, A.J., Rowe, H.D., Houston, J. (2010). Evidence for the development of the Andean rain shadow from a Neogene isotopic record in the Atacama Desert, Chile. *Earth and Planetary Science Letters* 292 (3-4), 371–382.

Reiners, P.W., Spell, T.L., Nicolescu, S., Zanetti, K.A. (2004). Zircon (U-Th)/He thermochronometry: He diffusion and comparisons with $^{40}Ar/^{39}Ar$ dating. *Geochimica et Cosmochimica Acta* 68 (8), 1857–1887.

Reiners, P.W., Thomson, S.N., Vernon, A., Willett, S.D., Zattin, M., Einhorn, J.C., Gehrels, G.E., Quade, J., Pearson, D.M., Murray, K.E., Cavazza, W. (2015). Low-temperature thermochronologic trends across the central Andes, 21°S–28°S. In: DeCelles, P.G., Ducea, M.N., Carrapa, B., Kapp, P.A. (Eds.) *Geodynamics of a Cordilleran Orogenic System: The Central Andes of Argentina and Northern Chile*. Geological Society of America.

Renaut, R., Gierlowski-Kordesch, E.H. (2010). Lakes. In: James, N.P., Dalrymple, R.W. (Eds.) *Facies Models*, vol. 4. Geological Association of Canada, St. John’s, pp. 541–573.

Reyes, F., Salfity, J.A. (1973). Consideraciones sobre la estratigrafia del Cretácico (Subgrupo Pirgua) del noroeste argentino. In: *Actas 5° Congr. Geol. Arg. Carlos Paz*, pp. 355–385.

Reyes, F., Salfity, J.A., Viramonte, J.G., Gutierrez, W. (1976). Consideraciones sobre el vulcanismo del Subgrupo Pirgua (Cretacico) en el norte argentino. *Actas VI Congreso Geológico Argentino* 1, 205–223.

Reynolds, J.H., Galli, C.I., Hernández, R., Idleman, B.D., Kotila, J.M., Hilliard, R.V., Naeser, C.W. (2000). Middle Miocene tectonic development of the Transition Zone, Salta Province, northwest Argentina: Magnetic stratigraphy from the Metán Subgroup, Sierra de González. *Geological Society of America Bulletin* 112 (11), 1736–1751.

Reynolds, J.H., Hernández, R., Galli, C.I., Idleman, B.D. (2001). Magnetostratigraphy of the Quebrada La Porcelana section, Sierra de Ramos, Salta Province, Argentina: age limits for the Neogene Orán Group and uplift of the southern Sierras Subandinas. *Journal of South*

American Earth Sciences 14 (7), 681–692.
Rickards, R., Ortega, G., Bassett, M., Boso, M., Monaldi, C.R. (2002). Talacastograptus, an unusual biserial graptolite, and other Silurian forms from Argentina and Bolivia. *Ameghiniana* 39 (3), 343–350.
Rocha-Campos, A.C., Basei, M.A., Nutman, A.P., Kleiman, L.E., Varela, R., Llambias, E., Canile, F.M., Da Rosa, O.d.C. (2011). 30 million years of Permian volcanism recorded in the Choiyoi igneous province (W Argentina) and their source for younger ash fall deposits in the Paraná Basin: SHRIMP U–Pb zircon geochronology evidence. *Gondwana Research* 19 (2), 509–523.
Rodríguez-Fernández, L.R., Heredia, N., Seggiaro, R.E., González, M.A. (1999). Estructura andina de la Cordillera Oriental en el área de la Quebrada de Humahuaca, Provincia de Jujuy, NO de Argentina. *Trabajos de Geología* 21, 321–333.
Roeder, D. (1988). Andean-age structure of Eastern Cordillera (Province of La Paz, Bolivia). *Tectonics* 7 (1), 23–39.
Rohais, S., Hamon, Y., Deschamps, R., Beaumont, V., Gasparrini, M., Pillot, D., Romero-Sarmiento, M.-F. (2019). Patterns of organic carbon enrichment in a lacustrine system across the K-T boundary: Insight from a multi-proxy analysis of the Yacoraite Formation, Salta rift basin, Argentina. *International Journal of Coal Geology* 210, 103208.
Rubinstein, C.V. (2005). Ordovician to Lower Silurian palynomorphs from the Sierras subandinas (Subandean ranges), northwestern Argentina: a preliminary report. *Carnets de Geologie* 2, 51–56.
Russo, A., Ferello, R., Chebli, G.A. (1979). Llanura Chaco Pampeana. In: *Geología Regional Argentina*. Academia Nacional de Ciencias, pp. 139–183.
Salazar-Mora, C.A., Huismans, R.S., Fossen, H., Egydio-Silva, M. (2018). The Wilson Cycle and Effects of Tectonic Structural Inheritance on Rifted Passive Margin Formation. *Tectonics* 37 (9), 3085–3101.
Salfity, J.A. (Ed.) (1994). *Cretaceous Tectonics of the Andes.* Vieweg+Teubner Verlag, Wiesbaden.
Salfity, J.A., Marquillas, R.A. (1994). Tectonic and Sedimentary Evolution of the Cretaceous-Eocene Salta Group Basin, Argentina. In: Salfity, J.A. (Ed.) *Cretaceous Tectonics of the Andes*. Vieweg+Teubner Verlag, Wiesbaden, pp. 266–315.
Sanchéz, M., Salfity, J.A. (1999). La cuenca Cámbrica del Grupo Mesón en el Noroeste Argentino: Desarrollo estratigráfico y paleogeográfico. *Acta Geológica Hispanica* 34 (2-3), 123–139.
Sarg, J.F., Suriamin, N., Tänavsuu-Milkeviciene, K., Humphrey, J.D. (2013). Lithofacies, stable isotopic composition, and stratigraphic evolution of microbial and associated carbonates, Green River Formation (Eocene), Piceance Basin, Colorado. *AAPG Bulletin* 97 (11), 1937–1966.
Saylor, J., Sundell, K.E. (2016). Quantifying comparison of large detrital geochronology data sets. *Geosphere* 12 (1), 203–220.
Schenk, C.J., Viger, R., Anderson, C.P. (1999). South America Geologic Map (geo6ag). *U.S. Geological Survey data release*.

Scheuber, E., Gonzalez, G. (1999). Tectonics of the Jurassic-Early Cretaceous magmatic arc of the north Chilean Coastal Cordillera (22°-26°S): A story of crustal deformation along a convergent plate boundary. *Tectonics* 18 (5), 895–910.

Schildgen, T.F., Robinson, R.A.J., Savi, S., Phillips, W.M., Spencer, J.Q.G., Bookhagen, B., Scherler, D., Tofelde, S., Alonso, R.N., Kubik, P.W., Binnie, S.A., Strecker, M.R. (2016). Landscape response to late Pleistocene climate change in NW Argentina: Sediment flux modulated by basin geometry and connectivity. *Journal of Geophysical Research: Earth Surface* 121 (2), 392–414.

Schoenbohm, L.M., Carrapa, B., McPherson, H.M., Pratt, J.R., Bywater-Reyes, S., Mortimer, E.E.J. (2015). Climate and tectonics along the southern margin of the Puna Plateau, NW Argentina: Origin of the late Cenozoic Punaschotter conglomerates. *Geological Society of America Memoirs* 212, 251–260.

Scisciani, V. (2009). Styles of positive inversion tectonics in the Central Apennines and in the Adriatic foreland: Implications for the evolution of the Apennine chain (Italy). *Journal of Structural Geology* 31 (11), 1276–1294.

Seggiaro, R.E., Aris, J., Heredia, N., Gallardo, E., Rodriguez, R., Gallastegui, G., Alonso, J.L. (2008). Estructuras extensionales ordovícicas en la Cordillera Oriental, Noroeste Argentino. *Actas XVII Congreso Geológico Argentino* 1, 43–44.

Seggiaro, R.E., Bulnes, M., Poblet, J., Aguilera, N.G., Rodríguez-Fernández, L.R., Heredia, N., Alonso, J.L. (2010). Paleozoic to present-day kinematic evolution of the frontal part of the Andes between parallels 23 and 24 S (Jujuy province, Argentina). *Trabajos de Geología* 30, 214–220.

Seggiaro, R.E., Gallardo, E. (2002). Evidencias de tectónica extensional durante el Paleozoico inferior en las quebradas de Coquena y Humahuaca. Cordillera Oriental. Norte Argentino. *Actas XV Congreso Geológico Boliviano*, 279–282.

Seggiaro, R.E., Gallardo, E., González, D. (2014). Tectónica superpuesta en la Sierra de Mojotoro, Cordillera Oriental Provincia de Salta. *Actas XIX Congreso Geológico Argentino* S22-63, 1669–1670.

Seggiaro, R.E., Villagrán, C., Celedón, M., Barrabino, E., Apaza, F. (2017). Reactivación de fallas paleozoicas durante la tectónica andina en la Cordillera Oriental-noroeste argentino. In: Muruaga, C., Grosse, P. (Eds.) *Ciencias de la Tierra y Recursos Naturales del NOA. Relatorio del XX Congreso Geológico Argentino*, San Miguel de Tucumán, pp. 603–623.

Sempere, T. (1995). Phanerozoic evolution of Bolivia and adjacent regions. In: Tankard, A.J., Suárez-Soruco, R., Welsink, H.J. (Eds.) *Petroleum basins of South America*. American Association of Petroleum Geologists, pp. 207–230.

Sempere, T., Carlier, G., Carlotto, V., Jacay, J. (1998). Rifting Pérmico superior-Jurásico medio en la Cordillera Oriental de Perú y Bolivia. In: *Memorias XIII Congreso Geologico de Bolivia, Potosi - Bolivia*, vol. 1, pp. 31–37.

Sempere, T., Carlier, G., Carlotto, V., Jacay, J., Jiménez, N., Rosas, S., Soler, P., Cárdenas, J., Boudesseul, N. (1999). Late Permian-early Mesozoic rifts in Peru and Bolivia, and their bearing on Andean-age tectonics. In: *IV International Symposium on Andean Geodynamics, Göttingen, Abstracts*, pp. 680–685.

Sempere, T., Carlier, G., Soler, P., Fornari, M., Carlotto, V., Jacay, J., Arispe, O., Néraudeau, D., Cárdenas, J., Rosas, S., Jiménez, N. (2002). Late Permian–Middle Jurassic lithospheric thinning in Peru and Bolivia, and its bearing on Andean-age tectonics. *Tectonophysics* 345 (1-4), 153–181.

Sharman, G.R., Malkowski, M.A. (2020). Needles in a haystack: Detrital zircon U-Pb ages and the maximum depositional age of modern global sediment. *Earth-Science Reviews* 203, 103109.

Sickmann, Z.T., Schwartz, T.M., Graham, S.A. (2018). Refining stratigraphy and tectonic history using detrital zircon maximum depositional age: an example from the Cerro Fortaleza Formation, Austral Basin, southern Patagonia. *Basin Research* 30 (4), 708–729.

Siks, B.C., Horton, B.K. (2011). Growth and fragmentation of the Andean foreland basin during eastward advance of fold-thrust deformation, Puna plateau and Eastern Cordillera, northern Argentina. *Tectonics* 30 (6), TC6017.

Sláma, J., Košler, J., Condon, D.J., Crowley, J.L., Gerdes, A., Hanchar, J.M., Horstwood, M.S., Morris, G.A., Nasdala, L., Norberg, N., Schaltegger, U., Schoene, B., Tubrett, M.N., Whitehouse, M.J. (2008). Plešovice zircon — A new natural reference material for U–Pb and Hf isotopic microanalysis. *Chemical Geology* 249 (1-2), 1–35.

Sobel, E.R., Seward, D. (2010). Influence of etching conditions on apatite fission-track etch pit diameter. *Chemical Geology* 271 (1-2), 59–69.

Sobel, E.R., Strecker, M.R. (2003). Uplift, exhumation and precipitation: tectonic and climatic control of Late Cenozoic landscape evolution in the northern Sierras Pampeanas, Argentina. *Basin Research* 15 (4), 431–451.

Sobolev, S.V., Babeyko, A.Y. (2005). What drives orogeny in the Andes? *Geology* 33 (8), 617–620.

Spiegel, C., Siebel, W., Kuhlemann, J., Frisch, W. (2004). Toward a comprehensive provenance analysis: A multi-method approach and its implications for the evolution of the Central Alps. In: Bernet, M., Spiegel, C. (Eds.) *Detrital thermochronology - Provenance analysis, exhumation, and landscape evolution of mountain belts*. *Special Paper 378*. Geological Society of America, pp. 37–50.

Stalder, N.F., Herman, F., Fellin, M.G., Coutand, I., Aguilar, G., Reiners, P.W., Fox, M. (2020). The relationships between tectonics, climate and exhumation in the Central Andes (18–36°S): Evidence from low-temperature thermochronology. *Earth-Science Reviews* 210, 103276.

Starck, D. (1995). Silurian-Jurassic stratigraphy and basin evolution of Northwestern Argentina. In: Tankard, A.J., Suárez-Soruco, R., Welsink, H.J. (Eds.) *Petroleum basins of South America*. American Association of Petroleum Geologists, pp. 251–267.

Starck, D. (2008). La Cuenca Carbonífera-¿Eomesozoica? en la Provincia de Jujuy, su Estratigrafía y Evolución Tectosedimentaria. *Relatorio del XVII Congreso Geológico Argentino, Jujuy*, 199–206.

Starck, D. (2011). Cuenca Cretácica-Paleógena del Noroeste Argentino. In: Kozlowski, E., Legarreta, L., Boll, A., Marshall, P. (Eds.) *VIII Congreso de Exploración y Desarrollo de Hidrocarburos - Simposio Cuencas Argentinas*. *Visión actual*, pp. 1–48.

Starck, D., Del Papa, C.E. (2006). The northwestern Argentina Tarija Basin: Stratigraphy, depositional systems, and controlling factors in a glaciated basin. *Journal of South American Earth Sciences* 22 (3-4), 169–184.
Starck, D., Gallardo, E., Schulz, A. (1992). La discordancia precarbónica en la porción argentina de la cuenca de Tarija. *Boletín de Informaciones Petroleras* 30, 2–14.
Starck, D., Gallardo, E., Schulz, A. (1993). The Pre-Carboniferous Unconformity in the Argentina Portion of the Tarija Basin. *Comptes Rendus XII ICC-P* 2, 373–384.
Starck, D., Vergani, G.D. (1996). Desarrollo tecto-sedimentario del Cenozoico en el sur de la Provincia de Salta - Argentina. *XIII Congreso Geológico Argentino y III Congreso de Exploración de Hidrocarburos, Buenos Aires, Actas* I, 433–452.
Strecker, M.R., Alonso, R.N., Bookhagen, B., Carrapa, B., Hilley, G.E., Sobel, E.R., Trauth, M.H. (2007). Tectonics and climate of the southern Central Andes. *Annual Review of Earth and Planetary Sciences* 35 (1), 747–787.
Strecker, M.R., Cerveny, P., Bloom, A.L., Malizia, D. (1989). Late Cenozoic tectonism and landscape development in the foreland of the Andes: Northern Sierras Pampeanas (26°-28°S), Argentina. *Tectonics* 8 (3), 517–534.
Strecker, M.R., Hilley, G.E., Bookhagen, B., Sobel, E.R. (2011). Structural, geomorphic, and depositional characteristics of contiguous and broken foreland basins: Examples from the eastern flanks of the Central Andes in Bolivia and NW Argentina. In: Busby, C., Azor, A. (Eds.) *Tectonics of Sedimentary Basins*. John Wiley & Sons, Ltd, Chichester, UK, pp. 508–521.
Streit, R.L., Burbank, D.W., Strecker, M.R., Alonso, R.N., Cottle, J.M., Kylander-Clark, A.R. (2017). Controls on intermontane basin filling, isolation and incision on the margin of the Puna Plateau, NW Argentina (~23°S). *Basin Research* 29 (S1), 131–155.
Sundell, K.E., 2022. AgeCalcML (Software). Arizona LaserChron Center.
Suppe, J. (1983). Geometry and kinematics of fault-bend folding. *American Journal of Science* 283 (7), 684–721.
Tänavsuu-Milkeviciene, K., Sarg, J.F., Bartov, Y. (2017). Depositional Cycles and Sequences In An Organic-Rich Lake Basin: Eocene Green River Formation, Lake Uinta, Colorado and Utah, U.S.A. *Journal of Sedimentary Research* 87 (3), 210–229.
Teixell, A., Arboleya, M.-L., Julivert, M., Charroud, M. (2003). Tectonic shortening and topography in the central High Atlas (Morocco). *Tectonics* 22 (5), 1051.
Tomezzoli, R. (1996). Stratigraphy of the Cuevo (Permian-Lower Triassic) and Tacurú (Jurassic) Groups along the Bermejo river (Orán, Salta, and Tarija, Bolivia). *Revista de la Asociación Geológica Argentina* 51 (1), 37–50.
Turner, J.C.M. (1959). Estratigrafía del cordón de Escaya y de la sierra de Rinconada (Jujuy). *Revista de la Asociación Geológica Argentina* 13, 15–39.
Turner, J.C.M., Mendez, V. (1975). Geología del sector Oriental de los departamentos de Santa Victoria e Iruya. Provincia de Salta. República Argentina. *Boletín Nacional de Ciencias* 51 (1-2), 11–24.
Uba, C.E., Heubeck, C., Hulka, C. (2006). Evolution of the late Cenozoic Chaco foreland basin, Southern Bolivia. *Basin Research* 18 (2), 145–170.

Uba, C.E., Kley, J., Strecker, M.R., Schmitt, A.K. (2009). Unsteady evolution of the Bolivian Subandean thrust belt: The role of enhanced erosion and clastic wedge progradation. *Earth and Planetary Science Letters* 281 (3-4), 134–146.

Uba, C.E., Strecker, M.R., Schmitt, A.K. (2007). Increased sediment accumulation rates and climatic forcing in the central Andes during the late Miocene. *Geology* 35 (11), 979–982.

Udden, J.A. (1914). Mechanical composition of clastic sediments. *Geological Society of America Bulletin* 25 (1), 655–744.

Valencio, D., Giudice, A., Mendía, J., Oliver, G. (1976). Paleomagnetismo y edades K/Ar del Subgrupo Pirgua, provincia de Salta, República Argentina. *Actas VI Congreso Geológico Argentino* 1, 527–542.

Van Kooten, W.S.M.T., Del Papa, C.E., Starck, D., Sobel, E.R., Cavalleri, P., Agüera, M., Van Schijndel, V., Glodny, J. (2022a). Evidence of Jurassic extension in NW Argentina: Characterization of fault-related strata at the Salta Group base using sandstone provenance and zircon U–Pb geochronology. *Journal of South American Earth Sciences* 120, 104048.

Van Kooten, W.S.M.T., Sobel, E.R., Del Papa, C.E., Payrola, P.A., Bande, A., Starck, D. (2021). Exhumation history of the Lomas de Olmedo basin: constraining multi-phase deformation using low-temperature thermochronology. *EGU General Assembly 2021*, EGU21-12429.

Van Kooten, W.S.M.T., Sobel, E.R., Del Papa, C.E., Payrola, P.A., Glodny, J. (2022b). Constraining Andean Propagation of Exhumation at the Limit of the Eastern Cordillera, NW Argentina, using Low-Temperature Thermochronology in a Structural Context. *Tectonics* 41 (8), e2022TC007342.

Vaucher, R., Vaccari, N.E., Balseiro, D., Muñoz, D.F., Dillinger, A., Waisfeld, B.G., Buatois, L.A. (2020). Tectonic controls on late Cambrian-Early Ordovician deposition in Cordillera oriental (Northwest Argentina). *International Journal of Earth Sciences* 109 (6), 1897–1920.

Vergani, G.D., Tankard, A.J. (1995). Tectonic Evolution and Paleogeography of the Neuquén Basin, Argentina. In: Tankard, A.J., Suárez-Soruco, R., Welsink, H.J. (Eds.) *Petroleum Basins of South America*. American Association of Petroleum Geologists.

Vermeesch, P. (2009). RadialPlotter: A Java application for fission track, luminescence and other radial plots. *Radiation Measurements* 44 (4), 409–410.

Vermeesch, P. (2018). IsoplotR: A free and open toolbox for geochronology. *Geoscience Frontiers* 9 (5), 1479–1493.

Vermeesch, P. (2021). Maximum depositional age estimation revisited. *Geoscience Frontiers* 12 (2), 843–850.

Villagrán, C., Seggiaro, R.E., Gallardo, E., Pereyra, R., Barrabino, E., Celedón, M. (2015). Análisis estructural en los alrededores del cerro Gólgota, quebrada del Toro, Salta. *Ciencias de la Tierra y Recursos Naturales del NOA. Relatorio del XX Congreso Geológico Argentino, San Miguel de Tucumán*, 110–111.

Viramonte, J.G., Kay, S., Becchio, R., Escayola, M.P., Novitski, I. (1999). Cretaceous rift related magmatism in central-western South America. *Journal of South American Earth Sciences* 12 (2), 109–121.

Wagner, G.A., Gleadow, A., Fitzgerald, P.G. (1989). The significance of the partial annealing zone in apatite fission-track analysis: Projected track length measurements and uplift chronology of the transantarctic mountains. *Chemical Geology: Isotope Geoscience section* 79 (4), 295–305.

Waisfeld, B., Sánchez, T. (1993). Trilobites Silúricos de la Formación Lipeón en el noroeste Argentino (Sierra de Zapla, provincia de Jujuy). *Ameghiniana* 30, 77–90.

Waisfeld, B.G., Vaccari, N.E. (2003). Trilobites. In: Benedetto, J. (Ed.) *Ordovician Fossils of Argentina*. Universidad Nacional de Córdoba, Secretaría de Ciencia y Tecnología, pp. 295–409.

Wentworth, C.K. (1922). A Scale of Grade and Class Terms for Clastic Sediments. *The Journal of Geology* 30 (5), 377–392.

Wiedenbeck, M., Allé, P., Corfu, F., Griffin, W.L., Meier, M., Oberli, F., Quadt, A. von, Roddick, J.C., Spiegel, W. (1995). Three natural zircon standards for U-Th-Pb, Lu-Hf, trace element and REE analyses. *Geostandards and Geoanalytical Research* 19 (1), 1–23.

Wilson, J.T. (1966). Did the Atlantic Close and then Re-Open? *Nature* 211 (5050), 676–681.

Wilson, R.W., Houseman, G.A., Buiter, S.J.H., McCaffrey, K.J.W., Doré, A.G. (2019). Fifty years of the Wilson Cycle concept in plate tectonics: an overview. *Geological Society, London, Special Publications* 470 (1), 1–17.

Wolf, R.A., Farley, K.A., Kass, D. (1998). Modeling of the temperature sensitivity of the apatite (U–Th)/He thermochronometer. *Chemical Geology* 148 (1-2), 105–114.

Wright, V.P. (1992). A revised classification of limestones. *Sedimentary Geology* 76 (3-4), 177–185.

Yates, D., Moore, D.S., McCabe, G.P. (1999). *The Practice of Statistics*. Freeman, New York.

Zapata, S., Sobel, E.R., Del Papa, C.E., Jelinek, A.R., Glodny, J. (2019a). Using a Paleosurface to Constrain Low-Temperature Thermochronological Data: Tectonic Evolution of the Cuevas Range, Central Andes. *Tectonics* 38 (11), 3939–3958.

Zapata, S., Sobel, E.R., Del Papa, C.E., Muruaga, C., Zhou, R. (2019b). Miocene fragmentation of the Central Andean foreland basins between 26 and 28°S. *Journal of South American Earth Sciences* 94, 102238.

Zeballo, F.J., Tortello, M. (2005). Trilobites del Cámbrico tardío Ordovícico temprano del área de Alfarcito, Tilcara, Cordillera Oriental de Jujuy, Argentina. *Ameghiniana* 42, 127–142.

Zerlauth, M., Ortner, H., Pomella, H., Pfiffner, A.O., Fügenschuh, B. (2014). Inherited tectonic structures controlling the deformation style: an example from the Helvetic nappes of the Eastern Alps. *Swiss Journal of Geosciences* 107 (2), 157–175.

Zhou, R., Schoenbohm, L.M., Sobel, E.R., Davis, D.W., Glodny, J. (2016). New constraints on orogenic models of the southern Central Andean Plateau: Cenozoic basin evolution and bedrock exhumation. *Geological Society of America Bulletin* 129 (1-2), 152–170.

Appendix A. Supporting Information Chapter 2

A.1 Zircon separation and imaging

Sample preparation (including crushing, sieving, magnetic separation with a strong hand magnet) for samples TAC1, TAC2 and BREN1 was done at the Universidad Nacional de Salta in Argentina. This was followed by magnetic separation using a Frantz® magnetic separator (frontal angle 10°, side angle 10°, current 1.2 A) and density separation using Sodium Polytungstate (SPT) and Diiodomethane (DI). The samples were hand-picked under a binocular microscope, mounted in epoxy and polished. The zircons were examined by backscatter electron (BSE) and cathodoluminescence (CL) imaging to determine different age domains and to avoid cracks and metamict zones. The imaging was done using a JEOL JXA-8200 electron microprobe, at the University of Potsdam.

A.2 LA-SF-ICP-MS U–Th–Pb dating

U-Pb data for samples TAC1, TAC2 and BREN1 were obtained at the LA ICP MS lab, University of Potsdam, and were acquired by laser ablation - sectorfield - inductively coupled plasma - mass spectrometry (LA-SF-ICP-MS) employing a single-collector Thermo Finnigan Element2 mass spectrometer coupled to an Elemental Scientific Lasers NWR193 excimer laser ablation system.

The ICP-MS is daily calibrated and optimised using NIST612. For a 50 µm ablation spot, using 10 Hz and 5 J/cm^2, we obtain around 2 Mcps on 238U, < 0.2 % oxide formation and $^{238}U/^{232}Th \approx 1$.

All age data presented here were obtained by single spot analyses with a spot diameter of 30 µm and a crater depth of approximately 20 µm. Ablation was performed under a He atmosphere. The He carrier gas was mixed by pure nitrogen and the sample Ar gas outside the ablation cell by a signal-smoothing device. Information on the data acquisition methods is available in Table A.1.

As primary standard GJ-1 (Jackson et al., 2004) was used to correct for down-hole fractionation and daily instrumental drift. For quality control the 91500 (Wiedenbeck et al., 1995), Plešovice (Sláma et al., 2008) and BB16 (Lana et al., 2017) zircon reference materials were analyzed after every 10 unknown spots. The results of standard measurements, which agree well with published ID-TIMS ages, and of unknowns analyzed are shown in Table A.2.

A.3 Data processing

Laser-induced fractionation, including elemental fractionation and downhole fractionation, and calibration drift were corrected by bracketing measurements of unknowns with the GJ-1 zircon reference material (Jackson et al., 2004) and data reduction using the VizualAge data reduction scheme (Petrus and Kamber, 2012) for the IOLITE software package (v4.5.5.4) (Paton et al., 2010; Paton et al., 2011). Downhole U-Pb elemental fractionation was corrected using an exponential downhole correction fit to the time-resolved data for each analysis.

Both blank counts and instrumental bias were corrected with an automatic spline function, while down-hole element fractionation was corrected using an exponential function. Common Pb correction was not applied to the data, only monitored. The remaining element fractionation and instrumental mass bias were corrected by normalization to the natural zircon reference material GJ-1.

The calculation of weighted mean, concordia and upper intercept ages (95 % confidence level) and the plotting of concordia diagrams were performed using Isoplot/Ex 4.15 (Ludwig, 2012).

Table A.1 LA-SF-ICP-MS U-Th-Pb dating methodology University of Potsdam.

Laboratory & Sample Preparation	
Laboratory name	LA ICP MS lab University of Potsdam
Sample type / mineral	Detrital zircons
Sample preparation	Conventional mineral separation, 1 inch resin mount, 1 µm polish to finish
Imaging	BSE & CL, JEOL JXA-8200 EMPA, 15nA, 11mm working distance
Laser ablation system	
Make, Model & type	ESI NWR193 Excimer laser
Ablation cell & volume	TwoVol2 Ablation Cell
Laser wavelength	193 nm
Pulse width	4ns
Fluence	3.0 J/cm^{-2} (fluence on sample)
Repetition rate	7 Hz
Spot size	30 µm
Sampling mode / pattern	static single spot analyses
Cell carrier gas	He (0.8 L/min), N2 (0.0035 L/min) and Ar (0.74 L/min) make-up gases combined outside the ablation cell by a signal-smoothing device
Pre-ablation laser warm-up (background collection)	3 cleaning shots followed by 15 seconds background collection
Ablation duration	25 seconds
Wash-out delay	5 seconds
ICP-MS parameters	
Make, Model & type	Thermo Finnigan Element2 single collector HR-SF-ICP-MS
Sample introduction	Via Nylon 10 tubing
RF power	1300 W
Plasma flow	16 l/min
Auxiliary flow	0.8 l/min
Sample gas flow	0.74 l/min
Acquisition parameters	
Detection system	Single collector secondary electron multiplier
Scanning mode	Peak hopping
Acquisition mode	Time resolved/ speed mode
Masses measured	202, 204, 206, 207, 208, 232, 233, 235, 238
Dead time	14 ns
Dwell times	ms
^{202}Hg, $^{204}Hg+Pb$, ^{206}Pb, ^{207}Pb, ^{208}Pb, ^{232}Th, ^{235}U, ^{238}U,	0.007, 0.014, 0.015, 0.018, 0.008, 0.001, 0.013
Data Processing	
Gas blank	15 seconds
Calibration strategy	GJ1 used as primary reference material, 91500, Plešovice and BB16 used as secondary reference material (Quality Control)

Reference Material info	91500 (Wiedenbeck et al. 1995), GJ-1 (Jackson et al. 2004), Plešovice (Sláma et al., 2008), BB16 (Lana et al., 2017)
Data processing package used	Iolite 4.5.5.4
Mass discrimination	Standard-sample bracketing with $^{207}Pb/^{206}Pb$ and $^{206}Pb/^{238}U$ normalized to reference material GJ-1
Common-Pb correction, composition and uncertainty	No common-Pb correction applied to the data
Uncertainty level & propagation	Ages are quoted at 2 sigma absolute. Propagated uncertainty of internal uncertainties (2 SE) and within run reproducibility of GJ-1 (2 SE)
Quality control / Validation	91500: Concordia age = 1067 ±1.2 Ma (2s, MSWD = 0.86) Plešovice: Concordia age = 342 ±0.56 Ma ±1 Ma (2s, MSWD = 0.84) BB16: Concordia age: 567 ±0.75 Ma (2s, MSWD = 0.65)

Table A.2 Detailed sample and standard data for LA-SF-ICP-MS measurements.

Institute for Geosciences, University of Potsdam						Data for Tera-Wasserburg plot						Data for Wetherill plot							Dates												
ID	Sample	f206c	^{206}Pb	U ppm	Th/U	^{238}U/^{206}Pb	1s%	^{207}Pb/^{206}Pb	1s%	^{208}Pb/^{206}Pb	1s%	^{207}Pb/^{235}U	1s%	^{206}Pb/^{238}U	1s%	Rho	^{208}Pb/^{232}Th	1s%	^{207}Pb/^{206}Pb	2s (abs)	2ssys (abs)	^{206}Pb/^{238}U	2s (abs)	2ssys (abs)	^{207}Pb/^{235}U	2s (abs)	2ssys (abs)	^{208}Pb/^{232}Th	2s (abs)	2ssys (abs)	% conc
BREN1_1	BREN1	0.48984	204420	62	1.5	2.43	0.4	0.13797	0.61	0.276484	1.228635	7.8774	0.6	0.41207	0.4	0.34	0.104779	0.810491	2196	21	21	2226	15	51	2215	11	11	2013.186	31.07225	122.0195	100.5
BREN1_3	BREN1	0.466774	275173	126	1.1	3.52	0.7	0.12772	0.45	0.164072	0.651315	5.0950	0.9	0.28747	0.7	0.84	0.059872	1.29806	2061	16	16	1627	22	42	1829	15	15	1177.111	30.14547	77.54668	88.9
BREN1_4	BREN1	0.053868	127710	200	0.6	11.86	0.5	0.05717	1.22	0.117767	1.772688	0.6723	1.2	0.08461	0.5	0.10	0.024642	1.423378	482	56	56	524	5	14	521	10	10	491.8925	13.83979	32.97156	100.6
BREN1_5	BREN1	2.356162	151627	203	0.7	9.78	0.6	0.06068	1.41	0.143089	2.479371	0.8646	1.5	0.10253	0.6	0.25	0.027793	1.750004	615	57	57	629	7	17	633	14	14	553.9073	19.11277	38.66914	99.4
BREN1_6	BREN1	0.366866	410972	647	0.1	11.36	0.6	0.05979	1.07	0.023393	2.642144	0.7333	1.1	0.08824	0.6	0.33	0.026356	2.404349	583	47	47	545	6	15	558	10	10	525.5638	24.93947	40.51064	97.7
BREN1_7	BREN1	0.414952	228418	276	0.1	9.13	0.4	0.06357	0.93	0.030341	1.995183	0.9685	0.9	0.10982	0.4	0.14	0.039321	1.928525	712	40	40	672	6	17	687	9	9	778.8958	29.48681	55.53327	97.8
BREN1_8	BREN1	0.312126	104787	133	0.8	9.61	0.5	0.06183	1.06	0.167198	1.201912	0.8918	1.0	0.10419	0.5	0.15	0.030366	1.077221	642	46	46	639	6	16	647	10	10	604.4628	12.83293	38.84598	98.8
BREN1_9	BREN1	0.647128	132623	181	1.7	10.12	0.5	0.06142	1.35	0.344641	1.399997	0.8432	1.3	0.09892	0.6	0.21	0.027518	0.95084	637	56	56	608	7	16	619	12	12	548.6188	10.29617	34.88213	98.2
BREN1_10	BREN1	0.207976	100942	135	1.0	10.28	0.5	0.06127	1.16	0.207036	1.138992	0.8287	1.2	0.09746	0.5	0.12	0.027491	1.116877	614	52	52	599	6	15	611	11	11	548.0084	12.07247	35.39154	98.2
BREN1_11	BREN1	0.15524	497312	138	0.8	2.18	0.3	0.17544	0.35	0.137546	0.866497	11.2391	0.4	0.46035	0.3	0.51	0.11756	0.593762	2608	11	11	2440	12	52	2542	7	7	2245.62	25.24961	133.294	96.0
BREN1_12	BREN1	0.595811	76221	106	0.8	11.91	0.4	0.05891	1.24	0.171086	1.554411	0.6883	1.2	0.08427	0.4	0.02	0.024679	1.126747	526	59	59	522	4	13	530	10	10	492.6196	10.9675	31.90188	98.5
BREN1_13	BREN1	-0.04535	478076	370	0.3	6.51	1.1	0.09247	0.92	0.067366	1.37243	2.0110	1.8	0.15550	1.1	0.90	0.052658	1.391374	1465	35	35	931	19	29	1112	24	24	1036.745	28.11967	68.26055	83.8
BREN1_14	BREN1	0.615411	232913	212	0.3	7.70	0.3	0.06545	0.67	0.069911	1.109351	1.1788	0.6	0.13001	0.3	0.16	0.036545	0.978769	776	28	28	788	5	19	789	7	7	725.207	13.94615	46.01698	99.8
BREN1_15	BREN1	0.302066	60089	72	1.1	10.03	0.5	0.06180	1.23	0.240352	1.250878	0.8608	1.3	0.10017	0.5	0.18	0.029055	1.008139	620	55	55	615	5	16	627	12	12	578.7146	11.50117	36.94686	98.2
BREN1_16	BREN1	-0.21765	162849	229	0.5	11.66	0.4	0.05754	1.05	0.100139	1.470108	0.6872	1.1	0.08595	0.4	0.25	0.024645	1.364734	493	46	46	532	4	13	530	9	9	491.9358	13.2573	32.70469	100.3
BREN1_17	BREN1	0.161552	399545	428	1.3	9.20	0.4	0.06065	0.75	0.298953	0.527985	0.9160	0.8	0.10886	0.4	0.27	0.036428	0.486744	624	32	32	666	5	17	659	8	8	723.1525	6.91725	44.28124	101.0
BREN1_18	BREN1	0.83363	157757	220	0.8	11.72	0.4	0.05877	0.93	0.1514	0.984557	0.6949	0.9	0.08544	0.4	0.14	0.024038	0.763598	532	40	40	528	4	13	534	7	7	480.0452	7.244909	30.08589	98.9
BREN1_19	BREN1	0.601049	228373	318	0.4	11.33	0.5	0.05772	0.92	0.07654	1.617404	0.7094	1.0	0.08840	0.5	0.26	0.023617	1.409796	503	41	41	546	5	14	543	8	8	471.6699	13.15026	31.5765	100.5
BREN1_20	BREN1	0.565955	278061	377	0.5	11.33	0.3	0.05876	0.71	0.090632	1.090656	0.7182	0.7	0.08832	0.4	0.30	0.024795	0.913705	544	31	31	546	4	14	549	6	6	494.9637	8.935234	31.39525	99.4
BREN1_21	BREN1	0.196365	553199	404	0.8	5.48	0.5	0.07221	0.61	0.154465	0.643806	1.8259	0.7	0.18301	0.5	0.55	0.048085	0.742472	985	25	25	1083	9	27	1054	10	10	949.1256	13.76241	58.68611	102.8
BREN1_22	BREN1	0.217561	177799	228	0.8	9.82	0.3	0.06099	0.77	0.156523	0.776611	0.8572	0.8	0.10181	0.4	0.23	0.028682	0.808291	621	34	34	625	4	16	627	7	7	571.4573	9.112625	35.87482	99.7
BREN1_23	BREN1	1.101456	84615	112	0.8	9.95	0.6	0.06084	1.16	0.149258	1.12477	0.8447	1.2	0.10084	0.6	0.39	0.027978	1.07573	595	51	51	619	7	16	620	11	11	557.5483	11.8208	35.82602	99.9
BREN1_24	BREN1	-0.21116	232317	307	1.5	10.07	0.4	0.05970	0.95	0.340031	0.73053	0.8205	1.0	0.09947	0.4	0.22	0.031219	0.775518	579	41	41	611	5	15	607	9	9	621.3023	9.48589	38.82189	100.6
BREN1_25	BREN1	0.098446	435445	185	1.0	3.09	0.8	0.11013	0.80	0.182026	1.01451	4.9353	0.8	0.32449	0.8	0.44	0.079287	1.118207	1795	29	29	1811	24	46	1807	13	13	1541.713	33.19699	97.21204	100.2
BREN1_26	BREN1	0.604211	333927	364	0.4	8.43	0.3	0.06154	0.69	0.075986	0.818379	1.0121	0.7	0.11873	0.3	0.16	0.033343	0.800932	654	31	31	723	4	18	709	7	7	662.8406	10.44333	41.46666	102.0
BREN1_27	BREN1	0.540052	110640	172	0.7	11.77	0.4	0.05963	0.99	0.13899	1.269012	0.7038	1.0	0.08527	0.4	0.24	0.024546	1.092752	568	43	43	527	4	13	539	9	9	489.9826	10.57717	31.61135	97.9
BREN1_28	BREN1	-0.05317	107845	141	1.6	9.59	0.6	0.06055	1.30	0.319167	1.221142	0.8724	1.2	0.10442	0.6	0.13	0.028113	0.998075	594	59	59	640	7	17	635	12	12	560.2878	11.02985	35.75337	100.9

BREN1_29	BREN1	0.398172	125334	156	0.9	9.34	0.4	0.06235	0.89	0.191691	0.802978	0.9241	0.9	0.10741	0.4	0.22	0.030196	0.797011	658	39	39	658	5	16	662	9	9	601.1714	9.443581	37.66784	99.3
BREN1_30	BREN1	-0.5255	69294	88	2.0	9.40	0.5	0.06394	1.33	0.452295	0.99182	0.9423	1.3	0.10675	0.5	0.12	0.028893	0.897138	697	58	58	654	6	17	671	13	13	575.6153	10.17382	36.34879	97.5
BREN1_31	BREN1	0.401546	197891	142	0.2	5.59	0.4	0.07378	0.92	0.045825	1.558572	1.8259	0.9	0.17934	0.4	0.09	0.053994	1.690019	1022	37	37	1063	8	26	1053	11	11	1062.038	34.9654	72.64982	101.0
BREN1_32	BREN1	0.351017	163992	217	0.5	9.88	0.4	0.06142	0.91	0.110264	0.936614	0.8596	0.9	0.10154	0.4	0.13	0.028949	1.08205	628	40	40	623	5	16	628	8	8	576.631	12.30275	37.0796	99.2
BREN1_33	BREN1	1.374376	145503	226	0.5	11.75	0.5	0.06506	0.81	0.086805	1.178324	0.7694	0.8	0.08556	0.5	0.34	0.0194	1.730177	761	35	35	529	5	14	578	7	7	388.1081	13.30558	27.15695	91.6
BREN1_34	BREN1	0.587522	99187	130	0.8	9.83	0.4	0.06136	0.95	0.178091	0.939836	0.8634	1.0	0.10191	0.4	0.21	0.028753	0.946432	629	41	41	625	5	16	630	9	9	572.7989	10.69473	36.37554	99.3
BREN1_35	BREN1	0.407522	338123	547	0.8	12.36	0.4	0.05629	0.78	0.189336	0.723211	0.6296	0.8	0.08106	0.4	0.20	0.024702	0.703081	448	35	35	502	3	13	495	6	6	493.1745	6.850311	30.76156	101.5
BREN1_36	BREN1	0.24307	84135	111	2.7	10.04	0.4	0.06020	1.07	0.616307	0.672283	0.8274	1.0	0.09989	0.4	0.11	0.027618	0.543354	584	49	49	614	4	16	612	9	9	550.603	5.902639	33.95675	100.4
BREN1_37	BREN1	-0.54062	73290	90	0.7	9.31	0.4	0.06229	1.22	0.163734	1.151443	0.9252	1.2	0.10766	0.5	0.14	0.03046	1.013585	642	53	53	659	6	17	661	12	12	606.2627	12.11227	38.7163	99.7
BREN1_38	BREN1	-0.05024	358721	233	0.5	4.92	0.4	0.08083	0.63	0.109561	1.828343	2.2803	0.7	0.20383	0.4	0.50	0.058146	0.764464	1211	25	25	1196	9	29	1205	10	10	1142.072	16.97876	70.41224	99.2
BREN1_39	BREN1	-0.24555	187232	284	0.3	11.83	0.3	0.05806	0.74	0.063608	1.070861	0.6798	0.7	0.08470	0.3	0.20	0.024282	1.112149	515	33	33	524	3	13	526	6	6	484.7649	10.65358	31.34154	99.7
BREN1_40	BREN1	0.605223	178773	231	1.1	9.90	0.4	0.06125	0.86	0.215997	0.743417	0.8566	0.9	0.10118	0.4	0.33	0.027661	0.756871	626	38	38	621	5	16	627	8	8	551.4216	8.236156	34.48313	99.2
BREN1_41	BREN1	-0.19391	118054	180	0.4	11.85	0.4	0.05831	0.97	0.08862	1.180506	0.6812	1.0	0.08447	0.4	0.18	0.024172	1.131856	514	44	44	523	4	13	526	8	8	482.5986	10.79676	31.27875	99.4
BREN1_42	BREN1	0.928101	167225	243	0.5	11.29	0.4	0.05798	0.87	0.091036	1.055852	0.7130	0.9	0.08880	0.4	0.14	0.023586	1.031078	510	39	39	548	4	14	545	7	7	471.0744	9.598104	30.21045	100.6
BREN1_43	BREN1	0.606923	288322	320	0.7	8.71	0.4	0.06540	0.61	0.131053	0.75167	1.0437	0.7	0.11523	0.4	0.53	0.031872	0.721763	777	26	26	703	5	18	724	8	8	634.0318	9.009179	39.47755	97.1
BREN1_44	BREN1	2.789275	70366	88	0.6	9.82	0.4	0.06193	1.38	0.131204	1.437391	0.8750	1.3	0.10226	0.4	0.11	0.029291	1.34284	630	58	58	628	5	16	636	12	12	583.2384	15.43484	38.59354	98.7
BREN1_45	BREN1	0.148692	170220	219	0.4	9.90	0.6	0.06102	1.22	0.082943	2.447828	0.8527	1.2	0.10141	0.6	0.34	0.027977	1.799403	628	50	50	623	8	17	627	12	12	557.4922	19.79036	39.20738	99.4
BREN1_46	BREN1	-0.24699	492275	499	0.2	7.55	0.5	0.06463	0.80	0.032847	1.529482	1.1881	0.8	0.13276	0.5	0.28	0.035734	1.621246	753	34	34	803	8	21	794	9	9	709.3493	22.59245	48.47224	101.2
BREN1_47	BREN1	1.001673	134942	101	0.7	5.80	0.3	0.07426	0.85	0.139178	0.847188	1.7771	0.9	0.17295	0.3	0.20	0.047572	0.924091	1034	34	34	1028	6	25	1035	11	11	938.9808	16.9501	58.92874	99.4
BREN1_48	BREN1	0.637871	239430	373	0.8	11.83	0.5	0.05845	1.03	0.153191	1.872197	0.6853	1.1	0.08463	0.5	0.36	0.022367	1.050062	527	46	46	524	5	14	529	9	9	447.0411	9.286062	28.75283	99.0
BREN1_49	BREN1	1.226146	99628	110	0.7	8.42	0.4	0.06362	1.00	0.13599	1.092699	1.0499	1.0	0.11921	0.4	0.20	0.033337	1.123143	695	43	43	726	6	18	726	10	10	662.5307	14.63302	42.67733	100.0
BREN1_50	BREN1	0.402004	233740	79	0.8	2.61	0.6	0.17296	0.47	0.174687	0.742983	9.2892	0.7	0.38573	0.5	0.75	0.113415	0.853967	2582	16	16	2101	19	49	2363	13	13	2169.731	35.15055	131.4762	88.9
BREN1_51	BREN1	0.805512	225171	297	0.9	10.01	0.3	0.06067	0.69	0.181054	0.828369	0.8410	0.7	0.10012	0.3	0.14	0.026323	0.704288	618	30	30	615	4	15	619	6	6	525.1028	7.302571	32.73397	99.3
BREN1_52	BREN1	0.15572	401374	308	0.4	5.82	0.3	0.07295	0.52	0.075345	1.688693	1.7402	0.5	0.17205	0.3	0.35	0.044885	0.736754	1005	21	21	1023	6	24	1024	7	7	887.2614	12.78828	54.9291	99.9
BREN1_53	BREN1	0.788752	146277	228	0.4	11.60	0.4	0.05876	0.90	0.081986	1.198399	0.7021	0.9	0.08642	0.3	0.16	0.024522	1.205368	540	39	39	534	4	13	539	7	7	489.4855	11.65838	31.96813	99.2
BREN1_54	BREN1	1.317543	107641	172	0.7	11.79	0.4	0.05756	1.28	0.140433	1.138874	0.6782	1.3	0.08508	0.4	0.13	0.023257	1.185942	468	58	58	526	4	13	523	10	10	464.5699	10.89154	30.29022	100.6
BREN1_55	BREN1	0.259132	316005	408	0.6	9.69	0.3	0.06014	0.61	0.12662	0.972949	0.8612	0.6	0.10338	0.3	0.27	0.027588	0.677965	598	27	27	634	4	16	630	6	6	549.9826	7.360208	34.21201	100.6
BREN1_56	BREN1	0.520734	226916	273	0.6	8.85	0.3	0.06244	0.74	0.117861	0.847918	0.9773	0.7	0.11304	0.3	0.23	0.030535	0.942278	671	32	32	690	4	17	691	7	7	607.7684	11.2815	38.53511	99.9
BREN1_57	BREN1	0.203964	423187	646	0.3	11.36	0.3	0.05761	0.57	0.061851	0.821584	0.7044	0.6	0.08816	0.3	0.27	0.023368	0.796768	510	25	25	545	3	13	542	5	5	466.8266	7.35375	29.3411	100.5
BREN1_58	BREN1	0.324431	271538	358	0.7	9.63	0.3	0.06146	0.84	0.138993	0.994969	0.8857	0.8	0.10394	0.3	0.20	0.027102	0.940328	641	37	37	637	4	16	643	8	8	540.4256	10.02577	34.31148	99.1

BREN1_59	BREN1	0.074814	1287269	277	0.8	1.59	0.3	0.28307	0.26	0.117678	0.942555	24.7612	0.3	0.63062	0.3	0.80	0.121117	0.62634	3380	8	8	3151	15	64	3298	7	7	2309.747	27.29119	136.8509	95.6
BREN1_60	BREN1	0.620419	145245	243	1.5	12.48	0.3	0.05686	0.83	0.293997	0.629638	0.6327	0.9	0.08025	0.3	0.26	0.021283	0.546805	465	39	39	498	3	12	497	7	7	425.6314	4.606568	26.33414	100.2
BREN1_61	BREN1	0.991426	53140	70	1.1	10.00	0.5	0.06150	1.56	0.23661	1.302278	0.8504	1.5	0.10015	0.5	0.16	0.027989	1.282335	617	69	69	615	6	16	623	14	14	557.757	14.10984	36.68643	98.8
BREN1_62	BREN1	0.105293	300860	486	0.3	11.82	0.4	0.05734	0.90	0.056158	1.363443	0.6732	0.9	0.08477	0.4	0.22	0.022756	1.405583	495	39	39	525	4	13	522	7	7	454.6872	12.64258	30.43293	100.5
BREN1_63	BREN1	0.570813	195533	305	0.6	11.84	0.6	0.05846	1.24	0.111482	1.328658	0.6867	1.3	0.08458	0.6	0.30	0.022321	1.301298	524	53	53	523	6	14	529	10	10	446.1208	11.48573	29.49389	98.8
BREN1_64	BREN1	-0.07141	183455	193	0.5	8.37	0.3	0.06753	0.68	0.076126	1.028485	1.1210	0.7	0.11969	0.4	0.28	0.027693	1.010809	839	28	28	729	5	18	762	8	8	551.9594	11.00836	35.28092	95.6
BREN1_65	BREN1	-0.15119	159051	190	0.7	9.62	0.3	0.06168	0.91	0.123024	1.016728	0.8910	0.9	0.10406	0.3	0.06	0.028763	0.945381	640	39	39	638	4	16	645	8	8	573.0243	10.6808	36.37569	98.9
BREN1_66	BREN1	0.260151	199041	299	0.6	11.92	0.3	0.05868	0.75	0.100512	0.818757	0.6858	0.7	0.08410	0.3	0.17	0.022912	0.825794	542	32	32	521	3	13	529	6	6	457.7921	7.475875	28.8488	98.3
BREN1_67	BREN1	0.8296	145069	173	0.4	9.39	0.4	0.06208	0.85	0.071977	1.224723	0.9200	0.9	0.10652	0.4	0.28	0.029964	1.155847	656	36	36	652	5	16	660	8	8	596.4875	13.59187	38.66086	98.8
BREN1_68	BREN1	0.597887	291584	450	1.0	11.95	0.4	0.05755	0.67	0.196505	0.882894	0.6708	0.7	0.08373	0.3	0.23	0.023781	0.755312	501	29	29	518	3	13	521	6	6	474.9987	7.090944	29.75349	99.6
BREN1_69	BREN1	1.916356	42664	52	1.1	9.82	0.5	0.06216	1.83	0.202781	1.631534	0.8807	1.8	0.10200	0.5	0.06	0.02916	1.423427	615	81	81	627	7	17	636	17	17	580.7195	16.29624	38.82083	98.5
BREN1_70	BREN1	-0.06069	248815	367	0.4	11.39	0.3	0.05822	0.70	0.077436	0.946386	0.7127	0.8	0.08796	0.3	0.36	0.023827	0.964323	531	31	31	543	3	14	545	7	7	475.8571	9.069259	30.33322	99.6
BREN1_71	BREN1	0.621781	296685	438	0.5	11.57	0.3	0.05794	0.68	0.081406	1.038149	0.6977	0.7	0.08653	0.3	0.18	0.02294	0.988707	514	30	30	535	3	13	537	6	6	458.3386	8.961231	29.2993	99.7
BREN1_72	BREN1	0.979784	176015	276	0.4	11.69	0.5	0.05768	1.07	0.066267	1.724314	0.6891	1.1	0.08579	0.5	0.30	0.023267	1.783328	497	47	47	531	5	14	531	9	9	464.7035	16.39228	32.69602	99.9
BREN1_73	BREN1	0.449755	256744	266	0.6	7.63	0.5	0.06594	0.94	0.105408	0.938726	1.2014	0.9	0.13112	0.5	0.23	0.035121	1.04206	797	38	38	794	7	20	800	10	10	697.5645	14.2916	44.56389	99.3
BREN1_74	BREN1	0.173942	192953	150	0.6	5.72	0.3	0.07353	0.73	0.116351	0.982577	1.7918	0.7	0.17500	0.3	0.21	0.048018	0.975655	1019	30	30	1039	7	25	1042	10	10	947.6339	18.06044	59.76544	99.8
BREN1_75	BREN1	0.764551	167065	178	0.2	7.18	0.4	0.06939	0.72	0.056735	1.353718	1.3496	0.8	0.13935	0.4	0.42	0.040808	1.329497	901	30	30	841	6	21	866	9	9	807.8713	21.05696	53.09732	97.2
BREN1_76	BREN1	0.500278	286450	508	0.3	11.90	0.3	0.05814	0.70	0.063162	1.040809	0.6802	0.7	0.08414	0.3	0.19	0.024086	0.966422	524	31	31	521	3	13	526	6	6	480.9725	9.189227	30.67247	99.0
BREN1_77	BREN1	1.239909	91037	131	0.8	9.33	0.7	0.06288	1.46	0.198746	1.454002	0.9397	1.4	0.10767	0.7	0.18	0.029755	1.404101	673	61	61	659	9	18	670	14	14	592.4775	16.38623	39.47773	98.3
BREN1_78	BREN1	1.469141	96696	144	1.6	9.97	0.4	0.06126	0.98	0.36525	0.673666	0.8552	0.9	0.10046	0.4	0.05	0.027822	0.724229	634	43	43	617	4	15	627	9	9	554.5693	7.924309	34.59268	98.4
BREN1_79	BREN1	0.63803	182880	264	0.4	9.77	0.3	0.06140	0.77	0.085799	1.01925	0.8733	0.8	0.10254	0.3	0.21	0.02855	1.020726	636	34	34	629	4	16	636	7	7	568.8151	11.44971	36.37248	98.9
BREN1_80	BREN1	-0.03328	554174	462	0.7	5.52	0.4	0.07255	0.65	0.159155	0.71071	1.8315	0.6	0.18134	0.4	0.34	0.046681	0.698271	998	26	26	1074	8	26	1056	8	8	922.0534	12.58866	56.89287	101.7
BREN1_81	BREN1	0.055247	559513	487	0.4	5.59	0.5	0.07257	0.85	0.088074	0.892518	1.8058	0.8	0.17906	0.5	0.22	0.044846	1.134816	995	35	35	1062	10	27	1047	11	11	886.548	19.67719	56.87709	101.4
BREN1_82	BREN1	1.411628	103336	183	0.3	11.98	0.4	0.05832	0.93	0.067292	1.314545	0.6775	0.9	0.08363	0.4	0.21	0.024529	1.359227	521	40	40	518	4	13	525	8	8	489.5611	13.15073	32.5514	98.7
BREN1_83	BREN1	1.469335	153305	259	1.1	11.80	0.6	0.05873	1.26	0.241559	0.901697	0.6934	1.3	0.08508	0.6	0.33	0.023868	1.066961	535	55	55	526	6	14	533	11	11	476.6935	10.05056	30.68333	98.7
BREN1_84	BREN1	-0.01355	183789	235	0.1	8.82	0.3	0.06200	0.80	0.022614	1.848221	0.9780	0.8	0.11355	0.3	0.33	0.032543	1.814107	663	34	34	693	4	17	692	8	8	646.6466	23.09961	45.49032	100.2
BREN1_85	BREN1	0.27114	396753	535	1.0	9.37	0.3	0.06125	0.52	0.226701	0.541514	0.9061	0.5	0.10687	0.3	0.36	0.032569	0.563077	643	22	22	654	3	16	655	5	5	647.7317	7.181791	39.90675	99.9
BREN1_86	BREN1	0.607971	115167	197	0.7	11.94	0.3	0.05763	1.01	0.148179	0.899125	0.6698	1.0	0.08397	0.3	0.12	0.02379	0.910143	484	46	46	520	3	13	520	8	8	475.1273	8.548411	30.14461	100.0
BREN1_87	BREN1	0.522337	196064	158	0.7	5.80	0.3	0.07258	0.67	0.139061	0.680901	1.7372	0.7	0.17271	0.3	0.23	0.046424	0.698874	994	26	26	1027	6	25	1021	9	9	916.987	12.53385	56.60752	100.6
BREN1_88	BREN1	0.9695	131829	192	0.5	10.52	0.3	0.06343	0.83	0.105755	0.96929	0.8343	0.8	0.09512	0.3	0.16	0.027068	0.987993	703	35	35	586	4	15	614	8	8	539.6688	10.52655	34.4403	95.3

BREN1_89	BREN1	0.008941	151531	235	0.5	11.30	0.4	0.05781	0.87	0.092289	1.163913	0.7096	0.9	0.08869	0.4	0.32	0.024382	1.08198	501	39	39	548	4	14	543	8	8	486.7562	10.40741	31.38021	100.9
TAC1_1	TAC1	0.223137	585470	360	0.5	5.91	0.8	0.07150	0.80	0.093358	0.992315	1.6754	0.9	0.17001	0.8	0.52	0.042195	1.060214	961	33	33	1012	14	23	998	11	11	835.1367	17.3445	31.58095	101.4
TAC1_2	TAC1	1.400533	81101	103	1.3	12.54	0.5	0.05794	1.28	0.268428	0.950345	0.6427	1.3	0.08026	0.5	0.21	0.021463	0.953917	485	55	55	498	5	10	502	10	10	429.1352	8.097886	15.90999	99.1
TAC1_3	TAC1	0.598638	207524	120	0.7	5.63	0.5	0.07458	0.70	0.14191	0.808371	1.8394	0.7	0.17770	0.5	0.27	0.047755	0.851043	1044	29	29	1055	9	21	1057	9	9	942.5449	15.67373	33.59204	99.8
TAC1_4	TAC1	1.091907	121403	123	0.6	9.75	0.5	0.06179	1.04	0.120659	1.023396	0.8775	1.0	0.10294	0.5	0.19	0.028014	1.042009	634	44	44	631	6	13	637	9	9	558.2518	11.47991	21.15838	99.1
TAC1_5	TAC1	1.256211	146279	171	0.7	11.07	0.6	0.05798	0.92	0.140029	0.88608	0.7279	0.9	0.09079	0.6	0.35	0.023753	1.019403	500	41	41	560	6	12	555	8	8	474.357	9.5582	17.89307	101.0
TAC1_6	TAC1	0.133544	793292	443	0.5	5.02	0.9	0.07714	0.92	0.095768	0.984024	2.1210	1.0	0.19898	1.0	0.55	0.047061	1.204915	1116	37	37	1169	21	29	1154	15	15	929.2876	21.91306	36.61917	101.3
TAC1_7	TAC1	5.332657	30146	20	0.5	6.01	0.6	0.07401	1.83	0.098277	2.334031	1.7034	1.8	0.16725	0.6	0.13	0.045634	2.345194	949	76	76	996	11	21	998	23	23	899.6615	41.22363	50.03532	99.8
TAC1_8	TAC1	0.133098	362642	225	0.9	5.58	0.4	0.07392	0.58	0.168124	0.66609	1.8410	0.6	0.17949	0.4	0.31	0.044886	0.653281	1036	24	24	1064	8	20	1058	8	8	887.3034	11.34074	30.21447	100.5
TAC1_9	TAC1	0.875883	191629	393	1.1	16.69	0.7	0.05415	1.16	0.238048	1.093668	0.4526	1.4	0.06030	0.7	0.42	0.017519	1.065063	379	59	59	377	5	8	379	9	9	350.9931	7.408636	13.44683	99.5
TAC1_10	TAC1	0.02997	778278	175	0.8	1.94	0.6	0.18029	0.48	0.144924	0.825693	12.9868	0.6	0.51684	0.6	0.61	0.122429	0.960754	2653	16	16	2685	25	48	2680	11	11	2333.741	42.27654	82.62346	100.2
TAC1_11	TAC1	0.504048	213406	139	1.3	5.56	0.4	0.07547	0.68	0.256973	0.749922	1.8906	0.8	0.18042	0.4	0.39	0.04609	0.666494	1072	29	29	1069	8	20	1075	10	10	910.5574	11.87419	31.09764	99.4
TAC1_12	TAC1	1.422563	95775	138	0.9	12.34	0.4	0.05874	1.10	0.191502	0.973104	0.6608	1.1	0.08112	0.4	0.10	0.022272	0.84907	517	49	49	503	4	10	513	8	8	445.1592	7.477299	16.05452	98.0
TAC1_13	TAC1	0.356824	138030	178	0.5	11.01	0.5	0.05914	0.99	0.094667	1.115973	0.7470	0.9	0.09109	0.5	0.13	0.024722	1.177643	545	44	44	562	5	11	565	8	8	493.4525	11.48403	19.47756	99.5
TAC1_14	TAC1	0.187834	274718	321	0.4	10.09	0.4	0.06048	0.67	0.081544	0.863594	0.8316	0.6	0.09928	0.4	0.27	0.026585	0.898306	611	29	29	610	4	12	615	6	6	530.1953	9.400661	19.32325	99.2
TAC1_15	TAC1	0.995718	123263	164	0.8	11.52	0.5	0.05857	0.98	0.163729	1.014322	0.7079	1.0	0.08710	0.5	0.23	0.023586	1.036193	536	43	43	538	5	11	542	9	9	471.0555	9.646436	17.84961	99.2
TAC1_16	TAC1	-0.68504	104188	132	0.8	11.08	0.5	0.05795	1.14	0.157369	1.05748	0.7300	1.2	0.09074	0.5	0.20	0.024802	1.074759	500	49	49	560	5	11	554	10	10	495.0366	10.51078	18.95759	101.1
TAC1_17	TAC1	0.205932	560450	127	0.9	1.92	0.6	0.19408	0.60	0.154877	1.141543	14.0145	0.6	0.52150	0.5	0.44	0.119084	0.990627	2773	20	20	2704	24	48	2749	11	11	2272.843	42.62588	81.45935	98.4
TAC1_18	TAC1	0.197743	184550	170	0.6	7.59	0.6	0.06851	0.75	0.118449	1.0632	1.2574	0.9	0.13209	0.6	0.51	0.037202	0.875188	872	30	30	799	9	17	825	10	10	738.0545	12.6858	26.60327	96.9
TAC1_19	TAC1	0.087868	128822	153	0.6	9.80	0.5	0.05953	0.95	0.11042	1.316369	0.8499	1.0	0.10270	0.5	0.36	0.025991	1.145597	565	41	41	630	6	13	622	9	9	518.443	11.72576	20.2522	101.3
TAC1_20	TAC1	0.311509	423630	303	0.6	5.91	0.5	0.07178	0.66	0.119104	0.803855	1.6849	0.7	0.16947	0.5	0.35	0.043015	0.88018	969	27	27	1009	9	20	1001	8	8	851.0305	14.657	30.6025	100.8
TAC1_21	TAC1	1.220494	214311	286	0.4	10.88	0.5	0.05944	0.90	0.093255	1.939268	0.7548	0.9	0.09233	0.5	0.24	0.02469	1.147566	568	39	39	569	6	12	571	8	8	492.8516	11.17472	19.27847	99.7
TAC1_22	TAC1	0.524258	632135	427	0.9	5.61	0.3	0.07455	0.51	0.200206	0.79046	1.8491	0.6	0.17838	0.3	0.43	0.049955	0.569411	1050	21	21	1058	7	19	1062	8	8	985.1355	10.94476	32.88338	99.7
TAC1_23	TAC1	0.4666	126347	204	0.8	13.26	0.5	0.05700	1.09	0.17355	0.948191	0.5966	1.1	0.07579	0.5	0.21	0.02065	1.168621	460	47	47	471	4	10	474	8	8	413.028	9.554293	16.28634	99.3
TAC1_24	TAC1	0.361867	168633	108	0.6	5.24	0.5	0.07718	0.90	0.113914	1.170381	2.0513	0.9	0.19132	0.5	0.22	0.050429	1.07397	1121	35	35	1128	10	22	1131	12	12	993.9098	20.82327	37.57661	99.8
TAC1_25	TAC1	0.191172	844145	589	0.5	5.80	0.5	0.07248	0.66	0.09624	0.593756	1.7390	0.6	0.17272	0.5	0.30	0.043393	0.763231	990	27	27	1027	10	20	1023	8	8	858.4321	12.83144	30.00407	100.4
TAC1_26	TAC1	0.54909	439272	446	0.4	8.92	0.5	0.06043	1.01	0.071083	1.367455	0.9465	0.9	0.11236	0.5	0.11	0.02989	1.262858	608	43	43	686	7	14	676	9	9	595.1993	14.81813	24.03959	101.6
TAC1_27	TAC1	0.586051	398230	138	0.2	3.05	1.2	0.14827	0.49	0.0674	1.00034	6.8958	1.3	0.33461	1.1	0.93	0.127837	0.839052	2323	16	16	1856	37	48	2085	24	24	2429.866	38.34371	83.09855	89.0
TAC1_28	TAC1	0.904965	718148	762	0.4	9.09	0.5	0.06989	0.56	0.158643	3.504735	1.0706	0.7	0.11072	0.5	0.52	0.032297	0.915961	914	24	24	677	7	14	738	7	7	642.2929	11.59068	23.47513	91.6
TAC1_29	TAC1	-0.59418	104509	137	1.0	11.03	0.5	0.05995	1.05	0.198183	0.91816	0.7513	1.0	0.09097	0.5	0.28	0.024281	0.990398	567	47	47	561	5	11	568	9	9	484.7801	9.486001	18.13109	98.9

TAC1_30	TAC1	0.378464	101969	140	1.1	11.54	0.4	0.05980	1.02	0.227667	0.874079	0.7193	1.0	0.08704	0.4	0.14	0.023331	0.911864	564	45	45	538	5	11	549	9	9	466.0502	8.400409	17.07159	98.0
TAC1_31	TAC1	0.955076	151126	191	1.1	10.64	0.4	0.05927	0.89	0.232776	0.721111	0.7733	0.9	0.09434	0.4	0.29	0.026003	0.770533	554	38	38	581	5	11	582	8	8	518.7782	7.893568	18.31493	99.9
TAC1_32	TAC1	0.480696	85128	110	1.3	10.71	0.5	0.06085	1.24	0.279105	0.939346	0.7869	1.2	0.09350	0.5	0.08	0.025322	0.928072	584	54	54	576	5	12	587	10	10	505.3279	9.263398	18.57677	98.2
TAC1_33	TAC1	0.556752	55041	65	0.4	9.32	0.6	0.06335	1.56	0.080501	2.20768	0.9487	1.6	0.10805	0.6	0.13	0.030013	2.135855	667	71	71	661	8	14	672	16	16	596.8229	25.06803	31.41516	98.4
TAC1_34	TAC1	0.50567	258986	176	0.7	5.46	0.5	0.07520	0.67	0.156162	1.719659	1.9143	0.7	0.18396	0.5	0.38	0.046976	0.771911	1063	28	28	1088	9	21	1084	10	10	927.5961	13.99163	32.41662	100.4
TAC1_35	TAC1	0.017936	123529	149	0.6	9.92	0.4	0.06038	0.98	0.12694	0.964931	0.8422	1.0	0.10113	0.4	0.30	0.027682	1.082763	587	42	42	621	5	12	618	9	9	551.7024	11.78762	21.15182	100.5
TAC1_36	TAC1	0.194268	571003	377	0.1	5.63	0.5	0.07289	0.67	0.025945	1.346361	1.7904	0.6	0.17751	0.5	0.37	0.048009	1.391507	1005	27	27	1053	10	20	1042	9	9	947.2141	25.72297	39.38292	101.1
TAC1_37	TAC1	0.76235	184146	336	0.4	15.52	0.4	0.05537	0.97	0.080996	1.229781	0.4940	1.0	0.06465	0.4	0.32	0.018424	1.14032	406	46	46	404	3	8	407	7	7	368.9202	8.336563	14.44285	99.3
TAC1_38	TAC1	1.513946	67806	94	0.9	11.72	0.5	0.05917	1.23	0.205292	1.067103	0.7009	1.2	0.08571	0.5	0.22	0.02429	1.120154	527	54	54	530	5	11	536	10	10	484.9171	10.73512	18.82223	98.8
TAC1_39	TAC1	0.629611	217521	144	1.4	5.61	0.4	0.07457	0.68	0.283794	0.715768	1.8413	0.7	0.17902	0.4	0.34	0.047296	0.705818	1042	28	28	1061	9	20	1058	9	9	933.8097	12.89376	32.16769	100.3
TAC1_40	TAC1	0.308592	132878	151	0.6	9.23	0.9	0.06093	1.45	0.12245	1.231075	0.9136	1.4	0.10895	0.9	0.27	0.028096	1.295268	612	61	61	666	11	16	656	14	14	559.9114	14.30912	22.85542	101.5
TAC1_41	TAC1	0.491861	282916	402	0.2	12.42	0.4	0.05681	0.68	0.038366	1.27698	0.6335	0.7	0.08070	0.4	0.35	0.022329	1.350944	470	30	30	500	4	10	497	6	6	446.1571	11.91882	18.56437	100.6
TAC1_42	TAC1	0.097314	390533	240	0.4	5.35	0.6	0.07549	0.68	0.083657	0.914914	1.9511	0.7	0.18757	0.6	0.45	0.04932	0.940401	1074	28	28	1108	12	22	1097	10	10	972.7396	17.86579	35.47558	101.0
TAC1_43	TAC1	0.044019	120540	146	1.2	11.10	0.5	0.05910	1.21	0.25395	0.80604	0.7377	1.2	0.09033	0.5	0.17	0.025	0.841169	552	51	51	557	5	11	559	10	10	499.0379	8.291399	17.93355	99.7
TAC1_44	TAC1	0.817581	978261	1147	0.1	10.35	0.4	0.06246	0.44	0.034148	0.940046	0.8320	0.5	0.09679	0.4	0.56	0.038786	0.793478	685	18	18	595	5	12	615	4	4	768.9276	11.97325	27.12837	96.9
TAC1_45	TAC1	0.81715	129107	171	0.8	11.78	0.5	0.05961	0.98	0.162182	1.138729	0.6998	1.0	0.08531	0.4	0.23	0.023517	0.955065	569	43	43	528	5	10	537	8	8	469.7126	8.868107	17.40775	98.3
TAC1_46	TAC1	1.258952	96859	131	0.9	11.99	0.5	0.05848	1.16	0.191172	0.954151	0.6728	1.1	0.08368	0.5	0.10	0.02269	0.949445	517	50	50	518	5	10	520	9	9	453.3796	8.512134	16.78228	99.6
TAC1_47	TAC1	0.412928	306723	403	0.5	12.05	0.4	0.05708	0.74	0.102357	0.89915	0.6555	0.7	0.08312	0.4	0.21	0.022652	0.848948	481	33	33	515	4	10	511	6	6	452.6806	7.599311	16.31833	100.7
TAC1_48	TAC1	-0.333	236565	320	0.9	12.02	0.4	0.05797	0.69	0.173906	0.645946	0.6655	0.7	0.08340	0.4	0.29	0.022566	0.6512	516	30	30	516	4	10	517	6	6	450.9883	5.80818	15.51686	99.9
TAC1_49	TAC1	-0.924	57714	81	0.8	11.76	0.6	0.06026	1.56	0.174342	1.414616	0.7062	1.5	0.08555	0.6	0.03	0.024778	1.261095	579	69	69	529	7	11	542	13	13	494.5412	12.32252	20.00828	97.7
TAC1_50	TAC1	0.271852	267764	324	0.6	10.35	0.4	0.05958	0.89	0.124619	1.092391	0.7936	0.8	0.09689	0.4	0.00	0.026504	0.802419	574	38	38	596	5	12	592	7	7	528.6677	8.373646	18.80254	100.6
TAC1_51	TAC1	-0.03049	1242995	574	0.4	3.64	1.1	0.09494	1.06	0.071963	1.466762	3.6142	1.0	0.27648	1.2	0.46	0.063724	1.620508	1518	40	40	1572	33	42	1551	16	16	1248.075	39.18247	55.28831	101.4
TAC1_52	TAC1	0.770222	206497	311	0.7	12.74	0.5	0.05606	0.80	0.139531	0.869444	0.6118	0.8	0.07879	0.5	0.22	0.021458	0.82257	440	36	36	489	4	10	485	6	6	429.0666	6.981634	15.36974	100.9
TAC1_53	TAC1	9.581253	64061	32	0.9	4.02	0.9	0.16873	2.18	0.389512	2.592801	6.0563	2.7	0.25249	0.9	0.77	0.145695	2.738859	2432	80	80	1449	23	33	1916	50	50	2720.781	140.7931	163.4015	75.6
TAC1_54	TAC1	-1.3316	47227	64	0.4	11.15	0.6	0.06158	1.54	0.089731	1.917166	0.7647	1.5	0.09029	0.6	0.04	0.026393	1.922211	596	70	70	557	7	12	574	13	13	526.0295	19.96425	26.06359	97.1
TAC1_55	TAC1	0.562342	205002	231	1.8	9.25	0.5	0.06138	0.96	0.384	0.683922	0.9169	1.0	0.10822	0.5	0.39	0.031682	0.710367	629	42	42	662	7	13	659	10	10	630.349	8.815516	21.87496	100.5
TAC1_56	TAC1	0.536853	340528	521	0.7	12.95	0.4	0.05637	0.62	0.152078	0.700073	0.6018	0.7	0.07736	0.4	0.38	0.022063	0.654553	452	28	28	480	4	9	478	5	5	441.044	5.713082	15.19559	100.5
TAC1_57	TAC1	0.198088	649295	686	0.1	9.04	1.0	0.06384	0.90	0.032339	1.958514	0.9796	1.1	0.11159	1.0	0.56	0.043321	1.750151	731	40	40	682	13	17	692	11	11	856.7104	29.38444	39.96356	98.5
TAC1_58	TAC1	-0.18416	165836	57	1.5	3.04	0.5	0.11092	0.86	0.268475	0.825379	5.0619	0.9	0.32972	0.5	0.34	0.085009	0.840526	1804	31	31	1836	16	34	1826	15	15	1648.561	26.62845	57.62962	100.5
TAC1_59	TAC1	0.066906	191737	123	0.4	5.34	0.4	0.07606	0.74	0.078819	1.022802	1.9683	0.7	0.18801	0.4	0.26	0.051493	1.10869	1080	30	30	1110	9	21	1102	10	10	1014.233	21.91634	38.69515	100.7

TAC1_60	TAC1	1.731623	106291	151	1.2	11.32	0.4	0.05852	1.09	0.254426	0.771919	0.7125	1.0	0.08853	0.4	0.09	0.024368	0.877625	527	48	48	547	5	11	544	9	9	486.521	8.436067	17.65329	100.5
TAC1_61	TAC1	0.682429	140940	238	0.7	13.24	0.4	0.05678	0.95	0.143398	0.908015	0.5926	1.0	0.07556	0.4	0.24	0.020401	0.884444	467	42	42	470	3	9	471	8	8	408.1443	7.148222	14.86942	99.7
TAC1_62	TAC1	0.731802	94153	140	0.7	11.22	0.5	0.05916	1.13	0.153467	1.177519	0.7303	1.1	0.08956	0.5	0.10	0.025358	1.188648	552	54	54	553	5	11	555	10	10	505.9771	11.87753	20.02348	99.5
TAC1_63	TAC1	-0.80401	77825	133	1.0	12.46	0.5	0.05846	1.29	0.190857	1.21242	0.6476	1.3	0.08056	0.5	0.20	0.021487	1.144349	500	57	57	499	5	10	504	10	10	429.5734	9.727024	16.81226	99.0
TAC1_64	TAC1	1.073249	212020	287	0.4	9.68	0.5	0.06138	0.82	0.088301	3.327765	0.8741	0.8	0.10364	0.5	0.18	0.029072	1.246783	638	34	34	636	5	12	636	7	7	578.9753	14.16397	23.16248	99.9
TAC1_65	TAC1	-0.00499	175187	143	1.4	5.70	0.4	0.07387	0.72	0.280681	0.683346	1.7935	0.8	0.17597	0.4	0.32	0.045853	0.736151	1025	30	30	1045	8	20	1041	10	10	905.9468	13.04714	31.42844	100.4
TAC1_66	TAC1	0.109192	54313	83	2.9	10.62	0.7	0.06081	1.61	0.587546	0.929526	0.7931	1.6	0.09485	0.7	0.10	0.025394	0.971201	590	72	72	584	8	13	591	14	14	506.7661	9.716955	18.83986	98.8
TAC1_67	TAC1	0.288693	74911	64	0.8	6.01	0.6	0.07343	1.29	0.169947	1.270716	1.6979	1.3	0.16708	0.6	0.22	0.047263	1.169509	1002	54	54	996	11	20	1001	17	17	932.9028	21.30376	36.29648	99.4
TAC1_68	TAC1	0.553854	471045	660	0.5	9.97	0.6	0.05927	0.88	0.103106	0.980439	0.8181	0.9	0.10054	0.6	0.34	0.025823	1.161222	563	39	39	617	8	13	606	8	8	515.2206	11.82066	20.2339	101.9
TAC1_69	TAC1	0.069062	620517	492	0.4	5.76	0.9	0.07207	0.93	0.083638	1.206054	1.7304	0.9	0.17478	0.9	0.41	0.042247	1.281689	978	38	38	1038	16	24	1019	11	11	836.1337	21.01842	33.78862	101.9
TAC1_70	TAC1	0.164525	325759	344	0.4	11.06	0.4	0.05811	0.60	0.081137	0.808789	0.7266	0.6	0.09059	0.4	0.41	0.024755	0.85865	520	27	27	559	4	11	554	5	5	494.1638	8.382996	17.8421	101.0
TAC1_71	TAC1	0.220122	236814	295	0.6	13.11	0.4	0.05714	0.76	0.118266	0.765782	0.6021	0.8	0.07633	0.4	0.23	0.020715	0.769756	479	34	34	474	3	9	478	6	6	414.3714	6.315301	14.665	99.3
TAC1_72	TAC1	0.295429	357827	200	1.5	5.86	0.4	0.07215	0.56	0.311283	0.485757	1.7000	0.6	0.17082	0.4	0.41	0.04745	0.487448	982	23	23	1017	7	19	1008	7	7	936.9051	8.921861	30.8459	100.9
TAC1_73	TAC1	0.728351	201028	203	0.5	10.52	0.4	0.05914	0.81	0.104811	0.878691	0.7750	0.8	0.09533	0.4	0.18	0.02664	0.938385	553	35	35	587	4	11	582	7	7	531.2661	9.84309	19.57648	100.8
TAC1_74	TAC1	3.881278	29036	33	0.3	11.85	0.6	0.05991	1.64	0.069487	2.777365	0.6984	1.6	0.08475	0.6	0.10	0.025662	2.668074	524	75	75	525	6	11	533	13	13	513.838	27.44109	32.06733	98.5
TAC1_75	TAC1	0.77375	279545	156	0.2	5.56	0.5	0.07312	0.68	0.044061	2.324541	1.8183	0.8	0.18045	0.5	0.51	0.049602	1.287309	1010	28	28	1069	10	21	1051	10	10	977.908	24.57859	39.40621	101.7
TAC1_76	TAC1	0.647115	217898	243	0.1	11.04	0.4	0.05864	0.67	0.017378	1.974441	0.7383	0.7	0.09077	0.4	0.33	0.025891	1.977962	545	30	30	560	4	11	561	6	6	516.0759	20.15566	26.00953	99.8
TAC1_77	TAC1	-0.08609	12215	13	0.8	10.36	1.0	0.06571	2.86	0.190853	2.704197	0.8767	2.7	0.09809	1.0	0.07	0.029379	2.395221	553	140	140	603	11	15	624	26	26	587.6032	28.36399	34.19757	96.6
TAC1_78	TAC1	0.032852	428468	501	0.0	11.29	0.4	0.05763	0.70	0.00618	2.534432	0.7048	0.7	0.08870	0.4	0.29	0.026492	2.573217	503	31	31	548	4	11	541	6	6	527.7794	26.82477	31.6606	101.3
TAC1_79	TAC1	0.495166	271779	217	0.8	7.45	0.4	0.06990	0.70	0.163725	0.718613	1.2990	0.8	0.13467	0.4	0.40	0.037303	0.738591	917	28	28	814	6	15	843	9	9	740.1048	10.73328	25.78405	96.6
TAC1_80	TAC1	0.184345	725176	735	0.3	9.27	0.3	0.05865	0.49	0.051478	0.748352	0.8767	0.5	0.10812	0.3	0.44	0.027382	0.798799	547	21	21	662	4	12	638	5	5	545.9081	8.607297	19.39744	103.6
TAC1_81	TAC1	0.946415	225502	181	0.6	7.24	0.5	0.06715	0.74	0.134633	1.19912	1.2845	0.7	0.13835	0.5	0.30	0.039049	0.850607	834	31	31	835	7	16	837	8	8	774.0581	12.91997	27.70122	99.8
TAC1_83	TAC1	0.419118	749938	428	0.5	5.26	0.6	0.07692	0.51	0.099724	0.679303	2.0445	0.6	0.19099	0.6	0.62	0.04918	0.710428	1120	20	20	1126	12	23	1129	9	9	970.2323	13.44516	33.36063	99.7
TAC1_84	TAC1	0.604395	379945	226	0.7	5.28	0.6	0.07762	0.65	0.143014	0.962725	2.0484	0.8	0.19057	0.6	0.57	0.052859	0.937062	1130	27	27	1124	13	23	1129	11	11	1040.754	19.01112	37.85031	99.5
TAC1_85	TAC1	2.9753	10945	13	0.4	10.86	0.9	0.06217	3.06	0.10308	3.67218	0.7934	3.0	0.09371	0.9	0.14	0.02855	3.698189	418	151	151	577	10	14	578	28	28	566.5357	41.32593	45.0868	99.9
TAC1_86	TAC1	0.040312	1149253	256	0.6	2.02	0.6	0.17511	0.53	0.111192	0.822783	11.9893	0.6	0.49545	0.6	0.64	0.116051	0.739082	2603	18	18	2596	25	46	2602	11	11	2218.488	31.06558	74.58635	99.8
TAC1_87	TAC1	0.066985	371329	237	0.9	5.94	0.5	0.07208	0.67	0.174245	0.683071	1.6886	0.7	0.16897	0.5	0.43	0.044084	0.621716	982	27	27	1006	9	19	1004	9	9	871.8158	10.60742	29.49764	100.2
TAC1_88	TAC1	1.908642	49150	62	0.9	11.93	0.6	0.05912	1.51	0.191932	1.312354	0.6837	1.5	0.08420	0.6	0.14	0.024526	1.299512	502	68	68	521	6	11	527	12	12	489.5299	12.57059	20.03868	98.8
TAC1_89	TAC1	1.52926	91861	113	1.0	11.58	0.5	0.05884	1.10	0.199522	1.010149	0.7066	1.1	0.08674	0.5	0.20	0.024237	1.101376	536	48	48	536	5	11	541	9	9	483.8896	10.5328	18.68052	99.2
TAC1_90	TAC1	2.606794	33650	43	1.0	12.15	0.6	0.05935	1.64	0.224525	1.381491	0.6797	1.6	0.08283	0.6	0.10	0.024029	1.34432	504	78	78	513	6	11	523	13	13	479.7172	12.74045	19.90165	98.0

TAC1_91	TAC1	0.148572	204720	236	0.4	10.82	0.5	0.05986	0.84	0.096944	1.100799	0.7657	0.8	0.09284	0.5	0.33	0.027344	1.098863	580	36	36	572	6	12	577	7	7	545.107	11.81867	20.99377	99.2
TAC1_92	TAC1	0.515385	145250	78	0.7	5.18	0.5	0.07584	1.16	0.152553	0.999137	2.0407	1.2	0.19372	0.5	0.16	0.055665	1.032598	1075	45	45	1141	11	22	1125	16	16	1094.533	22.01101	40.82925	101.4
TAC1_93	TAC1	0.539937	149926	144	0.9	8.99	0.6	0.06313	0.97	0.176776	0.874037	0.9752	1.0	0.11185	0.5	0.31	0.030975	1.02675	688	42	42	683	7	14	689	10	10	616.4145	12.4718	23.22808	99.2
TAC1_94	TAC1	-0.01187	148352	151	0.4	9.53	0.5	0.06181	0.99	0.076157	1.287377	0.9019	1.0	0.10540	0.5	0.23	0.031016	1.299826	646	42	42	646	6	13	651	10	10	617.104	15.80605	25.19261	99.2
TAC1_95	TAC1	0.325224	346868	475	0.7	12.18	0.4	0.05746	0.64	0.158075	0.692574	0.6592	0.7	0.08231	0.4	0.36	0.023794	0.705773	502	29	29	510	4	10	513	6	6	475.233	6.628008	16.53653	99.3
TAC1_96	TAC1	0.225502	903347	491	0.7	3.37	1.4	0.09968	1.14	0.141139	1.581828	4.1519	1.4	0.29867	1.4	0.67	0.070676	1.60153	1612	43	43	1683	42	50	1662	23	23	1379.869	42.66246	60.55487	101.3
TAC1_97	TAC1	1.397821	119599	237	0.3	12.56	0.5	0.06841	1.64	0.083752	3.543686	0.7596	1.9	0.08010	0.6	0.53	0.033803	3.446852	823	66	66	497	5	10	572	17	17	669.0278	45.01207	49.69822	86.8
TAC1_98	TAC1	0.267804	341856	394	1.1	7.29	0.5	0.06696	0.53	0.219796	0.544462	1.2863	0.7	0.13799	0.5	0.59	0.036604	0.597855	829	23	23	833	8	17	838	8	8	726.5331	8.534555	24.56003	99.4
TAC1_99	TAC1	0.727633	226786	417	1.0	11.42	0.4	0.05796	0.72	0.198133	0.662953	0.7070	0.7	0.08782	0.4	0.26	0.023409	0.648497	512	32	32	543	4	11	543	6	6	467.6395	5.994692	16.07259	100.0
TAC1_100	TAC1	0.038378	72324	129	0.4	10.99	0.5	0.06011	1.36	0.099683	1.45896	0.7616	1.4	0.09150	0.5	0.27	0.027615	1.504099	556	60	60	564	6	11	572	12	12	550.2438	16.32045	23.93268	98.6
TAC1_101	TAC1	0.064798	215305	221	0.5	6.23	0.5	0.07142	0.77	0.107383	1.063722	1.5948	0.8	0.16095	0.5	0.42	0.045094	1.230394	964	30	30	962	9	19	966	10	10	891.0324	21.44631	35.36458	99.6
TAC1_102	TAC1	1.196903	160024	107	0.7	4.21	0.5	0.08792	0.73	0.139107	0.841355	2.9012	0.7	0.23850	0.5	0.31	0.063719	0.923834	1375	29	29	1378	12	26	1381	11	11	1247.893	22.35495	44.98504	99.8
TAC1_103	TAC1	0.076665	578302	547	0.3	5.86	1.0	0.07125	0.95	0.063944	1.140158	1.6907	1.0	0.17187	1.0	0.47	0.043611	1.289866	955	39	39	1022	19	26	1004	12	12	862.5676	21.75184	34.83193	101.8
TAC1_104	TAC1	0.430328	67596	98	0.6	9.40	0.5	0.07094	1.23	0.140428	1.603837	1.0447	1.2	0.10651	0.5	0.21	0.035444	1.562885	912	51	51	652	6	13	724	13	13	703.3384	21.59383	31.0342	90.0
TAC1_105	TAC1	1.00535	86265	72	2.4	5.66	0.5	0.07394	0.88	0.470868	0.730245	1.8171	0.9	0.17731	0.5	0.30	0.047122	0.767484	1015	36	36	1052	9	20	1048	12	12	930.4069	13.96726	32.51215	100.4
TAC1_106	TAC1	0.266474	175139	247	0.5	9.95	0.4	0.06083	0.77	0.093639	0.996377	0.8521	0.8	0.10059	0.4	0.29	0.027741	1.001308	619	34	34	618	5	12	624	7	7	552.8993	10.92267	20.7121	99.0
TAC1_107	TAC1	-1.41986	68887	94	1.0	10.11	0.5	0.06069	1.17	0.21407	1.203537	0.8351	1.1	0.09941	0.5	0.18	0.028338	1.135633	598	51	51	611	6	12	615	11	11	564.5998	12.6433	21.96448	99.4
TAC1_108	TAC1	5.210642	82777	91	0.6	10.98	0.7	0.10207	2.89	0.23863	3.288194	1.3249	3.3	0.09206	0.7	0.73	0.049288	3.725336	1465	108	108	567	8	13	831	38	38	965.4718	69.94613	76.22296	68.2
TAC1_109	TAC1	0.973573	138349	152	1.0	11.42	0.4	0.05900	0.93	0.201947	0.8211	0.7205	0.9	0.08794	0.4	0.23	0.024585	0.805074	540	41	41	543	5	11	549	8	8	490.8194	7.8074	17.48476	98.9
TAC1_110	TAC1	-0.17329	231919	206	0.1	8.87	1.2	0.06241	1.28	0.031076	4.138857	0.9841	1.3	0.11391	1.2	0.43	0.029111	2.688643	680	56	56	695	15	20	694	13	13	579.5561	30.69133	35.79226	100.1
TAC1_111	TAC1	0.86985	593566	754	0.3	13.27	0.4	0.06409	0.57	0.069445	0.696941	0.6729	0.6	0.07544	0.4	0.43	0.025157	0.744204	733	24	24	469	3	9	522	5	5	502.1088	7.385431	17.63112	89.8
TAC1_112	TAC1	0.342392	527452	255	0.5	5.07	0.4	0.07554	0.51	0.100549	0.857027	2.0779	0.5	0.19763	0.4	0.45	0.049016	0.672473	1074	21	21	1162	9	21	1140	7	7	966.983	12.6884	32.97781	101.9
TAC1_113	TAC1	0.025445	918728	476	1.0	5.48	0.4	0.07137	0.42	0.23754	0.532595	1.8162	0.4	0.18303	0.4	0.47	0.056787	0.505934	963	17	17	1083	7	20	1050	6	6	1116.215	10.99348	36.73775	103.1
TAC1_114	TAC1	-0.10282	119423	129	0.3	11.16	0.8	0.06098	1.41	0.076829	2.000801	0.7664	1.4	0.09029	0.8	0.36	0.027712	1.941233	615	60	60	557	8	13	575	13	13	552.1399	21.15396	27.50526	96.9
TAC1_115	TAC1	0.130029	234467	126	0.2	5.75	0.5	0.07273	0.95	0.047929	1.690896	1.7746	0.9	0.17419	0.5	0.11	0.051022	1.570323	999	40	40	1035	9	20	1034	12	12	1005.231	30.79843	44.15479	100.0
TAC1_116	TAC1	0.801846	184884	200	0.9	11.00	0.4	0.05810	0.80	0.175408	0.743007	0.7359	0.8	0.09120	0.4	0.19	0.024701	0.756724	514	36	36	563	4	11	559	7	7	493.1261	7.375149	17.36674	100.7
TAC1_117	TAC1	-2.36599	42079	99	1.1	23.46	0.6	0.05287	1.77	0.227416	1.325993	0.3135	1.7	0.04288	0.6	0.09	0.012175	1.310038	270	78	78	271	3	6	275	8	8	244.5551	6.366751	10.09981	98.4
TAC1_118	TAC1	-0.29701	180313	188	0.5	9.98	0.5	0.06003	0.88	0.105358	0.962347	0.8379	0.9	0.10049	0.5	0.22	0.027721	1.060168	584	40	40	617	6	12	616	8	8	552.4875	11.5504	21.03167	100.2
TAC1_119	TAC1	0.468137	104682	120	2.3	10.66	0.5	0.05885	1.07	0.467743	0.713069	0.7682	1.1	0.09411	0.5	0.22	0.025294	0.600608	535	47	47	580	5	12	576	9	9	504.8411	5.990161	17.16854	100.6
TAC1_120	TAC1	5.89454	14429	39	1.9	24.30	0.9	0.08451	3.30	0.522822	1.895218	0.4885	3.2	0.04165	0.9	0.03	0.014744	1.881236	983	155	155	263	4	7	393	21	21	295.6489	11.03703	14.53951	66.9

TAC1_121	TAC1	1.20089	187042	293	0.3	11.98	0.5	0.05813	0.92	0.058698	1.338261	0.6768	0.9	0.08367	0.5	0.22	0.023632	1.32414	518	42	42	518	5	10	524	8	8	471.9262	12.34995	19.46571	98.9
TAC1_122	TAC1	0.163803	1472718	560	0.1	3.01	1.0	0.17142	0.40	0.037459	1.843103	8.1431	1.2	0.33840	1.0	0.92	0.118533	0.81726	2567	13	13	1874	34	45	2234	22	22	2262.399	35.14465	77.76858	83.9
TAC1_123	TAC1	0.043742	1796733	645	0.7	2.82	1.0	0.18283	0.90	0.174007	2.664831	9.0558	1.2	0.35731	1.0	0.39	0.112648	1.323933	2673	30	30	1968	33	46	2340	22	22	2156.372	54.17728	85.40099	84.1
TAC1_124	TAC1	0.183673	431032	552	0.5	10.60	0.5	0.05841	0.63	0.101327	0.812889	0.7698	0.7	0.09461	0.5	0.43	0.025214	0.871133	537	27	27	583	5	12	579	6	6	503.2222	8.659728	18.22559	100.7
TAC1_125	TAC1	0.183959	158372	236	1.0	12.59	0.6	0.05803	1.04	0.197502	1.040608	0.6442	1.0	0.07988	0.6	0.25	0.020935	1.075101	516	47	47	495	6	11	504	8	8	418.7024	8.91453	16.07499	98.3
TAC1_126	TAC1	1.128613	132471	165	0.9	10.96	0.5	0.05893	1.02	0.180637	0.865371	0.7472	1.0	0.09146	0.5	0.15	0.024752	0.913666	533	46	46	564	5	11	565	8	8	494.0909	8.919595	18.09961	99.9
TAC1_127	TAC1	3.22854	60171	79	0.8	11.70	0.5	0.05929	1.33	0.157486	1.379761	0.7071	1.3	0.08583	0.5	0.18	0.023909	1.263176	531	60	60	531	6	11	542	11	11	477.3665	11.91476	19.32641	98.0
TAC1_128	TAC1	0.228862	556176	615	0.4	9.67	0.7	0.05927	0.83	0.069603	1.146372	0.8488	0.9	0.10324	0.7	0.49	0.02632	1.209994	564	37	37	633	8	14	623	9	9	524.9871	12.54026	20.89976	101.7
TAC1_129	TAC1	-3.3E-05	1718942	528	0.2	2.57	1.1	0.12527	1.11	0.027903	5.697523	6.8328	1.3	0.39113	1.0	0.46	0.082304	1.454922	2025	39	39	2127	37	50	2086	23	23	1597.939	44.75098	66.81962	101.9
TAC1_130	TAC1	0.19758	230698	280	1.8	10.65	0.4	0.05940	0.74	0.428274	0.533459	0.7750	0.7	0.09416	0.4	0.17	0.029768	0.541034	563	32	32	580	4	11	582	6	6	592.8383	6.322513	19.88427	99.7
TAC1_131	TAC1	0.156126	252084	433	0.1	12.74	0.4	0.05678	0.69	0.023113	1.518863	0.6176	0.7	0.07869	0.4	0.37	0.023397	1.445408	466	30	30	488	3	12	488	6	6	467.2206	13.35073	31.39513	100.0
TAC1_132	TAC1	-0.03093	1764726	386	1.2	1.56	0.8	0.24501	0.58	0.213586	0.789877	21.7434	0.8	0.63990	0.8	0.74	0.157467	0.824934	3150	18	18	3187	39	75	3173	15	15	2954.845	45.42764	175.3495	100.4
TAC1_133	TAC1	1.210414	56249	91	0.8	11.99	0.5	0.06217	1.25	0.170287	1.331536	0.7214	1.3	0.08384	0.5	0.22	0.023895	1.199789	638	54	54	519	5	13	548	11	11	477.1165	11.31254	31.13938	94.6
TAC1_134	TAC1	0.279272	309493	233	1.2	5.56	0.4	0.07438	0.55	0.22651	0.568724	1.8522	0.6	0.18022	0.4	0.34	0.046661	0.615925	1046	23	23	1068	7	26	1065	8	8	921.5998	11.09381	56.49164	100.3
TAC1_135	TAC1	-0.2218	52269	80	1.3	11.27	0.5	0.05954	1.37	0.246904	1.07056	0.7338	1.4	0.08902	0.5	0.20	0.024649	1.050066	518	63	63	550	5	14	555	12	12	492.0303	10.20781	31.61063	99.1
TAC1_136	TAC1	0.760379	124890	204	0.7	12.10	0.4	0.05831	0.95	0.135808	0.897278	0.6684	0.9	0.08275	0.4	0.21	0.023104	0.89029	517	42	42	512	4	13	518	8	8	461.5667	8.123864	29.21813	98.9
TAC1_137	TAC1	0.011956	698168	598	0.4	6.13	0.8	0.07052	0.81	0.089123	1.174717	1.5991	0.8	0.16407	0.8	0.50	0.04424	1.045217	942	35	35	979	15	27	969	10	10	874.8238	17.8951	55.62703	101.0
TAC1_138	TAC1	0.546764	93625	144	0.8	11.83	0.5	0.05891	1.37	0.139887	1.241016	0.6886	1.3	0.08485	0.5	0.15	0.021325	1.226769	529	59	59	525	5	14	531	11	11	426.3945	10.35622	27.97145	98.8
TAC1_139	TAC1	9.00415	18443	56	0.8	22.84	0.8	0.05636	2.63	0.186884	2.269632	0.3404	2.5	0.04399	0.8	0.03	0.013077	2.047978	280	129	129	277	4	8	295	13	13	262.4595	10.6824	19.28243	94.1
TAC1_140	TAC1	0.065197	145811	218	0.4	12.32	0.4	0.05824	0.98	0.07821	1.347728	0.6545	0.9	0.08143	0.4	0.14	0.022599	1.24334	511	43	43	505	4	13	510	7	7	451.5578	11.1061	29.64818	98.9
TAC1_141	TAC1	0.324345	317801	381	0.1	9.83	0.3	0.06094	0.59	0.033996	2.222417	0.8600	0.6	0.10198	0.3	0.25	0.029552	1.2706	625	26	26	626	4	16	630	5	5	588.3637	14.73268	38.60307	99.3
TAC1_142	TAC1	-0.37867	172098	207	0.6	9.72	0.4	0.06013	0.78	0.122853	0.870261	0.8603	0.9	0.10311	0.4	0.38	0.028197	0.880025	594	34	34	633	5	16	628	8	8	561.8928	9.752676	35.4662	100.6
TAC1_143	TAC1	0.267085	425498	289	1.1	5.54	0.3	0.07479	0.50	0.212438	0.614903	1.8709	0.5	0.18073	0.3	0.26	0.046118	0.495491	1056	20	20	1071	6	26	1070	6	6	911.1711	8.827747	55.56018	100.1
TAC1_144	TAC1	0.391347	45714	88	3.8	15.52	0.8	0.05746	2.00	0.765025	1.125146	0.5109	1.8	0.06480	0.8	0.09	0.017385	1.002262	431	93	93	405	6	12	418	13	13	349.2796	6.683372	21.58011	96.7
TAC1_145	TAC1	0.543717	239830	166	0.6	5.66	0.4	0.07626	0.62	0.11795	0.818698	1.8711	0.7	0.17721	0.4	0.41	0.048044	0.813142	1097	25	25	1051	7	25	1070	9	9	948.1546	15.06502	58.97297	98.2
TAC1_146	TAC1	0.113431	390262	122	0.7	2.51	0.3	0.13981	0.45	0.122222	0.70135	7.7328	0.4	0.39987	0.3	0.34	0.097677	0.707253	2219	15	15	2168	12	48	2200	8	8	1882.778	25.41393	113.4564	98.6
TAC1_147	TAC1	0.306041	126345	198	0.8	12.40	0.4	0.05698	0.97	0.159191	0.897656	0.6384	1.0	0.08094	0.4	0.21	0.021874	0.915802	466	41	41	502	4	13	500	8	8	437.2644	7.924859	27.78249	100.4
TAC1_148	TAC1	0.044841	217232	157	0.6	5.78	0.4	0.07424	0.66	0.124012	0.805738	1.7782	0.6	0.17305	0.4	0.22	0.045665	0.861125	1034	27	27	1029	8	25	1036	8	8	902.2176	15.19393	56.38624	99.2
TAC1_149	TAC1	1.015876	187411	327	0.9	13.30	0.4	0.05616	0.76	0.183502	0.789337	0.5890	0.8	0.07530	0.4	0.31	0.019822	0.751421	452	34	34	468	3	12	469	6	6	396.6875	5.902962	24.88733	99.7
TAC1_150	TAC1	1.601206	132430	199	0.8	11.22	0.5	0.05910	1.02	0.166226	1.16574	0.7314	1.0	0.08933	0.5	0.27	0.023304	0.997789	540	46	46	551	5	14	556	9	9	465.5339	9.181314	29.77089	99.3

TAC1_151	TAC1	0.690834	169006	115	0.6	5.10	0.5	0.07876	0.87	0.131474	1.102751	2.1481	0.9	0.19641	0.5	0.32	0.051636	1.033212	1153	35	35	1156	10	28	1161	12	12	1017.18	20.49237	64.39048	99.5
TAC1_152	TAC1	0.225084	317355	233	0.3	5.59	0.4	0.07479	0.57	0.072013	0.758085	1.8603	0.6	0.17955	0.4	0.36	0.047538	0.782569	1057	24	24	1064	7	26	1066	8	8	938.4317	14.35388	58.24786	99.8
TAC1_153	TAC1	1.595377	104620	172	0.8	12.49	0.5	0.05905	1.10	0.188487	0.877254	0.6542	1.0	0.08040	0.5	0.11	0.021978	0.926286	532	49	49	498	4	13	510	8	8	439.3276	8.052724	27.94251	97.7
TAC1_154	TAC1	0.126246	1374207	596	0.7	3.18	0.9	0.10523	0.80	0.171739	0.851101	4.5921	0.7	0.31636	0.9	0.53	0.083876	0.779622	1711	30	30	1771	27	47	1746	13	13	1627.66	24.38045	99.28365	101.4
TAC1_155	TAC1	0.516223	189383	261	0.4	10.41	0.5	0.05846	0.75	0.083025	1.031487	0.7827	0.9	0.09645	0.5	0.51	0.025872	1.110162	534	33	33	593	6	15	585	8	8	516.1	11.31325	33.34163	101.4
TAC1_156	TAC1	0.662727	166320	379	0.9	17.16	0.4	0.05445	0.89	0.198298	0.774359	0.4383	0.9	0.05842	0.4	0.22	0.016138	0.719671	363	41	41	366	3	9	369	5	5	323.5489	4.619042	20.28533	99.2
TAC1_157	TAC1	0.363711	258726	343	0.5	9.94	0.6	0.06100	0.86	0.100959	1.06687	0.8500	0.9	0.10097	0.6	0.47	0.02668	1.009676	626	38	38	620	7	17	623	9	9	532.0876	10.60784	34.03031	99.5
TAC1_158	TAC1	0.631124	301647	448	1.0	11.55	0.4	0.05884	0.73	0.188188	0.751922	0.7066	0.7	0.08683	0.4	0.28	0.024163	0.710646	554	31	31	537	4	14	543	6	6	482.5342	6.778425	30.11783	98.8
TAC1_159	TAC1	0.45068	127484	202	0.7	12.06	0.4	0.05777	0.88	0.138474	1.007438	0.6629	0.9	0.08313	0.4	0.23	0.023278	0.97485	493	40	40	515	4	13	516	7	7	465.0034	8.957274	29.67181	99.8
TAC1_160	TAC1	0.165008	177979	94	0.8	4.06	0.5	0.08938	0.78	0.147975	0.836528	3.0488	0.8	0.24684	0.5	0.30	0.06443	0.805257	1400	29	29	1422	13	35	1417	12	12	1261.571	19.70134	77.84213	100.4
TAC1_161	TAC1	0.045134	375133	159	1.3	3.23	0.5	0.10545	0.60	0.215202	0.649873	4.5273	0.6	0.31102	0.5	0.48	0.076469	0.750666	1715	22	22	1745	14	41	1734	10	10	1488.872	21.56063	91.02635	100.6
TAC1_162	TAC1	0.453964	252225	362	0.6	11.08	0.5	0.05936	0.81	0.105988	0.875231	0.7445	0.9	0.09064	0.5	0.40	0.024384	0.873402	561	36	36	559	5	14	564	8	8	486.8584	8.40199	30.78416	99.2
TAC1_163	TAC1	0.282674	413203	505	0.6	9.65	0.4	0.06118	0.64	0.122272	1.779679	0.8799	0.6	0.10400	0.4	0.34	0.028263	0.710802	636	28	28	638	5	16	640	6	6	563.2482	7.897431	35.10571	99.6
TAC1_164	TAC1	0.162845	218795	371	1.2	12.98	0.6	0.05694	0.88	0.243592	1.171314	0.6086	1.0	0.07714	0.6	0.47	0.022581	0.902243	482	40	40	479	6	13	483	8	8	451.2771	8.052689	28.61891	99.2
TAC2_1	TAC2	0.89578	98872	71	2.1	5.70	0.7	0.07585	1.45	0.383518	1.041749	1.8594	1.3	0.17639	0.7	0.19	0.047146	1.101499	1059	58	63	1047	13	26	1065	18	19	930.8714	20.06588	40.10259	98.8
TAC2_2	TAC2	1.376617	354719	628	0.6	14.04	0.5	0.06389	0.78	0.125511	1.223522	0.6384	0.6	0.07136	0.5	0.13	0.022984	0.812029	724	34	41	444	4	11	501	5	6	459.2198	7.372698	18.8142	61.3
TAC2_3	TAC2	2.516048	147222	229	1.3	12.52	0.5	0. 06303	0.85	0.266751	0.815972	0.7070	0.8	0.08004	0.5	0.28	0.025003	0.695057	690	35	43	496	4	12	543	7	8	499.0854	6.852556	20.0049	72.0
TAC2_4	TAC2	0.28772	276181	474	0.2	13.77	0.8	0.05636	0.83	0.035491	1.451232	0.5738	0.9	0.07282	0.8	0.54	0.021138	1.384963	455	34	42	453	7	12	459	7	8	422.597	11.57331	19.69012	99.6
TAC2_5	TAC2	0.714235	232802	373	0.3	12.80	0.5	0.05736	0.76	0.05993	1.151321	0.6254	0.8	0.07846	0.4	0.37	0.022497	1.103637	489	34	42	487	4	12	492	6	7	449.5421	9.814775	19.58748	99.7
TAC2_6	TAC2	0.361136	345242	240	1.0	5.56	0.5	0.07496	0.64	0.184853	0.696628	1.8818	0.7	0.18032	0.5	0.44	0.048388	0.742314	1063	24	32	1069	9	26	1073	9	11	954.8378	13.83938	38.13254	100.6
TAC2_7	TAC2	1.061141	147361	183	1.9	10.04	0.6	0.06392	0.91	0.357154	0.715026	0.8815	0.8	0.10018	0.6	0.21	0.027585	0.848467	715	38	44	615	7	15	640	8	9	549.8899	9.204754	22.63835	86.1
TAC2_8	TAC2	0.869396	508379	867	0.6	13.88	0.6	0.06175	0.72	0.134596	0.748872	0.6191	0.7	0.07237	0.5	0.35	0.024656	0.772545	655	31	39	450	5	11	489	6	7	492.2336	7.513486	20.00156	68.8
TAC2_9	TAC2	3.437888	54147	35	0.5	5.97	0.7	0.07383	1.37	0.116473	1.763373	1.7234	1.4	0.16919	0.7	0.21	0.046662	1.557317	1006	57	62	1007	13	26	1012	18	19	920.8676	28.04726	44.32975	100.1
TAC2_10	TAC2	-0.00201	458666	555	0.5	11.21	0.5	0.05846	0.71	0.125658	0.948193	0.7240	0.7	0.08959	0.5	0.36	0.025847	0.765211	537	31	40	553	5	14	552	6	7	515.7344	7.793054	20.91662	103.0
TAC2_11	TAC2	2.532134	98970	151	0.6	14.42	0.6	0.06626	1.22	0.12176	1.141294	0.6378	1.1	0.06984	0.6	0.01	0.018469	1.219623	769	54	59	435	5	11	499	9	9	369.7873	8.935248	16.58063	56.6
TAC2_12	TAC2	4.102906	57547	124	0.9	19.34	0.8	0.06068	2.08	0.211129	1.833955	0.4322	2.0	0.05189	0.8	0.06	0.014155	1.627057	573	93	96	326	5	9	363	12	13	284.0374	9.179699	14.13932	56.9
TAC2_13	TAC2	-0.0058	536030	398	0.2	7.06	1.3	0.07570	0.78	0.053884	2.254629	1.5568	1.8	0.14692	1.3	0.93	0.052301	0.992835	1069	31	38	882	22	29	940	22	23	1029.877	19.9569	43.20542	82.5
TAC2_14	TAC2	0.561896	312287	438	0.3	12.96	0.5	0.05723	0.85	0.070135	1.309921	0.6148	0.9	0.07746	0.5	0.31	0.021263	0.999433	488	39	47	481	5	12	486	7	8	425.2033	8.412112	18.11605	98.5
TAC2_15	TAC2	0.440718	831045	262	0.7	2.83	0.5	0.12826	0.47	0.131607	0.570587	6.2963	0.6	0.35519	0.5	0.68	0.083905	0.925399	2070	16	26	1958	17	44	2014	11	14	1627.345	28.94287	66.26195	94.6
TAC2_16	TAC2	3.865265	564934	798	0.6	12.56	0.5	0.08919	0.66	0.212246	0.757627	0.9859	0.7	0.07990	0.5	0.47	0.039675	0.68697	1401	26	34	495	5	12	695	7	9	786.2653	10.5914	31.24285	35.4

TAC2_17	TAC2	0.741655	149583	278	0.7	13.28	0.7	0.05700	1.00	0.138159	1.050154	0.5975	1.1	0.07589	0.7	0.49	0.022212	1.157446	466	43	43	471	6	13	474	9	9	443.8852	10.16097	28.8692	99.5
TAC2_18	TAC2	-0.0651	689733	248	1.2	2.67	1.1	0.12590	0.91	0.228117	0.890932	6.5081	1.2	0.37691	1.1	0.67	0.088506	1.329263	2043	30	35	2060	40	58	2049	19	21	1713.476	43.64586	76.30046	100.9
TAC2_19	TAC2	1.089983	136050	715	0.2	41.16	0.6	0.04965	1.17	0.041109	1.906084	0.1672	1.1	0.02436	0.6	0.14	0.007212	1.931127	156	54	60	155	2	4	157	3	3	145.2159	5.588344	7.852021	99.2
TAC2_19_2	TAC2	0.462984	348131	571	0.7	11.93	1.3	0.06047	1.01	0.169032	2.127416	0.7147	1.5	0.08555	1.3	0.73	0.027498	1.825943	605	46	46	529	13	19	545	12	12	547.9805	19.74137	38.68495	97.0
TAC2_20	TAC2	1.340399	140746	201	1.1	11.33	0.5	0.05929	0.99	0.237417	0.787338	0.7228	1.0	0.08868	0.5	0.29	0.024756	0.857202	548	43	50	548	6	14	550	8	9	495.0494	8.52964	20.79341	99.9
TAC2_21	TAC2	0.641901	232664	384	0.1	13.50	0.5	0.05785	0.76	0.026124	1.586149	0.5939	0.8	0.07413	0.5	0.38	0.019351	1.881759	503	34	43	461	4	11	472	6	7	387.1111	14.42948	20.54008	91.6
TAC2_22	TAC2	-0.17019	466211	635	1.1	9.92	0.5	0.05977	0.68	0.24469	0.711882	0.8363	0.7	0.10128	0.5	0.44	0.032704	0.782478	585	29	29	622	6	16	617	7	7	650.3095	10.01351	40.6362	100.9
TAC2_23	TAC2	0.104122	381878	263	0.7	5.68	0.5	0.07295	0.68	0.135592	0.759002	1.7791	0.7	0.17655	0.5	0.39	0.046545	0.791191	1001	28	37	1048	10	25	1036	9	11	919.2711	14.21784	37.0828	104.7
TAC2_24	TAC2	0.052181	352578	520	0.3	12.07	0.7	0.05849	1.00	0.055926	1.367717	0.6671	0.9	0.08303	0.7	0.27	0.02078	1.21577	537	43	49	514	7	14	518	8	9	415.637	10.00451	18.60557	95.8
TAC2_25	TAC2	0.32177	203447	323	0.2	13.33	0.6	0.05722	1.01	0.048265	3.691632	0.5956	1.1	0.07557	0.6	0.36	0.019807	2.208652	472	45	51	470	6	12	473	8	9	396.1064	17.3384	22.9033	99.4
TAC2_26	TAC2	0.489363	144884	231	0.8	13.37	0.5	0.05694	1.04	0.172902	1.019147	0.5880	1.1	0.07495	0.5	0.26	0.020483	1.074871	467	45	52	466	5	12	468	8	9	409.7484	8.720335	17.75319	99.8
TAC2_27	TAC2	0.27332	378514	533	0.1	12.65	0.5	0.05608	0.68	0.02826	1.386803	0.6156	0.6	0.07940	0.5	0.28	0.022342	1.404325	444	30	39	492	5	12	487	5	6	446.4237	12.39107	20.8903	110.8
TAC2_28	TAC2	0.229269	1286612	716	0.5	5.07	0.4	0.07285	0.44	0.099806	0.544066	1.9977	0.5	0.19758	0.4	0.51	0.055139	0.5296	1005	18	29	1162	9	27	1114	6	9	1084.667	11.18756	41.79113	115.6
TAC2_29	TAC2	0.490811	258653	376	0.5	13.21	0.6	0.05765	1.09	0.102799	1.32175	0.6054	1.2	0.07597	0.6	0.40	0.019779	1.096312	503	50	57	472	6	12	480	9	10	395.8222	8.591796	17.23341	93.8
TAC2_30	TAC2	0.153372	1634174	985	0.5	5.55	0.6	0.07463	0.49	0.126134	2.235914	1.8726	0.6	0.18111	0.6	0.54	0.057026	0.689544	1053	20	30	1073	12	26	1070	8	10	1120.731	15.04069	44.2096	101.9
TAC2_31	TAC2	0.499597	103209	142	0.3	12.83	0.6	0.05806	1.10	0.073863	1.68977	0.6285	1.0	0.07844	0.6	0.21	0.023315	1.432863	500	48	54	487	6	12	493	8	9	465.6058	13.18953	21.95018	97.4
TAC2_32	TAC2	-1.13629	25275	28	0.8	10.34	0.8	0.06275	2.02	0.196508	1.789039	0.8514	2.0	0.09767	0.7	0.12	0.028386	1.805512	616	88	91	600	8	16	616	19	19	565.2329	20.14168	29.28926	97.4
TAC2_33	TAC2	0.221242	171516	243	0.4	10.31	0.6	0.06136	0.91	0.086157	1.083248	0.8265	1.0	0.09762	0.6	0.40	0.028428	1.06292	632	39	39	600	7	16	609	9	9	566.3854	11.86678	36.3504	98.5
TAC2_34	TAC2	0.050102	285761	171	0.6	5.73	0.5	0.07451	0.72	0.125583	0.787646	1.8120	0.7	0.17508	0.5	0.25	0.048314	0.814794	1045	30	38	1040	10	25	1048	8	11	953.418	15.17743	38.613	99.5
TAC2_35	TAC2	0.033337	390834	585	0.2	13.44	0.7	0.05653	0.99	0.037001	1.522239	0.5840	0.9	0.07475	0.7	0.31	0.017055	1.823653	463	42	48	465	6	12	466	7	8	341.709	12.35578	17.87416	100.4
TAC2_36	TAC2	0.990676	174183	135	0.4	5.83	0.6	0.07477	0.80	0.079253	1.115982	1.7633	0.8	0.17221	0.5	0.35	0.047268	1.187242	1049	33	40	1024	10	25	1030	10	12	932.9578	21.61757	40.88773	97.6
TAC2_37	TAC2	-0.00896	291828	495	0.2	12.85	0.4	0.05680	0.69	0.032117	1.337575	0.6057	0.7	0.07802	0.4	0.33	0.021487	1.385928	469	30	39	484	4	12	480	5	6	429.5133	11.7799	20.03117	103.2
TAC2_38	TAC2	2.907306	59065	92	1.0	11.98	0.6	0.05853	1.41	0.193452	1.191293	0.6675	1.3	0.08401	0.6	0.14	0.023338	1.221632	486	64	68	520	6	13	518	11	12	466.1207	11.24833	20.84512	106.9
TAC2_39	TAC2	0.548257	239069	416	0.3	13.63	0.6	0.05876	0.81	0.044147	1.395945	0.5925	0.8	0.07362	0.6	0.29	0.017814	1.447101	544	34	41	458	5	12	472	6	7	356.7428	10.23496	16.92798	84.1
TAC2_40	TAC2	0.185454	101016	153	1.1	11.94	0.5	0.05842	1.09	0.21482	0.940387	0.6704	1.0	0.08401	0.5	0.11	0.022791	0.951085	518	50	56	520	5	13	520	9	9	455.3886	8.564329	19.18144	100.5
TAC2_41	TAC2	0.154708	345499	570	0.3	13.05	0.7	0.05719	0.90	0.047912	1.300175	0.5994	0.9	0.07705	0.7	0.33	0.018439	1.445111	478	40	47	478	6	13	476	7	8	369.1868	10.577	17.50858	100.0
TAC2_42	TAC2	0.900683	518968	647	0.2	10.04	1.0	0.07534	0.74	0.038052	1.59998	1.0303	1.0	0.10074	0.9	0.75	0.031312	1.627206	1068	30	37	618	11	18	717	11	12	622.8769	19.95836	30.74174	57.9
TAC2_43	TAC2	0.517991	186891	137	0.5	5.94	0.5	0.07388	0.88	0.099941	1.177546	1.6993	1.0	0.16890	0.5	0.32	0.045556	1.359026	1024	37	43	1006	10	24	1006	12	14	899.997	23.91646	41.19629	98.2
TAC2_44	TAC2	1.000622	176990	289	0.6	14.31	0.8	0.05942	1.19	0.120975	1.441419	0.5839	1.3	0.07034	0.8	0.39	0.018249	1.729833	579	52	58	438	7	12	466	10	11	365.435	12.52492	18.63796	75.7
TAC2_45	TAC2	0.643019	374785	540	0.1	13.04	0.9	0.05944	0.86	0.0228	1.886212	0.6431	1.2	0.07743	0.9	0.68	0.018377	2.023412	578	37	45	481	8	14	504	10	10	367.8862	14.74893	20.26348	83.2

TAC2_46	TAC2	0.783768	113435	159	0.6	13.03	0.5	0.05888	1.05	0.134363	2.015452	0.6361	1.0	0.07705	0.5	0.23	0.020849	1.003972	531	47	53	478	5	12	498	8	9	416.9763	8.287027	17.78295	90.1
TAC2_47	TAC2	0.423216	289891	440	0.4	13.85	0.7	0.05787	0.95	0.07753	1.220065	0.5891	0.9	0.07271	0.7	0.36	0.020243	1.026604	513	40	47	452	6	12	469	7	8	405.0011	8.230464	17.35752	88.2
TAC2_48	TAC2	0.294423	236483	352	0.2	13.53	0.8	0.05691	1.04	0.053603	2.596473	0.5945	1.1	0.07466	0.8	0.48	0.022233	1.650168	465	47	54	464	7	13	472	8	9	444.2516	14.49891	22.15305	99.7
TAC2_49	TAC2	0.654573	158804	148	1.2	8.47	0.6	0.06531	0.80	0.246287	1.02282	1.0858	0.8	0.11878	0.6	0.42	0.033326	0.82752	766	34	41	723	8	18	744	9	10	662.454	10.78497	27.08151	94.4
TAC2_50	TAC2	-0.25661	331465	674	0.3	17.06	1.4	0.05757	2.03	0.045834	3.218976	0.4709	2.2	0.05907	1.4	0.45	0.013343	3.876529	489	89	92	370	10	13	391	14	14	267.8018	20.61568	22.97337	75.6
TAC2_51	TAC2	-0.14281	189240	111	0.7	5.43	0.7	0.07756	0.94	0.137844	1.163839	2.0142	0.9	0.18520	0.7	0.33	0.050053	1.05107	1124	39	45	1095	14	27	1118	13	15	986.8459	20.22448	41.88639	97.4
TAC2_52	TAC2	0.969924	115084	141	1.6	10.14	0.5	0.06086	0.97	0.300621	0.803709	0.8272	1.0	0.09917	0.5	0.26	0.027041	0.880013	606	42	48	609	6	15	610	9	10	539.1785	9.365797	22.34254	100.6
TAC2_53	TAC2	0.935635	436873	679	0.1	12.93	0.5	0.06269	0.81	0.042272	2.113754	0.6686	0.8	0.07766	0.5	0.19	0.031603	1.677607	675	35	43	482	4	12	519	6	7	628.2761	20.76975	31.43618	71.4
TAC2_54	TAC2	0.410806	284142	328	0.7	9.44	0.7	0.06055	1.06	0.126851	0.98429	0.8815	1.0	0.10627	0.7	0.33	0.026848	1.0402	600	46	52	651	9	17	640	10	11	535.4053	10.98586	22.93324	108.5
TAC2_55	TAC2	0.382996	125371	149	0.6	10.18	0.6	0.06113	1.04	0.117851	1.126426	0.8298	1.0	0.09843	0.5	0.31	0.028401	1.084252	623	43	49	605	6	15	611	10	11	565.866	12.10134	24.47545	97.2
TAC2_56	TAC2	1.282592	131471	184	0.5	10.12	0.7	0.06029	0.98	0.115455	1.119327	0.8289	1.1	0.09927	0.7	0.44	0.030254	1.167359	588	43	43	610	8	17	610	10	10	602.1702	13.84982	39.05604	99.9
TAC2_57	TAC2	0.607443	214509	366	0.2	13.57	1.1	0.05805	1.64	0.044762	3.099524	0.5881	1.7	0.07427	1.1	0.36	0.01683	4.815593	504	73	77	462	10	14	468	13	13	336.9229	32.19614	34.62682	91.6
TAC2_58	TAC2	-0.05198	150984	252	0.3	13.62	0.6	0.05784	1.37	0.06526	1.890526	0.5805	1.3	0.07347	0.7	0.28	0.018796	2.504443	507	57	62	457	6	12	463	10	11	376.1339	18.70052	23.50114	90.0
TAC2_59	TAC2	-3.17489	43188	61	0.7	11.87	1.1	0.07126	2.75	0.1304	2.926326	0.8353	2.7	0.08512	1.1	0.21	0.020692	2.807311	918	108	110	526	11	16	610	25	25	413.6872	22.98535	27.78355	57.3
TAC2_60	TAC2	0.323444	286483	364	0.5	11.05	0.4	0.05873	0.75	0.100615	1.114997	0.7339	0.7	0.09060	0.5	0.30	0.024411	0.853076	541	33	41	559	5	14	558	6	8	488.215	8.364979	20.47693	103.4
TAC2_61	TAC2	1.279633	116080	125	1.0	10.08	0.7	0.06138	1.12	0.23278	1.136964	0.8483	1.2	0.10003	0.8	0.37	0.027291	1.152364	652	48	53	614	9	16	623	12	13	544.0779	12.3665	23.90304	94.2
TAC2_62	TAC2	0.61745	239223	100	0.8	3.99	0.6	0.09214	0.72	0.166537	0.828341	3.1994	0.8	0.25169	0.6	0.47	0.067268	0.804266	1459	27	35	1446	15	34	1456	12	15	1315.302	20.48294	52.68906	99.1
TAC2_63	TAC2	-0.0262	113301	266	0.9	22.64	0.7	0.05408	1.18	0.216502	1.190165	0.3312	1.2	0.04445	0.7	0.38	0.013899	1.078228	337	56	62	280	4	8	290	6	7	278.945	5.971017	12.12755	83.1
TAC2_64	TAC2	0.170991	370488	427	0.5	11.32	0.4	0.05939	0.62	0.094794	1.130111	0.7285	0.6	0.08853	0.4	0.36	0.023066	0.832845	572	28	37	547	4	13	555	5	7	460.8407	7.589502	18.95597	95.6
TAC2_65	TAC2	0.413592	125643	153	0.8	11.79	0.6	0.05814	1.02	0.176867	0.984958	0.6863	1.1	0.08537	0.6	0.30	0.023411	0.983251	507	45	52	528	6	13	528	9	10	467.6259	9.087522	19.82302	104.2
TAC2_66	TAC2	0.142285	228137	142	0.5	6.04	0.6	0.07208	0.87	0.100306	1.50073	1.6547	0.9	0.16656	0.6	0.42	0.045899	1.14538	980	36	43	993	11	24	989	11	13	906.6432	20.32	39.45195	101.3
TAC2_67	TAC2	0.106053	574940	163	0.2	2.75	0.6	0.12380	0.55	0.044327	1.122882	6.2573	0.7	0.36587	0.6	0.61	0.089302	1.050443	2007	20	28	2008	20	45	2009	12	14	1727.413	34.83926	72.18578	100.1
TAC2_68	TAC2	-0.22736	200605	286	0.3	13.58	0.7	0.05821	1.00	0.061934	1.451124	0.5920	1.0	0.07399	0.7	0.34	0.018772	1.626916	515	45	52	460	6	12	471	8	8	375.7862	12.11247	18.65814	89.3
TAC2_69	TAC2	1.679603	68876	69	1.3	9.62	0.6	0.06347	1.37	0.295549	1.46539	0.9139	1.3	0.10478	0.6	0.22	0.029962	0.994147	664	57	62	642	7	16	655	13	14	596.5162	11.68697	25.27278	96.6
TAC2_70	TAC2	0.268336	225077	315	0.6	13.35	0.6	0.05689	0.82	0.137918	0.881223	0.5910	0.9	0.07531	0.6	0.46	0.021313	0.879831	467	37	44	468	6	12	470	7	8	426.1865	7.422388	17.71065	100.1
TAC2_71	TAC2	0.04745	493337	705	0.3	13.42	0.7	0.05661	0.78	0.096451	6.321546	0.5826	0.8	0.07479	0.7	0.44	0.02029	1.013457	464	36	44	465	6	12	466	6	7	405.943	8.151538	17.36408	100.1
TAC2_72	TAC2	0.057399	301859	159	0.9	4.88	0.5	0.08046	0.71	0.181388	0.794078	2.2826	0.7	0.20533	0.5	0.41	0.05439	0.832889	1201	28	36	1203	11	28	1204	10	12	1070.074	17.36729	43.37512	100.2
TAC2_73	TAC2	0.788355	157281	250	0.6	14.59	0.6	0.06346	0.86	0.113178	2.080354	0.6016	0.8	0.06889	0.6	0.26	0.017987	1.32105	713	38	45	429	5	11	477	6	7	360.212	9.437447	16.56855	60.2
TAC2_74	TAC2	0.524134	138671	182	0.6	10.46	0.6	0.06057	1.17	0.11167	1.626044	0.7949	1.1	0.09583	0.7	0.28	0.023176	1.777442	591	50	56	591	8	15	592	10	11	462.8186	16.29029	23.88697	100.0
TAC2_75	TAC2	1.403753	204658	322	0.4	13.01	0.6	0.06389	1.01	0.094155	1.523567	0.6807	1.1	0.07736	0.6	0.33	0.025998	1.485318	726	43	50	480	6	12	525	9	10	518.439	15.20055	24.73069	66.1

TAC2_76	TAC2	0.257032	401917	633	0.2	12.99	0.7	0.05630	0.82	0.037675	1.253543	0.6008	0.8	0.07733	0.7	0.50	0.019781	1.61432	446	37	45	480	6	13	477	6	7	395.7464	12.65229	19.57756	107.5
TAC2_77	TAC2	0.150762	397700	154	1.3	3.25	0.6	0.10701	0.72	0.273693	0.979772	4.5441	0.7	0.30945	0.6	0.43	0.081337	0.84154	1739	27	34	1737	19	41	1736	12	14	1579.922	25.58974	63.36115	99.9
TAC2_78	TAC2	0.447524	273810	429	0.3	13.29	0.4	0.05672	0.74	0.050635	1.099073	0.5907	0.8	0.07528	0.4	0.25	0.018055	1.337548	466	33	42	468	3	11	470	6	7	361.5509	9.585416	16.68807	100.4
TAC2_79	TAC2	2.11763	106985	51	1.5	4.43	2.0	0.13459	0.84	0.215801	0.890962	4.5306	2.1	0.24717	2.2	0.92	0.048545	3.606703	2141	30	35	1416	56	63	1710	35	36	951.9045	66.5402	75.26187	66.1
TAC2_80	TAC2	0.374511	353280	198	1.0	4.89	0.5	0.07936	0.63	0.199481	0.691493	2.2455	0.7	0.20462	0.5	0.53	0.054311	0.731803	1171	24	33	1200	11	28	1194	10	12	1068.651	15.24081	42.5243	102.4
TAC2_81	TAC2	0.040236	323295	478	0.1	12.88	0.5	0.05647	0.66	0.03312	1.166537	0.6059	0.7	0.07779	0.5	0.50	0.022751	1.250083	458	29	38	483	5	12	480	6	7	454.5192	11.23446	20.48618	105.4
TAC2_82	TAC2	0.974033	267525	484	0.2	13.17	0.6	0.05687	0.75	0.0379	1.482552	0.6014	0.8	0.07647	0.6	0.43	0.023204	1.376805	474	34	34	475	5	13	477	6	6	463.4408	12.61102	30.88388	99.5
TAC2_83	TAC2	-0.09115	163346	230	0.5	12.27	0.7	0.05820	1.05	0.114391	1.234098	0.6539	1.1	0.08195	0.7	0.40	0.023021	1.061631	510	46	52	508	6	13	510	9	10	459.9293	9.652497	19.83808	99.6
TAC2_84	TAC2	0.021778	799924	320	0.6	3.47	0.8	0.10003	0.66	0.110037	0.929334	3.9923	0.8	0.28925	0.8	0.63	0.072585	0.876376	1616	25	33	1639	21	39	1631	12	14	1415.772	23.95808	57.35464	101.4
TAC2_85	TAC2	-0.04148	451227	139	1.1	2.84	0.7	0.11449	0.93	0.195042	0.970881	5.6285	1.0	0.35087	0.6	0.45	0.089158	0.981236	1866	33	39	1944	23	50	1919	17	19	1725.873	32.44041	70.87977	104.2
TAC2_86	TAC2	0.900748	136152	222	0.9	14.44	0.5	0.05978	0.92	0.19124	1.062698	0.5756	1.0	0.06952	0.5	0.32	0.019633	0.785174	570	41	48	434	4	11	460	7	8	392.9235	6.110525	16.04394	76.1
TAC2_87	TAC2	-0.15985	110763	129	0.7	10.06	0.6	0.05997	1.12	0.153492	1.221501	0.8284	1.1	0.09977	0.6	0.28	0.028149	1.095923	573	50	55	614	7	15	610	10	11	560.9022	12.12256	24.32194	107.1
TAC2_88	TAC2	3.304424	79664	143	1.7	14.16	1.3	0.06989	1.43	0.332197	0.995579	0.6885	1.1	0.07246	1.1	0.25	0.019715	1.244789	875	59	64	451	10	14	531	9	10	394.4741	9.725674	17.78726	51.5
TAC2_89	TAC2	0.613472	287711	480	0.9	13.09	0.5	0.05674	0.78	0.188189	0.771797	0.6004	0.7	0.07649	0.6	0.28	0.023066	0.717098	475	36	44	475	5	12	477	6	7	460.8724	6.532806	18.55368	100.0
TAC2_90	TAC2	1.929785	314883	496	0.4	12.65	0.6	0.07164	0.81	0.105199	0.804431	0.7833	0.6	0.07941	0.6	0.01	0.03097	1.035242	958	33	41	492	5	12	587	6	7	616.3012	12.57056	26.34029	51.4
TAC2_91	TAC2	-0.27771	217905	340	1.0	11.96	0.8	0.05836	1.11	0.191218	0.955688	0.6739	1.2	0.08410	0.8	0.43	0.023489	1.093104	521	50	56	520	8	14	521	10	10	469.1785	10.12264	20.34867	99.9
TAC2_92	TAC2	0.382606	219250	371	1.2	13.49	0.6	0.05677	0.94	0.240524	0.998118	0.5811	0.9	0.07447	0.6	0.19	0.021914	0.707851	463	42	49	463	5	12	465	7	8	438.0925	6.133787	17.6201	100.0
TAC2_93	TAC2	0.059306	182023	426	0.7	18.90	0.6	0.05357	0.89	0.130431	0.972496	0.3939	0.9	0.05334	0.6	0.40	0.014868	0.935434	333	41	48	335	4	9	336	5	6	298.257	5.53578	12.56571	100.4
TAC2_93_2	TAC2	0.155079	202083	511	0.7	18.00	0.6	0.05349	0.87	0.136532	0.979127	0.4124	0.8	0.05593	0.6	0.30	0.015942	0.838087	324	40	40	351	4	9	350	5	5	319.6486	5.315633	20.23121	100.1
TAC2_94	TAC2	0.212161	232521	383	0.2	13.55	0.6	0.05667	0.80	0.048382	1.29605	0.5789	0.8	0.07428	0.6	0.38	0.021331	1.193676	461	34	42	462	5	12	463	6	7	426.4704	10.07254	18.97851	100.2
TAC2_95	TAC2	-0.30379	210316	292	0.8	11.54	0.6	0.05869	0.83	0.152446	0.917994	0.7005	0.9	0.08748	0.6	0.47	0.024278	0.846903	539	36	44	540	7	14	538	7	8	484.7491	8.111749	19.9788	100.2
TAC2_96	TAC2	-0.1125	451660	714	0.2	13.20	0.6	0.05557	0.76	0.041014	1.964845	0.5812	0.8	0.07604	0.6	0.43	0.020493	1.097466	419	35	44	472	6	12	464	6	7	409.9227	8.905155	17.84795	112.7
TAC2_97	TAC2	0.718691	556615	713	0.5	10.67	0.5	0.06650	0.66	0.079256	0.902712	0.8566	0.7	0.09404	0.5	0.44	0.021178	1.019225	809	28	37	579	6	14	628	7	8	423.4937	8.541228	18.11374	71.6
TAC2_98	TAC2	0.056933	209460	283	0.7	11.60	0.6	0.05886	0.96	0.12995	1.121718	0.7003	0.9	0.08645	0.6	0.32	0.023459	1.090438	543	41	48	534	6	14	538	7	8	468.5957	10.1018	20.3442	98.3
TAC2_99	TAC2	0.425423	320307	503	0.7	13.10	0.5	0.05700	0.81	0.158988	0.769922	0.5982	0.9	0.07654	0.5	0.41	0.022563	0.869554	473	36	43	476	5	12	475	6	7	450.9208	7.75437	18.68478	100.7
TAC2_100	TAC2	0.060573	653822	485	0.4	6.12	0.8	0.07090	0.75	0.072654	1.060454	1.5996	0.9	0.16462	0.8	0.60	0.04258	1.028613	943	31	39	982	15	26	968	11	12	842.5758	16.97657	35.74931	104.1
TAC2_101	TAC2	1.166438	136476	460	1.1	24.58	0.6	0.05216	0.99	0.261379	1.043072	0.2957	1.1	0.04088	0.6	0.35	0.013223	0.839505	257	46	53	258	3	7	262	5	5	265.4821	4.428245	10.9867	100.7
TAC2_102	TAC2	0.79273	99602	268	0.4	19.69	0.7	0.05552	1.12	0.077366	1.716771	0.3915	1.2	0.05107	0.7	0.42	0.01561	1.609225	389	50	50	321	4	9	334	7	7	312.9297	9.990339	21.56299	96.1
TAC2_103	TAC2	0.187728	267379	487	0.1	13.24	0.5	0.05590	0.82	0.028615	1.447399	0.5892	0.9	0.07587	0.5	0.39	0.021675	1.492025	424	37	45	471	5	12	469	7	7	433.2015	12.78451	20.7419	111.1
TAC2_104	TAC2	0.011883	287287	534	0.9	13.13	0.6	0.05688	0.94	0.193892	0.914193	0.6033	0.9	0.07637	0.6	0.26	0.022776	0.919969	474	42	49	474	5	12	478	7	8	455.1266	8.2808	19.05176	100.0

TAC2_106	TAC2	0.430058	194069	376	0.3	13.74	0.7	0.05643	1.09	0.063693	1.559017	0.5753	1.0	0.07298	0.7	0.23	0.021149	1.47558	456	49	55	454	6	12	460	8	8	422.8746	12.34873	20.17365	99.6
TAC2_107	TAC2	0.320248	283714	539	0.3	13.39	0.7	0.05649	1.00	0.075432	2.086304	0.5951	1.0	0.07520	0.7	0.25	0.02143	1.298705	465	46	53	467	6	12	473	7	8	428.4656	11.00988	19.55432	100.4
TAC2_108	TAC2	0.183979	124024	240	0.9	13.97	0.6	0.05680	1.10	0.192282	0.886973	0.5751	1.1	0.07196	0.6	0.28	0.021277	0.92999	443	50	56	448	5	11	460	8	9	425.4751	7.829282	17.85623	101.0
TAC2_109	TAC2	0.36883	413370	683	0.3	11.94	0.5	0.05685	0.62	0.057124	0.88105	0.6742	0.7	0.08411	0.5	0.51	0.023273	0.837906	480	27	37	520	5	13	522	6	7	464.9352	7.701997	19.14032	108.4
TAC2_110	TAC2	0.534756	119931	224	0.4	13.68	0.6	0.05618	1.07	0.083661	2.001308	0.5809	1.1	0.07341	0.6	0.25	0.021423	1.427478	432	50	57	457	5	12	463	8	9	428.262	12.0931	20.17516	105.6
TAC2_111	TAC2	0.122746	154482	211	1.3	10.00	0.5	0.06136	0.84	0.255422	0.823579	0.8655	0.9	0.10045	0.5	0.44	0.028158	0.863469	636	35	42	617	6	15	631	9	10	561.1344	9.556498	23.16157	97.1
TAC2_112	TAC2	0.405722	203959	365	0.7	13.45	0.6	0.05598	0.92	0.167486	2.234697	0.5881	1.0	0.07462	0.6	0.38	0.022925	1.013951	434	43	50	464	5	12	468	8	8	458.0385	9.183436	19.5556	106.8
TAC2_113	TAC2	1.100555	89320	121	0.7	10.30	0.6	0.06075	1.17	0.138685	1.231578	0.8302	1.2	0.09709	0.6	0.25	0.028271	1.226275	593	54	60	597	7	15	610	11	12	563.2505	13.62403	25.1823	100.7
TAC2_114	TAC2	0.190591	404066	412	0.3	7.88	0.5	0.06427	0.64	0.055177	2.392167	1.1413	0.6	0.12743	0.5	0.40	0.035407	0.965933	739	27	37	773	8	19	773	7	9	703.0183	13.33656	29.50605	104.6
TAC2_115	TAC2	0.647314	406854	232	0.4	5.13	1.0	0.07903	1.04	0.093926	1.252953	2.1200	1.1	0.19661	1.0	0.52	0.04927	1.537145	1159	42	47	1156	21	33	1153	15	16	971.5999	29.13941	46.41977	99.8
TAC2_116	TAC2	0.49609	598636	378	0.3	5.85	0.9	0.07348	0.86	0.072792	1.175024	1.7157	0.9	0.17203	1.0	0.59	0.048492	1.230655	1015	34	41	1023	18	29	1013	11	13	956.7217	22.934	42.28232	100.8
TAC2_117	TAC2	1.434456	260027	131	0.3	4.97	0.7	0.09024	0.75	0.103951	1.150891	2.5224	0.9	0.20278	0.7	0.55	0.072256	1.329303	1422	29	37	1190	15	30	1277	13	15	1413.185	35.23505	61.60177	83.6
TAC2_118	TAC2	0.103754	268241	337	0.1	12.25	0.5	0.06328	0.78	0.047061	1.991221	0.7137	0.8	0.08214	0.5	0.46	0.034419	1.326433	700	34	42	509	5	13	546	7	8	683.539	17.83817	31.22954	72.6
TAC2_119	TAC2	0.638946	346510	521	0.2	14.59	0.6	0.05962	0.79	0.043929	1.894265	0.5660	0.8	0.06880	0.6	0.32	0.016227	1.687896	580	36	44	429	5	11	455	6	7	325.239	10.88805	16.42356	74.0
TAC2_120	TAC2	1.226279	28029	28	1.8	9.59	0.8	0.06300	2.03	0.446443	1.536188	0.9164	2.0	0.10524	0.8	0.15	0.029274	1.184068	585	91	94	645	10	18	652	20	20	582.9455	13.60689	25.78828	110.2
TAC2_121	TAC2	-1.53878	42964	56	2.3	9.44	0.8	0.06230	1.66	0.446522	1.09554	0.9161	1.7	0.10669	0.8	0.27	0.030251	1.011728	630	68	68	654	10	18	655	16	16	602.1827	12.00041	38.42943	99.9
TAC2_122	TAC2	0.502169	314767	267	0.4	8.48	0.8	0.06573	0.72	0.110539	1.353966	1.0916	1.1	0.11920	0.8	0.75	0.040669	1.020503	784	30	38	727	11	20	746	11	12	805.3712	16.09566	34.09974	92.7
TAC2_123	TAC2	1.083661	116403	112	0.2	9.45	0.6	0.06960	0.87	0.064522	1.542769	1.0291	0.9	0.10662	0.6	0.35	0.042027	1.462814	895	37	44	653	7	16	717	9	10	831.2938	23.83304	39.14783	72.9
TAC2_124	TAC2	-0.01712	284670	397	0.2	13.27	0.6	0.05700	0.80	0.047062	1.079849	0.5987	0.8	0.07565	0.6	0.39	0.021478	1.142807	471	35	43	470	5	12	475	6	7	429.4108	9.70959	18.88345	99.8
TAC2_125	TAC2	0.272699	798072	637	0.2	7.58	0.5	0.06941	0.52	0.047092	0.948108	1.2782	0.6	0.13243	0.5	0.56	0.039453	0.93355	904	21	31	801	8	19	835	7	9	781.8162	14.31371	32.54326	88.7
TAC2_126	TAC2	0.053172	208135	277	1.0	12.18	0.6	0.05812	1.06	0.25946	0.96498	0.6649	1.0	0.08251	0.7	0.23	0.024776	0.872496	513	48	55	511	6	13	517	8	9	494.6089	8.525358	20.48395	99.7
TAC2_127	TAC2	0.520841	270858	416	0.1	13.62	0.8	0.05645	1.00	0.031435	1.768886	0.5783	1.1	0.07406	0.8	0.47	0.019596	2.281043	461	44	51	460	7	13	462	8	9	391.9923	17.75436	23.1374	99.8
TAC2_128	TAC2	2.421728	161079	323	0.5	16.24	2.8	0.06108	2.36	0.106923	14.90355	0.5266	2.4	0.06358	2.5	0.56	0.011019	9.495394	602	105	108	397	19	21	428	17	17	221.0123	41.60995	42.44012	65.9
TAC2_129	TAC2	0.177645	408508	803	0.1	12.95	1.7	0.05580	1.88	0.028958	4.013877	0.5848	2.0	0.07783	1.6	0.49	0.019302	3.441762	428	81	85	483	15	19	467	15	15	386.2807	26.31869	30.0856	112.9
TAC2_130	TAC2	0.583683	311706	587	0.2	13.22	1.0	0.05641	1.29	0.035155	1.975222	0.5839	1.4	0.07632	1.0	0.45	0.02059	2.314206	443	58	63	474	9	14	466	10	11	411.7396	18.86548	24.4413	107.0
TAC2_131	TAC2	0.321199	280281	237	0.6	6.17	0.6	0.07159	0.72	0.119898	0.932541	1.5900	0.9	0.16284	0.7	0.57	0.045736	1.169612	968	30	38	972	12	24	965	11	12	903.4419	20.66452	39.51466	100.5

LA-ICP-MS RUN 16.03.2022						Data for Tera-Wasserburg plot						Data for Wetherill plot							Dates												
ID	Note	f206c	^{206}Pb	Uppm	Th/U	$^{238}U/^{206}Pb$	1s%	$^{207}Pb/^{206}Pb$	1s%	$^{208}Pb/^{206}Pb$	1s%	$^{207}Pb/^{235}U$	1s%	$^{206}Pb/^{238}U$	1s%	Rho	$^{208}Pb/^{232}Th$	1s%	$^{207}Pb/^{206}Pb$	2s (abs)	2ssys (abs)	$^{206}Pb/^{238}U$	2s (abs)	2ssys (abs)	$^{207}Pb/^{235}U$	2s (abs)	2ssys (abs)	$^{208}Pb/^{232}Th$	2s (abs)	2ssys (abs)	% conc
915_3	Z_91500	1.901209	122997	77	0.5	5.60	0.5	0.07595	1.12	0.111043	1.576221	1.8916	1.1	0.17907	0.5	0.23	0.050754	1.499805	1086	48	53	1062	10	25	1078	16	17	1000.197	29.21253	47.2435	98.5
915_4	Z_91500	1.296405	128006	79	0.5	5.64	0.5	0.07562	1.27	0.108821	1.561477	1.8702	1.3	0.17759	0.5	0.16	0.050053	1.553986	1062	51	55	1054	9	25	1067	17	18	986.5905	29.91316	47.33998	98.7
915_5	Z_91500	0.730065	123907	85	0.5	5.64	0.5	0.07415	1.08	0.112716	1.464332	1.8303	1.1	0.17764	0.5	0.24	0.051819	1.407074	1035	43	48	1054	10	25	1054	14	16	1020.635	28.00562	47.15597	100.0
915_6	Z_91500	1.798511	122328	85	0.5	5.64	0.5	0.07540	1.36	0.11206	1.35448	1.8630	1.4	0.17763	0.5	0.21	0.052056	1.490409	1056	57	62	1054	10	25	1064	18	19	1025.207	29.81197	48.39898	99.0
915_7	Z_91500	1.255572	126085	81	0.6	5.62	0.5	0.07471	1.01	0.110724	1.356203	1.8415	0.9	0.17812	0.5	0.11	0.050665	1.361294	1049	42	48	1056	10	25	1060	13	14	998.4158	26.52262	45.6371	99.7
915_8	Z_91500	0.368762	121607	78	0.5	5.60	0.5	0.07420	1.09	0.108918	1.419856	1.8354	1.0	0.17889	0.5	0.17	0.050256	1.446143	1041	41	47	1061	9	25	1059	14	15	990.4975	27.95277	46.24831	100.1
915_9	Z_91500	0.988303	124317	83	0.6	5.62	0.5	0.07562	1.16	0.110842	1.447834	1.8703	1.1	0.17811	0.6	0.10	0.049582	1.461421	1074	44	49	1056	11	25	1070	14	15	977.6126	27.89028	45.83952	98.7
915_10	Z_91500	1.393291	117543	80	0.6	5.62	0.6	0.07585	1.59	0.111848	1.507656	1.8761	1.5	0.17830	0.6	0.05	0.051394	1.453089	1067	64	68	1057	12	26	1069	20	21	1012.611	28.72252	47.37885	98.9
915_11	Z_91500	0.539077	118983	74	0.5	5.60	0.5	0.07465	1.24	0.10565	1.757361	1.8607	1.3	0.17862	0.5	0.35	0.048932	1.836679	1038	51	55	1061	10	26	1064	18	19	964.8476	34.60685	49.87605	99.7
915_12	Z_91500	0.917289	117023	72	0.6	5.62	0.5	0.07520	1.44	0.112684	1.644062	1.8758	1.5	0.17842	0.5	0.27	0.052034	1.696011	1052	60	65	1058	10	25	1069	20	21	1024.753	33.90685	51.00923	99.0
915_13	Z_91500	0.450253	122741	79	0.6	5.60	0.5	0.07619	1.34	0.107679	1.292274	1.8850	1.3	0.17857	0.5	0.00	0.048787	1.26425	1080	55	59	1060	10	26	1072	17	18	962.4079	23.75147	42.97167	98.9
915_14	Z_91500	1.006004	125164	80	0.6	5.59	0.5	0.07533	1.27	0.112112	1.575966	1.8791	1.3	0.17943	0.5	0.23	0.05139	1.537543	1063	50	55	1064	9	25	1070	17	18	1012.31	30.37372	48.37949	99.4
915_15	Z_91500	1.318666	123185	74	0.5	5.63	0.6	0.07412	1.21	0.108732	1.567277	1.8355	1.2	0.17831	0.6	0.20	0.049558	1.624427	1025	49	54	1058	11	26	1055	15	17	977.0685	30.97147	47.75031	100.2
915_16	Z_91500	-0.22016	118779	70	0.5	5.59	0.6	0.07311	1.65	0.111623	2.4008	1.8230	1.7	0.17924	0.6	0.21	0.051724	2.358016	997	66	70	1063	12	26	1051	22	23	1018.615	46.92419	60.3391	101.1
915_17	Z_91500	1.57344	123773	80	0.5	5.64	0.5	0.07495	1.20	0.113157	1.476611	1.8408	1.1	0.17791	0.5	0.07	0.050813	1.481617	1046	49	54	1055	10	25	1057	15	16	1001.256	28.9217	47.1276	99.8
915_18	Z_91500	-0.24864	125644	82	0.5	5.58	0.4	0.07377	1.06	0.109857	1.338106	1.8247	1.1	0.17904	0.5	0.24	0.049628	1.387282	1024	43	49	1062	9	25	1054	14	15	978.5172	26.52799	45.0821	100.7
915_19	Z_91500	1.232877	123741	84	0.6	5.64	0.5	0.07539	1.54	0.109805	1.716423	1.8587	1.5	0.17733	0.5	0.16	0.05001	1.78502	1051	62	66	1052	10	25	1062	20	21	985.6981	34.35907	50.2675	99.1
915_20	Z_91500	1.380666	113451	78	0.6	5.64	0.5	0.07430	1.24	0.108003	1.615969	1.8355	1.2	0.17770	0.5	0.09	0.049545	1.55246	1036	52	57	1054	9	25	1057	16	18	976.8509	29.62389	46.91091	99.7
915_21	Z_91500	0.376904	114280	79	0.5	5.61	0.6	0.07520	1.41	0.110962	1.618859	1.8521	1.3	0.17841	0.6	0.08	0.050908	1.652747	1058	55	59	1058	11	26	1063	17	18	1003.015	32.35502	49.39034	99.5
915_22	Z_91500	0.167061	116362	82	0.5	5.65	0.5	0.07522	1.06	0.109525	1.407151	1.8363	1.0	0.17741	0.5	0.13	0.049763	1.469358	1055	43	49	1053	9	25	1058	13	15	980.9835	28.13347	46.08253	99.5
915_23	Z_91500	1.441473	113605	71	0.5	5.61	0.6	0.07569	1.32	0.107807	1.827702	1.8590	1.2	0.17856	0.6	0.16	0.049512	1.829528	1069	53	57	1059	11	26	1064	16	17	976.1809	34.87373	50.36298	99.5
915_24	Z_91500	1.089471	112901	70	0.5	5.61	0.5	0.07529	1.36	0.11059	1.744666	1.8550	1.3	0.17864	0.5	0.08	0.051558	1.618511	1051	57	61	1059	10	25	1062	18	19	1015.518	32.04192	49.50503	99.8
915_25	Z_91500	1.599431	119240	86	0.5	5.59	0.5	0.07394	1.34	0.111074	1.597161	1.8237	1.3	0.17942	0.5	0.17	0.051544	1.646621	1019	57	61	1064	10	25	1051	18	19	1015.319	32.60316	49.87453	101.2
915_27	Z_91500	1.027776	123025	88	0.5	5.59	0.5	0.07502	1.05	0.109677	1.331739	1.8523	1.1	0.17934	0.5	0.27	0.050178	1.303761	1056	41	46	1063	9	25	1061	14	15	989.1102	25.13805	44.52845	100.2
915_28	Z_91500	1.860416	115285	80	0.5	5.57	0.8	0.07450	1.52	0.110172	1.645475	1.8517	1.5	0.17965	0.7	0.25	0.051268	1.70115	1042	59	63	1065	14	27	1060	20	21	1010.032	33.48785	50.29464	100.4
GJ1_0	Z_GJ1	1.679163	255294	290	0.0	10.21	0.3	0.06070	0.71	0.008155	3.167721	0.8193	0.7	0.09805	0.3	0.09	0.031913	2.68674	623	30	39	603	3	14	607	6	8	633.5342	33.51416	41.09218	99.4
GJ1_1	Z_GJ1	1.313653	240121	286	0.0	10.29	0.3	0.06077	0.68	0.00784	3.007949	0.8188	0.7	0.09732	0.3	0.20	0.029466	2.894788	623	28	37	599	3	14	606	6	8	585.5657	33.43376	40.03144	98.7
GJ1_2	Z_GJ1	1.505996	240793	288	0.0	10.20	0.2	0.05896	0.67	0.007873	3.023016	0.8064	0.7	0.09816	0.2	0.14	0.030318	2.788546	554	29	38	604	3	14	600	6	7	602.329	33.06867	40.05654	100.7

GJ1_3	Z_GJ1	1.372475	234004	287	0.0	10.25	0.3	0.05958	0.70	0.007684	2.66827	0.8056	0.7	0.09770	0.3	0.30	0.030999	2.704113	579	32	41	601	3	14	600	7	8	615.6925	32.82479	40.16054	100.2
GJ1_4	Z_GJ1	1.084851	239766	287	0.0	10.22	0.2	0.06042	0.69	0.008034	3.074742	0.8194	0.6	0.09795	0.2	0.07	0.030801	2.83944	604	30	39	602	3	14	607	6	7	611.6885	34.21012	41.2041	99.2
GJ1_5	Z_GJ1	1.249175	241804	288	0.0	10.24	0.3	0.06009	0.69	0.007783	2.633779	0.8118	0.7	0.09782	0.3	0.17	0.031108	2.597718	594	31	40	602	3	14	603	6	7	617.9144	31.6619	39.2717	99.8
GJ1_6	Z_GJ1	1.124406	233231	287	0.0	10.23	0.3	0.06054	0.65	0.007741	2.931069	0.8181	0.6	0.09788	0.3	0.17	0.030786	2.853465	609	28	37	602	3	14	607	6	7	615.4273	35.20828	42.34153	99.2
GJ1_7	Z_GJ1	1.846432	241060	288	0.0	10.23	0.3	0.06061	0.72	0.00757	2.897429	0.8205	0.7	0.09789	0.3	0.14	0.03024	2.74856	609	31	39	602	3	14	607	6	8	600.8294	32.54882	39.61038	99.1
GJ1_8	Z_GJ1	1.496457	238320	286	0.0	10.23	0.3	0.06052	0.70	0.007632	2.72846	0.8198	0.7	0.09781	0.3	0.20	0.031071	2.727694	607	30	39	602	3	14	607	6	8	617.0553	33.18735	40.48822	99.1
GJ1_9	Z_GJ1	1.310837	252525	288	0.0	10.22	0.3	0.06052	0.74	0.008016	2.621418	0.8257	0.7	0.09788	0.3	0.05	0.030515	2.439791	608	33	42	602	3	14	610	7	8	606.483	29.16184	37.0073	98.7
GJ1_10	Z_GJ1	1.503518	240496	286	0.0	10.24	0.3	0.05967	0.68	0.007635	3.090281	0.8107	0.7	0.09783	0.3	0.13	0.030481	3.063882	577	29	38	602	3	14	602	6	7	605.2769	36.53562	43.02926	100.0
GJ1_11	Z_GJ1	1.376238	240467	287	0.0	10.25	0.3	0.05975	0.71	0.007553	2.941823	0.8047	0.7	0.09776	0.3	0.30	0.029661	2.817157	588	30	39	601	3	14	599	6	8	589.4447	32.73531	39.52501	100.3
GJ1_12	Z_GJ1	1.39505	244354	287	0.0	10.23	0.3	0.05985	0.69	0.007424	2.785559	0.8106	0.7	0.09793	0.3	0.10	0.030064	2.813872	583	30	39	602	3	14	602	6	7	597.3249	33.17118	40.06591	100.1
GJ1_13	Z_GJ1	1.680759	249386	287	0.0	10.21	0.3	0.06001	0.66	0.008124	2.835772	0.8201	0.7	0.09806	0.3	0.24	0.032476	2.71646	590	29	38	603	4	14	607	6	7	644.5034	34.43263	42.06431	99.3
GJ1_14	Z_GJ1	1.712066	243610	287	0.0	10.25	0.3	0.06009	0.59	0.007415	2.856921	0.8144	0.6	0.09766	0.3	0.24	0.029934	2.795734	610	25	35	601	3	14	605	5	7	594.801	32.7856	39.68122	99.3
GJ1_15	Z_GJ1	1.218105	251244	287	0.0	10.23	0.3	0.05968	0.67	0.007731	2.765996	0.8116	0.7	0.09791	0.3	0.24	0.031651	2.868847	581	29	37	602	3	14	602	6	7	628.2479	35.48131	42.59954	100.0
GJ1_16	Z_GJ1	0.87268	253022	287	0.0	10.24	0.3	0.06023	0.66	0.007847	2.607531	0.8165	0.6	0.09780	0.3	0.16	0.031134	2.601817	598	28	37	601	3	14	605	6	7	618.4377	31.69077	39.28582	99.4
GJ1_17	Z_GJ1	1.761374	252102	288	0.0	10.23	0.3	0.06009	0.66	0.00804	2.592496	0.8128	0.6	0.09789	0.3	0.13	0.032145	2.64022	596	29	38	602	3	14	603	6	7	638.1025	33.20488	40.95467	99.8
GJ1_18	Z_GJ1	1.10094	243292	286	0.0	10.23	0.3	0.06069	0.71	0.007871	2.94608	0.8192	0.7	0.09781	0.3	0.15	0.031186	2.909888	612	31	40	602	4	14	607	6	8	619.1265	35.51272	42.45404	99.2
GJ1_19	Z_GJ1	1.395038	240553	288	0.0	10.23	0.3	0.05995	0.71	0.007333	2.861056	0.8140	0.7	0.09787	0.3	0.00	0.028942	2.713796	589	31	40	602	3	14	604	6	7	575.4885	30.78415	37.61947	99.6
GJ1_20	Z_GJ1	1.194773	232927	287	0.0	10.24	0.3	0.06049	0.76	0.007963	2.577991	0.8189	0.7	0.09784	0.3	0.03	0.031937	2.560741	602	33	41	602	3	14	607	7	8	634.1402	31.9881	39.87777	99.1
GJ1_21	Z_GJ1	1.399092	232906	287	0.0	10.22	0.3	0.06030	0.68	0.007539	2.912524	0.8137	0.7	0.09789	0.3	0.22	0.030046	2.778431	603	29	37	602	3	14	604	6	8	597.0163	32.73827	39.7024	99.8
GJ1_22	Z_GJ1	0.856061	228097	287	0.0	10.22	0.3	0.06027	0.68	0.008065	2.944401	0.8121	0.7	0.09781	0.3	0.13	0.031587	2.90935	598	30	39	602	3	14	603	6	7	626.9462	35.89474	42.91311	99.8
GJ1_23	Z_GJ1	1.460751	230382	287	0.0	10.20	0.3	0.05950	0.67	0.007775	3.035399	0.8157	0.7	0.09811	0.3	0.22	0.030159	2.749433	577	29	38	603	3	14	605	6	8	603.3943	33.41406	40.65926	99.8
GJ1_24	Z_GJ1	1.143659	235005	287	0.0	10.26	0.3	0.06058	0.69	0.008049	2.559551	0.8182	0.7	0.09762	0.3	0.19	0.031218	2.610272	609	30	39	600	3	14	606	6	8	620.0714	31.87423	39.46861	99.1
GJ1_25	Z_GJ1	1.155593	235001	287	0.0	10.21	0.3	0.06004	0.72	0.007677	2.651846	0.8159	0.8	0.09808	0.3	0.30	0.030093	2.626858	588	32	40	603	3	14	605	7	8	598.0694	30.98988	38.28936	99.8
GJ1_26	Z_GJ1	0.889472	222628	287	0.0	10.26	0.3	0.06088	0.72	0.007845	2.824915	0.8189	0.7	0.09759	0.3	0.04	0.031431	2.828146	625	32	40	600	3	14	606	6	8	623.9845	34.73195	41.88467	99.0
GJ1_27	Z_GJ1	1.203516	231084	287	0.0	10.23	0.3	0.05936	0.69	0.007549	2.82748	0.8046	0.7	0.09787	0.3	0.20	0.030727	2.880194	571	31	40	602	3	14	599	6	8	610.201	34.63863	41.53786	100.5
GJ1_28	Z_GJ1	1.06855	232462	287	0.0	10.23	0.3	0.05998	0.71	0.007511	2.901798	0.8122	0.7	0.09787	0.3	0.12	0.031013	2.879567	590	30	39	602	3	14	603	6	8	615.7767	34.96084	41.92703	99.9
GJ1_29	Z_GJ1	1.308531	233947	287	0.0	10.24	0.3	0.06066	0.75	0.007445	2.972078	0.8244	0.8	0.09783	0.3	0.16	0.030001	2.853601	613	32	40	602	3	14	609	7	8	596.0583	33.53969	40.3344	98.7
Ples_3	Z_Pleso-vice	1.038682	364107	908	0.1	18.64	0.8	0.05362	0.98	0.030198	1.961158	0.3934	0.9	0.05395	0.7	0.44	0.013423	2.790867	339	44	51	339	5	9	337	5	6	269.3543	14.99109	18.15403	100.4
Ples_4	Z_Pleso-vice	0.165276	360091	819	0.2	18.32	0.7	0.05338	1.28	0.03167	2.062639	0.3985	1.3	0.05476	0.7	0.27	0.013464	4.379337	327	58	64	344	5	9	340	7	8	270.0927	23.57689	25.71355	101.0
Ples_5	Z_Pleso-vice	0.293498	411836	1001	0.2	18.35	0.6	0.05283	0.75	0.034316	1.3768	0.3968	0.8	0.05447	0.6	0.47	0.014194	1.632332	317	35	44	343	4	8	339	5	5	284.8277	9.232447	14.19377	101.0

Ples_6	Z_Plesovice	0.373016	420400	904	0.2	18.41	0.6	0.05260	0.90	0.032497	1.488755	0.3962	0.8	0.05447	0.6	0.25	0.013726	1.687502	300	41	48	342	4	9	339	5	5	275.4934	9.236652	13.93449	100.9
Ples_7	Z_Plesovice	0.09873	344655	802	0.1	18.31	0.7	0.05335	1.14	0.029488	2.087146	0.3978	1.2	0.05467	0.7	0.29	0.014396	2.250985	327	52	58	343	5	9	340	7	7	288.8169	12.90414	16.90929	101.0
Ples_8	Z_Plesovice	0.339713	338022	704	0.1	18.43	0.7	0.05293	1.04	0.030672	1.808177	0.3959	1.0	0.05449	0.7	0.22	0.015102	1.942992	308	47	53	342	4	9	338	6	6	302.8742	11.67585	16.35642	101.1
Ples_9	Z_Plesovice	0.072291	306712	725	0.1	18.35	0.7	0.05282	1.02	0.027774	1.960596	0.3942	1.0	0.05471	0.7	0.30	0.014492	2.404674	307	47	54	343	5	9	337	6	6	290.7235	13.86724	17.69571	101.8
Ples_10	Z_Plesovice	0.662777	347463	866	0.1	18.47	0.7	0.05296	1.03	0.030015	2.036571	0.3940	1.1	0.05425	0.7	0.40	0.014509	3.356477	312	46	53	341	5	9	337	6	7	290.9498	19.45179	22.3698	101.1
Ples_11	Z_Plesovice	-0.12977	405984	1036	0.2	18.42	0.9	0.05340	1.13	0.031138	1.863444	0.3989	1.2	0.05462	0.9	0.41	0.012969	2.650358	328	51	57	343	6	10	340	7	7	260.3596	13.75716	16.94581	100.7
Ples_12	Z_Plesovice	0.196293	349794	769	0.1	18.40	1.1	0.05343	1.23	0.031225	2.193407	0.3965	1.4	0.05471	1.0	0.50	0.013811	5.054126	331	58	64	343	7	11	339	8	8	276.969	27.89091	29.80867	101.4
Ples_14	Z_Plesovice	0.41479	341415	828	0.1	18.32	0.6	0.05262	1.00	0.029747	1.834155	0.3944	1.0	0.05469	0.6	0.25	0.014958	1.641144	293	46	53	344	4	9	337	6	6	300.0366	9.771352	14.97645	102.0
BB16_1	BB16	0.963799	229377	298	0.4	11.00	0.5	0.05751	1.11	0.074844	1.40196	0.7420	1.0	0.09106	0.5	0.05	0.026354	1.318567	495	49	54	562	5	14	563	9	10	525.6803	13.68304	24.05234	99.8
BB16_2	BB16	0.223079	227288	279	0.3	10.99	0.3	0.05872	0.69	0.073977	0.917992	0.7406	0.7	0.09121	0.3	0.28	0.0254	1.003583	539	30	39	563	3	13	562	6	7	506.8358	10.04137	21.55207	100.1
BB16_3	BB16	0.188129	263662	376	0.4	11.00	0.4	0.05917	0.74	0.076808	0.871009	0.7446	0.7	0.09104	0.4	0.27	0.025404	0.956552	562	31	39	562	4	13	564	6	8	506.9412	9.578441	21.35336	99.6
BB16_4	BB16	0.27063	217334	272	0.3	11.01	0.4	0.05921	0.63	0.072685	0.955795	0.7447	0.7	0.09103	0.3	0.35	0.025192	0.978714	563	28	37	562	4	13	565	6	7	502.7435	9.72051	21.28018	99.4
BB16_5	BB16	0.109737	249101	356	0.4	10.98	0.3	0.05864	0.69	0.075462	0.918454	0.7383	0.7	0.09122	0.3	0.21	0.025052	0.989089	547	31	39	563	3	13	560	6	7	499.996	9.769256	21.20985	100.4
BB16_7	BB16	0.257657	277274	377	0.4	10.96	0.4	0.05917	0.76	0.073676	0.903094	0.7400	0.8	0.09127	0.4	0.33	0.02416	1.010329	556	34	42	563	5	14	561	7	8	482.4156	9.628147	20.55821	100.3
BB16_8	BB16	-0.41953	247381	281	0.3	10.95	0.4	0.05863	0.84	0.075184	1.060978	0.7445	0.8	0.09133	0.4	0.23	0.025774	1.088815	538	37	44	563	4	13	564	7	8	514.2537	11.06009	22.29877	99.9
BB16_9	BB16	0.270552	292969	404	0.4	10.92	0.5	0.05839	0.84	0.074649	1.035354	0.7352	0.8	0.09173	0.5	0.27	0.024061	1.159979	532	38	45	566	5	14	559	7	8	483.0714	12.12968	23.33318	101.3
BB16_10	BB16	0.239314	257193	368	0.4	11.03	0.4	0.05859	0.65	0.075561	0.926268	0.7364	0.7	0.09095	0.4	0.37	0.025101	1.03805	540	29	39	561	4	13	560	6	7	500.946	10.2734	21.48164	100.2
BB16_11	BB16	-0.03278	232410	339	0.4	10.99	0.3	0.05865	0.76	0.075744	1.005616	0.7390	0.7	0.09104	0.3	0.17	0.025458	1.060492	536	33	41	562	4	13	561	6	8	507.9782	10.64037	21.88673	100.1
BB16_12	BB16	0.269063	264564	319	0.3	10.98	0.3	0.05897	0.60	0.076233	0.806215	0.7362	0.6	0.09118	0.4	0.40	0.025196	0.863321	553	26	36	562	4	13	559	5	7	502.8492	8.573159	20.78147	100.6
BB16_13	BB16	0.286466	293056	463	0.4	10.89	0.5	0.05873	0.83	0.074976	0.940768	0.7346	0.9	0.09188	0.5	0.37	0.024334	1.067093	540	36	44	567	5	14	558	7	9	485.8492	10.24369	20.97168	101.5

LA-ICP-MS RUN 06.04.2022						Data for Tera-Wasserburg plot						Data for Wetherill plot							Dates												
ID	Note	f206c	^{206}Pb	Uppm	Th/U	^{238}U/^{206}Pb	1s%	^{207}Pb/^{206}Pb	1s%	^{208}Pb/^{206}Pb	1s%	^{207}Pb/^{235}U	1s%	^{206}Pb/^{238}U	1s%	Rho	^{208}Pb/^{232}Th	1s%	^{207}Pb/ ^{206}Pb	2s (abs)	2ssys (abs)	^{206}Pb/ ^{238}U	2s (abs)	2ssys (abs)	^{207}Pb/ ^{235}U	2s (abs)	2ssys (abs)	^{208}Pb/^{232}Th	2s (abs)	2ssys (abs)	% conc
915_1	Z_91500	0.922756	120158	74	0.5	5.58	0.4	0.07511	0.92	0.101448	1.050534	1.8717	0.9	0.17991	0.4	0.18	0.047783	1.0675	1045	37	37	1066	8	20	1068	12	12	942.8952	19.66232	35.63079	99.8
915_2	Z_91500	1.025909	115151	68	0.5	5.56	0.5	0.07535	0.86	0.100237	1.149063	1.8901	0.8	0.18072	0.4	0.28	0.047784	1.202939	1055	35	35	1071	9	20	1074	11	11	942.7617	22.16542	37.07998	99.7
915_3	Z_91500	0.098208	137985	94	0.5	5.55	0.6	0.07439	1.11	0.102755	1.537319	1.8637	1.2	0.18075	0.6	0.28	0.046829	1.474979	1037	47	47	1071	12	22	1067	16	16	924.5048	26.6801	39.53938	100.4
915_4	Z_91500	1.249591	121271	83	0.5	5.59	0.4	0.07532	0.94	0.104696	1.067682	1.8755	0.9	0.17964	0.4	0.19	0.048444	1.098484	1055	37	37	1065	9	20	1069	12	12	955.6269	20.48708	36.40026	99.6
915_5	Z_91500	0.90297	127314	83	0.5	5.56	0.5	0.07366	0.92	0.103083	1.138493	1.8390	0.9	0.18007	0.5	0.25	0.048456	1.207386	1009	39	39	1067	10	21	1056	12	12	955.7992	22.54274	37.62198	101.0
915_6	Z_91500	1.890951	123370	81	0.5	5.56	0.4	0.07561	0.83	0.105675	1.08281	1.8894	0.8	0.18031	0.4	0.20	0.049053	1.158654	1070	33	33	1068	7	20	1076	11	11	967.2684	21.87061	37.49149	99.3
915_7	Z_91500	1.32513	117953	78	0.5	5.58	0.4	0.07593	0.94	0.101054	1.184492	1.8938	0.9	0.17956	0.4	0.21	0.048298	1.19856	1078	38	38	1064	8	20	1075	13	13	955.1564	22.76315	38.16934	99.0

915_8	Z_91500	0.219386	116615	77	0.5	5.57	0.4	0.07563	0.87	0.10286	1.098821	1.8772	0.8	0.17986	0.4	0.17	0.049454	1.11062	1063	35	35	1066	7	20	1071	11	11	977.2331	21.54893	38.00156	99.5
915_9	Z_91500	0.906825	118612	79	0.5	5.59	0.4	0.07557	1.10	0.102663	1.165312	1.8667	1.0	0.17917	0.4	0.02	0.049731	1.194198	1060	46	46	1063	8	20	1068	14	14	980.3454	22.84901	38.40355	99.6
915_10	Z_91500	-0.30403	115498	79	0.5	5.58	0.4	0.07505	0.81	0.101092	1.15443	1.8683	0.8	0.17967	0.4	0.17	0.049197	1.153724	1048	33	33	1065	8	20	1067	10	10	970.0056	21.83428	37.53476	99.8
915_11	Z_91500	0.494093	124676	80	0.5	5.57	0.4	0.07500	0.85	0.102314	1.017541	1.8568	0.9	0.17967	0.4	0.24	0.049596	1.100453	1053	35	35	1065	8	20	1063	12	12	977.761	21.00832	37.28077	100.1
915_12	Z_91500	0.300847	119102	76	0.5	5.60	0.4	0.07578	0.89	0.101158	1.044208	1.8713	0.9	0.17911	0.4	0.17	0.0489	1.098522	1065	36	36	1062	7	19	1067	12	12	964.3845	20.69305	36.76533	99.5
915_13	Z_91500	1.194459	121131	77	0.5	5.57	0.4	0.07551	0.87	0.101016	1.06352	1.8714	0.8	0.17988	0.4	0.09	0.048818	1.142458	1063	36	36	1066	8	20	1069	11	11	962.7792	21.48477	37.17533	99.7
915_14	Z_91500	-0.5095	116269	74	0.5	5.57	0.4	0.07535	0.95	0.103222	1.233372	1.8663	0.9	0.18008	0.4	0.13	0.04947	1.211319	1059	39	39	1067	8	20	1066	12	12	975.2446	23.04728	38.38401	100.1
915_15	Z_91500	1.284871	119143	73	0.5	5.57	0.4	0.07516	0.86	0.101261	1.12031	1.8613	0.8	0.18014	0.4	0.16	0.048535	1.11537	1050	35	35	1067	8	20	1064	11	11	957.3294	20.84821	36.65966	100.3
915_16	Z_91500	0.572297	118662	72	0.5	5.56	0.4	0.07528	0.82	0.107742	1.052919	1.8713	0.8	0.18017	0.4	0.22	0.050775	1.135811	1059	33	33	1068	8	20	1068	11	11	1000.379	22.19208	38.549	100.0
915_17	Z_91500	0.607755	117427	70	0.5	5.60	0.5	0.07542	0.88	0.101515	1.185542	1.8688	0.9	0.17934	0.5	0.31	0.048702	1.16712	1064	35	35	1063	9	20	1066	12	12	960.5244	21.88976	37.34497	99.7
915_18	Z_91500	0.285285	120918	68	0.5	5.56	0.5	0.07453	0.93	0.100988	1.094129	1.8501	0.9	0.18017	0.5	0.27	0.049871	1.065319	1032	38	38	1068	9	20	1060	12	12	983.1655	20.44479	37.10146	100.7
915_19	Z_91500	0.786816	123730	81	0.5	5.57	0.5	0.07516	1.02	0.103024	1.402212	1.8712	0.9	0.18024	0.5	0.11	0.049917	1.297526	1054	41	41	1068	9	21	1068	12	12	983.9204	24.896	39.72334	100.0
915_20 (1)	Z_91500	1.598718	119723	78	0.5	5.60	0.4	0.07544	0.84	0.101314	0.960226	1.8646	0.8	0.17928	0.4	0.22	0.049467	1.024736	1062	34	34	1063	8	20	1066	11	11	975.3809	19.52051	36.40681	99.6
915_21	Z_91500	1.184255	122511	88	0.5	5.57	0.5	0.07566	0.88	0.100854	1.135476	1.8879	0.8	0.17999	0.4	0.12	0.048809	1.204716	1064	36	36	1067	9	20	1074	11	11	962.5557	22.6507	37.85585	99.3
915_22 (1)	Z_91500	1.610093	121379	91	0.5	5.56	0.5	0.07400	0.96	0.101207	1.159502	1.8477	0.9	0.18049	0.4	0.11	0.048773	1.236116	1020	39	39	1069	9	20	1059	12	12	961.8458	23.20673	38.15558	101.0
915_23	Z_91500	1.906004	122493	77	0.5	5.55	0.4	0.07564	0.89	0.102767	1.074521	1.8950	0.8	0.18066	0.4	0.14	0.048539	1.094012	1063	36	36	1070	8	20	1076	11	11	957.4789	20.44873	36.43365	99.5
915_24 (1)	Z_91500	1.342299	114508	69	0.5	5.55	0.4	0.07429	0.82	0.103229	1.034451	1.8646	0.8	0.18039	0.4	0.28	0.05009	1.043739	1031	34	34	1069	9	20	1066	11	11	987.3199	20.11329	37.02702	100.2
915_26 (1)	Z_91500	0.582807	123726	92	0.5	5.58	0.5	0.07571	1.00	0.105045	1.206182	1.8968	1.1	0.17964	0.5	0.31	0.050826	1.264218	1076	41	41	1065	10	21	1076	14	14	1001.458	24.71362	40.06642	99.0
GJ1_1	Z_GJ1	1.666645	251383	287	0.0	10.24	0.3	0.05966	0.61	0.008158	2.699308	0.8102	0.6	0.09772	0.3	0.24	0.031549	2.627895	586	26	26	601	3	11	603	6	6	626.304	32.44182	38.06716	99.7
GJ1_2	Z_GJ1	1.478479	241460	286	0.0	10.25	0.3	0.06001	0.83	0.007738	3.640028	0.8156	0.9	0.09771	0.3	0.28	0.028933	3.230228	595	36	36	601	4	11	604	8	8	575.2166	36.61167	40.92361	99.4
GJ1_3	Z_GJ1	1.21715	244831	287	0.0	10.22	0.3	0.06037	0.70	0.008054	3.723458	0.8201	0.7	0.09800	0.3	0.14	0.030389	2.567936	604	30	30	603	4	11	607	6	6	603.9102	30.54377	36.07097	99.3
GJ1_4	Z_GJ1	0.916254	249201	287	0.0	10.22	0.3	0.05989	0.76	0.008739	5.31706	0.8116	0.7	0.09803	0.3	0.22	0.031671	3.227173	582	34	34	603	4	11	604	7	7	628.3172	39.74901	44.43884	99.8
GJ1_5	Z_GJ1	1.078043	242457	287	0.0	10.22	0.3	0.06050	0.66	0.00797	2.741421	0.8207	0.7	0.09798	0.3	0.18	0.030748	2.731286	607	29	29	603	3	11	607	6	6	610.7257	32.84196	38.14295	99.2
GJ1_6	Z_GJ1	1.675652	245614	287	0.0	10.21	0.3	0.05997	0.66	0.008017	2.795265	0.8162	0.6	0.09796	0.3	0.16	0.031275	2.801167	588	29	29	602	3	11	605	6	6	620.871	34.2662	39.54268	99.6
GJ1_7	Z_GJ1	1.237515	241658	287	0.0	10.25	0.2	0.05975	0.66	0.008168	2.589227	0.8101	0.7	0.09765	0.3	0.14	0.03166	2.512746	582	29	29	601	3	11	602	6	6	628.6406	31.08578	36.94103	99.8
GJ1_9	Z_GJ1	1.292632	234939	287	0.0	10.23	0.3	0.06026	0.65	0.007966	3.240039	0.8182	0.7	0.09786	0.3	0.18	0.030418	2.715568	598	28	28	602	3	11	607	6	6	604.1579	32.30903	37.58029	99.2
GJ1_10	Z_GJ1	1.589756	234673	287	0.0	10.25	0.3	0.05984	0.69	0.007787	4.589226	0.8123	0.7	0.09774	0.3	0.09	0.029157	2.889043	584	31	31	601	3	11	603	6	6	579.4234	32.91969	37.70434	99.7
GJ1_11	Z_GJ1	0.76326	233296	287	0.0	10.23	0.3	0.05999	0.69	0.00824	2.794871	0.8135	0.6	0.09793	0.3	0.12	0.031783	2.71317	594	30	30	602	3	11	604	6	6	634.3795	34.37198	39.98903	99.7
GJ1_12	Z_GJ1	1.799083	242409	287	0.0	10.22	0.2	0.06051	0.66	0.008078	3.01653	0.8169	0.6	0.09794	0.2	0.14	0.030286	2.849807	607	28	28	602	3	11	606	6	6	601.5435	33.75113	38.7838	99.4
GJ1_14	Z_GJ1	0.975983	252810	287	0.0	10.20	0.2	0.06068	0.71	0.007607	3.056247	0.8198	0.7	0.09804	0.2	0.17	0.030499	3.046336	617	30	30	603	3	11	607	6	6	605.6825	36.34692	41.12895	99.3

GJ1_15	Z_GJ1	1.455725	249861	287	0.0	10.24	0.3	0.06061	0.68	0.007657	3.036008	0.8150	0.6	0.09781	0.3	0.13	0.029834	2.7307	610	30	30	602	3	11	604	6	6	592.8859	31.91366	37.06688	99.5
GJ1_16	Z_GJ1	1.286722	247552	287	0.0	10.28	0.3	0.06023	0.67	0.007493	2.666156	0.8112	0.7	0.09742	0.3	0.11	0.030327	2.686612	607	30	30	599	3	11	602	6	6	602.6062	31.92454	37.23789	99.5
GJ1_17	Z_GJ1	0.934233	253565	287	0.0	10.23	0.3	0.06018	0.67	0.007827	2.628973	0.8123	0.7	0.09794	0.3	0.17	0.031366	2.580383	595	30	30	602	3	11	603	6	6	622.934	31.68271	37.36503	99.9
GJ1_18	Z_GJ1	1.21846	237732	287	0.0	10.23	0.3	0.06037	0.82	0.007843	3.325173	0.8157	0.8	0.09792	0.3	0.20	0.031947	3.407193	605	35	35	602	3	11	605	8	8	633.9462	42.53602	47.06307	99.6
GJ1_19	Z_GJ1	0.762402	247471	287	0.0	10.26	0.3	0.06067	0.67	0.007912	3.000301	0.8184	0.7	0.09765	0.3	0.29	0.030495	2.762681	616	29	29	601	3	11	606	6	6	605.7475	32.97181	38.18169	99.1
GJ1_20	Z_GJ1	1.581475	245143	287	0.0	10.20	0.3	0.06029	0.68	0.008002	3.242305	0.8188	0.7	0.09815	0.3	0.13	0.03154	2.754324	598	30	30	604	3	11	606	6	6	626.1055	33.96831	39.36602	99.5
GJ1_21	Z_GJ1	1.436485	240930	287	0.0	10.21	0.3	0.05955	0.66	0.007809	3.45078	0.8105	0.7	0.09800	0.3	0.19	0.030469	2.966072	571	30	30	603	3	11	602	6	6	604.9	35.26151	40.13971	100.1
GJ1_22	Z_GJ1	0.823791	240270	287	0.0	10.22	0.3	0.05995	0.67	0.007745	2.708714	0.8117	0.6	0.09804	0.3	0.05	0.030821	2.405744	587	29	29	603	3	11	604	6	6	612.4454	29.0447	34.97056	99.8
GJ1_23	Z_GJ1	1.471045	232108	287	0.0	10.29	0.3	0.06068	0.69	0.007917	3.12653	0.8192	0.7	0.09730	0.3	0.24	0.03109	3.115708	618	30	30	599	3	11	607	7	7	617.3107	37.82413	42.59362	98.7
GJ1_24	Z_GJ1	1.43023	228455	287	0.0	10.26	0.3	0.06042	0.71	0.008137	4.215596	0.8183	0.7	0.09752	0.3	0.12	0.032208	3.350527	605	31	31	600	4	11	606	7	7	638.947	42.09355	46.71875	98.9
GJ1_25	Z_GJ1	1.149797	236053	288	0.0	10.21	0.3	0.05973	0.69	0.007794	2.820053	0.8125	0.7	0.09808	0.3	0.22	0.030887	2.802736	580	31	31	603	3	11	603	6	6	613.2818	33.85834	39.06657	100.0
GJ1_26	Z_GJ1	0.827074	238327	287	0.0	10.19	0.3	0.05962	0.64	0.007484	3.01203	0.8144	0.7	0.09815	0.3	0.30	0.029403	2.966408	578	28	28	604	3	11	604	6	6	584.1063	34.10029	38.81683	99.9
GJ1_27	Z_GJ1	0.495792	227966	287	0.0	10.27	0.3	0.06007	0.78	0.008319	3.301082	0.8146	0.7	0.09755	0.3	0.05	0.033461	3.350602	588	34	34	600	4	11	604	7	7	662.9948	43.68106	48.48049	99.3
GJ1_28	Z_GJ1	1.173582	236605	287	0.0	10.19	0.3	0.05987	0.70	0.008181	8.707656	0.8164	0.7	0.09810	0.3	0.10	0.030063	2.741644	582	30	30	603	3	11	605	6	6	597.2547	32.26733	37.439	99.7
GJ1_29	Z_GJ1	0.552672	227788	286	0.0	10.27	0.3	0.06011	0.73	0.007582	2.683393	0.8105	0.7	0.09753	0.3	0.19	0.030145	2.670347	590	32	32	600	3	11	602	7	7	598.9872	31.55717	36.86893	99.6
GJ1_30	Z_GJ1	0.823253	233335	287	0.0	10.23	0.3	0.06040	0.66	0.00761	3.06435	0.8174	0.6	0.09788	0.3	0.12	0.030523	3.126452	608	28	28	602	3	11	606	5	5	605.7322	37.3314	42.00826	99.4
Ples_1	Z_Pleso-vice	0.14628	367893	703	0.1	18.42	0.4	0.05323	0.71	0.030149	1.091226	0.4010	0.7	0.05442	0.4	0.28	0.014237	1.102317	324	31	31	342	2	7	342	4	4	285.6892	6.255111	11.08733	99.9
Ples_2	Z_Pleso-vice	0.499947	294158	665	0.1	18.30	0.4	0.05350	0.71	0.029996	1.482601	0.4057	0.7	0.05469	0.4	0.26	0.014934	1.528893	341	31	31	343	3	7	346	4	4	299.5274	9.088958	13.21306	99.2
Ples_3	Z_Pleso-vice	0.445216	340078	742	0.2	18.44	0.4	0.05377	0.68	0.030897	1.276035	0.4050	0.7	0.05435	0.4	0.33	0.013688	1.238887	349	32	32	341	3	7	345	4	4	274.7307	6.762145	11.10238	98.9
Ples_4	Z_Pleso-vice	1.07911	374080	820	0.2	18.32	0.4	0.05335	0.60	0.031261	1.326411	0.4041	0.6	0.05471	0.4	0.23	0.01462	1.352991	337	28	28	343	2	7	344	3	3	293.2927	7.880836	12.26402	99.7
Ples_5	Z_Pleso-vice	0.386562	346518	786	0.1	18.33	0.5	0.05348	0.78	0.030211	1.450447	0.4040	0.8	0.05470	0.5	0.39	0.014468	1.475155	340	37	37	343	3	7	344	5	5	290.2803	8.503112	12.60062	99.7
Ples_6	Z_Pleso-vice	0.619228	249151	529	0.1	18.38	0.5	0.05335	0.89	0.028435	1.835093	0.4006	0.9	0.05450	0.5	0.27	0.015214	1.719503	337	38	38	342	3	7	342	5	5	305.0961	10.41773	14.28493	99.9
Ples_7	Z_Pleso-vice	0.809479	242426	522	0.1	18.40	0.4	0.05318	0.87	0.027558	1.654755	0.3991	0.9	0.05447	0.4	0.17	0.01481	1.519977	316	39	39	342	2	7	340	5	5	297.0716	8.966823	13.07584	100.4
Ples_8	Z_Pleso-vice	0.314108	400652	809	0.2	18.40	0.4	0.05315	0.71	0.032502	1.308575	0.3986	0.7	0.05441	0.4	0.25	0.014627	1.326602	324	32	32	342	3	7	340	4	4	293.4436	7.728703	12.16831	100.4
Ples_9	Z_Pleso-vice	0.646634	366919	672	0.2	18.43	0.4	0.05291	0.72	0.031464	1.080454	0.3980	0.7	0.05440	0.4	0.14	0.014875	1.098355	311	34	34	341	2	7	340	4	4	298.3964	6.505785	11.56002	100.5
Ples_10 (1)	Z_Pleso-vice	0.083848	361875	780	0.2	18.45	0.4	0.05292	0.72	0.031675	1.303903	0.3991	0.8	0.05434	0.4	0.28	0.01527	1.342138	321	33	33	341	3	7	341	4	4	306.2299	8.159446	12.75797	100.2
Ples_11	Z_Pleso-vice	0.298562	312609	818	0.1	18.43	0.4	0.05328	0.79	0.029154	1.577996	0.4002	0.8	0.05441	0.4	0.27	0.014875	1.624014	331	35	35	342	3	7	341	5	5	298.364	9.621317	13.56155	100.0
Ples_12 (1)	Z_Pleso-vice	0.396769	274349	534	0.1	18.41	0.5	0.05332	0.86	0.02819	1.715322	0.4021	0.8	0.05435	0.5	0.16	0.015449	1.769888	341	38	38	341	3	7	343	5	5	309.7676	10.88574	14.72926	99.5
Ples_13 (1)	Z_Pleso-vice	0.395612	435690	1071	0.2	18.42	0.4	0.05315	0.59	0.033131	0.919285	0.4011	0.6	0.05438	0.4	0.39	0.014776	1.021334	327	26	26	341	3	7	342	4	4	296.4122	6.010927	11.23733	99.7
BB16_1	BB16	0.671444	277133	315	0.4	10.85	0.5	0.05857	0.74	0.075373	1.210048	0.7489	0.8	0.09244	0.5	0.37	0.023757	1.160703	546	35	35	570	6	12	567	7	7	474.463	10.88694	18.6411	100.5

BB16_3	BB16	0.245292	252176	327	0.4	10.94	0.4	0.05891	0.60	0.077689	0.891328	0.7519	0.6	0.09163	0.3	0.33	0.025243	0.951645	550	26	26	565	4	11	569	5	5	503.7585	9.469095	18.63696	99.4
BB16_4	BB16	0.591524	267655	346	0.4	10.86	0.4	0.05880	0.71	0.076122	0.871257	0.7515	0.7	0.09214	0.4	0.18	0.024925	0.957037	546	32	32	568	4	11	568	6	6	497.4951	9.40187	18.42734	100.0
BB16_5	BB16	0.310028	270550	367	0.4	10.89	0.4	0.05945	0.73	0.075422	0.925233	0.7552	0.7	0.09202	0.4	0.30	0.024578	1.027816	567	32	32	567	4	11	570	6	6	490.6415	9.963192	18.54224	99.5
BB16_6	BB16	0.728752	236901	295	0.4	10.93	0.4	0.05905	0.70	0.074708	0.951588	0.7450	0.7	0.09169	0.4	0.30	0.024973	1.004486	551	31	31	565	4	11	564	6	6	498.4194	9.888333	18.70794	100.2
BB16_7	BB16	0.026908	282778	365	0.4	10.88	0.4	0.05904	0.75	0.075452	1.01003	0.7485	0.7	0.09206	0.4	0.16	0.024804	1.093095	552	33	33	568	4	11	566	6	6	495.0965	10.69203	19.06101	100.2
BB16_8	BB16	0.251	281059	344	0.4	10.87	0.4	0.05894	0.86	0.076278	0.934308	0.7470	0.8	0.09220	0.4	0.30	0.024727	1.023494	552	37	37	568	4	11	566	7	7	493.6115	9.980842	18.63092	100.5
BB16_9	BB16	0.205388	278227	293	0.4	10.84	0.3	0.05859	0.68	0.075701	0.870694	0.7447	0.7	0.09232	0.3	0.25	0.025223	0.903145	542	29	29	569	4	11	564	6	6	503.3914	8.977351	18.37771	100.9
BB16_10	BB16	-0.07922	273680	341	0.4	10.83	0.4	0.05824	0.73	0.073972	0.936591	0.7441	0.7	0.09237	0.4	0.28	0.024499	1.02971	528	32	32	569	4	11	564	6	6	489.0984	9.952737	18.49856	101.0
BB16_11	BB16	-0.04239	251831	404	0.4	10.88	0.3	0.05892	0.62	0.075363	0.916565	0.7526	0.7	0.09211	0.3	0.40	0.024802	0.846561	557	27	27	568	4	11	569	6	6	495.1072	8.279676	17.8186	99.8
BB16_12	BB16	0.359919	205782	225	0.4	10.90	0.4	0.05878	0.77	0.073185	1.061029	0.7513	0.8	0.09204	0.4	0.24	0.025987	1.150548	548	35	35	568	5	11	568	7	7	518.3908	11.77098	20.27218	99.9
BB16_13	BB16	0.183281	226635	331	0.4	10.93	0.4	0.05904	0.69	0.073816	0.99559	0.7530	0.7	0.09166	0.4	0.28	0.025104	1.009994	555	30	30	565	4	11	570	6	6	500.9991	9.995782	18.83697	99.3

LA-ICP-MS RUN 08.04.2022						Data for Tera-Wasserburg plot						Data for Wetherill plot							Dates												
ID	Note	f206c	^{206}Pb	Uppm	Th/U	$^{238}U/^{206}Pb$	1s%	$^{207}Pb/^{206}Pb$	1s%	$^{208}Pb/^{206}Pb$	1s%	$^{207}Pb/^{235}U$	1s%	$^{206}Pb/^{238}U$	1s%	Rho	$^{208}Pb/^{232}Th$	1s%	$^{207}Pb/^{206}Pb$	2s (abs)	2ssys (abs)	$^{206}Pb/^{238}U$	2s (abs)	2ssys (abs)	$^{207}Pb/^{235}U$	2s (abs)	2ssys (abs)	$^{208}Pb/^{232}Th$	2s (abs)	2ssys (abs)	% conc
915_1	Z_91500	1.770903	109072	80	0.5	5.62	0.4	0.07601	0.85	0.104573	1.773201	1.8802	0.9	0.17875	0.4	0.30	0.050953	1.143353	1080	34	34	1060	8	26	1073	12	12	1003.808	22.37441	64.22835	98.8
915_2	Z_91500	1.587441	112634	80	0.5	5.57	0.4	0.07487	0.91	0.100782	1.185526	1.8639	0.9	0.18029	0.4	0.18	0.048062	1.218902	1047	37	37	1068	8	26	1066	12	12	948.1192	22.5613	61.26422	100.2
915_4	Z_91500	1.627279	113365	84	0.5	5.62	0.4	0.07544	0.86	0.104715	1.110905	1.8631	0.9	0.17845	0.4	0.28	0.049858	1.078485	1064	37	37	1058	9	26	1064	12	12	982.8436	20.69433	62.58084	99.4
915_5	Z_91500	0.458623	117861	85	0.5	5.60	0.5	0.07538	0.90	0.102474	1.002226	1.8761	0.9	0.17950	0.5	0.27	0.050384	0.983681	1060	37	37	1064	9	26	1068	12	12	993.0405	19.06071	62.61549	99.6
915_6	Z_91500	1.041633	112146	77	0.5	5.62	0.5	0.07534	0.86	0.102144	1.148674	1.8724	0.9	0.17878	0.5	0.30	0.051014	1.05827	1061	36	36	1060	9	26	1067	12	12	1005.075	20.76402	63.85637	99.3
915_7	Z_91500	0.314243	113329	80	0.5	5.58	0.5	0.07561	0.94	0.101746	1.147186	1.8765	0.9	0.17980	0.4	0.18	0.051464	1.121948	1061	39	39	1066	9	26	1070	12	12	1013.642	22.17753	64.75251	99.6
915_8	Z_91500	0.810853	113400	83	0.5	5.59	0.5	0.07527	1.04	0.101973	1.052184	1.8574	1.0	0.17955	0.5	0.11	0.05134	1.103579	1046	42	42	1064	9	26	1063	13	13	1011.347	21.77509	64.50829	100.1
915_9	Z_91500	1.587647	110230	79	0.5	5.61	0.5	0.07517	0.91	0.102404	1.181284	1.8648	0.9	0.17928	0.5	0.26	0.051203	1.165063	1055	38	38	1063	10	26	1065	12	12	1008.59	22.92922	64.75702	99.8
915_10	Z_91500	2.431365	101535	73	0.5	5.60	0.5	0.07504	1.16	0.101279	1.397345	1.8540	1.1	0.17894	0.5	0.12	0.049584	1.400724	1049	46	46	1061	9	26	1062	15	15	977.3664	26.70346	64.46337	99.9
915_11	Z_91500	1.526564	103840	74	0.5	5.59	0.5	0.07560	1.08	0.103898	1.291063	1.8796	1.0	0.17969	0.5	0.06	0.050547	1.223566	1056	45	45	1065	10	26	1070	13	13	996.0774	23.7883	64.39079	99.5
915_12	Z_91500	1.153893	102080	82	0.5	5.59	0.4	0.07442	0.99	0.10175	1.20369	1.8572	1.0	0.17955	0.4	0.16	0.050125	1.200006	1030	41	41	1064	9	26	1062	13	13	987.8177	23.12392	63.65498	100.2
915_13	Z_91500	0.523765	108722	85	0.5	5.58	0.5	0.07475	1.02	0.106306	1.2551	1.8590	1.0	0.18007	0.5	0.27	0.051623	1.182401	1047	40	40	1067	10	27	1065	13	13	1016.691	23.42295	65.31289	100.2
GJ1_1	Z_GJ1	0.598329	218558	287	0.0	10.24	0.3	0.06011	0.69	0.007638	3.095838	0.8162	0.7	0.09787	0.3	0.32	0.030188	2.795537	598	30	30	602	4	15	606	7	7	599.7429	33.03556	49.13069	99.4
GJ1_2	Z_GJ1	1.577963	216395	286	0.0	10.23	0.3	0.05992	0.72	0.007256	2.730735	0.8139	0.7	0.09787	0.3	0.20	0.029116	2.814283	593	31	31	602	3	15	604	6	6	578.6796	32.12162	47.59593	99.7
GJ1_3	Z_GJ1	1.007227	217969	288	0.0	10.24	0.3	0.06009	0.82	0.008059	2.959601	0.8143	0.8	0.09782	0.3	0.05	0.032989	2.884214	587	35	35	602	3	15	604	7	7	654.3651	37.14514	54.31966	99.7
GJ1_4	Z_GJ1	1.246166	215739	286	0.0	10.26	0.3	0.06022	0.70	0.007835	3.199117	0.8111	0.7	0.09760	0.3	0.21	0.030476	2.90983	595	31	31	600	3	15	603	6	6	605.2112	34.70575	50.51669	99.6

GJ1_5	Z_GJ1	0.844257	219438	289	0.0	10.21	0.3	0.06058	0.68	0.008303	2.970067	0.8200	0.7	0.09807	0.3	0.21	0.032025	2.773486	609	29	29	603	3	15	608	6	6	635.5523	34.69689	51.8311	99.2
GJ1_6	Z_GJ1	1.326104	224255	288	0.0	10.21	0.3	0.05994	0.69	0.007713	2.707352	0.8165	0.7	0.09807	0.3	0.26	0.03007	2.703117	584	31	31	603	3	15	605	6	6	604.3066	33.11127	50.17554	99.7
GJ1_7	Z_GJ1	0.944112	220370	286	0.0	10.24	0.3	0.05996	0.68	0.007936	2.642761	0.8126	0.7	0.09775	0.3	0.15	0.030897	2.644526	587	30	30	601	3	15	603	6	6	613.7736	32.00329	49.1059	99.7
GJ1_8	Z_GJ1	1.256294	213782	288	0.0	10.24	0.3	0.06031	0.76	0.008178	3.086365	0.8164	0.7	0.09772	0.3	0.13	0.030716	3.042738	597	33	33	601	3	15	605	7	7	609.8282	36.62844	52.09931	99.4
GJ1_9	Z_GJ1	0.667402	212365	286	0.0	10.21	0.3	0.06001	0.65	0.008138	3.119133	0.8151	0.7	0.09802	0.3	0.22	0.032142	2.729798	592	29	29	603	3	15	605	6	6	637.8323	34.29375	51.68162	99.6
GJ1_10	Z_GJ1	0.357843	219383	288	0.0	10.25	0.3	0.06020	0.70	0.007629	3.41833	0.8143	0.6	0.09765	0.3	0.02	0.03045	3.126065	601	30	30	601	3	15	604	6	6	604.409	37.18521	52.1818	99.4
GJ1_11	Z_GJ1	0.713056	218296	286	0.0	10.23	0.3	0.06012	0.72	0.007324	2.731347	0.8133	0.7	0.09779	0.3	0.13	0.02974	2.728638	590	31	31	602	3	15	604	6	6	590.9492	31.80428	47.9415	99.6
GJ1_12	Z_GJ1	0.762048	220963	284	0.0	10.20	0.3	0.06025	0.73	0.007328	2.652268	0.8207	0.7	0.09818	0.3	0.22	0.030041	2.489012	597	31	31	604	3	15	608	6	6	597.0612	29.31894	46.62496	99.3
GJ1_13	Z_GJ1	0.087336	227597	289	0.0	10.24	0.3	0.05979	0.69	0.007813	3.386792	0.8133	0.7	0.09786	0.3	0.04	0.031547	2.720059	579	30	30	602	3	15	603	6	6	626.2079	33.52208	50.6198	99.8
GJ1_14	Z_GJ1	0.85131	228382	288	0.0	10.23	0.3	0.05997	0.74	0.007499	2.648329	0.8136	0.7	0.09789	0.3	0.07	0.030875	2.487939	591	31	31	602	3	15	603	7	7	613.3722	30.09448	47.87069	99.8
GJ1_15	Z_GJ1	0.613964	222521	285	0.0	10.27	0.3	0.06025	0.68	0.007584	2.656781	0.8141	0.7	0.09758	0.3	0.14	0.031745	2.692362	596	30	30	600	3	15	604	6	6	630.0869	33.43193	50.77591	99.4
GJ1_16	Z_GJ1	1.687764	211969	287	0.0	10.23	0.3	0.06028	0.69	0.007593	3.06425	0.8153	0.7	0.09788	0.3	0.20	0.029217	2.946625	596	30	30	602	3	15	604	6	6	580.4784	33.73896	48.78651	99.6
GJ1_18	Z_GJ1	0.713764	214801	286	0.0	10.23	0.3	0.06056	0.68	0.014896	45.65911	0.8155	0.6	0.09790	0.3	0.21	0.031518	2.70483	610	29	29	602	3	15	606	6	6	625.6207	33.29484	50.43453	99.4
GJ1_19	Z_GJ1	0.066404	218609	288	0.0	10.24	0.2	0.06043	0.68	0.007569	2.618646	0.8151	0.7	0.09781	0.3	0.15	0.030409	2.613934	603	29	29	602	3	15	605	6	6	607.3433	31.71514	48.99239	99.4
GJ1_20	Z_GJ1	1.247132	215349	287	0.0	10.21	0.3	0.06002	0.65	0.007795	3.142527	0.8164	0.7	0.09811	0.3	0.23	0.031369	3.025141	592	29	29	603	3	15	606	6	6	622.3784	37.09455	52.91647	99.6
GJ1_21	Z_GJ1	0.997342	215043	288	0.0	10.26	0.3	0.06016	0.68	0.007573	2.858685	0.8127	0.7	0.09759	0.3	0.18	0.030687	2.905629	593	30	30	600	3	15	604	6	6	609.1944	34.85767	50.77684	99.5
GJ1_22	Z_GJ1	0.984419	212966	286	0.0	10.25	0.3	0.05998	0.73	0.007885	2.83908	0.8118	0.7	0.09772	0.3	0.08	0.030919	2.715293	585	32	32	601	3	15	602	6	6	617.6512	33.54397	50.7029	99.8
GJ1_23	Z_GJ1	0.356903	216501	288	0.0	10.22	0.3	0.06042	0.74	0.007758	3.346974	0.8212	0.7	0.09802	0.3	0.04	0.03075	2.929951	602	33	33	603	3	15	608	6	6	610.6574	35.20264	51.0545	99.2
GJ1_24	Z_GJ1	1.099931	202766	289	0.0	10.26	0.3	0.05963	0.73	0.007453	2.837572	0.8096	0.7	0.09755	0.3	0.17	0.030287	2.884417	571	32	32	600	3	15	601	6	6	601.4155	34.16293	49.95843	99.8
GJ1_25	Z_GJ1	0.925809	198738	286	0.0	10.21	0.3	0.05973	0.72	0.00784	2.620582	0.8152	0.7	0.09803	0.3	0.22	0.030323	2.58726	578	31	31	603	3	15	604	7	7	602.452	30.71626	47.73415	99.8
GJ1_26	Z_GJ1	0.671791	196853	287	0.0	10.21	0.3	0.06036	0.71	0.007904	2.624768	0.8183	0.7	0.09799	0.3	0.24	0.031545	2.631671	598	31	31	603	3	15	606	6	6	626.2591	32.45723	49.94285	99.4
GJ1_27	Z_GJ1	0.81739	200791	288	0.0	10.23	0.3	0.06047	0.72	0.007399	3.236888	0.8186	0.7	0.09794	0.3	0.18	0.030525	3.184514	607	32	32	602	3	15	606	6	6	605.8886	37.98153	52.82093	99.4
GJ1_28	Z_GJ1	0.524304	194912	285	0.0	10.22	0.3	0.06010	0.76	0.008004	3.459641	0.8157	0.8	0.09797	0.3	0.21	0.032178	3.29996	592	34	34	602	4	15	604	7	7	637.9533	41.46528	56.70049	99.7
GJ1_29	Z_GJ1	0.689451	197578	289	0.0	10.22	0.3	0.06020	0.81	0.007253	3.320534	0.8155	0.8	0.09796	0.3	0.01	0.029274	3.144022	587	36	36	602	3	15	604	7	7	581.3622	36.06639	50.47061	99.7
GJ1_30	Z_GJ1	1.145914	196122	287	0.0	10.26	0.3	0.05993	0.75	0.007628	3.173122	0.8094	0.7	0.09753	0.3	0.13	0.031015	3.088827	588	33	33	600	3	15	601	7	7	615.4357	37.45742	52.87724	99.8
Ples_1	Z_Pleso-vice	0.079654	379342	916	0.1	18.30	0.4	0.05280	0.72	0.029109	1.487087	0.4006	0.7	0.05471	0.4	0.32	0.01551	1.530184	317	31	31	343	3	9	342	4	4	311.0127	9.44754	21.21761	100.5
Ples_2	Z_Pleso-vice	0.369679	402230	940	0.1	18.41	0.5	0.05290	0.81	0.030251	1.27612	0.4001	0.8	0.05451	0.5	0.28	0.014739	1.320645	316	37	37	342	3	9	342	5	5	295.6707	7.752544	19.65659	100.1
Ples_3	Z_Pleso-vice	0.560079	394838	946	0.1	18.35	0.4	0.05284	0.65	0.029515	1.29564	0.4003	0.7	0.05466	0.4	0.43	0.014413	1.31163	310	30	30	343	3	9	342	4	4	289.1865	7.531583	19.20986	100.4
Ples_4	Z_Pleso-vice	0.206518	534535	1312	0.3	18.25	0.5	0.05259	0.65	0.047847	0.964176	0.3991	0.7	0.05484	0.5	0.48	0.014058	1.061003	305	30	30	344	4	9	341	4	4	282.1358	5.944217	18.24008	101.0
Ples_5	Z_Pleso-vice	0.430721	478449	1154	0.2	18.19	0.6	0.05275	0.86	0.03964	1.33059	0.4032	0.9	0.05515	0.6	0.36	0.015242	1.360349	304	39	39	346	4	9	344	5	5	305.6983	8.25752	20.42671	100.7

Ples_6	Z_Pleso-vice	0.435262	389343	860	0.1	18.20	0.4	0.05237	0.84	0.029715	1.312376	0.4000	0.8	0.05491	0.4	0.25	0.015792	1.374531	283	39	39	345	3	9	341	5	5	316.6254	8.637893	21.18223	101.0
Ples_9	Z_Pleso-vice	0.675283	386974	927	0.1	18.29	0.5	0.05345	0.82	0.029256	1.45128	0.4035	0.8	0.05478	0.5	0.34	0.01527	1.511558	333	37	37	344	3	9	344	5	5	306.2377	9.183616	20.82939	100.0
Ples_10	Z_Pleso-vice	0.467248	435321	1070	0.2	18.20	0.5	0.05243	0.92	0.031398	1.559595	0.4017	1.0	0.05512	0.5	0.25	0.014982	1.515037	293	44	44	346	4	9	342	6	6	300.5137	9.038109	20.46401	101.0
Ples_12	Z_Pleso-vice	0.1667	408440	1109	0.1	18.16	0.7	0.05256	0.93	0.029233	1.761071	0.4045	0.9	0.05534	0.7	0.30	0.014737	1.743258	301	42	42	347	5	10	345	5	5	295.6319	10.23204	20.76095	100.8
Ples_13	Z_Pleso-vice	0.162496	384438	1005	0.2	18.20	0.5	0.05286	0.81	0.036687	1.335032	0.4015	0.7	0.05495	0.5	0.27	0.014736	1.355996	306	37	37	345	3	9	343	4	4	295.6109	7.957531	19.7364	100.5
BB16_1	BB16	-0.11022	266646	385	0.4	10.86	0.3	0.05870	0.67	0.074594	0.845145	0.7504	0.7	0.09215	0.3	0.17	0.025223	0.820383	548	29	29	568	3	14	568	6	6	503.4122	8.159641	31.66094	100.1
BB16_2	BB16	-0.16491	259127	350	0.4	10.88	0.3	0.05842	0.70	0.074757	0.975925	0.7447	0.7	0.09205	0.3	0.20	0.024357	0.999161	538	30	30	568	4	14	565	6	6	486.2927	9.602915	31.09313	100.5
BB16_3	BB16	0.317509	254989	366	0.4	10.94	0.3	0.05857	0.72	0.075969	0.915302	0.7444	0.7	0.09160	0.3	0.25	0.024682	0.987108	535	31	31	565	3	14	564	6	6	492.7039	9.60839	31.46024	100.2
BB16_4	BB16	0.24044	254579	368	0.4	10.90	0.3	0.05900	0.66	0.074044	0.913405	0.7505	0.6	0.09193	0.3	0.18	0.024324	1.026295	558	28	28	567	4	14	568	5	5	485.6431	9.852757	31.15178	99.7
BB16_5	BB16	1.12136	232964	330	0.4	10.90	0.4	0.05882	0.72	0.076072	1.007914	0.7492	0.7	0.09178	0.4	0.24	0.025823	1.049881	553	31	31	566	4	14	567	6	6	515.1826	10.67878	33.08057	99.8
BB16_6	BB16	0.020078	187232	238	0.4	10.95	0.4	0.05974	0.97	0.074492	1.213957	0.7593	1.0	0.09157	0.4	0.15	0.026812	1.277119	590	42	42	565	4	14	572	8	8	534.6386	13.48516	35.18414	98.7
BB16_7	BB16	0.95698	194383	267	0.4	10.92	0.4	0.05925	1.00	0.075752	1.222228	0.7528	1.0	0.09171	0.4	0.33	0.026999	1.238023	560	44	44	566	4	14	568	9	9	538.3203	13.14393	35.22011	99.5
BB16_8	BB16	0.591779	243119	358	0.3	10.91	0.4	0.05891	0.78	0.076021	1.098979	0.7474	0.8	0.09193	0.4	0.27	0.026165	1.11081	553	33	33	567	5	14	566	7	7	521.9285	11.44249	33.70238	100.2
BB16_9	BB16	0.567167	230951	329	0.4	10.91	0.4	0.05895	0.86	0.076725	1.088027	0.7481	0.9	0.09191	0.4	0.28	0.025705	1.120331	552	37	37	567	5	14	566	8	8	512.8712	11.34364	33.15623	100.1
BB16_10	BB16	-0.028	239509	352	0.4	10.92	0.4	0.05911	0.73	0.075544	1.083265	0.7527	0.8	0.09169	0.4	0.27	0.025186	1.142269	560	33	33	565	4	14	569	7	7	502.6366	11.33323	32.56928	99.4
BB16_11	BB16	0.055357	227222	319	0.4	10.96	0.4	0.05919	0.82	0.076647	1.026102	0.7501	0.8	0.09137	0.4	0.17	0.025438	1.016984	559	35	35	564	4	14	567	7	7	507.6073	10.19439	32.49262	99.4
BB16_12	BB16	0.268371	202335	330	0.3	10.94	0.4	0.05892	0.80	0.074922	0.894602	0.7508	0.8	0.09168	0.4	0.17	0.025432	0.880575	541	35	35	565	4	14	568	7	7	507.5027	8.821865	32.06957	99.5
BB16_13	BB16	-0.49249	172973	257	0.4	10.91	0.4	0.05875	0.94	0.075561	1.295779	0.7473	1.0	0.09175	0.4	0.29	0.02699	1.336049	538	42	42	566	4	14	565	8	8	538.1248	14.18169	35.61432	100.1

Appendix B. Supporting Information Chapter 3

This appendix contains Table B.1 and Figure B.1 to B.3 that support observations and conclusions presented in the main text. Table B.1 contains full single-grain results from apatite (AHe) and zircon (ZHe) (U-Th-Sm)/He analyses. Outliers are marked in grey and are not included in the weighted mean age. Figure B.1 supports (U-Th-Sm)/He data graphically. Apatite fission track (AFT) data is supported by radial plots in Figure B.2. Figure B.3 shows QTQt thermal models using either AHe, AFT or ZHe single-grain ages. All supporting tables and figures were also uploaded to the Zenodo online repository (https://doi.org/10.5281/zenodo.6358993).

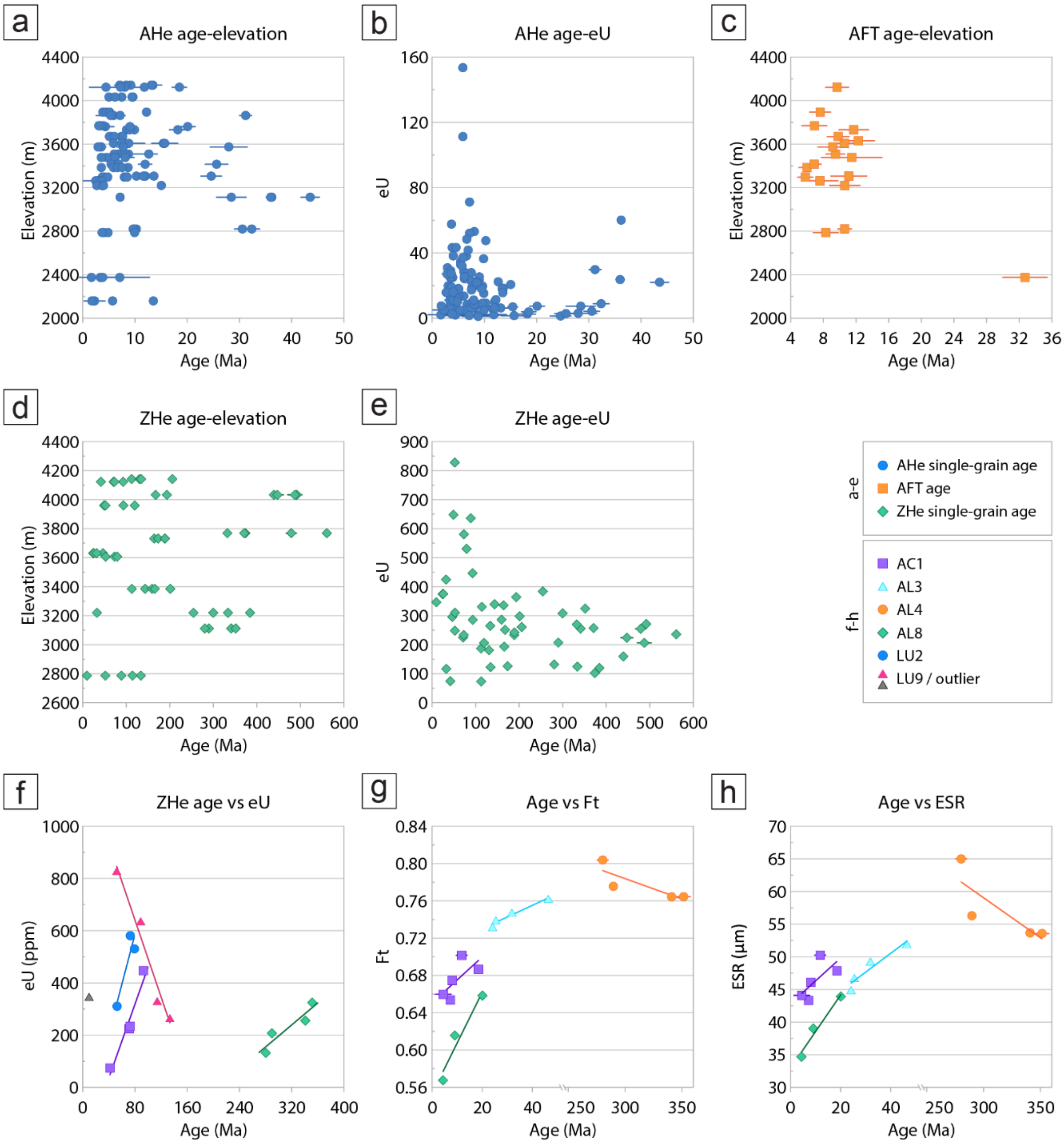

Figure B.1 Supporting diagrams for apatite (AHe) and zircon (ZHe) (U-Th-Sm)/He analysis. AHe ages are plotted against (a) sampling elevation, and (b) eU. Apatite fission track (AFT) ages are plotted against (c) sampling elevation. ZHe ages are plotted against (d) sampling elevation, and (e) eU. AHe and ZHe samples that show an (f) age-eU, (g) age- F_T and/or (h) age-ESR relationship are drawn in the lowermost diagrams with the corresponding trends.

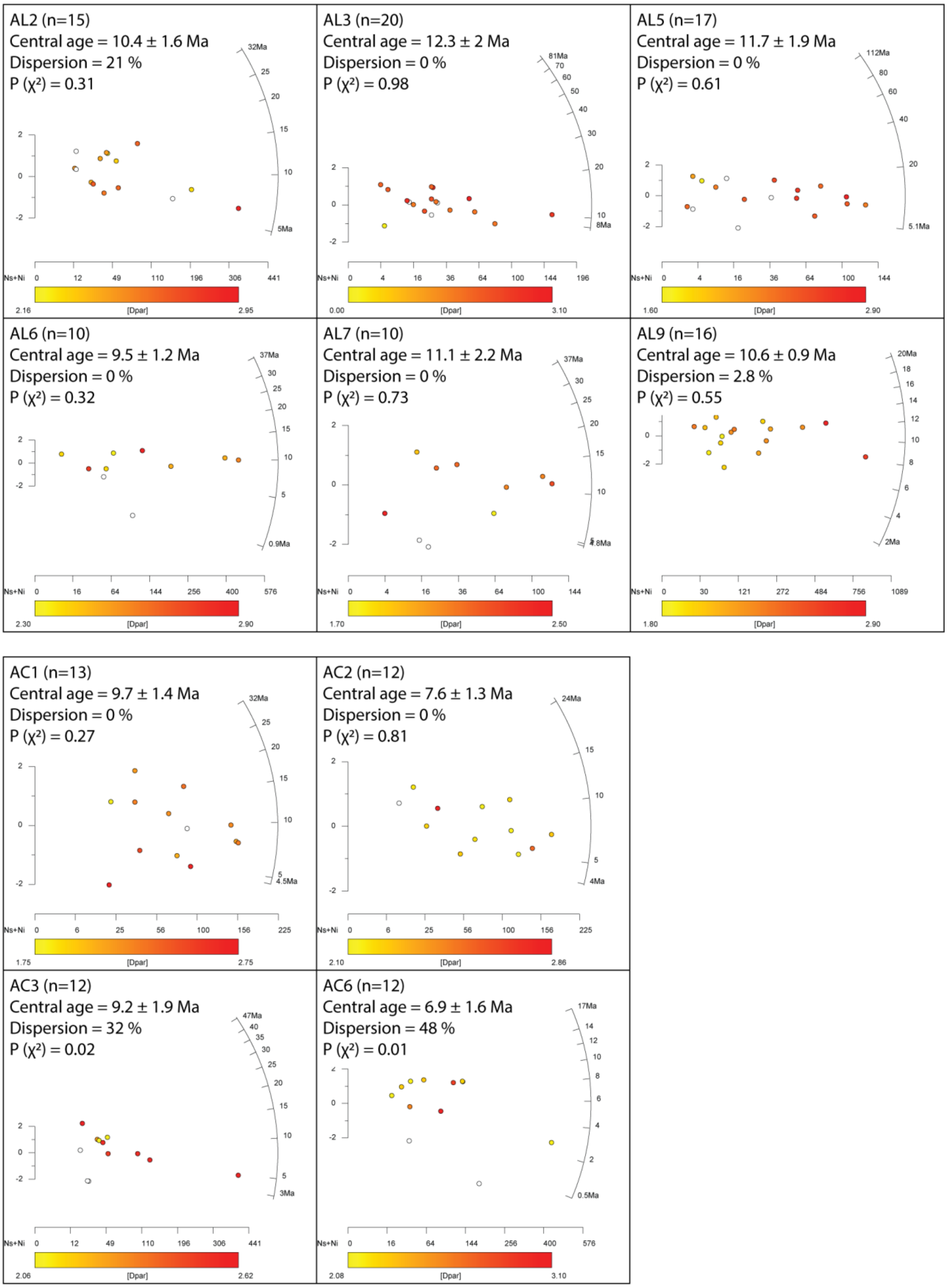
AL2 (n=15)
Central age = 10.4 ± 1.6 Ma
Dispersion = 21 %
P (χ²) = 0.31
AL3 (n=20)
Central age = 12.3 ± 2 Ma
Dispersion = 0 %
P (χ²) = 0.98
AL5 (n=17)
Central age = 11.7 ± 1.9 Ma
Dispersion = 0 %
P (χ²) = 0.61
AL6 (n=10)
Central age = 9.5 ± 1.2 Ma
Dispersion = 0 %
P (χ²) = 0.32
AL7 (n=10)
Central age = 11.1 ± 2.2 Ma
Dispersion = 0 %
P (χ²) = 0.73
AL9 (n=16)
Central age = 10.6 ± 0.9 Ma
Dispersion = 2.8 %
P (χ²) = 0.55
AC1 (n=13)
Central age = 9.7 ± 1.4 Ma
Dispersion = 0 %
P (χ²) = 0.27
AC2 (n=12)
Central age = 7.6 ± 1.3 Ma
Dispersion = 0 %
P (χ²) = 0.81
AC3 (n=12)
Central age = 9.2 ± 1.9 Ma
Dispersion = 32 %
P (χ²) = 0.02
AC6 (n=12)
Central age = 6.9 ± 1.6 Ma
Dispersion = 48 %
P (χ²) = 0.01
Ns+Ni
[Dpar]

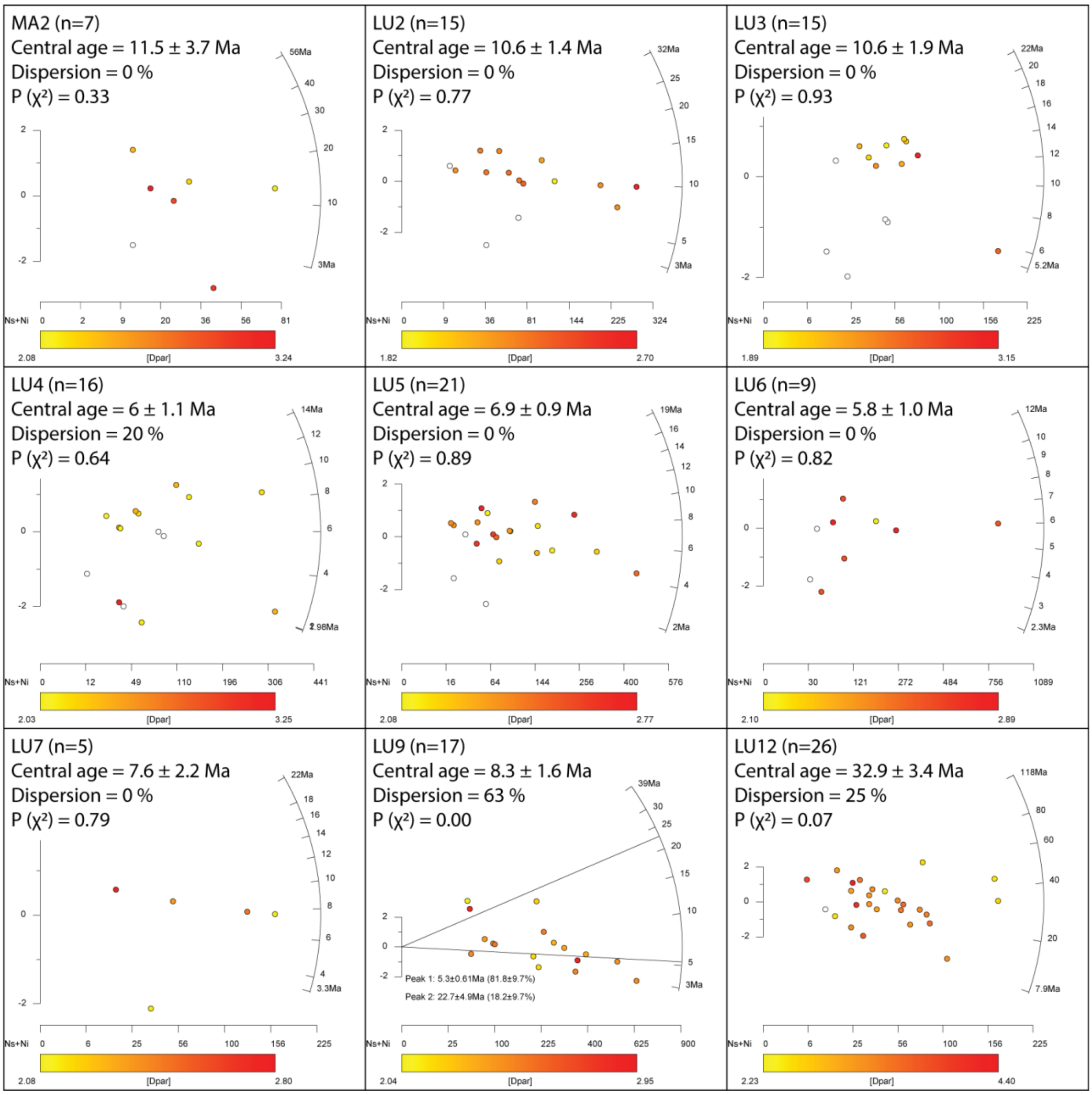

Figure B.2 Radial plots for apatite fission track data generated in RadialPlotter (Vermeesch, 2009), showing relationships between the AFT single-grain age, uncertainty and Dpar. For bimodal samples, age peaks are drawn as radial lines. Data points are color-coded for corrected Dpar values. Note that axis scaling varies between plots.

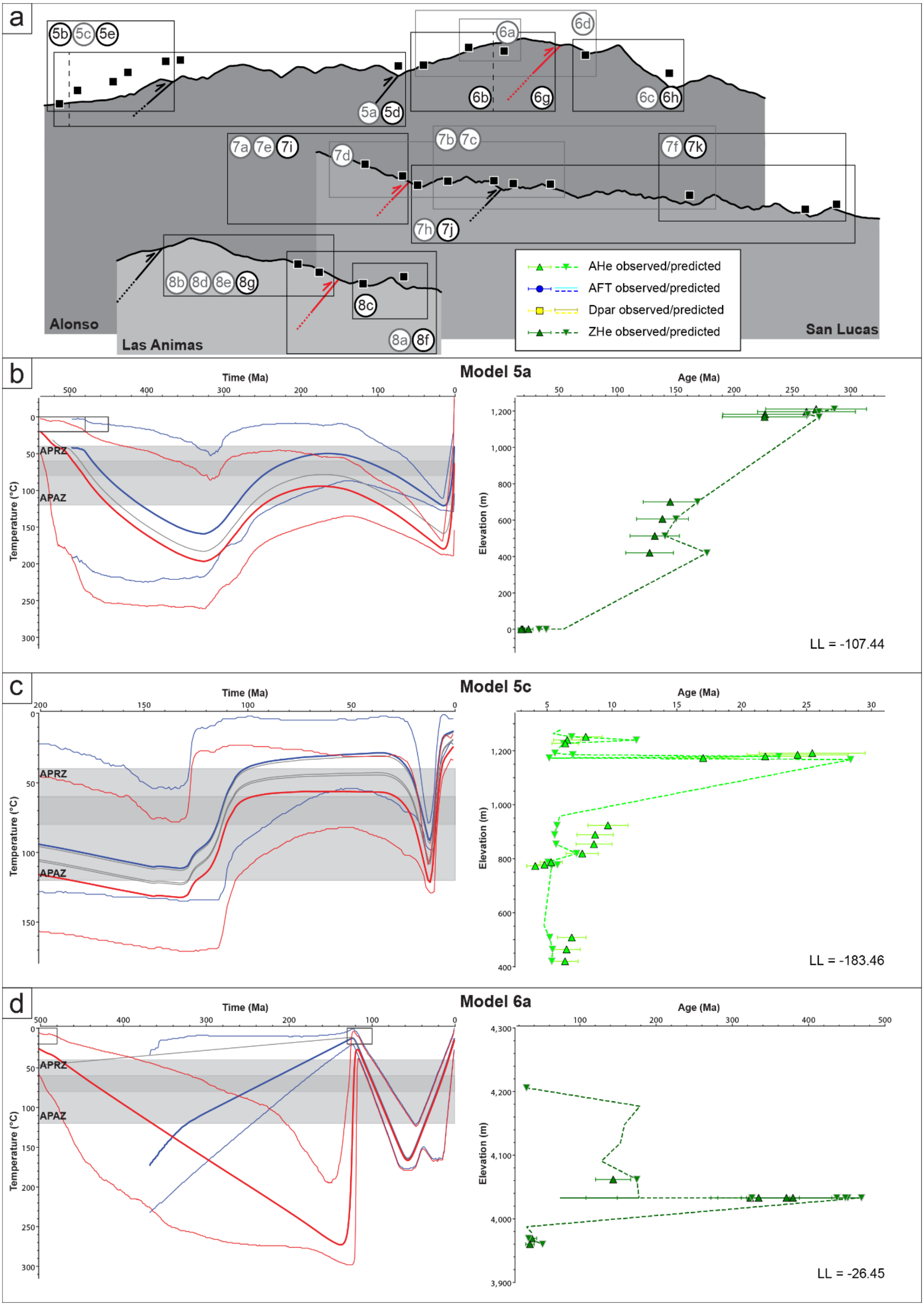
a
5b 5c 5e
6a
6d
5a 5d
6b
6g
6c 6h
7a 7e 7i
7d
7b 7c
7f 7k
7h 7j
8b 8d 8e 8g
8c
8a 8f
AHe observed/predicted
AFT observed/predicted
Dpar observed/predicted
ZHe observed/predicted
Alonso
Las Animas
San Lucas
b
Model 5a
Time (Ma)
Temperature (°C)
APRZ
APAZ
Age (Ma)
Elevation (m)
LL = -107.44
c
Model 5c
Time (Ma)
Temperature (°C)
APRZ
APAZ
Age (Ma)
Elevation (m)
LL = -183.46
d
Model 6a
Time (Ma)
Temperature (°C)
APRZ
APAZ
Age (Ma)
Elevation (m)
LL = -26.45

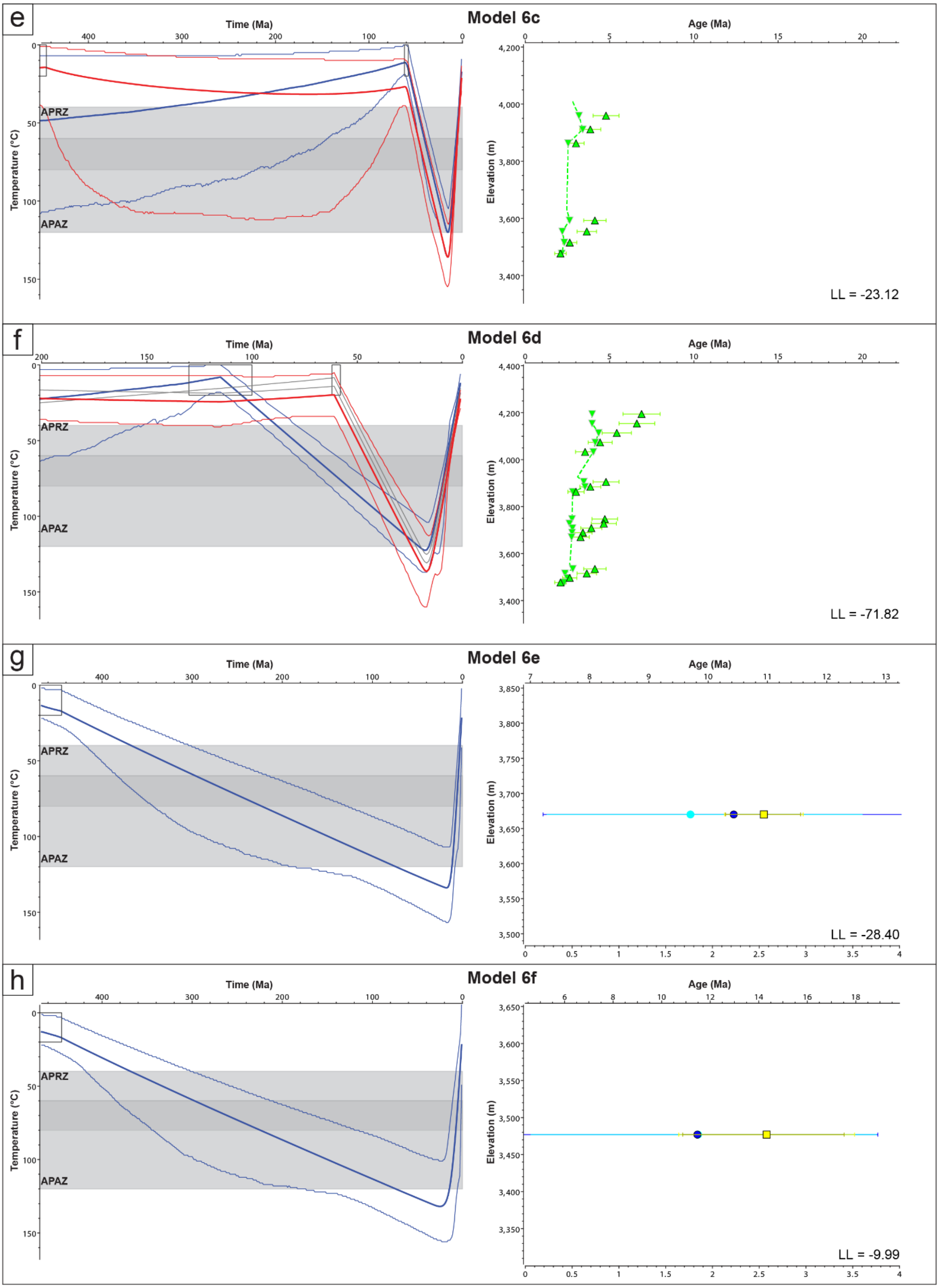
e
Model 6c
Time (Ma)
Temperature (°C)
APRZ
APAZ
Age (Ma)
Elevation (m)
LL = -23.12
f
Model 6d
Time (Ma)
Temperature (°C)
APRZ
APAZ
Age (Ma)
Elevation (m)
LL = -71.82
g
Model 6e
Time (Ma)
Temperature (°C)
APRZ
APAZ
Age (Ma)
Elevation (m)
LL = -28.40
h
Model 6f
Time (Ma)
Temperature (°C)
APRZ
APAZ
Age (Ma)
Elevation (m)
LL = -9.99

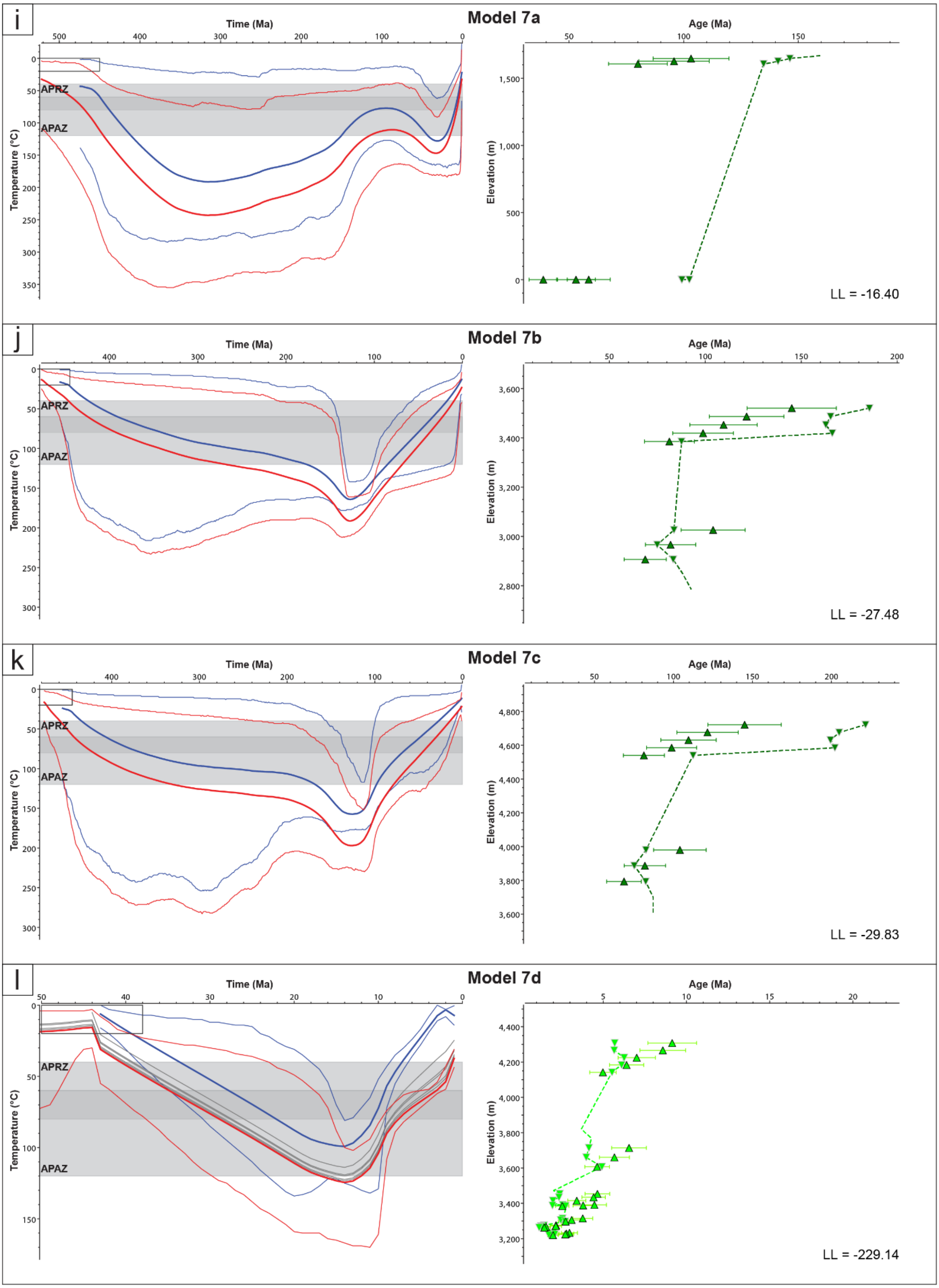
i
Model 7a
Time (Ma)
Temperature (°C)
APRZ
APAZ
Age (Ma)
Elevation (m)
LL = -16.40
j
Model 7b
LL = -27.48
k
Model 7c
LL = -29.83
l
Model 7d
LL = -229.14

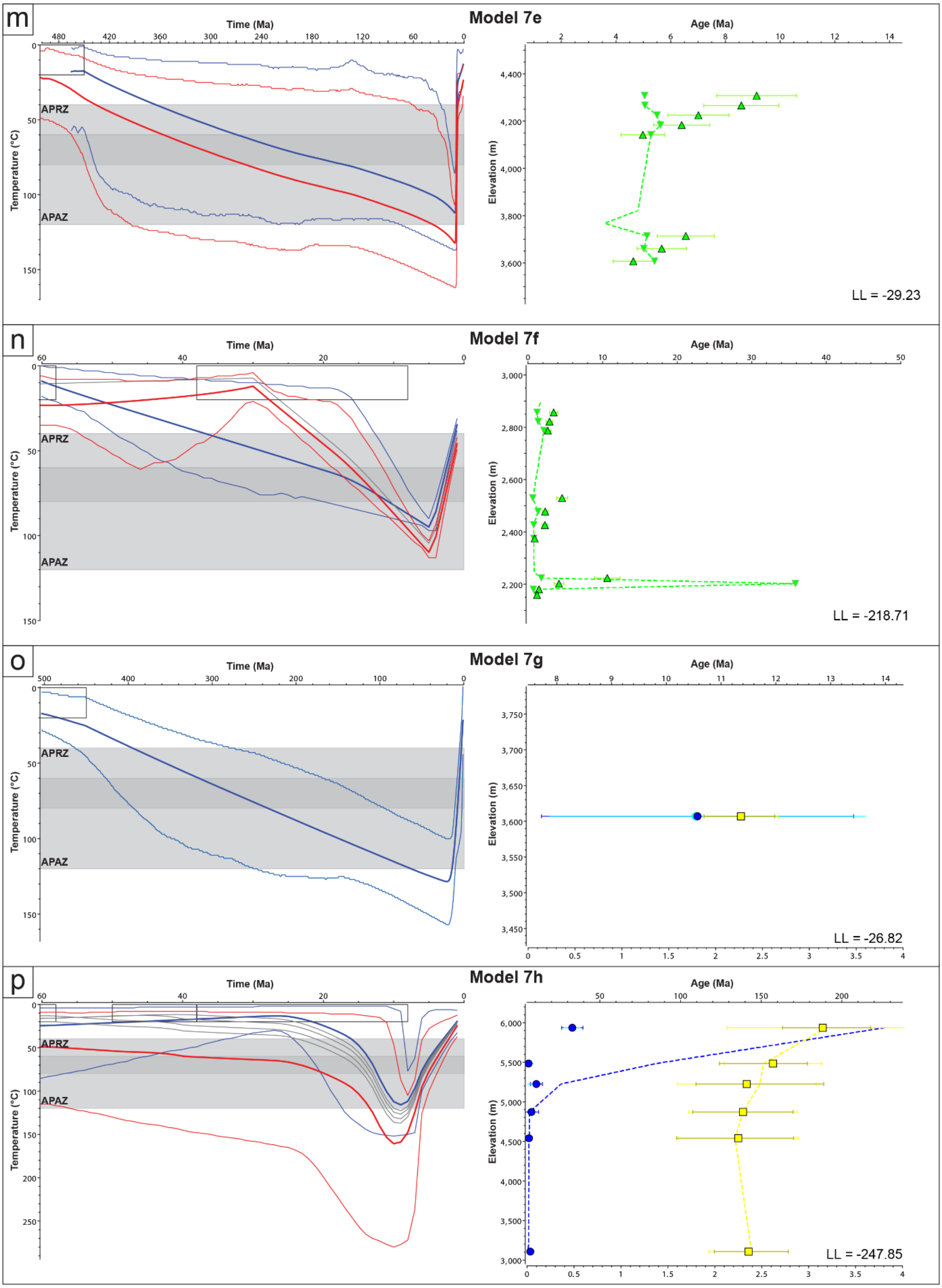
m
Model 7e
Time (Ma)
Temperature (°C)
APRZ
APAZ
Age (Ma)
Elevation (m)
LL = -29.23
n
Model 7f
Time (Ma)
Temperature (°C)
APRZ
APAZ
Age (Ma)
Elevation (m)
LL = -218.71
o
Model 7g
Time (Ma)
Temperature (°C)
APRZ
APAZ
Age (Ma)
Elevation (m)
LL = -26.82
p
Model 7h
Time (Ma)
Temperature (°C)
APRZ
APAZ
Age (Ma)
Elevation (m)
LL = -247.85

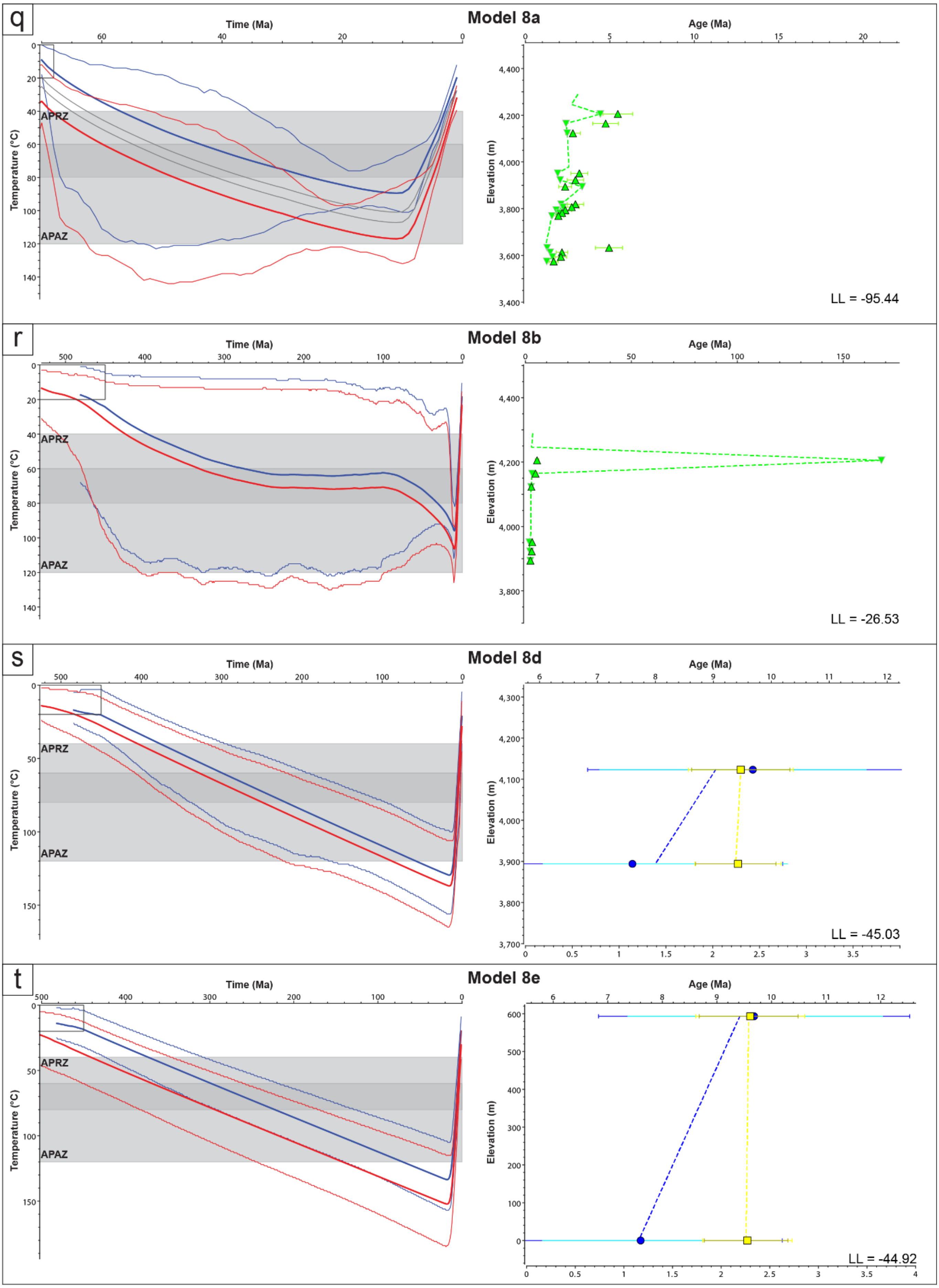
q
Model 8a
Time (Ma)
Temperature (°C)
APRZ
APAZ
Age (Ma)
Elevation (m)
LL = -95.44
r
Model 8b
Time (Ma)
Temperature (°C)
APRZ
APAZ
Age (Ma)
Elevation (m)
LL = -26.53
s
Model 8d
Time (Ma)
Temperature (°C)
APRZ
APAZ
Age (Ma)
Elevation (m)
LL = -45.03
t
Model 8e
Time (Ma)
Temperature (°C)
APRZ
APAZ
Age (Ma)
Elevation (m)
LL = -44.92

Figure B.3 Single-method models for the Alonso (leeward: b-c; windward: d-h), San Lucas (i-p), Las Animas (q-t) showing 95 % confidence intervals for the hot and cold sample (left) and relationships between observed and predicted single-grain AHe and ZHe, as well as sample AFT ages (right).

Table B.1 Full results of (U-Th-Sm)/He analyses for apatite and zircon. Outliers are marked in grey.

Apatite (U-Th-Sm)/He data																			
TB[a]	Sample	Aliquot	UTM E[b]	UTM N[b]	Z (m)	Age (Ma)	± 2σ (Ma)	U (ppm)	Th (ppm)	^{147}Sm (ppm)	eU (ppm)	Th/^{238}U	He (n-mol/g)	F_T	ESR (µm)[c]	# T[d]	WM (Ma)[e]	SE (Ma)[f]	%[g]
1	AL5	*a1*	265330	7407390	3732	18.2	1.6	1.5	4.7	3.8	2.6	3.3	0.2	0.71	52.5	r	9.0	0.4	3.9 %
		a2	265330	7407390	3732	9.9	0.5	9.5	24.3	29.8	15.2	2.6	0.6	0.69	47.6	0			
		a3	265330	7407390	3732	8.4	0.2	18.9	4.6	26.0	20.0	0.3	0.7	0.76	62.6	r			
		a4	265330	7407390	3732	9.0	0.3	18.3	21.5	10.4	23.3	1.2	0.8	0.72	53.1	1			
	AL6	a1	264129	7406152	3509	6.7	0.8	5.5	12.5	21.2	8.4	2.4	0.2	0.71	51.8	1	6.9	0.5	6.8 %
		a2	264129	7406152	3509	6.0	0.8	8.5	21.2	32.9	13.5	2.6	0.3	0.65	43.5	1			
		a3	264129	7406152	3509	8.8	5.5	0.7	5.8	1.9	2.1	8.5	0.1	0.64	42.1	1			
		a4	264129	7406152	3509	12.6	0.5	16.7	23.9	47.9	22.3	1.5	1.1	0.68	46.3	r			
		a5	264129	7406152	3509	8.2	1.0	3.7	13.3	18.6	6.8	3.8	0.2	0.64	41.2	0			
	AL7	a1	263544	7405230	3306	13.6	0.7	14.4	16.7	9.9	18.3	1.2	1.0	0.71	51.9	2	11.7	0.6	5.1 %
		a2	263544	7405230	3306	10.3	0.2	43.9	15.2	42.3	47.5	0.4	2.0	0.75	59.5	1			
		a3	263544	7405230	3306	24.6	2.0	0.6	3.0	1.6	1.3	4.9	0.1	0.77	65.3	2			
		a4	263544	7405230	3306	12.0	0.7	7.5	11.5	17.7	10.2	1.6	0.5	0.72	52.7	2			
		a5	263544	7405230	3306	11.6	0.6	3.2	10.8	16.3	5.8	3.5	0.3	0.74	57.6	2			
	AL8	a1	262789	7405469	3112	36.2	0.7	45.0	64.5	31.5	60.1	1.5	7.1	0.60	37.5	1	35.7	2.6	7.3 %
		a2	262789	7405469	3112	36.0	0.8	20.6	13.2	11.9	23.7	0.7	3.1	0.67	45.7	1			
		a3	262789	7405469	3112	28.5	2.8	3.0	18.3	8.9	7.3	6.2	0.7	0.59	36.8	1			
		a4	262789	7405469	3112	7.2	0.3	2.1	294.2	67.5	71.2	148.3	1.8	0.63	40.9	2			
		a5	262789	7405469	3112	43.5	1.8	14.4	32.6	23.7	22.0	2.3	3.0	0.58	35.6	1			
	AL9	a1	262168	7404701	2820	10.3	0.3	8.0	5.4	23.4	9.3	0.7	0.4	0.76	62.6	2	10.0	0.1	1.2 %
		a2	262168	7404701	2820	9.8	0.4	35.7	2.9	39.4	36.4	0.1	1.3	0.66	44.2	1			
		a3	262168	7404701	2820	32.4	1.5	8.5	1.4	24.0	8.9	0.2	1.0	0.61	38.9	2			
		a4	262168	7404701	2820	30.6	1.5	3.9	1.7	6.7	4.3	0.5	0.5	0.70	49.4	2			
		a5	262168	7404701	2820	9.7	0.7	18.2	6.1	27.6	19.6	0.3	0.7	0.65	43.2	2			
2	AL4*	a1	265693	7407476	3761	9.0	0.8	12.5	54.5	28.9	25.3	4.5	0.8	0.62	39.0	1	9.4	3.3	35.6 %
		a2	265693	7407476	3761	4.3	1.7	6.8	34.8	40.3	15.0	5.3	0.2	0.57	34.7	0			
		a3	265693	7407476	3761	20.1	1.5	6.1	5.4	23.4	7.3	0.9	0.5	0.66	43.9	2			
3	LU1	a1	268703	7390777	4142	9.2	0.6	4.8	15.2	44.2	8.4	3.3	0.3	0.73	54.7	0	9.8	1.1	11.2 %
		a2	268703	7390777	4142	13.4	0.7	12.7	22.7	14.6	18.0	1.9	0.9	0.67	46.1	1			
		a3	268703	7390777	4142	8.3	0.2	8.1	60.9	53.9	22.4	7.8	0.8	0.75	60.9	r			
		a4	268703	7390777	4142	13.1	2.0	5.4	3.8	9.9	6.2	0.7	0.3	0.65	42.8	0			
		a5	268703	7390777	4142	7.1	1.0	4.9	1.3	3.8	5.2	0.3	0.1	0.69	48.8	r			
	AC1*	a1	269588	7386416	4123	8.1	0.3	41.9	47.4	18.1	53.1	1.2	1.6	0.67	46.1	1	7.7	0.4	5.5 %
		a2	269588	7386416	4123	18.5	1.4	2.1	7.6	3.6	3.9	3.7	0.3	0.69	47.8	0			
		a3	269588	7386416	4123	7.2	1.2	3.3	15.5	18.6	7.0	4.8	0.2	0.65	43.3	2			
		a4	269588	7386416	4123	4.5	3.2	1.6	1.6	0.9	2.0	1.0	0.0	0.66	44.1	r			
		a5	269588	7386416	4123	11.8	2.2	1.4	3.1	4.1	2.2	2.3	0.1	0.70	50.3	r			

	TAC1	a1	272118	7406576	4033	9.6	0.8	2.8	26.4	17.5	9.1	9.6	0.3	0.70	50.1	2	7.3	0.8	11.0 %
		a2	272118	7406576	4033	9.4	0.4	16.2	8.1	84.3	18.1	0.5	0.7	0.68	46.8	2			
		a3	272118	7406576	4033	5.0	0.3	8.4	41.7	23.8	18.2	5.2	0.4	0.70	50.3	2			
		a4	272118	7406576	4033	7.5	0.3	27.2	3.2	42.0	27.9	0.1	0.8	0.72	53.8	2			
		a5	272118	7406576	4033	6.2	0.7	1.7	13.8	7.4	5.0	8.2	0.1	0.71	52.6	2			
	AC2	a1	270123	7386139	3894	3.9	0.3	37.1	26.2	18.1	43.3	0.7	0.6	0.61	38.5	1	4.3	0.3	7.9 %
		a2	270123	7386139	3894	4.5	1.3	2.8	17.2	18.4	6.8	6.4	0.1	0.65	42.3	1			
		a3	270123	7386139	3894	5.1	1.0	6.0	31.2	10.6	13.3	5.4	0.2	0.61	38.3	2			
		a4	270123	7386139	3894	12.2	0.5	6.9	18.9	10.6	11.3	2.8	0.6	0.73	55.9	r			
	AL2	a1	270624	7405026	3670	7.4	0.5	3.8	81.5	5.6	23.0	22.0	0.6	0.64	41.3	2	6.3	0.5	7.2 %
		a2	270624	7405026	3670	5.4	0.4	14.2	86.3	10.1	34.5	6.3	0.6	0.63	40.3	2			
		a3	270624	7405026	3670	7.6	0.7	7.5	48.9	9.3	19.0	6.8	0.5	0.61	38.3	2			
		a4	270624	7405026	3670	5.1	0.6	2.9	63.8	15.0	17.9	22.7	0.3	0.64	41.1	r			
		a5	270624	7405026	3670	6.1	0.6	3.5	106.9	7.9	28.6	31.6	0.6	0.65	42.3	2			
	LU2	*a1*	270443	7390822	3607	15.4	1.0	3.8	13.5	26.9	6.9	3.7	0.4	0.72	53.8	0	6.8	0.6	8.1 %
		a2	270443	7390822	3607	15.7	2.5	1.0	2.3	1.5	1.6	2.3	0.1	0.72	54.0	r			
		a3	270443	7390822	3607	8.8	3.1	0.1	4.2	12.7	1.1	39.5	0.0	0.77	64.2	r			
		a4	270443	7390822	3607	5.9	0.2	28.8	351.1	18.4	111.3	12.6	2.8	0.79	70.0	r			
		a5	270443	7390822	3607	7.4	0.9	1.7	17.5	10.5	5.8	10.5	0.2	0.75	60.8	r			
4	MA3	a1	272520	7398204	3863	5.9	0.1	107.4	196.3	14.9	153.5	1.9	3.2	0.66	43.5	r	6.4	0.4	6.6 %
		a2	272520	7398204	3863	5.3	2.8	3.2	7.0	1.8	4.9	2.2	0.1	0.58	35.8	2			
		a3	272520	7398204	3863	7.2	0.3	29.7	95.0	12.4	52.0	3.3	1.4	0.67	45.1	r			
		a4	272520	7398204	3863	31.2	1.2	27.6	9.2	39.3	29.8	0.3	2.9	0.58	35.5	1			
	AC6	a1	272000	7384350	3769	3.4	0.6	8.9	8.8	11.3	10.9	1.0	0.1	0.68	47.0	2	3.5	0.2	4.6 %
		a2	272000	7384350	3769	3.1	0.8	3.2	7.8	19.1	5.1	2.5	0.1	0.72	52.7	2			
		a3	272000	7384350	3769	3.9	0.2	19.3	23.6	87.8	24.9	1.3	0.4	0.73	55.0	2			
		a4	272000	7384350	3769	3.5	0.4	7.1	6.9	23.2	8.7	1.0	0.1	0.75	59.2	r			
		a5	272000	7384350	3769	3.1	0.5	12.2	32.3	15.5	19.8	2.7	0.2	0.63	40.1	2			
	AC3	a1	270778	7385071	3574	3.4	1.0	1.0	42.5	11.1	11.0	42.0	0.1	0.62	39.9	0	4.1	0.8	19.4 %
		a2	270778	7385071	3574	3.5	0.9	10.3	60.7	33.3	24.6	6.1	0.3	0.59	36.5	0			
		a3	270778	7385071	3574	7.7	1.2	4.8	22.1	30.9	10.0	4.7	0.3	0.63	40.5	r			
		a4	270778	7385071	3574	28.0	3.6	1.3	7.2	36.3	3.0	5.7	0.3	0.61	38.9	r			
		a5	270778	7385071	3574	2.9	0.6	10.9	85.2	37.2	30.9	8.1	0.3	0.57	34.9	0			
	MA2	a1	274321	7397718	3477	6.2	0.7	11.0	56.1	28.8	24.2	5.3	0.5	0.58	35.7	1	5.1	0.6	11.1 %
		a2	274321	7397718	3477	8.1	1.7	1.3	30.5	5.7	8.5	24.0	0.2	0.57	34.8	0			
		a3	274321	7397718	3477	4.6	0.6	21.2	94.3	33.2	43.3	4.6	0.6	0.57	35.3	0			
		a4	274321	7397718	3477	6.2	0.5	17.9	32.3	5.2	25.5	1.9	0.6	0.67	45.4	2			
		a5	274321	7397718	3477	3.6	0.8	7.3	77.6	25.6	25.5	11.0	0.3	0.58	36.1	0			
	LU5	a1	274792	7391378	3415	6.6	0.3	28.1	42.6	9.4	38.1	1.6	0.9	0.68	46.2	2	6.3	0.4	5.7 %
		a2	274792	7391378	3415	25.6	2.2	1.0	7.9	11.4	2.8	8.2	0.3	0.70	50.4	r			
		a3	274792	7391378	3415	11.9	1.3	4.1	9.4	2.1	6.3	2.4	0.3	0.64	42.0	2			
		a4	274792	7391378	3415	6.9	0.3	36.9	20.5	23.4	41.7	0.6	1.1	0.68	46.2	2			
		a5	274792	7391378	3415	5.4	0.4	24.1	37.6	31.2	33.0	1.6	0.6	0.63	40.1	2			

	LU4	a1	273074	7392891	3385	5.9	0.2	30.2	29.5	13.1	37.1	1.0	0.8	0.64	42.2	2	5.2	0.8	15.5 %
		a2	273074	7392891	3385	8.7	0.4	19.1	11.1	4.4	21.7	0.6	0.7	0.69	48.1	2			
		a3	273074	7392891	3385	3.6	0.2	14.1	63.5	31.6	29.0	4.7	0.4	0.71	52.6	1			
		a4	273074	7392891	3385	6.6	0.3	44.6	15.9	36.0	48.4	0.4	1.2	0.67	45.6	0			
		a5	273074	7392891	3385	7.5	0.7	7.7	40.7	28.2	17.3	5.4	0.4	0.60	37.7	1			
	LU6	a1	275647	7391245	3297	4.0	0.1	36.1	9.0	37.5	38.2	0.3	0.6	0.77	64.1	2	4.2	0.2	5.7 %
		a2	275647	7391245	3297	3.7	0.5	12.4	1.9	18.2	12.8	0.2	0.2	0.74	57.7	1			
		a3	275647	7391245	3297	4.8	0.2	10.1	9.3	18.4	12.2	1.0	0.2	0.78	68.3	r			
		a4	275647	7391245	3297	8.0	0.5	5.9	22.4	16.2	11.2	3.9	0.4	0.76	61.6	r			
		a5	275647	7391245	3297	8.5	0.4	10.0	49.7	45.0	21.7	5.1	0.8	0.76	62.6	1			
	LU7	a1	277533	7391911	3263	2.9	1.0	23.1	16.9	28.0	27.0	0.8	0.2	0.54	32.8	1	3.4	0.3	7.3 %
		a2	277533	7391911	3263	3.5	1.7	6.7	0.7	23.4	6.9	0.1	0.1	0.63	40.0	r			
		a3	277533	7391911	3263	2.5	2.4	3.9	4.7	8.7	5.0	1.2	0.0	0.60	37.4	2			
		a4	277533	7391911	3263	3.7	0.6	26.2	5.1	21.1	27.4	0.2	0.3	0.59	37.0	1			
	LU3	a1	271736	7393079	3220	3.7	0.2	8.4	45.5	42.9	19.1	5.6	0.3	0.74	56.9	2	3.5	0.3	7.5 %
		a2	271736	7393079	3220	15.0	0.2	19.5	5.0	16.0	20.6	0.3	1.3	0.77	66.6	r			
		a3	271736	7393079	3220	3.7	0.3	6.0	55.2	18.8	19.0	9.5	0.3	0.72	53.8	1			
		a4	271736	7393079	3220	2.7	0.2	5.3	44.6	24.6	15.8	8.7	0.2	0.74	58.0	2			
		a5	271736	7393079	3220	4.0	0.5	5.4	24.5	29.0	11.2	4.7	0.2	0.72	53.3	1			
	LU9	*a1*	283558	7390518	2787	9.9	0.5	2.2	11.5	31.4	4.9	5.4	0.2	0.77	65.8	1	4.1	0.3	6.1 %
		a2	283558	7390518	2787	4.0	0.3	13.4	11.3	14.6	16.0	0.9	0.3	0.72	53.2	2			
		a3	283558	7390518	2787	4.9	0.4	7.7	10.4	30.8	10.2	1.4	0.2	0.70	50.3	2			
		a6	283558	7390518	2787	3.7	0.1	41.9	67.0	7.1	57.6	1.7	0.8	0.72	53.3	2			
	LU12	a1	289357	7386938	2375	3.4	0.7	2.8	11.8	11.0	5.6	4.3	0.1	0.69	49.0	2	3.5	0.4	10.3 %
		a2	289357	7386938	2375	3.8	2.6	1.4	4.5	9.3	2.4	3.4	0.0	0.61	38.9	2			
		a3	289357	7386938	2375	1.7	2.5	1.4	2.9	5.6	2.1	2.2	0.0	0.63	40.7	2			
		a4	289357	7386938	2375	7.1	5.7	0.7	4.0	7.6	1.6	6.1	0.0	0.60	37.1	2			
	LU11	*a1*	288034	7387380	2159	121.5	4.4	2.1	9.5	15.3	4.4	4.6	2.1	0.70	49.8	2	4.3	1.8	41.7 %
		a2	288034	7387380	2159	13.5	0.3	12.8	12.0	40.1	15.6	1.0	0.9	0.77	66.5	2			
		a3	288034	7387380	2159	2.3	2.0	4.8	0.8	19.4	5.0	0.2	0.0	0.63	40.9	r			
		a4	288034	7387380	2159	1.7	0.5	4.7	12.0	40.8	7.6	2.6	0.1	0.73	56.5	r			
		a5	288034	7387380	2159	5.7	0.2	25.7	26.9	22.2	32.0	1.1	0.7	0.73	54.8	1			

Zircon (U-Th-Sm)/He data																			
TB[a]	Sample	Aliquot	UTM E[b]	UTM N[b]	Z (m)	Age (Ma)	± 2σ (Ma)	U (ppm)	Th (ppm)	^{147}Sm (ppm)	eU (ppm)	Th/^{238}U	He (nmol/g)	F_T	ESR (µm)[c]	# T[d]	WM (Ma)[e]	SE (Ma)[f]	%[g]
1	AL5	z1	265330	7407390	3732	164.3	2.1	325.8	43.2	0.5	336.0	0.1	233.7	0.77	54.2	2	178.5	5.3	3.0 %
		z2	265330	7407390	3732	173.4	2.4	105.0	89.8	0.4	126.1	0.9	90.9	0.76	51.4	2			
		z3	265330	7407390	3732	188.5	2.4	193.0	170.7	0.6	233.2	0.9	176.4	0.73	45.9	2			
		z4	265330	7407390	3732	189.0	1.1	220.0	94.7	0.5	242.2	0.4	192.1	0.77	52.4	2			
	AL8*†	z1	262789	7405469	3112	289.8	1.8	149.2	247.0	50.7	207.2	1.7	257.6	0.78	56.3	2	313.9	15.5	4.9 %
		z2	262789	7405469	3112	280.4	4.9	93.8	161.6	25.0	131.8	1.8	164.1	0.80	65.0	2			
		z3[h]	262789	7405469	3112	340.9	3.4	175.3	341.8	13.0	255.6	2.0	369.0	0.76	53.7	2			
		z4[h]	262789	7405469	3112	351.5	6.0	229.1	406.5	19.6	324.6	1.8	483.9	0.76	53.6	2			
2	AL3*	z1	270128	7405319	3631	24.1	0.2	370.7	16.0	-0.3	374.4	0.0	35.7	0.73	44.9	2	27.0	1.9	6.9 %
		z2	270128	7405319	3631	25.5	0.3	340.6	146.6	0.6	375.1	0.4	38.2	0.74	46.7	2			
		z3	270128	7405319	3631	46.4	0.9	254.1	177.5	0.9	295.8	0.7	56.7	0.76	52.0	2			
		z4	270128	7405319	3631	31.9	0.7	327.7	411.8	1.0	424.5	1.3	54.7	0.75	49.3	2			
3	LU1	z1	268703	7390777	4142	112.3	1.1	172.8	59.8	0.3	186.8	0.4	81.1	0.71	41.6	2	125.3	5.7	4.5 %
		z2	268703	7390777	4142	130.7	2.8	133.5	203.5	0.6	181.3	1.6	94.5	0.73	46.3	2			
		z3	268703	7390777	4142	205.8	2.0	243.1	76.0	0.2	260.9	0.3	227.1	0.77	53.5	2			
		z4	268703	7390777	4142	134.2	1.8	102.1	88.1	0.7	122.8	0.9	69.0	0.77	53.3	2			
	AC1†	z1	269588	7386416	4123	71.1	1.3	179.2	195.4	0.6	225.1	1.1	63.5	0.73	45.8	2	78.3	5.5	7.0 %
		z2	269588	7386416	4123	41.7	1.5	63.2	47.3	1.3	74.3	0.8	12.3	0.73	45.9	2			
		z3	269588	7386416	4123	92.8	0.6	404.0	181.3	0.7	446.6	0.5	164.8	0.73	45.4	2			
		z4	269588	7386416	4123	72.6	2.4	231.2	10.1	0.0	233.6	0.0	69.0	0.75	48.4	2			
	TAC1	z1	272118	7406576	4033	491.9	7.9	251.3	85.9	0.3	271.4	0.4	574.4	0.76	51.9	2	339.2	62.6	18.5 %
		z2	272118	7406576	4033	167.6	3.0	210.1	175.6	0.8	251.3	0.9	176.0	0.76	52.5	2			
		z3	272118	7406576	4033	193.2	3.7	344.4	83.7	0.4	364.1	0.3	285.4	0.74	46.7	2			
		z5	272118	7406576	4033	439.3	9.4	152.7	29.0	0.1	159.5	0.2	286.5	0.73	44.5	2			
		z6	272118	7406576	4033	447.3	13.8	210.2	58.5	0.7	224.0	0.3	416.0	0.74	46.8	2			
		z7	272118	7406576	4033	3382.7	165.3	23.6	19.0	0.3	28.0	0.8	469.1	0.68	38.4	2			
		z8	272118	7406576	4033	487.3	16.5	187.1	82.2	0.4	206.4	0.5	426.6	0.75	49.8	2			
	MA1	z1	271055.1	7399705	3960	49.0	0.6	542.8	448.1	2.3	648.1	0.9	121.0	0.70	40.9	2	50.6	1.1	2.2 %
		z2	271055.1	7399705	3960	52.2	2.0	180.4	289.0	1.0	248.3	1.7	50.0	0.71	43.0	2			
		z3	271055.1	7399705	3960	119.3	2.8	165.9	172.1	0.6	206.3	1.1	93.3	0.70	40.1	2			
		z4	271055.1	7399705	3960	93.4	0.8	245.2	172.5	0.7	285.7	0.7	106.3	0.73	45.8	2			
	LU2†	z1	270443	7390822	3607	52.6	1.2	272.7	160.8	0.7	310.5	0.6	65.1	0.74	46.3	2	67.2	6.9	10.2 %
		z2	270443	7390822	3607	72.9	0.8	540.4	171.5	2.1	580.7	0.3	166.7	0.73	44.2	2			
		z3	270443	7390822	3607	79.2	0.7	458.1	308.3	2.5	530.5	0.7	168.4	0.74	46.9	2			
4	AC6	z1	272000	7384350	3769	332.3	5.3	261.5	36.6	0.3	270.1	0.1	390.0	0.78	56.3	2	415.4	35.7	8.6 %
		z2	272000	7384350	3769	560.8	10.0	202.5	142.2	0.9	235.9	0.7	550.8	0.74	46.5	2			
		z3	272000	7384350	3769	373.6	5.9	77.0	107.2	1.0	102.2	1.4	167.2	0.79	59.5	2			
		z4	272000	7384350	3769	479.2	12.2	227.8	115.0	1.2	254.8	0.5	526.3	0.77	52.9	2			

		z5	272000	7384350	3769	371.0	8.8	184.0	312.5	1.0	257.4	1.8	371.4	0.70	41.3	2			
	LU4	z1	273074	7392891	3385	112.7	5.8	41.1	137.7	1.3	73.4	3.5	32.5	0.72	45.3	2	153.6	13.1	8.5 %
		z2	273074	7392891	3385	201.1	5.7	280.2	75.9	0.5	298.0	0.3	236.0	0.72	42.8	2			
		z3	273074	7392891	3385	143.4	2.8	314.9	104.7	4.2	339.5	0.3	182.4	0.69	38.2	2			
		z4	273074	7392891	3385	159.3	1.8	232.6	229.0	3.1	286.4	1.0	170.8	0.68	38.5	2			
		z5	273074	7392891	3385	165.6	7.5	183.9	40.0	1.8	193.3	0.2	127.9	0.73	44.9	2			
	LU3	z1	271736	7393079	3220	299.8	9.7	303.3	20.2	0.1	308.0	0.1	389.4	0.76	50.9	2	314.7	23.7	7.5 %
		z2	271736	7393079	3220	384.3	5.0	114.0	25.4	0.1	120.0	0.2	195.6	0.76	51.0	2			
		z3	271736	7393079	3220	333.7	3.9	117.8	28.7	0.1	124.5	0.3	168.9	0.73	45.1	2			
		z4	271736	7393079	3220	254.3	9.5	377.6	25.8	0.2	383.6	0.1	398.5	0.74	46.5	2			
		z5	271736	7393079	3220	32.5	0.7	98.8	75.5	0.3	116.5	0.8	15.4	0.75	50.2	2			
	LU9[†]	*z1*	283558	7390518	2787	52.0	0.5	816.9	47.0	1.3	827.9	0.1	189.6	0.81	66.1	2	110.6	10.7	9.7 %
		z2	283558	7390518	2787	9.7	0.1	325.6	88.9	1.1	346.5	0.3	14.6	0.80	62.8	2			
		z3	283558	7390518	2787	133.5	1.1	224.8	170.9	1.2	265.0	0.8	150.1	0.78	55.9	2			
		z4	283558	7390518	2787	114.2	1.2	307.7	96.2	2.8	330.3	0.3	146.9	0.72	42.4	2			
		z5	283558	7390518	2787	88.8	0.8	609.0	115.2	4.0	636.0	0.2	236.9	0.77	53.8	2			

[a]Corresponding tectonic block, for numbers see Figure 3.2
[b]UTM zone 20K
[c]Equivalent spherical radius
[d]Number of crystal terminations
[e]Weighted mean age calculated in IsoplotR, excluding outliers
[f]Standard error (1σ) of the weighted mean age
[g]Percentage of SE of the weighted mean age
[h]Aliquots were heated four times
[*]Samples with age-F_T relationship
[†]Samples with age-eU relationship

Appendix C. Supporting Information Chapter 4

This appendix contains Figure C.1 to C.4 and Table C.1 that support observations and conclusions presented in the main text. Figure C.1 supports (U-Th-Sm)/He data graphically by providing plots showing relationships between cooling ages, eU, F_T and ESR. Apatite fission track (AFT) data is supported by radial plots in Figure C.2–C.4. Table C.1 contains full single-grain results from apatite (AHe) and zircon (ZHe) (U-Th-Sm)/He analyses. All supporting tables and figures were also uploaded to the Zenodo online repository (https://doi.org/10.5281/zenodo.7988837).

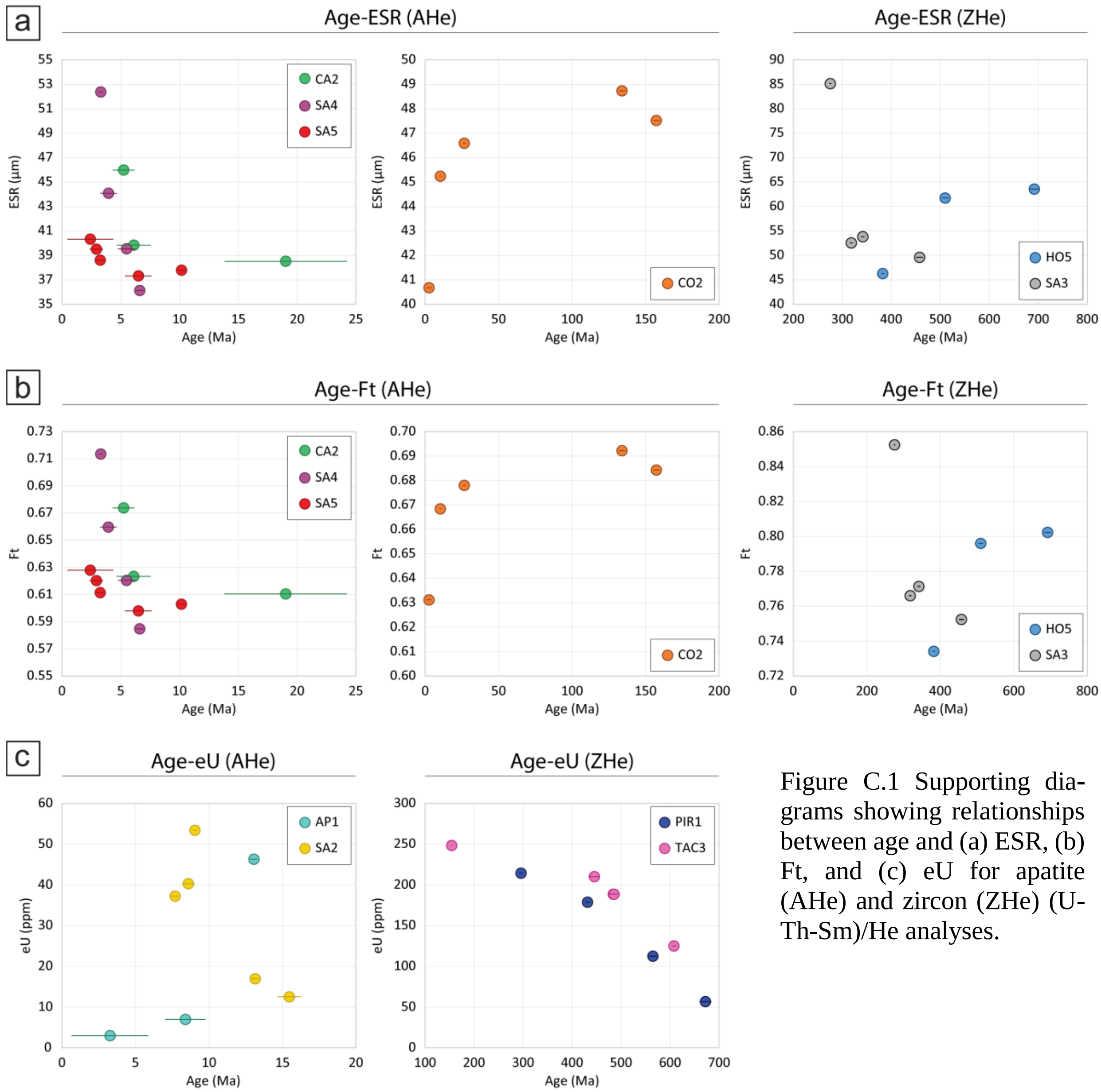

Figure C.1 Supporting diagrams showing relationships between age and (a) ESR, (b) Ft, and (c) eU for apatite (AHe) and zircon (ZHe) (U-Th-Sm)/He analyses.

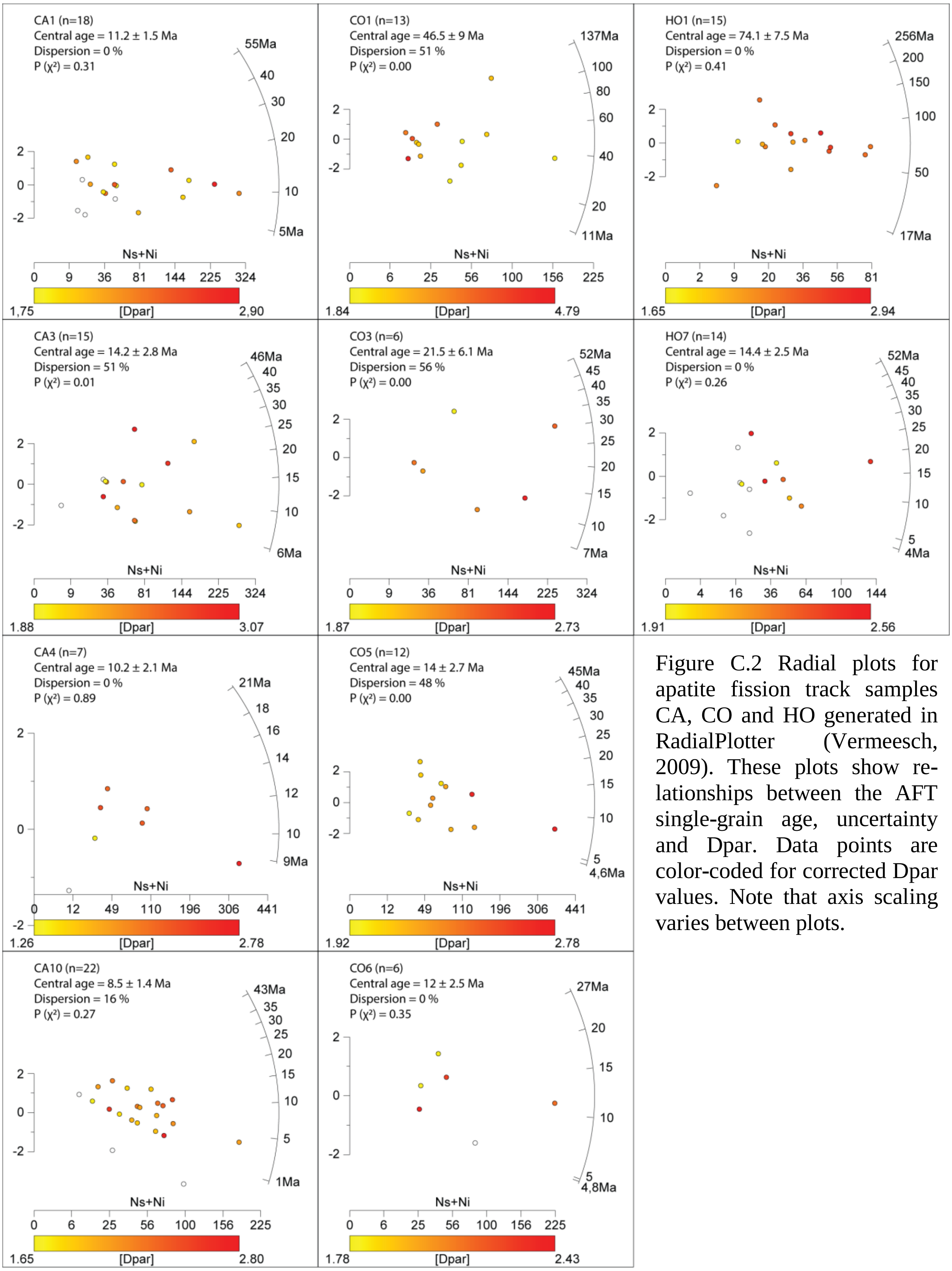

Figure C.2 Radial plots for apatite fission track samples CA, CO and HO generated in RadialPlotter (Vermeesch, 2009). These plots show relationships between the AFT single-grain age, uncertainty and Dpar. Data points are color-coded for corrected Dpar values. Note that axis scaling varies between plots.

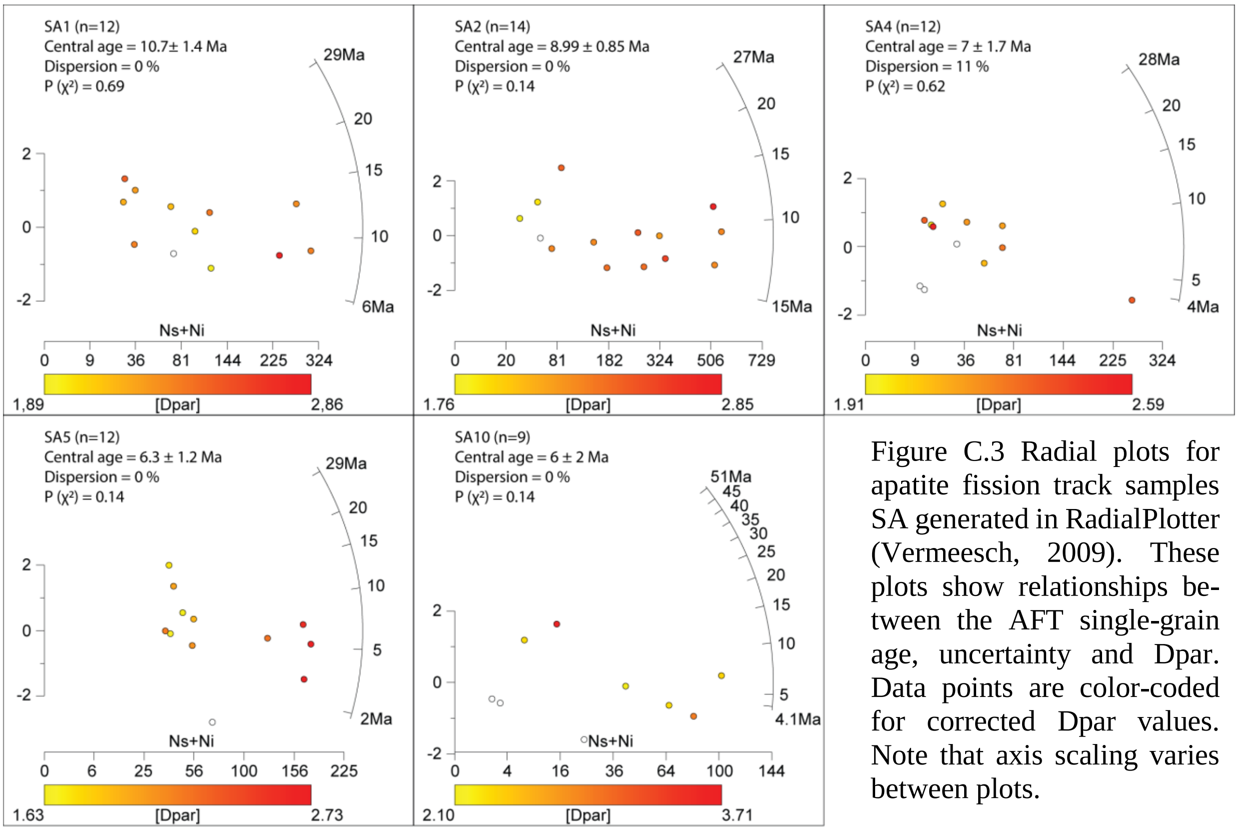

Figure C.3 Radial plots for apatite fission track samples SA generated in RadialPlotter (Vermeesch, 2009). These plots show relationships between the AFT single-grain age, uncertainty and Dpar. Data points are color-coded for corrected Dpar values. Note that axis scaling varies between plots.

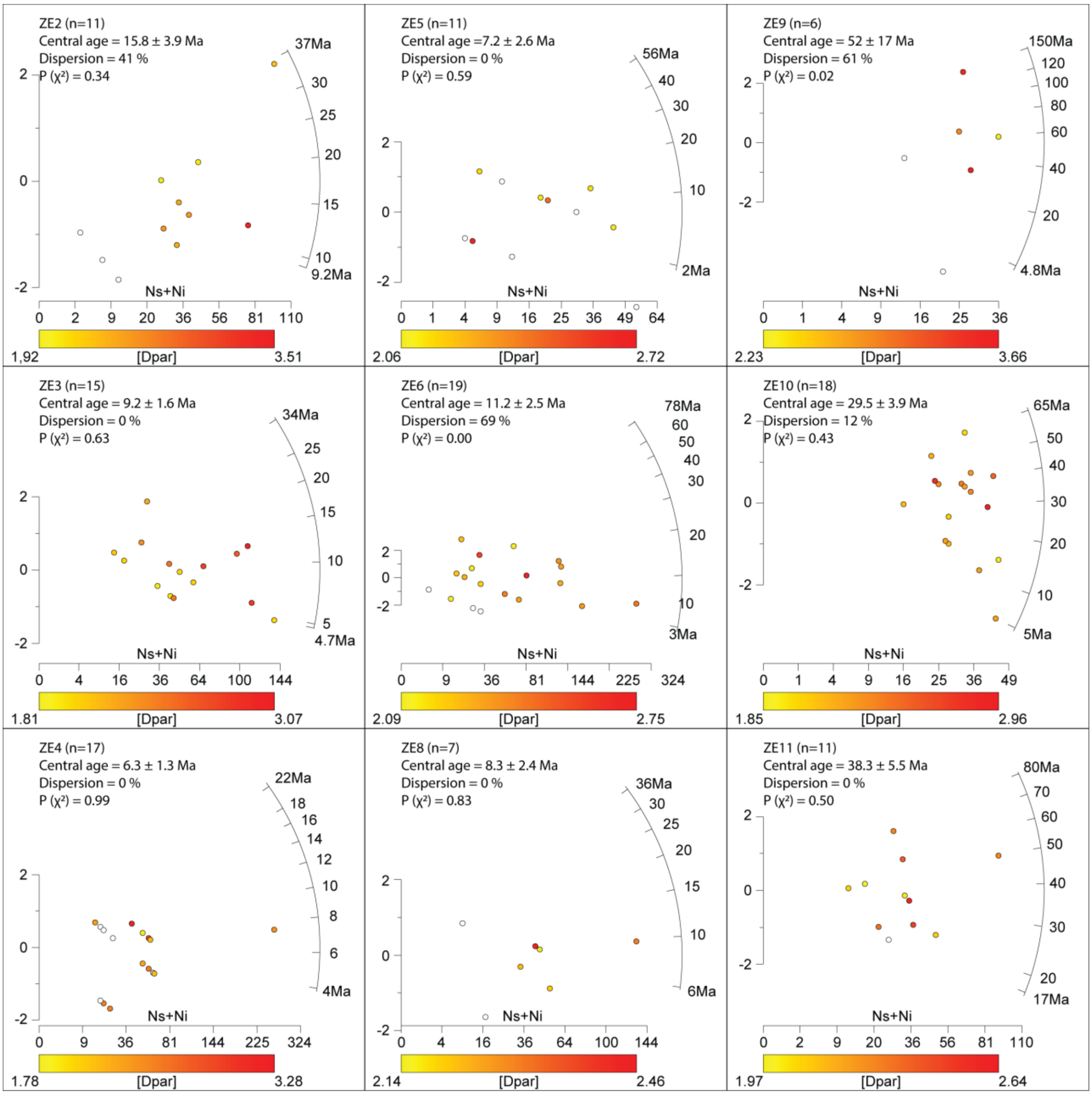

Figure C.4 Radial plots for apatite fission track samples ZE generated in RadialPlotter (Vermeesch, 2009). These plots show relationships between the AFT single-grain age, uncertainty and Dpar. Data points are color-coded for corrected Dpar values. Note that axis scaling varies between plots.

Table C.1 Full, single-grain (U-Th-Sm)/He analyses for apatite and zircon. Outliers are marked in grey.

Apatite (U-Th-Sm)/He data																	
Sample	Aliquot	UTM E[a]	UTM N[a]	Z (m)	Age (Ma)	± 2σ (Ma)	U (ppm)	Th (ppm)	^{147}Sm (ppm)	eU (ppm)	Th/^{238}U	He (nmol/g)	F_T	ESR (µm)[b]	# T[c]	WM (Ma)[d]	SE (Ma)[e]
AP1[†]	*a1*	278998	7435444	3662	3.3	2.6	2.1	3.7	1.9	3.0	1.8	0.0	0.65	43.4	2	10.6	1.7
	a2	278998	7435444	3662	8.4	1.4	5.0	8.3	7.2	7.0	1.7	0.2	0.65	42.5	1		
	a3	278998	7435444	3662	13.1	0.2	27.6	79.6	7.8	46.3	3.0	2.4	0.72	53.9	1		
CA1	*a1*	278228	7418767	4414	11.2	0.9	18.3	5.0	19.6	19.5	0.3	0.7	0.56	33.8	0	6.8	0.2
	a2	278228	7418767	4414	37.4	1.9	2.9	19.9	17.9	7.6	7.0	1.0	0.65	42.3	2		
	a3	278228	7418767	4414	7.0	0.4	29.2	47.0	23.6	40.3	1.7	1.0	0.63	40.9	2		
	a4	278228	7418767	4414	6.6	0.4	26.6	59.2	34.7	40.5	2.3	0.9	0.60	37.3	r		
CA2[*]	*a1*	279564	7418488	4079	19.0	5.2	1.0	3.9	16.0	1.9	4.0	0.1	0.61	38.5	2	5.5	0.4
	a2	279564	7418488	4079	5.2	0.9	7.4	0.6	24.0	7.5	0.1	0.1	0.67	46.0	r		
	a3	279564	7418488	4079	6.1	1.4	3.6	24.1	28.5	9.3	6.9	0.2	0.62	39.8	2		
CA3	a1	280501	7418016	3894	7.1	0.2	48.0	101.1	28.5	71.7	2.2	1.7	0.62	39.6	1	6.2	0.4
	a2	280501	7418016	3894	5.9	0.7	9.0	21.3	67.4	14.0	2.4	0.3	0.62	39.2	2		
	a3	280501	7418016	3894	5.9	1.0	5.3	11.3	51.8	8.0	2.2	0.2	0.65	42.9	2		
	a4	280501	7418016	3894	5.7	1.1	5.5	18.4	30.0	9.9	3.4	0.2	0.59	37.0	1		
	a5	280501	7418016	3894	2.6	0.1	46.6	10.2	110.6	49.0	0.2	0.5	0.69	48.0	0		
CA4	a1	277480	7418741	4606	8.9	1.0	10.6	15.1	21.0	14.1	1.5	0.4	0.60	37.4	2	7.3	0.8
	a2	277480	7418741	4606	5.7	0.4	8.6	38.8	27.9	17.8	4.6	0.4	0.68	46.6	2		
	a3	277480	7418741	4606	8.0	0.2	71.1	43.5	7.0	81.3	0.6	2.5	0.71	51.0	2		
CA10	a1	292930	7414695	3348	4.2	0.3	11.2	20.7	7.1	16.0	1.9	0.3	0.73	54.9	2	4.3	0.1
	a2	292930	7414695	3348	4.0	0.5	9.6	21.7	24.3	14.7	2.3	0.2	0.66	44.7	1		
	a3	292930	7414695	3348	3.1	0.4	10.5	15.9	55.2	14.2	1.6	0.2	0.72	52.8	1		
	a4	292930	7414695	3348	4.4	0.2	62.5	6.9	13.2	64.1	0.1	1.1	0.70	50.0	r		
CO1	a1	279398	7426515	3669	7.8	0.4	5.2	26.4	24.4	11.4	5.3	0.4	0.75	60.1	2	4.8	0.7
	a2	279398	7426515	3669	3.0	0.4	2.2	20.6	16.4	7.1	9.5	0.1	0.70	49.8	1		
	a3	279398	7426515	3669	6.3	0.3	11.8	20.3	28.4	16.5	1.8	0.4	0.71	51.2	r		
	a4	279398	7426515	3669	4.5	0.3	3.2	22.2	13.0	8.5	7.1	0.2	0.74	57.9	0		
	a5	279398	7426515	3669	3.9	0.7	2.0	15.1	15.6	5.6	7.7	0.1	0.73	54.9	0		
CO2[*]	a1	280434	7426637	3985	10.4	0.5	22.2	1.7	24.3	22.6	0.1	0.9	0.67	45.2	1	27.8	19.0
	a2	280434	7426637	3985	2.7	1.7	0.4	17.4	16.2	4.4	49.9	0.0	0.63	40.7	2		
	a3	280434	7426637	3985	26.6	0.9	26.8	4.1	44.7	27.8	0.2	2.7	0.68	46.6	2		
	a4	280434	7426637	3985	157.4	2.1	22.4	4.5	50.6	23.4	0.2	14.0	0.68	47.5	2		
	a5	280434	7426637	3985	134.0	2.2	60.2	21.1	58.0	65.2	0.4	33.2	0.69	48.7	2		
CO3	*a1*	281464	7426391	4368	13.8	2.3	2.1	2.1	3.4	2.6	1.0	0.1	0.66	43.7	2	5.7	0.4
	a2	281464	7426391	4368	7.0	0.2	23.8	92.5	36.9	45.5	4.0	1.3	0.75	60.3	2		
	a3	281464	7426391	4368	6.2	0.3	15.5	18.2	86.3	19.8	1.2	0.5	0.72	53.8	2		
	a4	281464	7426391	4368	4.8	0.4	3.1	13.6	3.0	6.3	4.6	0.1	0.74	57.0	r		
	a5	281464	7426391	4368	5.0	0.8	1.2	9.9	3.4	3.5	8.9	0.1	0.72	53.1	2		

CO4	a1	283020	7426783	4668	5.7	1.3	3.6	18.8	4.8	8.0	5.4	0.1	0.60	37.7	1	11.3	3.1
	a2	283020	7426783	4668	7.8	0.5	6.5	25.7	19.0	12.5	4.1	0.4	0.71	52.1	1		
	a3	283020	7426783	4668	18.2	6.9	0.5	3.1	1.9	1.2	6.9	0.1	0.63	40.4	r		
	a4	283020	7426783	4668	21.4	2.5	2.4	8.9	21.5	4.5	3.8	0.3	0.60	37.4	2		
CO5	*a1*	283450	7425718	4886	10.2	0.2	41.9	24.1	81.2	47.6	0.6	1.8	0.66	44.0	2	6.4	0.4
	a2	283450	7425718	4886	5.9	0.5	13.3	42.0	35.1	23.2	3.3	0.5	0.63	40.7	1		
	a3	283450	7425718	4886	7.4	0.4	18.3	2.1	32.4	18.8	0.1	0.5	0.68	46.7	2		
	a4	283450	7425718	4886	6.0	0.7	5.9	20.0	40.8	10.6	3.5	0.2	0.67	46.0	1		
CO6	*a1*	283881	7425413	5093	7.1	0.6	6.4	19.4	28.2	11.0	3.1	0.3	0.68	46.5	2	6.5	0.1
	a2	283881	7425413	5093	6.5	0.3	27.3	160.1	45.2	65.0	6.0	1.4	0.63	40.0	1		
	a3	283881	7425413	5093	6.6	0.6	6.0	1.0	6.4	6.2	0.2	0.2	0.74	58.3	r		
	a4	283881	7425413	5093	7.6	1.8	1.6	1.0	5.7	1.8	0.6	0.1	0.71	52.1	1		
HO1	a1	275622	7428427	3329	9.1	2.3	1.6	11.3	24.2	4.3	7.3	0.1	0.63	40.5	0	10.8	2.1
	a2	275622	7428427	3329	5.8	0.7	1.2	2.9	1.3	1.9	2.6	0.0	0.80	75.2	r		
	a3	275622	7428427	3329	10. 8	1.2	1.7	5.7	3.8	3.0	3.5	0.1	0.73	56.5	1		
	a4	275622	7428427	3329	12.2	1.8	6.7	22.3	24.5	12.0	3.4	0.5	0.57	34.7	r		
	a5	275622	7428427	3329	21.3	2.1	0.9	4.3	2.6	1.9	4.8	0.2	0.71	52.3	r		
HO6	*a1*	276232	7424548	3604	2.4	1.8	3.9	5.5	2.7	5.2	1.5	0.0	0.62	39.5	2	7.3	0.3
	a2	276232	7424548	3604	7.7	0.5	6.6	19.6	18.1	11.2	3.1	0.3	0.66	44.2	r		
	a3	276232	7424548	3604	8.5	0.9	7.5	5.6	25.0	8.8	0.8	0.3	0.66	44.5	1		
	a4	276232	7424548	3604	6.7	0.6	4.2	7.3	2.1	5.9	1.8	0.2	0.71	52.2	r		
	a5	276232	7424548	3604	6.8	0.8	5.9	65.5	92.5	21.3	11.5	0.5	0.59	36.8	2		
HO7	a1	275315	7423806	3604	6.1	0.6	7.2	6.5	46.7	8.7	0.9	0.2	0.76	63.8	2	6.2	0.4
	a2	275315	7423806	3604	6.7	0.2	24.0	23.7	28.8	29.6	1.0	0.8	0.75	61.2	2		
	a3	275315	7423806	3604	5.4	0.4	7.1	31.0	6.8	14.4	4.5	0.3	0.74	58.1	0		
	a4	275315	7423806	3604	5.4	0.5	13.4	73.6	9.4	30.7	5.7	0.6	0.66	44.5	0		
	a5	275315	7423806	3604	7.8	0.6	32.4	1.7	88.1	32.8	0.1	0.9	0.62	39.7	2		
PIR1	*a1*	274082	7422808	3819	16.3	1.3	6.7	2.8	51.9	7.4	0.4	0.5	0.66	44.8	2	5.9	0.3
	a2	274082	7422808	3819	5.5	0.3	12.9	47.5	13.7	24.1	3.8	0.5	0.67	45.9	1		
	a3	274082	7422808	3819	6.5	0.6	11.6	68.7	45.9	27.8	6.1	0.6	0.60	37.9	2		
	a4	274082	7422808	3819	32.5	0.7	23.5	39.1	22.9	32.7	1.7	3.9	0.68	46.4	2		
	a5	274082	7422808	3819	5.5	1.2	9.2	6.2	10.4	10.6	0.7	0.2	0.61	38.3	2		
SA1	*a1*	289076	7433384	4716	2.6	0.5	3.2	20.9	23.9	8.1	6.7	0.1	0.72	53.3	0	6.7	0.3
	a2	289076	7433384	4716	7.3	0.6	12.3	14.9	5.7	15.8	1.2	0.4	0.67	46.0	0		
	a3	289076	7433384	4716	7.3	1.0	9.2	9.1	18.4	11.3	1.0	0.3	0.62	39.3	2		
	a4	289076	7433384	4716	5.7	0.8	2.9	9.4	5.0	5.1	3.4	0.1	0.70	49.5	2		
	a5	289076	7433384	4716	6.4	0.3	14.5	8.2	19.0	16.4	0.6	0.4	0.72	53.5	2		
SA2†	a1	289808	7433432	4525	15.5	0.8	11.9	2.6	32.3	12.5	0.2	0.7	0.70	50.3	1	10.4	1.2
	a2	289808	7433432	4525	13.1	0.3	15.5	6.0	12.8	16.9	0.4	1.0	0.79	70.0	r		
	a3	289808	7433432	4525	7.7	0.2	37.0	0.9	18.3	37.2	0.0	1.2	0.77	65.3	r		
	a4	289808	7433432	4525	9.0	0.1	45.4	34.0	30.5	53.4	0.8	2.1	0.80	73.7	2		
	a5	289808	7433432	4525	8.6	0.5	35.9	18.8	37.4	40.3	0.5	1.2	0.66	44.0	0		

SA4*	a1	293534	7421603	4280	3.3	0.2	7.4	75.6	29.1	25.1	10.6	0.3	0.71	52.4	1	4.6	0.7
	a2	293534	7421603	4280	3.9	0.7	3.0	34.0	36.1	11.0	11.6	0.2	0.66	44.1	2		
	a3	293534	7421603	4280	6.6	0.3	52.5	74.2	40.3	69.9	1.5	1.5	0.58	36.1	0		
	a4	293534	7421603	4280	5.5	0.7	4.9	65.1	21.5	20.2	13.8	0.4	0.62	39.5	0		
SA5*	a1	294499	7418946	3972	3.2	0.4	13.1	116.9	14.8	40.5	9.2	0.4	0.61	38.6	1	4.3	1.8
	a2	294499	7418946	3972	2.9	0.6	3.0	52.5	21.8	15.3	18.3	0.2	0.62	39.5	2		
	a3	294499	7418946	3972	10.2	0.4	13.9	67.5	33.9	29.7	5.0	1.0	0.60	37.8	2		
	a4	294499	7418946	3972	6.5	1.1	16.5	15.2	16.4	20.0	1.0	0.4	0.60	37.3	1		
	a5	294499	7418946	3972	2.4	2.0	1.2	29.6	3.4	8.2	25.2	0.1	0.63	40.3	2		
SA6	a1	294566	7416508	3606	4.4	3.4	1.0	10.1	22.6	3.3	10.9	0.0	0.59	36.5	2	4.4	0.8
	a2	294566	7416508	3606	5.7	0.3	30.1	31.6	28.5	37.5	1.1	0.8	0.71	51.3	r		
	a3	294566	7416508	3606	3.2	0.7	2.8	15.5	9.5	6.5	5.7	0.1	0.69	47.8	r		
	a4	294566	7416508	3606	0.9	0.5	3.7	42.8	8.8	13.7	12.1	0.0	0.66	44.0	r		
SA10	a1	299523	7411307	2760	2.3	0.8	12.9	23.1	27.1	18.3	1.9	0.1	0.57	35.3	r	2.8	0.3
	a2	299523	7411307	2760	2.5	0.3	12.5	56.0	12.4	25.7	4.6	0.2	0.66	44.4	r		
	a3	299523	7411307	2760	3.4	0.1	44.4	89.9	14.1	65.5	2.1	0.8	0.66	43.5	r		
	a4	299523	7411307	2760	3.0	3.3	1.6	10.3	6.2	4.0	6.7	0.0	0.62	39.2	r		
TAC2	a1	274077	7423106	3771	5.7	0.2	10.5	34.4	44.0	18.6	3.4	0.4	0.72	53.7	2	5.2	0.7
	a2	274077	7423106	3771	3.5	0.3	6.0	20.7	31.6	10.9	3.6	0.2	0.73	54.8	2		
	a3	274077	7423106	3771	7.4	1.0	8.9	30.4	30.5	16.0	3.5	0.4	0.59	36.3	1		
	a4	274077	7423106	3771	5.2	0.6	5.9	27.2	27.7	12.3	4.8	0.2	0.68	46.8	2		
TAC3	a1	274525	7424769	3468	7.3	0.8	5.3	23.0	17.5	10.7	4.5	0.3	0.66	44.4	0	6.5	0.5
	a2	274525	7424769	3468	5.6	0.9	4.5	25.2	30.6	10.5	5.7	0.2	0.67	45.1	2		
	a3	274525	7424769	3468	5.4	1.2	2.9	15.6	10.9	6.6	5.5	0.1	0.64	42.0	1		
	a4	274525	7424769	3468	8.5	0.5	12.3	26.5	23.6	18.5	2.2	0.6	0.69	48.4	2		
	a5	274525	7424769	3468	6.0	0.6	5.7	26.4	27.5	11.9	4.8	0.3	0.68	46.2	2		
ZE2	*a1*	287856	7440249	4795	133.8	4.2	4.6	14.3	32.3	7.9	3.2	3.4	0.56	34.3	0	5.9	0.2
	a2	287856	7440249	4795	6.0	0.7	17.8	44.7	67.0	28.3	2.6	0.5	0.57	34.6	2		
	a3	287856	7440249	4795	11.4	0.8	11.8	41.6	35.6	21.6	3.6	0.8	0.59	36.5	2		
	a4	287856	7440249	4795	5.9	0.6	25.5	18.1	25.7	29.8	0.7	0.6	0.61	38.2	2		
	a5	287856	7440249	4795	5.1	1.3	5.6	25.6	5.9	11.6	4.7	0.2	0.57	34.9	2		
ZE3	a1	288733	7439679	4547	21.4	1.0	13.2	16.1	15.6	17.0	1.3	1.2	0.62	39.7	2	17.7	1.3
	a2	288733	7439679	4547	14.7	1.3	9.3	36.7	15.0	18.0	4.1	0.8	0.55	33.5	1		
	a3	288733	7439679	4547	20.3	1.6	6.0	23.5	29.9	11.6	4.0	0.8	0.58	35.9	1		
	a4	288733	7439679	4547	18.9	1.0	13.7	37.0	12.1	22.4	2.8	1.4	0.59	36.4	1		
	a5	288733	7439679	4547	14.5	1.6	2.9	18.1	7.3	7.1	6.5	0.4	0.62	39.7	1		
	a6	288733	7439679	4547	8.3	0.8	12.5	13.0	27.5	15.6	1.1	0.4	0.63	40.3	1		
ZE4	a1	287123	7439286	4469	7.9	0.8	25.9	26.4	7.2	32.1	1.1	0.8	0.61	38.2	2	10.0	1.6
	a2	287123	7439286	4469	15.6	0.8	11.1	40.6	10.8	20.6	3.8	1.1	0.64	41.7	2		
	a3	287123	7439286	4469	28.4	2.8	4.8	14.4	10.7	8.2	3.1	0.8	0.62	39.0	0		
	a4	287123	7439286	4469	11.7	0.7	7.1	32.3	28.9	14.7	4.7	0.7	0.71	51.6	0		
	a5	287123	7439286	4469	7.0	0.5	34.6	49.7	5.8	46.2	1.5	1.0	0.58	35.3	0		

ZE6	a1	286380	7439116	4279	13.4	1.1	12.8	30.3	4.1	20.0	2.4	0.8	0.56	34.3	1	16.8	3.3
	a2	286380	7439116	4279	33.5	2.3	4.2	36.4	10.4	12.7	9.0	1.4	0.58	36.0	0		
	a3	286380	7439116	4279	17.5	1.2	13.3	22.8	16.0	18.7	1.8	1.0	0.58	35.5	1		
	a4	286380	7439116	4279	19.3	0.9	8.9	50.3	39.0	20.7	5.8	1.3	0.60	37.5	1		
	a5	286380	7439116	4279	8.9	0.5	26.7	78.1	28.5	45.0	3.0	1.3	0.59	36.4	2		
ZE8	a1	286011	7438216	4014	4.4	0.5	11.0	33.3	36.2	18.8	3.1	0.3	0.68	46.6	2	4.4	0.7
	a2	286011	7438216	4014	5.6	0.6	8.9	1.0	100.0	9.1	0.1	0.2	0.69	49.0	2		
	a3	286011	7438216	4014	3.0	0.4	3.0	35.8	15.7	11.4	12.3	0.1	0.69	48.0	2		
	a4	286011	7438216	4014	2.9	0.4	9.4	34.7	19.7	17.6	3.8	0.2	0.64	42.2	2		
	a5	286011	7438216	4014	7.5	0.4	21.1	2.2	3.6	21.6	0.1	0.6	0.65	43.0	0		
ZE9	a1	285526	7437805	3833	5.9	0.5	13.2	20.1	33.6	17.9	1.6	0.4	0.68	46.5	r	11.3	3.3
	a2	285526	7437805	3833	4.5	1.7	1.5	7.9	11.9	3.3	5.5	0.1	0.66	44.5	0		
	a3	285526	7437805	3833	15.7	1.2	9.2	1.5	46.2	9.5	0.2	0.5	0.65	42.5	2		
	a4	285526	7437805	3833	18.0	1.0	8.3	23.8	26.8	13.9	3.0	0.9	0.67	45.4	2		
	a5	285526	7437805	3833	24.4	2.8	2.4	15.3	40.9	6.0	6.5	0.5	0.56	34.2	r		
ZE10	a1	284804	7437689	3832	7.6	1.0	6.1	32.0	30.0	13.7	5.4	0.3	0.58	35.9	1	8.0	0.7
	a2	284804	7437689	3832	10.9	0.5	9.4	17.5	30.2	13.5	1.9	0.6	0.72	54.5	2		
	a3	284804	7437689	3832	6.5	0.2	15.1	132.2	43.0	46.2	9.0	1.1	0.68	46.9	1		
	a4	284804	7437689	3832	6.5	0.3	12.5	66.8	48.4	28.2	5.5	0.7	0.68	47.2	0		
	a5	284804	7437689	3832	9.5	0.4	7.8	51.7	28.7	19.9	6.9	0.7	0.71	50.9	0		
ZE11	a1	283832	7437649	3739	12.5	1.0	2.5	21.5	13.0	7.6	8.9	0.4	0.70	50.1	1	7.7	1.1
	a2	283832	7437649	3739	6.0	0.7	19.1	6.9	12.2	20.7	0.4	0.4	0.63	40.3	2		
	a3	283832	7437649	3739	10.5	0.3	3.6	22.7	17.8	9.0	6.4	0.4	0.76	63.5	2		
	a4	283832	7437649	3739	5.7	0.7	9.1	37.4	31.1	17.9	4.3	0.3	0.60	38.0	1		
	a5	283832	7437649	3739	6.1	0.8	5.2	44.4	21.2	15.7	8.8	0.3	0.61	38.6	1		

Zircon (U-Th-Sm)/He data																	
Sample	Aliquot	UTM N[a]	UTM E[a]	Z (m)	Age (Ma)	± 2σ (Ma)	U (ppm)	Th (ppm)	^{147}Sm (ppm)	eU (ppm)	Th/^{238}U	He (nmol/g)	F_T	ESR (µm)[b]	# T[c]	WM (Ma)[d]	SE (Ma)[e]
AP2	z1	277302	7435139	3866	115.6	1.9	76.3	27.1	0.3	82.7	0.4	38.8	0.75	48.0	2	119.0	3.3
	z2	277302	7435139	3866	126.2	3.8	407.6	321.6	1.0	483.2	0.8	235.8	0.71	41.9	2		
	z3	277302	7435139	3866	125.1	2.7	582.1	267.4	1.6	644.9	0.5	320.9	0.73	45.0	2		
	z4	277302	7435139	3866	110.5	1.8	253.1	132.2	1.3	284.1	0.5	124.2	0.73	44.7	2		
CA3	z1	280501	7418016	3894	404.4	3.9	279.9	147.5	0.7	314.5	0.5	543.7	0.77	52.5	2	404.9	0.7
	z2	280501	7418016	3894	318.3	4.1	79.6	42.5	0.5	89.6	0.6	126.6	0.80	62.6	2		
	z3[f]	280501	7418016	3894	403.4	3.1	266.8	110.1	0.6	292.6	0.4	509.3	0.77	54.1	2		
	z4	280501	7418016	3894	406.0	2.3	218.8	60.6	1.1	233.0	0.3	415.7	0.79	57.6	2		
CA8	z1	290050	7414244	2765	144.0	6.6	86.9	135.0	0.6	118.6	1.6	63.8	0.68	38.9	2	107.5	39.6
	z2	290050	7414244	2765	71.8	0.9	405.1	85.3	0.0	425.1	0.2	116.5	0.70	40.4	2		
	z3	290050	7414244	2765	42.6	0.7	157.4	136.3	1.0	189.4	0.9	31.1	0.71	42.3	2		
	z4	290050	7414244	2765	302.7	4.3	65.1	59.8	0.8	79.2	0.9	98.0	0.74	47.3	2		

CA10	z1	292930	7414695	3348	6.9	0.1	301.3	77.4	0.5	319.5	0.3	8.4	0.70	40.0	2	15.6	6.5
	z2	292930	7414695	3348	6.8	0.1	762.1	156.4	0.8	798.9	0.2	19.8	0.68	37.4	2		
	z3	292930	7414695	3348	51.5	1.1	66.6	123.8	0.9	95.7	1.9	19.3	0.72	45.1	2		
	z4	292930	7414695	3348	81.2	0.9	84.1	66.2	0.0	99.7	0.8	30.8	0.70	40.6	2		
	z5	292930	7414695	3348	9.4	0.1	619.3	22.2	0.5	624.5	0.0	22.9	0.72	42.8	2		
	z6	292930	7414695	3348	7.9	0.1	446.4	305.6	0.5	518.2	0.7	15.2	0.69	38.6	2		
HO1	z1	275622	7428427	3329	181.7	3.1	248.7	226.8	1.4	302.0	0.9	210.5	0.70	40.7	2	175.1	11.8
	z2	275622	7428427	3329	197.8	4.2	105.5	84.3	1.0	125.3	0.8	97.8	0.72	43.6	2		
	z3^{f}	275622	7428427	3329	149.6	1.9	114.9	124.1	0.9	144.0	1.1	88.3	0.75	49.7	2		
HO5*	z1^{f}	276734	7424820	3730	691.8	8.8	167.2	155.6	0.8	203.8	1.0	646.0	0.80	63.6	2	512.8	71.6
	z2	276734	7424820	3730	509.8	6.4	83.6	96.7	0.4	106.3	1.2	242.5	0.80	61.7	2		
	z3	276734	7424820	3730	382.5	3.4	184.0	157.4	1.0	221.0	0.9	345.7	0.73	46.3	2		
PIR1†	z1	274082	7422808	3819	431.6	5.3	164.8	59.3	0.4	178.8	0.4	343.3	0.79	60.2	2	469.1	72.6
	z2	274082	7422808	3819	295.8	3.7	187.5	114.7	0.2	214.4	0.6	268.5	0.77	52.7	2		
	z4	274082	7422808	3819	672.1	12.1	52.5	18.1	0.2	56.7	0.4	168.2	0.77	53.5	2		
	z5	274082	7422808	3819	564.9	8.7	95.2	72.9	0.1	112.4	0.8	257.4	0.72	43.2	2		
SA3*	z1	292502	7426625	4468	318.2	3.0	151.6	65.5	0.3	167.0	0.4	225.6	0.77	52.6	2	310.5	16.1
	z2	292502	7426625	4468	341.7	3.5	240.2	95.9	0.5	262.8	0.4	384.8	0.77	53.8	2		
	z3	292502	7426625	4468	457.5	6.6	122.2	66.4	0.2	137.8	0.6	266.1	0.75	49.6	2		
	z4	292502	7426625	4468	275.5	1.9	220.8	76.8	0.5	238.8	0.4	309.9	0.85	85.2	2		
SA10	z1^{f}	299523	7411307	2760	399.2	4.6	271.6	201.1	2.8	318.9	0.8	499.8	0.70	41.0	2	258.0	79.6
	z3	299523	7411307	2760	166.8	3.4	127.1	111.8	1.2	153.4	0.9	94.7	0.68	37.3	2		
SA11	z1	301469	7411570	2446	359.9	4.9	204.9	126.9	0.9	234.7	0.6	343.2	0.73	45.4	2	368.9	4.9
	z2^{f}	301469	7411570	2446	379.7	4.2	286.4	99.1	0.9	309.7	0.4	524.9	0.80	62.2	2		
	z3	301469	7411570	2446	367.0	7.2	313.3	37.2	0.5	322.0	0.1	488.8	0.74	47.0	2		
	z4	301469	7411570	2446	329.1	3.8	212.5	141.3	1.8	245.7	0.7	346.3	0.77	54.4	2		
TAC2	*z1*	274077	7423106	3771	424.5	2.2	278.3	22.6	0.3	283.6	0.1	510.4	0.76	49.9	2	452.7	2.4
	z2	274077	7423106	3771	454.0	9.7	145.7	121.9	0.1	174.4	0.9	315.7	0.71	42.4	2		
	z3	274077	7423106	3771	451.9	6.5	165.3	74.0	0.2	182.7	0.5	350.9	0.76	50.7	2		
	z4	274077	7423106	3771	335.3	3.7	140.6	47.1	0.7	151.7	0.3	205.1	0.73	44.2	2		
	z5	274077	7423106	3771	549.5	10.6	134.7	59.9	0.3	148.8	0.5	347.7	0.75	49.3	2		
TAC3†	z1	274525	7424769	3468	484.1	11.6	160.5	119.8	0.6	188.7	0.8	344.8	0.67	36.7	2	485.4	1.8
	z2	274525	7424769	3468	608.1	3.6	116.1	38.3	0.3	125.0	0.3	314.1	0.73	44.2	2		
	z3	274525	7424769	3468	154.6	1.2	240.8	32.0	0.2	248.4	0.1	149.7	0.71	41.9	2		
	z4	274525	7424769	3468	485.7	4.8	176.4	52.1	0.1	188.6	0.3	359.5	0.70	39.6	2		
	z5	274525	7424769	3468	445.8	10.2	184.7	108.3	0.4	210.2	0.6	370.4	0.71	41.2	2		
ZE3	z1	288733	7439679	4547	5.9	0.1	365.2	319.4	1.4	440.3	0.9	10.4	0.74	47.5	2	35.7	19.0
	z2	288733	7439679	4547	6.1	0.1	220.3	193.5	1.4	265.8	0.9	6.3	0.72	44.6	2		
	z3	288733	7439679	4547	153.5	2.8	113.1	97.7	1.0	136.0	0.9	80.8	0.71	41.8	2		
	z4	288733	7439679	4547	79.7	0.7	342.8	344.8	1.0	423.8	1.0	140.6	0.77	53.3	2		
	z5	288733	7439679	4547	52.2	0.6	621.4	118.4	0.7	649.2	0.2	136.6	0.75	47.7	2		
	z6	288733	7439679	4547	90.9	1.5	318.5	211.0	0.4	368.1	0.7	131.8	0.72	44.4	2		

ZE11	z1	283832	7437649	3739	320.3	9.3	198.7	105.5	0.7	223.5	0.5	285.4	0.72	43.3	2	352.6	68.0
	z2	283832	7437649	3739	552.3	9.3	135.3	57.2	0.8	148.7	0.4	357.1	0.77	53.1	2		
	z3	283832	7437649	3739	248.0	3.0	133.0	121.5	0.6	161.5	0.9	167.5	0.76	51.6	2		

[a]UTM zone 20K

[b]Equivalent spherical radius

[c]Number of crystal terminations

[d]Weighted mean age calculated in IsoplotR, excluding outliers

[e]Standard error of the weighted mean age

[f]Aliquots were heated > 2 times

[*]Samples with age-F_T relationship

[†]Samples with age-eU relationship